UNIVERSITY OF GLASGOW

QUANTITATIVE MEASUREMENT USING SCANNING THERMAL MICROSCOPY

PRESENTED BY

YUNFEI GE

A THESIS SUBMITTED IN PARTIAL FULFILMENT FOR THE DEGREE OF DOCTOR OF PHILOSOPHY

IN THE

SCHOOL OF ENGINEERING

JULY 11, 2016

Abstract

This thesis reports on the development of quantitative measurement using micromachined scanning thermal microscopy (SThM) probes. These thermal probes employ a resistive element at their end, which can be used in passive or active modes. With the help of a review of SThM, the current issues and potentials associated with this technique are revealed. As a consequence of this understanding, several experimental and theoretical methods are discussed, which expand our understanding of these probes.

The whole thesis can be summarized into three parts, one focusing on the thermal probe, one on probe-sample thermal interactions, and the third on heat transfer within the sample. In the first part, a series of experiments are demonstrated, aimed at characterizing the probe in its electrical and thermal properties, benefiting advanced probe design, and laying a fundamental base for quantifying the temperature of the probe. The second part focuses on two artifacts observed during the thermal scans – one induced by topography and the other by air conduction. Correspondingly, two devices, probing these artifacts, are developed. A topography-free sample, utilizing a pattern transfer technique, minimises topography-related artifacts that limited the reliability of SThM data; a controlled temperature 'Johnson noise device', with multiple-heater design, offers a uniform, accurate, temperature distribution. Analyzing results of scan from these samples provides data for studying the thermal interactions within the probe and the tip-sample interface. In the final part, the observation is presented that quantification of measurements depends not only on an accurate measurement tool, but also on a deep understanding of the heat transfer within the sample resulting from the nanoscopic contact. It

is believed that work in this thesis contributes to SThM gaining wider application in the scientific community.

AUTHOR DECLARATION

I declare that, except where explicit reference is made to the contribution of others, the substance of this thesis is the result of my own work and has not been submitted for any other degree at the University of Glasgow or any other institution.

Selected portions of the work described herein have been published, in press or submitted elsewhere as listed below:

[1] **Yunfei Ge**, Yuan Zhang, Jonathan M. R. Weaver, Haiping Zhou, and Phillip S. Dobson, "Topography-free sample for thermal spatial response measurement of scanning thermal microscopy," *Journal of Vacuum Science and Technology B*, vol. 33, no. 6, 06FA03, 2015. DOI: 10.1116/1.4933172

[2] **Yunfei Ge**, Yuan Zhang, Jamie A. Booth, Jonathan M. R. Weaver, and Phillip S. Dobson, "Quantification of probe-sample interactions of a scanning thermal microscope using a nanofabricated calibration sample having programmable size," *Nanotechnology*, vol. 27, no. 32, 325503, 2016. DOI: 10.1088/0957-4484/27/32/325503

[3] **Yunfei Ge**, Yuan Zhang, Jonathan M. R. Weaver, and Phillip S. Dobson, "Dimension and shape-dependent thermal transport in finite dimensional rectangular thin films investigated by scanning thermal microscopy," Submitted.

ACKNOWLEDGEMENT

First of all, I would like to thank my supervisor Dr. Phil Dobson, with whom I had the privilege and the fortune to work for nearly four years. He is both an excellent mentor, guiding me through my studies and research as a researcher, and good friend, enabling me to develop as a person. There is nothing more enjoyable than those moments that I can immediately share my popped-out ideas (sometimes naive) and confusions (sometimes too simple) with him at any time by any means. Without Phil's patience, creativity, encouragement and dedication, this thesis will never be completed.

I would also like to thank Prof. John Weaver, whose creative ideas can always push me digging the work deeply and inspire me. I am grateful for his contributions on building the measurement instrumentations, his advice on theoretical calculations and his continuous support on paper works.

A special thank goes to Dr. Yuan Zhang. She not only initiated me into the art of nanofabrication, taught me the thermal scan skills, or passed on all her ideas, but also, which is possibly the most important, recognized my strengths and weaknesses and imparted her positive attitude towards the science to me.

I would like to thank Dr. Xu Li, for his experienced viewpoint of nanotechnology, and profound knowledge of almost everything. I am really grateful for his time talking with me and easing out my anxiety.

I will also give my appreciation to QUANTIHEAT European project for provision of resources and financial support.

Finally, I cannot be more grateful for the support from my parents. Mum and Dad, I will never forget the time you staying with me at the other side of the FaceTime or mobile when I was disappointed, and the moments we shared our tears and laughers. I know how much you have sacrificed for me. I love you both forever.

CONTENTS

1 INTRODUCTION: TEMPERATURE AND MEASUREMENT TECHNIQUES 1

1.1 THERMAL TRANSPORT IN NANOSCALE 3

1.2 TECHNIQUES FOR MEASURING TEMPERATURE IN SUB-MICRON SCALES 6

1.2.1 Thermometry based on optical signals 6

1.2.2 Thermometry based on electrical signals 9

1.3 SThM AS THE FINAL RESEARCH DIRECTION 11

1.4 THESIS ORGANIZATIONS 14

2 SCANNING THERMAL MICROSCOPY (SThM): REVIEW AND UNDERSTANDING 17

2.1 DEVELOPMENT OF THE SThM 19

2.2 SThM WITH VARIOUS THERMAL SENSORS 21

2.2.1 Thermoelectric sensors 21

2.2.2 Thermal resistive sensors 24

2.3 QUANTIFYING THE SThM MEASUREMENT 28

2.3.1 Probe calibration 28

2.3.2 Uncertain factors in passive mode measurement 33

2.3.3 Uncertain factors in active mode measurement 34

2.3.4 Determination of uncertain factors 34

2.4 ARTIFACTS IN SThM MEASUREMENT 41

2.5 SUMMARY 45

3 CHARACTERIZATION AND OPTIMIZATION OF THERMAL PROBE WITH NULLING PROBE DESIGN 47

3.1 CHARACTERIZATION OF THE SThM PROBE 50

3.1.1 Temperature coefficient of resistance 50

3.1.2 Failure analysis of the probe 55

3.1.3 Stability test of probes 61

3.1.4 Self-heating test of the probe 64

3.2 NULLING PROBE DESIGN AND SIMULATION 69

3.2.1 Design strategy 69

3.2.2 Probe simulation 71

3.3 THERMAL BENDING COMPENSATED SiN_x PROBE 74

3.3.1 Principle and issue 74

3.3.2 Process development with large patterns 77

3.3.3 Process development with actual-size patterns 80
3.3.4 Test of thermal bending compensated probe 83
3.4 FABRICATION AND TEST OF NULLING PROBE 85
3.5 SUMMARY 87
4 TOPOGRAPHY-FREE SAMPLE FOR THERMAL SPATIAL RESPONSE MEASUREMENT 88
4.1 SAMPLE DESIGN AND FABRICATION 90
4.1.1 Pattern-transfer based process 90
4.1.2 Design of the pattern 94
4.1.3 Development of the process 95
4.2 EXPERIMENTAL SETUP 101
4.3 SCANNING RESULTS AND DISCUSSION 102
4.3.1 Demonstration of 35 nm wide gold wire 102
4.3.2 Analysis of the incompletely resolved phenomenon 104
4.3.3 An exception thermal scan – 25 nm wide wire 110
4.4 CONCLUSION 113
5 QUANTIFICATION OF PROBE-SAMPLE INTERACTIONS OF A STHM USING A NANOFABRICATED CALIBRATION SAMPLE HAVING PROGRAMMABLE SIZE 115
5.1 JN DEVICE DESIGN AND FABRICATION 117
5.1.1 Device design strategy 117
5.1.2 Batch fabrication lithography design 119
5.1.3 Device fabrication 121
5.2 EXPERIMENTAL METHODS 124
5.2.1 Finite element analysis of the JN device 124
5.2.2 SThM setup for temperature measurement 126
5.3 RESULTS AND DISCUSSION 129
5.3.1 Experimental verification of the FEA model 129
5.3.2 Probe calibration 131
5.3.3 1D heat transfer model for probe-sample interactions 133
5.3.4 Analysis of thermal interactions and determination of contact radius 138
5.3.5 Characterization of the SThM probe using JN device 142
5.4 CONCLUSION 150
6 ANALYSIS OF HEAT TRANSFER IN THIN FILMS WITH FINITE DIMENSIONS 151
6.1 MOTIVATIONS 152
6.2 SAMPLE DESIGN AND FABRICATION 156

6.2.1 Pattern design 156
6.2.2 Sample fabrication 158
6.3 EXPERIMENTAL METHODS 160
6.4 MODEL FOR NANOSCOPIC TO FINITE-DIMENSIONAL CONTACT HEAT TRANSFER 164
6.5 EXPERIMENTAL RESULTS AND DISCUSSION 170
6.5.1 Determination of equivalent temperature coefficient of the substrate "h_s" 170
6.5.2 Determination of size effect by both modelling and measurement 171
6.5.3 Investigation of shape dependence of thermal spreading resistance . 178
6.5.4 Determination of effective contact radius 184
6.6 CONCLUSION 188
7 FINAL REMARKS 190
7.1 SUMMARY AND CONCLUSIONS 190
7.2 OUTLOOK 194
BIBLIOGRAPHY 197
APPENDIX I 214
APPENDIX II 216
APPENDIX III 218
APPENDIX IV 220
i. Code for determining the "h_s" value 220
ii. Code for determining the R_{Au} of 200 nm and 400 nm wide wires 221
iii. Code for determining the R_{Au} with different contact positions 222

LIST OF FIGURES

Figure 1.1 Thermal propagation mechanisms for varying mean free path of the heat carriers and the characterization length of the material. (a), (b) and (c) represents diffusive, ballistic and diffusive-ballistic thermal transport respectively..... 4
Figure 1.2 Illustration of the challenge of SThM. The contact area between the SThM and the sample is down to nanoscale, which results in a thermal coupling much weaker than that to the base..... 12
Figure 2.1 Description of the working principle of the SThM. The dashed connection line represents that the SThM can be established based on two types of AFM – the displacement system of which is either the sample stage or probe stage..... 20
Figure 2.2 Schematic diagram of the fabrication of the grooved SThM probe. (I) 100 nm SiN_x deposited on the both sides of a 3 inch 400 μm thick double-side polished silicon wafer, (II) bottom side silicon KOH wet etching to define the position of cantilever, (III) define the pyramid on the top side using SiN_x as mask, (IV) strip the SiN_x mask by 1:5 HF:H_2O, (V) define the groove on the cantilever by photolithography and dry etching, (VI) 500 nm SiN_x deposited on both sides by low pressure chemical vapour deposition (LPCVD), (VII) define the shape of the cantilever on the top side, (VIII) strip the SiN_x on the bottom side for the probe final defining and releasing, (IX) metallisation on the cantilever, first 40 nm platinum at the end of the tip and then 150 nm gold as wires, and (X) TMAH wet etching for final release of the probe..... 26
Figure 2.3 Schematic diagram shows the heat transfer interactions between the probe and the sample, together with the thermal resistance network showing the relationship between each interaction for (a) the probe working in passive mode scanning on the active sample, and (b) the probe working in active mode by Joule heating scanning on the passive sample..... 32
Figure 2.4 Schematic of heat transfer through the whole probe when contacting the probe onto the sample for (a) the heated doped silicon probe working in active mode (as it is seldom used in passive mode), and (b) the SiN_x probe, which has the same profile in both active and passive mode. Both probes are represented by their thermal profiles..... 39
Figure 2.5 Schematic of a SThM probe interacting with the sample by contact with a valley and peak, showing the source of topographical artifacts. The sample is at a uniform temperature, and the probe scans with a constant force. At the bottom showing the atomic scale explanation of the topographic artifacts..... 43

Figure 3.1 Thermal resistance network between the SThM probe in passive mode and the active sample. 49
Figure 3.2 Experimental setup showing the measurement of the probe TCR. 52
Figure 3.3 Plot of the temperature of SThM probe with platinum resistance element versus its resistance. R^2 is the coefficient of determination indicating the linearity of the fitted line. 54
Figure 3.4 Plot of the temperature of SThM probe with palladium resistance element versus its resistance. R^2 is the coefficient of determination indicating the linearity of the fitted line. 54
Figure 3.5 Plots of current versus the voltage applied on the probe measured by a probe station in 2-terminal operation mode. The data has been categorised using different colours corresponding to each of the four groups. 56
Figure 3.6 SEM image of the failed probes from Group (a) 1, (b) 2 and (c) 4. 58
Figure 3.7 (a) Plot of the probe temperature rise versus the power applied to the probe for four groups corresponding to the Figure 3.5, and (b) plot of the 1st order derivation of the temperature rise to the power for the probes in Group 3. 60
Figure 3.8 Experimental setup for the probe stability test. The mbed NXP LCP 1768 [23] was used to record the voltage across the probe. One probe is shown in the figure with the other two sharing the same setup. 62
Figure 3.9 Plots of the probe resistance versus time indicating probe stability for probe biased by 1 mA, 1.5 mA and 2 mA. 63
Figure 3.10 Schematic of the circuit used to dynamically measure the self-heating current of the probe. 65
Figure 3.11 Plots of output voltage recorded by the oscilloscope versus time. Probes biased under five different currents are examined and demonstrated individually in different colours. 66
Figure 3.12 Thermal resistance network of Joule heated probe in air. 68
Figure 3.13 (a), (b), (c), and (d) illustrate four designs of nulling probe with the change of position and size of heaters on the cantilever. Thermocouple and Johnson noise thermometer are the same for all designs as shown in the inset. 70
Figure 3.14 Simulation results of four probe designs showing the temperature distribution on the cantilever, with the inset showing the temperature of the tip. 72
Figure 3.15 Plots of temperature distribution from the tip (0) to the base of the cantilever (150 μm) for all designs. 73
Figure 3.16 Schematic diagram showing the position of the groove on the cantilever, as well as the groove working principle. 75
Figure 3.17 SEM image showing the AZ4562 photo resist profile (a) after development, and (b) after dry etching by the original recipe. 76
Figure 3.18 SEM image of (a) silicon substrate with the AZ4562 after hardbake, (b) the profile of the silicon substrate and the AZ4562 after dry etching, (c) and (d) the profile of the silicon shallow etching after stripping the AZ4562. 78

Figure 3.19 SEM images show the profile of sidewalls after mixing the CF_4 with O_2. 79
Figure 3.20 SEM images (a) and (b) show the profile of sidewalls achieved by increasing the plasma pressure from 55 mTorr to 65 mTorr, (c) increasing the pressure to 75 mTorr and (d) reducing the pressure to 45 mTorr. 79
Figure 3.21 SEM image shows the profile of sidewalls by transferring the recipe developed with the large patterns to the actual-size patterns for (a) Area 1, (b) Area 2, with (c) and (d) shows the corresponding area of (a) and (b) respectively after 75 nm thick NiCr deposited. 80
Figure 3.22 Optical microscopy images show the profile of AZ4562 (a) before and (b) after 120 °C oven hardbake. 81
Figure 3.23 SEM images showing the profile of silicon shallow etched sidewalls for (a) Area 1 and (b) Area 2 as the result of raising the hardbake temperature from 120 °C to 180 °C, with (c) and (d) showing the corresponding profile to (a) and (b) respectively after increasing the ratio of O_2 in the plasma. All profiles are checked by depositing a 75 nm thick NiCr onto the sample. 82
Figure 3.24 Calibration of both the normal probe (blue squares) and the thermal bending compensated probe (red circles), plotted as the temperature of the device against the voltage from Wheatstone bridge. 84
Figure 3.25 SEM image corresponding to (a) design a, and (b) design b of nulling probe demonstrated in Figure 3.13. An enlarged imaged showing the tip is placed between them. 86
Figure 3.26 Plots of temperature distribution on the trace from the tip to the base of the cantilever. Black squares and blue circles represent the scanning results of design (a) and (b), while the green line and red line shows the data from the corresponding FEA model. 86
Figure 4.1 Schematic shows the misalignment between two levels of lithography for an etched trench and the metal deposited aiming to fill it. Offset error and rotation error are both illustrated, except for the scale error which changes the size of each alignment layer. 91
Figure 4.2 Fabrication process flow of the topography-free sample. 93
Figure 4.3 (a) Design of the pattern of topography-free sample with the marker strategy for alignment in EBL, and (b) Enlarged image showing the single pattern design: three 1 μm long gold wires positioned at the centre of the gap formed by two gold pads. 95
Figure 4.4 The sample surface after release etching without the SiN_x layer to enhance the adhesion. Simple patterns, varying with the shape in square (a) and circle (b) and their size, are designed for testing the process more efficiently. 97
Figure 4.5 (a) Optical microscope image of the topography-free sample with high stress SiN_x adhesion enhancement layer and (b) AFM height image of the same

sample, the scan region is indicated by the dashed square in (a). Wrinkles are highlighted in regions A and B. 98
Figure 4.6 Step heights between gold and SiN_x on the sample surface after release etch versus the thickness of SiN_x. The inset image shows the AFM scan used for obtaining the step height. 99
Figure 4.7 (a) SEM image of the pattern after release etching, (b) detail of the narrow wire zoomed in from (a), (c) tapping mode AFM topographic image showing the same area as (a), and (d) detail of the narrow wire zoomed in from (c) showing a residual topographic variation of less than 2 nm. 100
Figure 4.8 Photo of the complete topography-free sample shows that the general view of the sample. 100
Figure 4.9 Schematic diagrams showing the electrical arrangement used to bias the probe and to detect the probe electrical resistance change. 102
Figure 4.10 (a) Backscatter SEM image shows the 35 nm narrow gold wire, (b) AFM topographic image shows the same wire as (a), (c) thermal image of the same feature scanned by SThM probe, (d) plot of the line trace for SEM image, and (e) topography and thermal signals. Dotted circles in (d) and (e) indicate the signal of the gold wire and SiN_x. 103
Figure 4.11 (a) Heat transfer interactions between the probe and the sample, together with the thermal resistance network showing the relationship between each interaction, and (b) different thermal diffusion as a result of variation in the width of gold wires. Gold wire 1 and gold wire 2 indicate the narrow and relatively wide wire, respectively. Heat spreading is represented by hemispherical areas surrounding the gold wires. 104
Figure 4.12 (a) SEM image shows the 75 nm narrow gold wire, (b) AFM topographic image, (c) thermal image showing the same feature scanned by SThM probe, and plots of the line traces from (d) SEM image and (e) topography and thermal signals. Dotted circles in (d) and (e) indicate the signal of the gold wire and SiN_x. 108
Figure 4.13 Plot of the thermal intensity ratio versus the width of the gold wire. The inset image shows the 5 × 50 pixels rectangular regions used to obtain the averaged signal from wire, gold pad and SiN_x. 109
Figure 4.14 (a) SEM image showing the 25 nm narrow gold wire, (b) AFM topographic image, (c) thermal image showing the same feature scanned by SThM probe, and plots of the line traces from (d) SEM image and (e) topography and thermal signals. Dotted circles in (d) and (e) indicating the signal of the gold wire and SiN_x. 111
Figure 4.15 (a) SEM image showing the 35 nm narrow gold wire with 250 nm length, (b) plot of line trace from SEM image, (c) AFM topographic image and (d) thermal image showing the same feature scanned using a SThM probe. 112
Figure 5.1 (a) General view of the design of the components on the membrane, (b) close up of one of the large heaters IV, (c) close up of the dashed square in (a), and (d)

three-dimensional cross-section view taken through line A-A′ showing the membrane supported by the silicon substrate. The surface (111) is 54.7° with the horizontal surface (110) and acts as a etch-stop surface. 117
Figure 5.2 Mask design for one single device (top) with three images closed-up showing the detail (bottom). 120
Figure 5.3 Wafer layout design used for a batch of devices. Both EBL and photolithography layer are designed simultaneously in one layout, which can be split during the fabrication. The signs "S" and "L" correspond to the small and large flat of the silicon wafer. 121
Figure 5.4 Fabrication process of the JN device in the steps (a) to (f). 122
Figure 5.5 SEM image of the JN device: (a) general view of the whole device including the membrane (dark grey area) and gold connecting wires (brightest wires), (b) details of features from the dashed square I in figure (a) showing four large heaters and four large gold shields on the membrane, (c) details of features in the dashed square II in figure (b) showing four small heaters and four small gold shields, and (d) details of features in the dashed square III in figure (c) showing the 2 μm diameter gold contact target with the NiCr 4-terminal split resistor surrounding it. Photo (e) shows the complete JN device bonding onto a specifically designed PCB. 123
Figure 5.6 3D model built in COMSOL MULTIPHYSICS® for simulating the thermal performance of the JN device. (a) is the general view of the device covered by a block of air, (b) (c) and (d) shows the 'Thin Layer' set on the SiN_x membrane, all gold elements and all NiCr layers. 126
Figure 5.7 Schematic of the experimental setup for passive SThM probe scanning of the *in-situ* JN device. The probe forms a Wheatstone bridge with R_M, R_1, and R_2. T_1 and T_2 are transformers used for exciting and measuring the output of the bridge. 127
Figure 5.8 Plot of the average temperature on the 4-terminal resistor versus the power on heaters obtained from the experiment (black diamonds) and FEA model (red circles) for JN device working in (a) large heaters and (b) small heaters mode; (c) and (d) shows the temperature distribution at the centre of the membrane for each case. 131
Figure 5.9 The temperature of the 4-terminal resistor on the JN device versus the DC output of the lock-in amplifier for the small heater and large heater. Parameters of the linear fit are shown with the R^2 value. The error bars are one standard deviation as obtained from the random variation in the data points. 132
Figure 5.10 Schematic diagram shows the geometry of the passive probe scanning on the active sample. Three regions of heat exchange between the probe and sample through air conduction are determined by the separation and are shown as A, B, and C marked in different colours. 133
Figure 5.11 (a) and (b) illustrate the JN device temperature distribution from the FEA model. A 65 μm long trace A-A′ across the centre of the membrane shows the section

used for the data plotted in (c) showing the temperature difference from the ambient. (d) and (e) demonstrate a comparison, for the same region, between experimental data and modelled data corrected in using the heat transfer equation by different G_{ts}. 137
Figure 5.12 (a) Constriction model between the tip and surface based on the DMT model determined contact radius, (b) associated thermal resistance network, (c) constriction model between the tip and surface with the apex radius equal to the contact radius and (d) associated thermal resistance network. 139
Figure 5.13 (a) – (e) shows the five parts A-E of the probe, each having different dimensions, materials and air conduction regimes. The probe with 69° and 13° oriented components as used in the coordinates of the calculation, and (f) model used for calculating the heat flow thermal resistance through the probe. 144
Figure 5.14 Thermal resistance network for the lumped model of the probe contacting a heated surface. The voltage source represents the temperature of JN device, in this instance providing a uniform temperature beneath the probe cantilever. 145
Figure 5.15 Probe temperature obtained from the thermal scan experiment (blue squares) and from the lumped system model (red circles). 148
Figure 5.16 Probe temperature versus the sample temperature with a heated region of 16 μm (black squares) and 0 as an extreme condition (red circles). 149
Figure 6.1 Patterns designed to investigate the size dependence of thermal conductivity measurements. (a) shows four blocks, in which contains gold wires in the same width but different length, (b) shows an enlarged view of one block, demonstrating the pattern arrangement with constant feature width but variable length (increasing left to right), and (c) shows an enlarged image demonstrating the detail of a single pattern. 157
Figure 6.2 Optical image of the sample surface after release for (a) 400 nm and (b) 800 nm thick low stress ICP-CVD SiN_x. A simple pattern was employed to permit rapid process optimization. 159
Figure 6.3 Sample surface after release with 500 nm thick low stress ICP380 SiN_x film observed by optical microscopy. 160
Figure 6.4 The schematic diagram of the circuit used for driving the probe working in either the passive or active mode. 162
Figure 6.5 Heat transfer in finite-dimension gold film. (a) top view of the film on a substrate that is regarded as bulk, (b) heat transfer mechanisms in spherical coordinates of a radial fin, the diameter of which equals to the width of gold wire, and (c) heat transfer mechanisms in a plane wall connected to the radial fin. 166
Figure 6.6 Thermal resistance network of a probe in contact with SiN_x. $R_{tip\text{-}SiN}$ is the thermal interfacial resistance between the tip and SiN_x, R_{SiN} is thermal spreading resistance of SiN_x substrate, R_i^{SiN} and R_i^{pt} are thermal resistance due to thermal

conduction within the probe and Riairwith Risubrepresents the air conduction effect on the sample. 172
Figure 6.7 Thermal resistance network for probe contacting on the gold wire. A and B inherit from the model shown in Figure 5.14 with the addition of R_i^{sub}. C, D and E share the same structure as A and B and have been simplified here. 174
Figure 6.8 Thermal image of a gold wire on topography-free sample with 400 nm width and 700 nm length. The thermal signal is shown as the output of the measurement instrumentation and represented as electrical voltage. 175
Figure 6.9 Plots of tip temperature from both measurement (black squares in (a) and blue triangles in (b)) and thermal resistance network (red diamonds in (a) and purple circles in (b)) versus the length of gold wire in (a) 200 nm wide and (b) 400 nm wide. 176
Figure 6.10 Design of (a) "Dogbone" patterns with (b) individual wires named as "fake Dogbone" in the same schematic. 179
Figure 6.11 Thermal images of "Dogbone" patterns with widths (a) 200 nm, (b) 300 nm, (c) 400 nm and (d) 500 nm, in comparison to isolated wires with the same widths (e), (f), (g) and (h). 181
Figure 6.12 Plots of the SThM tip temperature when measuring the "Dogbone" pattern. Blue squares and red circles indicate the measured and modelled tip temperature of the "Dogbone", for comparison, the measured tip temperature for isolated wires is shown by black diamonds. The inset figure gives the plot of thermal resistance of the "Dogbone" pattern (green squares) with that of individual wires (orange triangles). 182
Figure 6.13 Contour showing the thermal resistance against the width and length of gold wires with both the length and width varying. 184
Figure 6.14 Principle of the effective contact radius measurement. 185
Figure 6.15 Schematic of probe in contact with a gold wire at the position away from the centre. 185
Figure 6.16 Thermal resistance difference between the probe contacting at the edge and the centre of the gold wire. ΔR_1 is for 200 nm wide wire (black squares), and ΔR_2 is for 400 nm (red circles). 187
Figure 6.17 (a) Thermal image of gold wire with two traces (A-A′ and B-B′) at top and bottom edges, and (b) plots of the thermal response for these two traces against scan length. 188

LIST OF TABLES

Table 3.1 Eight SThM probes in four groups with different test conditions····· 56
Table 5.1 Thermal conductivity of each element in JN device····· 125
Table 5.2 Values of each thermal resistor used in the lump-heat-capacity system 146

NOMENCLATURE

ABBREVIATION	TERM
AFM	Atomic force microscopy
BEXP	Beam exit argon ion cross-section polishing
C-AFM	Conductive atomic force microscopy
CMP	Chemical mechanical planarization
DMT	Derjaguin, Muller, and Toporov
EBL	Electron beam lithography
FEA	Finite element analysis
FIB	Focused ion beam
GTE	Global thermal equilibrium
ICP-CVD	Inductively coupled plasma chemical vapour deposition
JN	Johnson noise
LPCVD	Low pressure chemical vapour deposition
LTE	Local thermal equilibrium
MFP	Mean free path
ODE	Ordinary differential equation
PMMA	Poly(methyl methacrylate)
RIE	Reactive ion etching
SEM	Scanning electron microscopy
SPM	Scanning probe microscopy
SNOM	Scanning near-field optical microscopy
SNR	Signal-to-noise ratio
STM	Scanning tunneling microscopy
SThM	Scanning thermal microscopy
STP	Scanning thermal profiler

TCR	Temperature coefficient of resistance
W-F	Wiedemann-Franz

1

INTRODUCTION: TEMPERATURE AND MEASUREMENT TECHNIQUES

The measurement of temperature has been a fundamental tool in fields of science and engineering ever since the pioneering work of researchers such as Celsius and Fahrenheit in the 18th century. Despite this maturity, modern applications continue to challenge the technology of temperature measurement by pushing it into ever more demanding scenarios. Over the past 20 years, the trend described by Moore's Law has seen modern electronic and opto-electronic devices such as silicon-on-insulator transistors and light-emitting diodes shrink to nanometre scale [1]. This has had a positive impact on nearly every aspect of human life, but has put increasing demands on the thermal characterization of devices and materials at the nanoscale [2,3].

In particular, more extreme self heating generated by semiconductor components results in more errors and is associated with reduced lifetime [4]. To minimise these effects, it is necessary to reduce energy dissipation or efficiently remove heat from the device. The latter approach, in particular, relies on the conduction of heat through the device and its surrounding materials. One method to maximise this conduction makes use of composite

substrates. These samples are produced by directly bonding or growing the semiconductor devices onto materials with high thermal conductivity, such as diamond [5,6] and SiC [7]. In addition, advanced nanofabrication methods are permitting the production of an increasing number of nanoscale devices and structures based around new materials such as carbon nanotubes [8], nanowires [9], superlattices [10] and graphene [11], which have found their applications in practical work. For example, carbon nanotubes have been demonstrated as the channel of field-effect transistors in place of bulk silicon, making use of their excellent electrical and thermal properties [4], graphene's excellent thermal conductivity makes it a promising material for thermal management and applications in electronic interconnects [12], and nanowires have opened new possibilities for improving the efficiency of thermoelectric materials due to their low thermal conductivity [13]. All of the above require knowledge of energy transfer at small scales, and more specifically, heat.

Heat results from the transfer of thermal energy flowing through objects with different temperature, as they move towards thermodynamic equilibrium. However, heat is an intermediate quantity, which can be defined only in relation to energy change and can hardly be measured. In contrast, temperature is a function of material state, which can be used as a property to describe the state of a system, and is said to be an intensive parameter based on the thermal equilibrium. The concept of temperature is essentially an equation of state and is defined as [14]

$$T = \left(\frac{\partial U}{\partial S}\right)_{V,N_1 \ldots N_r} \qquad \text{eq. 1.1}$$

with respect to each of the parameters, the internal energy U, the entropy S, the volume V and the number of particles N. Major challenges associated with the investigation of temperature at the nanoscale therefore arise; for example, thermal equilibrium can only be established if there is a sufficiently large statistical ensemble. This chapter will attempt to illustrate these challenges.

1.1 Thermal Transport at the Nanoscale

Thermal transport is measured as the temperature distribution in an object. This means that an absolute limit must exist, beyond which the quantitative measurement of temperature will be impeded by the size of the system [15]. In a material, it has been widely recognized that there are two particles that predominantly carry heat, these are phonons (or lattice vibration) and electrons. Phonons are the main heat carriers in semiconductors and insulators, while electrons dominate in metals [16]. When discussing heat transfer at the macroscale, heat carriers have a large wave vector. Therefore, Fourier's law can be used to describe heat transfer, as the mean free path of the carrier is significantly smaller than the scale of the object [17]

$$q = -kA\frac{\partial T}{\partial x} \qquad \text{eq. 1.2}$$

where q is the heat flux, k is a constant called thermal conductivity, A is the area perpendicular to the direction of heat flow and $\frac{\partial T}{\partial x}$ is the temperature gradient in the direction of heat flow. It can be seen from equation 1.2 that thermal conductivity depends on the existence of a temperature gradient within a material.

According to kinetic theory, thermal conductivity can be defined as

$$k = \frac{1}{3}cv\lambda \qquad \text{eq. 1.3}$$

where c is the specific heat per unit volume, v is the average speed of sound, and λ is the mean free path between the heat carrier scattering events. Scattering can always happen at boundaries, impurities, defects and with other heat carriers, which has been proved as the storage of local thermodynamic equilibrium. Therefore, when considering heat transport at the macroscopic scale, with the characteristic dimension of a material (L) being much larger than the mean free path (λ), a thermal gradient is established and the thermal conductivity is defined, as shown in Figure 1.1 (a) [18].

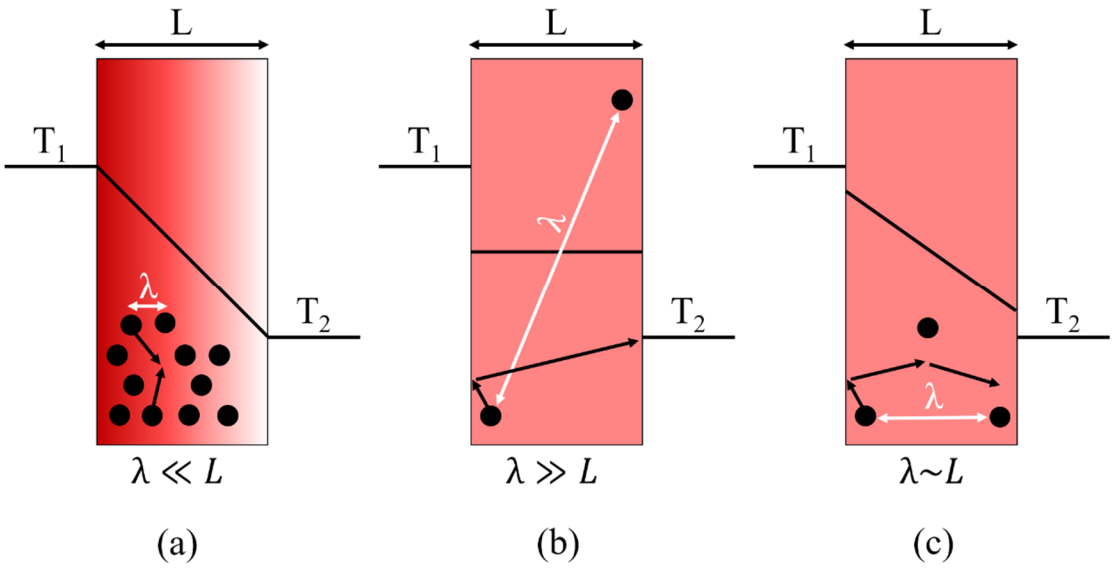

Figure 1.1 Thermal propagation mechanisms for varying mean free path of the heat carriers and the characterization length of the material. (a), (b) and (c) represents diffusive, ballistic and diffusive-ballistic thermal transport respectively.

However, when the mean free path is much greater than the characteristic dimension, as shown by (b) in Figure 1.1, heat carrier scattering will only occur at boundaries and this is called ballistic thermal transport. Under this condition, thermal transport cannot be described using Fourier's law, which is based on the thermal gradient. A new model, derived from radiative transfer, has been proposed [19], recognizing that the temperature of the boundaries dominates heat transport. This description can be written as

$$q = \sigma(T_1^4 - T_2^4) \qquad \text{eq. 1.4}$$

where σ is the Stefan-Boltzmann constant and T_1 and T_2 are the boundary temperatures.

In reality, many nanoscale devices fall into an intermediate state where their critical dimensions are of the same order as the carrier mean free path ($\lambda \sim L$) as shown in Figure 1.1 (c). In this situation, both diffusive and ballistic transport must be considered, making the problem complicated. An in-depth theoretical discussion about nanoscale thermal transport is beyond the scope

of this thesis but can be found in the existing literature [20–26]. In contrast, this thesis is primarily focused around investigating thermal transport on nanometer length scales by employing experimental methods. It aims to develop tools to assist our understanding of nanoscale heat transfer with specific application to high spatial resolution thermometers. To this end, the present work focuses on developing and understanding advanced thermometers capable of measuring temperature with high sensitivity and resolution. In order to achieve an effective tool, the heat transfer mechanisms between the thermometer and the sample must also be considered.

It stands to reason that the drive to develop advanced thermometry techniques has been largely led by the rapid evolution of research at sub-micrometre scales, where conventional thermometers are ineffective. Modern nanostructured materials and devices have found promising thermal applications in many fields. For example, nanowires with diameters less than 20 nm can exhibit thermal conductivities two orders of magnitude lower than bulk material, making them a promising thermoelectric material [13]. However, their thermal characterization requires a high spatial resolution measurement, which is a challenge for conventional thermometry methods. Adapting to these new measurement requirements is more complex than simply decreasing the size of conventional tools. For instance, shrinking the size of traditional thermistors or thermocouples and integrating them onto a sample presents great difficulty and complexity in fabrication. Also, their sensitivity will be negatively impacted by a weak thermal signal and relatively large noise [27]. Beyond these considerations, it is also desirable to extend thermal characterization beyond temperature measurement of active samples, and into the investigation of thermal properties for passive samples. The ability to characterize and optimize the properties of nanostructured materials such as amorphous [28] and multilayer materials [29] is highly desirable for modern applications. This therefore places a requirement on the measurement technique to work not only as a thermometer, but also to include the ability to deliver thermal excitation.

The following section reviews techniques currently used for measuring temperature at small length scales.

1.2 Techniques for Measuring Temperature in Sub-micron Scales

The importance of temperature to a wide range of disciplines has already be recognised, and this brings the requirement for thermometry under complicated and challenging conditions. For example, measurement may need to be carried out under liquid [30] or on soft materials [31] in the biomedical and chemical fields. The semiconductor industry requires temperature mapping of microcircuits *in-situ* [32,33] necessitating a method resistant electromagnetic interference.

The wide variety of application areas means that a wide range of temperature measurement techniques are available: ranging from conventional technologies such as thermocouples and thermal resistance devices adapted to the nanoscale, to remote optical approaches such as Raman, thermoreflectance and interferometry.

It is possible to group these techniques in various ways, for example if the method is remote or contact, or if the non-contact is far-field or near-field. Regardless of the grouping criteria, a clear understanding of the merits and drawbacks of each method is desirable for selecting an appropriate technique. In this section, the measurement methods will be clarified and listed according to the signal generated, in particular, optical or electrical.

1.2.1 Thermometry based on optical signals

1. Infrared thermography [34]

Infrared thermometers determine temperature by measuring the radiation intensity from an object at a specific wavelength and making the blackbody assumption (known as Plank's law). They operate by focusing the

thermal radiation emitted by the target onto an infrared detector and are able to measure temperature from cryogenic to over 6000 K. In practice, few objects are true blackbodies and Plank's law can only be used with the knowledge of the surface emissivity. Furthermore, spatial resolution in these systems is dictated by the diffraction limit of the optical wavelength, can only reach 3 μm even in the best conditions. In addition, careful consideration needs to be given to stray reflections from other sources as these can act to disturb the measurement, making the technique complicated and potentially inaccurate.

2. Raman scattering thermometry [35]

Raman scattering is based on the inelastic scattering of monochromatic light. When a specimen with a lattice vibration frequency of ω_μ is irradiated with light having a frequency of ω_i, two types of Raman scattered light, Stokes, with frequency of $(\omega_i - \omega_\mu)$, and anti-Stokes, with frequency of $(\omega_i + \omega_\mu)$ can be detected. By determining the ratio between the intensity of anti-Stokes and Stokes, which is a temperature dependent only value, the absolute temperature can be calculated. The setup of this technique involves a light source, always a laser, and a high-resolution Raman spectrometer for measuring the wavelength and intensity of the scattered light. The sample can be directly measured without preparation and the thermal spatial resolution can be down to around 1 μm. However, one of the disadvantages of this technique is that it is time-consuming with a speed as low as 0.5 point per second. Also, it can only be used on materials that have a clear Raman response. In addition, its temperature accuracy is only around 5 K, resulting in low sensitivity to small temperature changes [36].

3. Thermoreflectance [37]

Thermoreflectance thermometry measures the temperature by detecting the local change in a material's reflectivity and comparing this with a calibration of its optical index versus temperature. The advantage of this technique is that it allows one to work with light at wavelengths much smaller than that of infrared thermometry, so the spatial resolution can be significantly

improved down to 100 nm. The difficulty with the method mainly revolves around quantitative measurement, which requires a calibration of the reflectivity index. In addition, the thermoreflectance coefficient is wavelength, material and even surface texture dependent, meaning that temperature measurement is susceptible to inaccuracies [38].

4. Interferometry [39]

Interferometry measures both the refractive index variation and the thermal expansion of a sample. The technique employs two light beams, one falling outside the region of interest, and the other passing through it. Any distortion of the incident wavefront from the region of interest, caused by thermally induced refractive index change or local deformation can then be detected by interferometric means. Although this technique can reach 100 nm spatial resolution, the crosstalk with sample deformation caused by strain or stress deteriorates its accuracy. This is combined with the fact that its spatial resolution is lower in the transverse direction [36].

5. Near-field scanning optical microscopy [40]

Optical measurement methods are typically limited by the diffraction of the light, resulting in a spatial resolution that can barely reach the sub-micron scale. Scanning near-field optical microscopy (SNOM) removes this limitation. By combining the atomic force microscopy (AFM) tip with an integrated aperture in the order of 50 nm, it permits the acquisition of light from the sample in the near field. In this way, spatial resolution can be significantly improved below the Rayleigh limit, and results have been reported down to 10 nm. The main limitations of this technique are that it can only access surface (i.e. not sub-surface) temperature and, a vacuum is necessary for quantitative measurement [41].

1.2.2 Thermometry based on electrical signals

1. Built-in temperature sensors

Integrated thermal resistors and thermocouples are the most common devices used for obtaining the temperature of a sample. They are typically implemented by fabricating a tiny temperature sensor onto or embedded into the sample. The temperature in the region of the sensor can then be obtained by the interpretation of the sensor resistance or thermovoltage in relation to its temperature coefficient or Seebeck coefficient [42].

A related method, known as noise thermometry, determines the temperature of the sensor from the noise generated by thermal fluctuations of carriers in the resistor, a phenomenon known as Johnson noise. Johnson noise thermometry has been used to establish the temperature scale between a few millikelvins to thousands kelvins with an accuracy of about 0.1 % [43]. Accurate detection of Johnson noise requires sensitivity in the nano volt range, making this technique complicated from an instrumentation point of view. In addition, spatial resolution is dictated by the dimension of sensor, which can be challenging for sizes below 1 μm.

Another electrical approach utilizing an AC signal is the 3ω method, which employs a one-dimensional metal film deposited on a sample to act as both a heater and thermometer. This approach relies upon passing an alternating current through this thermal resistor so that the small third-harmonic signal in the voltage across the resistor can then detected. This component is only dependent on the temperature of the resistor and effectively eliminates the effect of the input electrical signal from the measurement. This mechanism has allowed the 3ω method to not only be used to detect sample temperature, but also to measure thermal conductivity [44] and specific heat [45]. Through further development of the application, this technique has been extended to research on thin films [46,47], nanowires [48], nanotubes [49] and even liquid materials [50]. However, this technique is relatively inaccurate due to the assumptions necessary for interpretation of its data. Specifically, the analytical solution of resistor temperature rise is based

on the assumption that thermal penetration into the substrate is large compared to the heater width. Also, in common with all static sensing techniques, it is impossible to generate a temperature map using the basic 3ω method [44].

2. Electron thermal microscopy [51]

Electron thermal microscopy overcomes the spatial resolution limits of optical thermal microscopy by observing the liquid-solid transition in an array of nanoscale islands on a sample. This technique benefits from the small wavelength of electrons used for imaging in an electron microscope, enabling spatial resolution down to 10 nm. Thermal maps are produced in real-time (30 thermal images per second), in the same manner as the conventional scanning electron microscopy. However, this technique is not widely applicable to practical applications due to its use of vacuum conditions, specialist surface preparation, and complicated setup for *in-situ* measurement [36].

3. Scanning thermal microscopy (SThM) [52]

Similar to SNOM, SThM exploits AFM by employing a nanofabricated thermocouple or thermistor at the very end of an otherwise conventional AFM probe. As a result, it offers spatial resolution that is comparable with the near-field scanning optical microscopy [52]. The difference is that SThM works by placing the probe tip in contact with the sample, and the tip temperature is then measured as it is modified by tip-sample heat transfer. SThM can be regarded as a technique that employs a built-in temperature sensor on an AFM probe instead of on the sample itself. Therefore, all built-in temperature sensor techniques as mentioned above can be exploited in this technique. This means that SThM inherits both the high spatial resolution of scanning probe microscopy (SPM) and the easy operation and interpretation of built-in sensors. As an added advantage, this technique also provides simultaneous measurement of temperature and surface topography. This allows it to potentially overcome one drawback of SNOM – the fact that the result is susceptible to the topography of a surface [15]. Moreover, the system is flexible and can be adapted to measure either the temperature distribution or the

thermal properties of the sample by simply modifying the degree of self-heating experienced by the thermal sensor. The primary drawback of SThM is that the scanning speed of the AFM system together with the time constant of the modified tip can make the image acquisition time slow. Furthermore, its contact measurement scheme limits its use to solid samples, and brings difficulty in extending its application. Finally, quantifying SThM data relies on a very thorough understanding of tip-sample heat transfer for any individual dataset.

1.3 SThM as the Final Research Direction

Multiple thermal measurement techniques have been listed and briefly evaluated in the previous section. The choice of technique for any given application is highly dependent upon the specific demands of the task. For example, AFM-based techniques, such as SNOM and SThM, together with electron thermal microscopy, are suitable for high-resolution temperature measurement; Raman scattering microscopy and electron thermal microscopy are able to produce high-speed thermal images making them ideal for measuring transient systems. However, amongst all of these techniques, SThM has proven to be the most popular in recent years due to its relative ease of use, high spatial resolution and ability to achieve both *in situ* and quantitative temperature measurement. It is because of this that it has been playing a key role in recent nano-thermal research, such as probing ballistic thermal transport [53] as well as the impact of interfacial effects on thermal transport [54].

Now, it is time to answer the question proposed at the beginning of this chapter: can the thermal equilibrium still be established and is there a sufficiently large statistical ensemble? Figure 1.2 demonstrates a situation in which a substrate is contacted by a SThM. Due to its sharp tip, the probe is significantly better coupled to its base (which is a bulk silicon substrate and always treated as a thermal reservoir) than that to the sample through the nanosized contact area. Therefore, the thermal probe can never reach global

thermal equilibrium (GTE) in contact with a sample, since the thermal resistance of the tip-sample contact is typically several orders of magnitude larger than that between the thermal sensor and the base. A question will arise according to this, which is what does the SThM probe really detect?

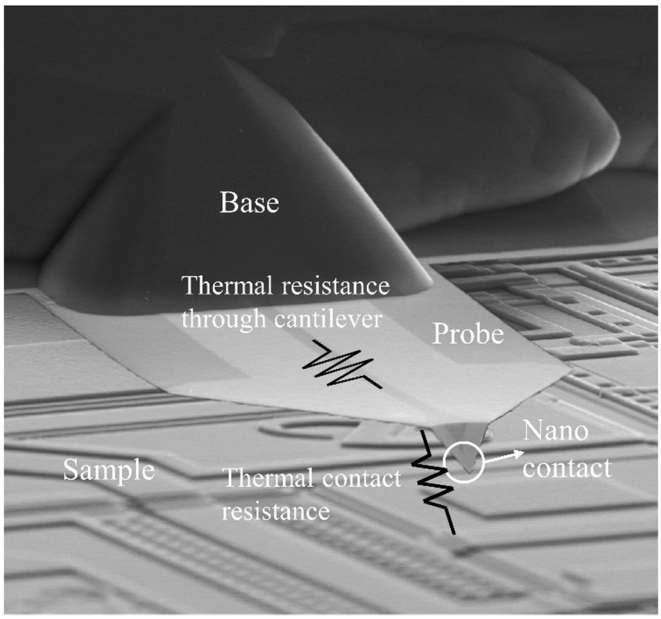

Figure 1.2 Illustration of the challenge of SThM. The contact area between the SThM and the sample is down to nanoscale, which results in a thermal coupling much weaker than that to the base.

In fact, SThM is used for acquiring heat flux, which contains information not only about the temperature difference between the thermal sensor and the sample, but also changes in thermal resistance that will affect the heat flux, for example thermal contact resistance, thermal spreading resistance of the sample, thermal resistance within the cantilever and thermal resistance due to air conduction. The well-known topographically induced and air-conduction artifacts are both results of these disturbances on heat flux. According to this challenge for SThM, this thesis investigates extracting temperature information from this confusing system by understanding the thermal probe and its interactions with the sample. Chapters 4 and 5 will focus on research into these two artifacts with assistance of specifically designed passive samples and active devices.

As the probe function is dictated by a thermal sensor, it will infer temperature instead of heat flux. Hence, it is necessary to make the definition of temperature clear in this thermal sensor, as no global thermodynamic equilibrium can be established in SThM. According to the law of thermodynamics, a sufficiently large statistical ensemble and thermodynamic equilibrium are two essential elements to define the concept of temperature [55]. The thermal sensor element in SThM has a volume of around one cubic micrometre, which will absolutely fulfil the requirement of a large statistical ensemble. Then, although the system is always in non-GTE, local thermodynamic equilibrium (LTE) within the sensor element can still prevail, due to each element within the sensor being similar to that of its neighbouring element. Consequently, temperature of the thermal sensor can be defined at each location. In order to avoid the condition where LTE is invalid, the thermal sensor has to be used at steady state, in which no large thermal changes are occurring. Therefore, in Chapter 3, the time constant of the probe will be measured and compared to calculation. This value will then be used to determine the probe's maximum scan speed as well as informing the novel 'nulling probe' working conditions.

One of the most commonly used SThM probes – a microfabricated thermal-resistor silicon nitride (SiN_x) probe, was initially developed in Glasgow [56]. The quantity of the probes available combined with an intimate knowledge of the probe design put Glasgow in a strong position to undertake in depth research into SThM. Current innovations in SThM have made a number of new demands on the probes available. In particular, they require probes that are more sensitive to temperature change, more easily modelled when interacting with the sample, and less prone to unwanted scan artifacts that can lead to misinterpretation of data. To this end, a better understanding of the probe and the thermal interactions with the sample, using both experimental and numerical methods, will benefit probe redesign and optimization.

1.4 Thesis Organization

Work in this thesis is organised in seven chapters. Following this introductory chapter, each chapter will start with an introduction describing the motivation, except for the final chapter, which is concerned with a summary and outlook. Subsequently, all methods and techniques are introduced in each chapter before the results are presented and discussed.

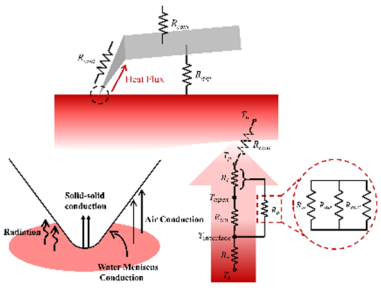

Chapter 2 starts with a review of the development of the SThM technique, followed by the introduction of various SThM probes based on different thermal sensors. Subsequently, it illustrates the design and fabrication process of the most recently used thermal probe. The major problem associated with SThM, which is the capability of quantitative measurement is also discussed in detail. Finally, artifacts, due to topography and air conduction, are described.

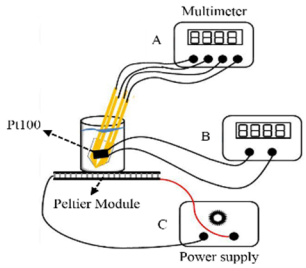

In Chapter 3, we first examine the characteristics of the currently used, micromachined SiN_x probe from multiple aspects. Then, based on the characterized property, a novel probe named as a 'nulling probe' is demonstrated through its design and performance using finite element analysis. With the requirement of a high-temperature working condition, the fabrication process of a thermal bending compensated probe is discussed. Finally, a demonstration of the current status for the nulling probe is shown.

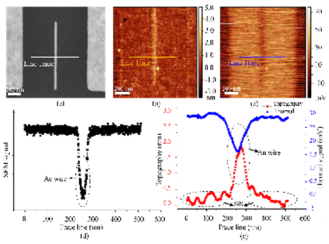

In Chapter 4, a new sample, named as a topography-free sample, is designed in order to understand topographically induced artifacts. The sample is fabricated based on a pattern transfer technique and scanned using a thermal probe working in active

mode. With assistance of this sample, a topography-artifact free thermal image can be achieved, which helps understand the thermal interactions between the probe and sample.

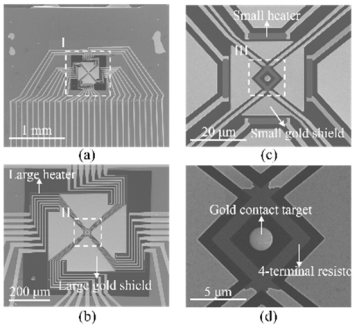

In Chapter 5, a membrane based Johnson noise temperature measurement device is demonstrated from design and modelling, through to fabrication. With assistance of its unique layout of heaters, the device is able to provide a uniform temperature distribution across the whole membrane. Its temperature can be accurately measured using an embedded 4-terminal Johnson noise thermometer. When scanned using a passive probe, the air conduction effect is demonstrated. Subsequently, a one-dimensional heat transfer equation expressing the thermal interactions between the probe and sample is used to determine the thermal coupling of the probe. Finally, a lumped-system model is built, which is based on the knowledge of probe dimensions and materials, providing a convenient method to model the probe.

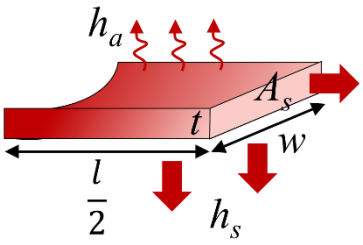

In Chapter 6, we introduce a combined-fin model for thin film samples contacted by a thermal probe in active mode. The model is proposed in order to investigate the variation of thermal resistance dependent on sample dimensions. This method assists in the interpretation of thermal resistance and the calculation of thermal conductivity for samples with shapes different from the probe contact area. Finally, this sample is used to determine the spatial resolution of our thermal probe, as well as the effective contact area.

2

SCANNING THERMAL MICROSCOPY (STHM): REVIEW AND UNDERSTANDING

As briefly introduced in Chapter 1, scanning thermal microscopy (SThM) is a technology based around atomic force microscopy (AFM) [52]. SThM has undergone continuous development since first introduced nearly 30 years ago. Due to its high spatial resolution, which it inherits from AFM, SThM has assisted in pushing thermal research down to nanometre length scales. As a consequence, the development of SThM reflects the progress made in understanding the fundamentals of heat transfer in the nanoscale.

SThM can be considered as operating in one of two modes, active or passive [52]. These two modes are dictated by the instrumentation and the type of probe employed, and are distinguished by whether or not the SThM probe is actively Joule heated above the ambient temperature. Various methods can make use of these two modes in order to map sample surface temperature and image thermal properties. During the lifetime of SThM, there has been constant effort to determine the measurand with increased accurately and sensitively. This has generated improved probes with advanced techniques permitting challenging research to be carried out. However, it has also been recognized that there are still a number of factors impeding the truly reliable measurement of the real temperature and accurate

thermal properties. The work being done to understand these limitations will be reviewed in this chapter with the aim of quantifying SThM measurements and predicting the future development of SThM. Associated with these uncertainties, SThM is prone to exhibiting measurement artifacts [57]. These can be seen on many scans and make it difficult to obtain a clear thermal map or correctly interpret the signal into reliable thermal properties of a material. The work trying to understand these artifacts is essentially to progress our understanding of heat transfer mechanisms present in SThM. These efforts will also be reviewed, with the aim of informing the development of advanced samples, specifically focused on the research of these artifacts.

This chapter is arranged as 4 sections. Section 2.1 provides a review of the development of SThM since its invention, in particular, probes that are currently most popular in use. As Glasgow is the originator of one of these thermal probes, their fabrication will also be described in this section, which will benefit the probe optimization in Chapter 3. Section 2.2 introduces the working modes of SThM, along with measurement methods used for each mode. Specifically, two instrumentation setups will be described in detail. In Section 2.3, the heat transfer mechanisms between the probe and the sample together with their uncertainties will be considered for a probe working in air. Finally, two major artifacts stemming from sample topography and air-conduction will be introduced and reviewed in Section 2.4.

2.1 Development of the SThM

Since 1982, the year that Binning *et al*. [58] demonstrated the scanning tunneling microscopy (STM) by the principle of vacuum tunneling [59], scanning probe microscopy (SPM) has offered a viable approach for imaging samples at the nanoscale. One of the disadvantages of STM, the requirement of a conductive surface, was overcome by the invention of the atomic force microscopy (AFM) [60]. By measuring the Van der Waal force between the atoms on the tip and the sample surface, a lateral resolution of 3 nm with a vertical resolution less than 0.1 nm could be achieved. In the same year, Williams *et al*. [61] first exploited temperature as an intermediate variable to measure the topography of a sample with an instrument called a scanning thermal profiler (STP). Working in close proximity to the sample surface, the distance between the heated tip and the sample surface was controlled by detecting and maintaining their thermal exchange using a thermocouple at the end of the tip and a piezoelectric element to control their separation. Being inspired by the STP, a combination of the tunneling technology with a thermal sensor has emerged and showed its ability to map temperature down to nanometer scale and thermoelectric potentials down to the atomic scale [62,63].

In 1992, the emergence of AFM based thermal microscopy opened access to temperature measurement at the shortest length scales without a requirement for vacuum conditions [64]. Following this, Majumdar *et al*. [65] developed a thermal microscope, permitting topographic and thermal signals to be obtained simultaneously. This work also permitted thermal microscopy of active samples having an external bias, as the technique substituted a tradition AFM probe with two thermocouple junctions, one of which was used as the thermometer and the other was the cold junction. This approach could be regarded as a prototype for SThM, as it shares the same basic principle and setup.

A schematic of the basic SThM setup is shown in Figure 2.1. The contact force between the thermal probe and the sample is detected in the same

manner as a conventional AFM, by reflecting a laser beam off the probe cantilever onto a photo-detector. The signal is recorded by the AFM control unit as the magnitude of cantilever deflection and in the meanwhile, a feedback signal is generated to move the piezoelectric displacement system and maintain a constant contact force. Either the sample stage or the probe stage can be attached to the displacement system, with each offering certain advantages in sample compatibility and positional stability. At the same time, the thermal sensor located on the probe is monitored and controlled by a separate temperature controller and detector unit. The signal output by this unit can then be fed back into an AFM control unit, for recording alongside the topographic signals. Although these basic principles and the setup of SThM have remained unchanged since the first SThM, various thermal methods employing different sensors have allowed SThM to function in diverse areas.

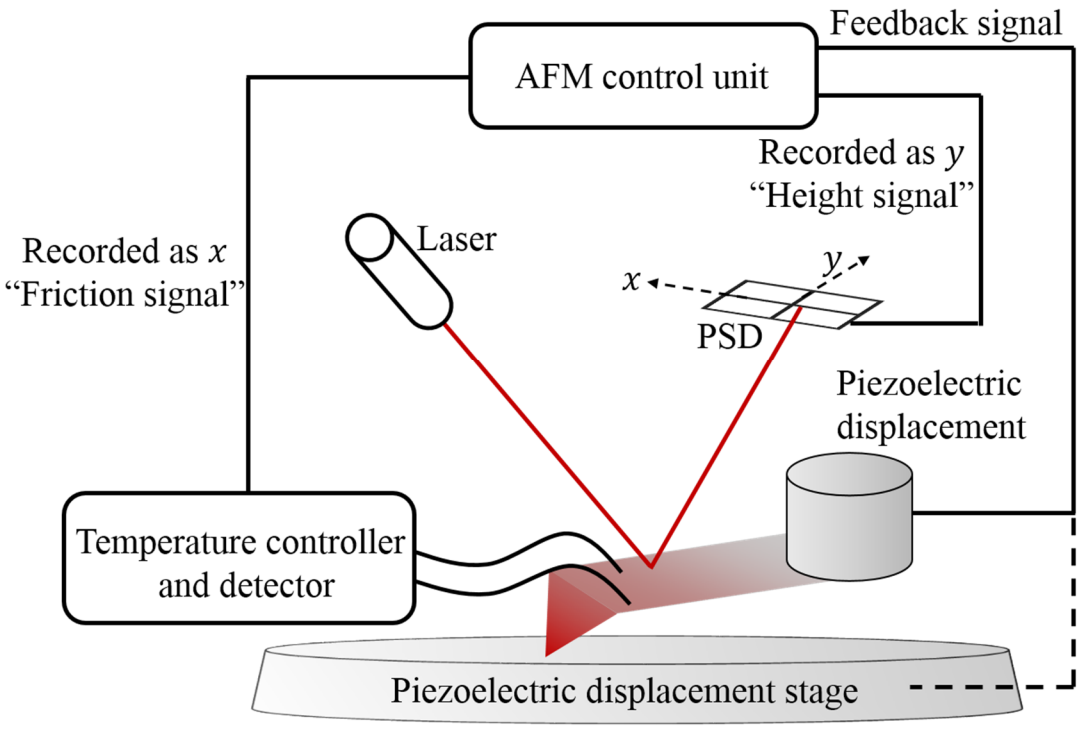

Figure 2.1 Description of the working principle of the SThM. The dashed connection line represents that the SThM can be established based on two types of AFM – the displacement system of which is either the sample stage or the probe stage.

2.2 SThM with Various Thermal Sensors

It has been found that various physical effects susceptible to thermal change can be exploited as the thermal sensor in SThM. These include the thermoacoustic effect, used in the scanning Joule expansion microscope [66], the photothermal expansion effect, used in the AFM-infrared spectroscopy [67], the temperature dependent fluorescence emitted by the particle attached to the AFM probe, used in the scanning fluorescent probe [68], and the most commonly used temperature-electric technique. Specifically thermoelectric and thermal-resistance thermometry are used due to their relative ease of use and manufacture, together with their familiarity from the long history of use in thermometry at the macroscopic scale. The work described in this thesis was carried out using a resistance thermometry probe. However, due to its close relationship with the thermoelectric probe, and the insights the thermoelectric probe offers, SThM probes based on both effects are reviewed in this section.

2.2.1 Thermoelectric sensors

Thermoelectric sensors utilize thermal effects that directly change the electrical signal generated by a sensor. One example is to employ a Schottky diode at the very end of the AFM tip. When biasing the Schottky junction with a voltage (U), the electrical current passing through the diode (I) can be written as [69]

$$I(U,T,P) = I_D(T)\left(\exp\left(-\frac{qU}{k_BT}\right) - 1\right) + I_{ph}(P) \qquad \text{eq. 2.1}$$

where I_D is the temperature dependent dark current, q is the electron charge, k_B is the Boltzmann constant, T is the temperature and I_{ph} is the photocurrent dependent on the optical power P. This shows that temperature variations can be detected by monitoring changes in the current. Schottky diodes have been successfully fabricated at the tip of doped GaAs [70] and silicon probes [71], achieving a sensitivity of ~ 3 mV/K when applying a 1.0 – 1.5 mA forward

current. Although Schottky-diode-based SThM probes offer accessible fabrication and highly sensitive temperature measurement, it can be seen from the eq. 2.1 that besides temperature, the current was also sensitive to illumination. This has a potential impact on the probe's accuracy and imposes rigid demands on the microscope configuration and scanning environment. Furthermore, as the tip is made of high thermal conductivity materials, heat path between the tip and the sample would change the sample temperature and bring a large deviation to the measurement result compared to its real temperature.

Another, more popular thermoelectric-based probe, employing a thermocouple as the sensor, as in the first SThM mentioned above, is named the wire thermocouple probe [65]. By advancing these probes using nanofabrication technology, the thermocouple can be built onto a more conventional AFM probe instead of being individually hand-made. Luo *et al*. [72] proposed a method to fabricate Au/Ni, Au/Pt and Au/Pd thermocouples with the radius of the very end of the SiN_x tip ranging from 100 nm to 500 nm. This improved the thermal spatial resolution of the SThM down to 24 nm compared with that of wire thermocouple probes reckoned as just sub-micrometre [65]. However, their complicated fabrication process made their manufacture time-consuming and high-cost. Shi *et al*. [42] addressed this with an optimized fabrication process, allowing thermal probes to be batch fabricated - more than 300 probes on a single wafer. Batch fabrication allowed probes to be manufactured in a more economical and controllable way. However, one drawback to the particular fabrication processes employed was that the tip radius could vary over a wide range from 100 nm to 600 nm, due to it being defined by photolithography. Closely following this work, Mills *et al*. [73] proposed another design strategy for a batch fabrication process of thermocouple probes, combining photolithography with electron beam lithography (EBL). This made use of a novel resist float coating technique [74], which was developed to solve the problems of resist spinning on a topographic wafer (~ 10 μm variation due to the definition of pyramids). By

combining this innovation with high-resolution EBL, a tip with radius of approximately 50 nm was reliably achieved. Microfabricated thermocouple probes avoid the light sensitivity of the Schottky probe and typically feature a low thermal conductivity tip, normally made of SiO_2 or SiN_x, offering a higher sample temperature sensitivity and smaller sample thermal perturbation. However, due to the necessity of a cold reference junction, the accuracy of their temperature measurement is largely dictated by the stability of the cold junction, which, in a typical SThM instrument, is uncontrolled and always assumed to remain at ambient (or at least a stable) temperature due to the air conduction. The most recent thermocouple probes overcome this by employing ultra-high vacuum conditions [75].

Recent work has employed the thermoelectric effect to determine the interface temperature between the probe and sample in realisation of its importance in thermal transport. To achieve this, the sample is coated with a metal having high thermal conductivity (in practice, Au is always used), and the probe tip is coated with another metal, forming a thermocouple junction when the probe and sample are brought into contact with each other [76,77]. The work is more likely to be an optimization of optical absorption microscopy [62], by replacing the STM with the contact mode AFM. The drawback to this method is the fact that the thermal sensor is composed of the tip and sample, requiring a thin Au layer to be deposited over the surface. If the sample is electrically conductive, a layer of Al_2O_3 must first be deposited prior to the Au, acting as an insulation layer. Although this makes the fabrication and measurement setup extremely complicated, this method offers a possibility to intuitively measure the effect of the contact interface, at which the temperature cannot be defined since there is no physical size. Instead, it measures the temperature discontinuity resulting from the interface, and thus the thermal interfacial resistance can be determined.

2.2.2 Thermal resistive sensors

The first category of probes employing a thermal resistive sensor are those based around the metallic resistor. These make use of the property whereby the electrical resistivity of a material is related to its temperature. In this case, a metallic resistor can be used to detect temperature change through the following relationship as

$$R(T) = R(T_0)(1 + \alpha(T - T_0)) \qquad \text{eq. 2.2}$$

where R is the resistance of the metallic sensor changing with temperature from T_0 to T, and α is the temperature coefficient of resistance (TCR), with units of K^{-1}.

The first metallic resistor probe was demonstrated in 1994 [78], immediately after the emergence of the wire thermocouple probe, and was known as the Wollaston probe. This name was given by the particular type of wire (Wollaston wire) used in the manufacture of the probe. It shares the same form as the wire thermocouple probe, but uses an alloy wire of platinum and rhodium as the thermal sensor instead of the thermocouple junction. The Wollaston probe can only be fabricated individually by hand, making the probe irreproducible and expensive [79,80]. One major advantage afforded by the 5 μm diameter metallic tip is that the Wollaston probe is able to sustain high temperatures (> 600 K), and is robust when compared to other AFM probes [81,82]. However, the limitation of the large tip-sample contact area impedes its use in measurements at the nanoscale [52,83].

Similar to the development of thermocouple probes, the resistive probe size was reduced by employing nanofabrication to produce a resistive metallic element at the very end of a more conventional AFM tip. In 1999, Mills *et al*. [84] utilized a commercial thermal probe (from Digital Instruments) with a 250 nm thick platinum strap deposited by focused ion beam (FIB) at the tip end acting as the resistive thermometer, successfully detecting subsurface voids. These probes had a tip diameter smaller than 1 μm, enabling a thermal spatial

resolution of the order 100 nm [84,85]. Experimental studies started to exploit the fact that thermal resistive probes could work as a thermometer as well as a heater, motivating efforts to improve upon their design. Zhou *et al*. [86] used a self-alignment approach to overcome the challenge of fabricating a nanosensor at the apex of the tip and successfully developed a batch fabrication process. Following this development, metallic resistive probes in Glasgow were produced based on the same process, combined with improvement of the tip materials [87] and connection method of the nanosensor [88]. One drawback to the microfabricated metallic resistance probe is thermally induced cantilever bending, which is caused by the difference in the thermal expansion of multiple layered materials used in the probe. Zhang *et al*. [56] solved this problem by fabricating a groove with depth equalled the thickness of the metal layers along the length of the cantilever. The working principle of this groove is discussed explicitly in Chapter 3.3. This is the probe currently used in Glasgow and is often named as the 'grooved probe'. Figure 2.2 shows a schematic of the fabrication process. The process is similar to that described in Ref. [86], but differs in that the cantilever is etched to form a groove before SiN_x deposition and subsequent metallisation. The detailed fabrication process is described in its caption.

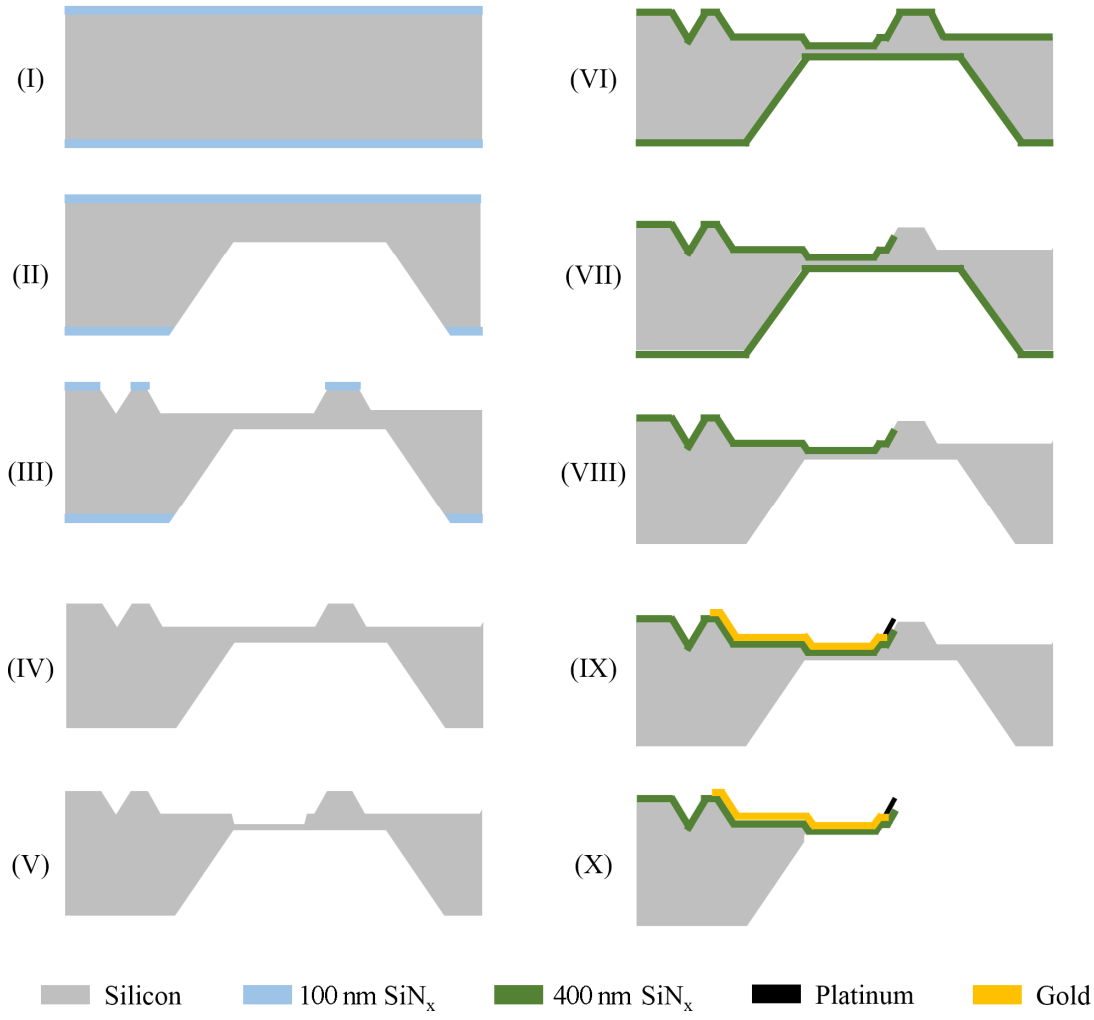

Figure 2.2 Schematic diagram of the fabrication of the grooved SThM probe. (I) 100 nm SiN_x deposited on the both sides of a 3 inch 400 µm thick double-side polished silicon wafer, (II) bottom side silicon KOH wet etching to define the position of cantilever, (III) define the pyramid on the top side using SiN_x as mask, (IV) strip the SiN_x mask by 1:5 HF:H_2O, (V) define the groove on the cantilever by photolithography and dry etching, (VI) 500 nm SiN_x deposited on both sides by low pressure chemical vapour deposition (LPCVD), (VII) define the shape of the cantilever on the top side, (VIII) strip the SiN_x on the bottom side for the probe final defining and releasing, (IX) metallisation on the cantilever, first 40 nm platinum at the end of the tip and then 150 nm gold as wires, and (X) TMAH wet etching for final release of the probe.

During the development of metallic resistance probes, some have been specially designed to address particular questions, such as the probe designed by Shi's group to study phonon transport [89], the carbon nanotube probe by Tovee *et al*. [90] designed for enhanced probe performance when measuring high thermal conductivity materials, and the dual-cantilever probe aimed at mitigating the effect of the tip-sample contact resistance developed by Zhang *et al*. [91]. One area where microfabricated thermal resistor probes have not excelled is in applications requiring a high degree of probe self-heating. This is due to the fact that these probes incorporate thin metallic films as resistors and electromigration-induced failure is inevitable at high current densities.

Another category of thermal resistive probe is based around the doped silicon probes first developed in IBM, and initially intended for data storage and thermal lithography [92]. The doped silicon probe consists of cantilever formed from two highly doped silicon legs (dopant concentration of 10^{20} cm^{-3}) acting as low resistance conducting wires while a lower doped silicon bridge (dopant concentration of 10^{16} – 10^{18} cm^{-3}) at their end acts as the thermal resistance sensor and/or heater [93]. Although semiconductors exhibit excellent TCR, they are nonlinear with power applied, which makes them challenging for use as accurate temperature sensors. Therefore, the doped silicon probes are often used in the active mode as heaters [94]. Without suffering the effects of thermal bending and electromigration, these probes can reliably work at temperatures as high as 600 K [95]. In common with many metallic resistance probes, the doped silicon probes are also batch fabricated, which means that their shapes [96,97], as well as materials [98,99], are controllable. They also offer a sharper tip than most metallic resistance probes, resulting in a smaller contact radius with the sample and a higher spatial resolution [100].

2.3 Quantifying the SThM Measurement

SThM probes can be operated in one of two ways: passive mode and active mode. When used in "passive mode" (temperature measurement with minimal self-heating) [57], SThM offers an ideal tool for obtaining sample temperature at the nanoscale with high spatial resolution. However, as the tip thermometer is typically either a thermocouple [73,101] or a thermal resistor [56], the temperature change can only be acquired indirectly as an electrical signal. Moreover, the heat path created through the contact between the probe and sample will exhibit a thermal resistance [52,72,100], leading to a probe temperature that is lower than that of the sample. Therefore, for quantitative measurements, a temperature calibration, relating a known sample temperature to the measured electrical output of the probe, is essential. When working in active mode, the probe itself acts as both a heat source and a thermometer to measure the thermophysical properties of the sample [52]. In this mode, the probe can be held either at a constant temperature by a feedback loop and its varying heater power monitored or at a fixed power and its temperature monitored. Both approaches permit differences in the thermal properties of the sample to be distinguished. However, for either active or passive mode measurements to be made quantitative, it is necessary to use calibration to link the output of the probe to the thermal properties or temperature of the sample.

2.3.1 Probe calibration

Several methods have been developed to calibrate SThM probes working in passive mode. For example, a Peltier module was first used for calibrating a thermocouple probe by Luo *et al*. [72]. However, the poor accuracy and temperature uniformity of the Peltier module restricted the quality of the calibration. To address some of these limitations, a 4-terminal-resistor calibration device was developed, employing thin aluminium line heaters on an oxidized silicon substrate [42]. Although the 4-terminal configuration improved the accuracy of the on-sample temperature measurement, the non-

uniformity of the heater temperature distribution remained a major drawback. Recently, the combination of a resistance heater with a membrane has been used to improve the uniformity of the temperature across the measurement area [102]. In this instance, even though the platinum heaters were embedded in a two-layer LPCVD SiN_x membrane, a homogeneous temperature distribution still could not be achieved. This resulted from the fact that heat could easily dissipate through the membrane to the substrate, generating a circular temperature distribution. The same structure was utilized by Dobson *et al.* [88] who fabricated a Johnson noise thermometer surrounded by a U-shaped NiCr heater on a SiN_x membrane. The advantage of this device was that the temperature of the calibration region could be obtained directly from the Johnson noise thermometer, improving the accuracy of the measurement. However, the problem of temperature uniformity remained, meaning that the average temperature of the thermometer could not be guaranteed to be the same as that of the probe calibration region.

For a probe working in active mode, a series of calibrations can be performed on flat bulk samples with well-known thermal conductivities, over a range covering the thermal conductivity of the measurand [103]. However, it is impossible to determine the real thermal conductivity of material with some geometries, such as a thin film without considering the effect of the supporting substrate. Thus, it is desirable for the thermal conductivity of the sample and the electrical output of the probe to be linked without the use of reference samples. David *et al*. [104] constructed a steady state thermal-resistive model taking both the probe and the interaction with sample into account. The model was built around the Wollaston probe, which has a simple shape as confirmed by SEM and is made from a relatively uniform material. As the nanofabricated probes have a much more complex geometry, a detailed knowledge of the probe shape and materials is necessary when formulating a model. Another approach is employed by AC models, which utilize the 3ω method (as described in Section 1.2.2) to determine the modelling parameters from the amplitude of the 3ω signal swept in frequency. These models have

been used for both the Wollaston probes [105] and nanofabricated probes [106]. Through this method, the differentiation of each probe shape and material can be achieved and thus included in the model. The limitation of AC models exits in the complexity of the experimental setup and complicated calculations. Beyond modelling, Kim *et al*. [107] quantitatively obtained the thermal conductivity of a sample using the so-called 'double-scan technique'. The sample was scanned twice, once in contact and once non-contact mode, which could then be described using the same heat transfer equation with different boundary conditions at the tip-sample interface. Subtracting the non-contact mode equation from the contact mode quantifies the power passing through the tip-sample contact, allowing the effect of other heat paths to be neglected. This offers a direct measurement and is a relatively easily setup, however the reproduction of results claimed for the method has remained a challenge.

Use of the data obtained from a calibrated probe requires minimal knowledge of the heat transfer mechanisms at play, and the measurement itself is derived directly by comparing the probe output to a calibration plot. However, it must be recognised that any measurement can only be accurate if the sample being measured has similar properties and temperature distribution to the calibration sample [100]. This does leave a requirement for more reliable and accurate methods for the quantification of thermal measurements to be proposed. A detailed understanding of the heat transfer mechanism between the probe and the sample, in the form of a thermal resistance network, first proposed by Luo *et al.* [72] in 1997, has shown much promise for interpreting SThM measurements. Subsequent development of this approach, through the exploration of both the probes and measurement methods, has permitted the heat transfer mechanisms to be more comprehensively and clearly understood [93,100,108–111]. A summary of them will be presented here by describing a practical situation, in which the grooved nanofabricated probe is mounted on a specific probe holder and brought into contact with a surface.

Schematics showing the heat transfer mechanisms for a probe working in both passive and active modes are shown in Figure 2.3 (a) and (b). The probe is mounted on a probe holder, which angles the cantilever 13° from horizontal, while the tip is at 56° to the cantilever. When the probe contacts a sample under ambient conditions, heat exchange between the probe and the sample will occur through multiple paths as listed below

1. at the constriction area between the probe and the sample, through the direct solid-solid contact resistance R_{int} ;

2. in the vicinity of the constriction area, through radiation (R_{rad}), conduction through any water meniscus (R_w), and conduction through any air (R_{air}). These three thermal paths can be combined in parallel to give a single equivalent path with resistance R_p ;

3. along the cantilever, by conduction through any air in the gap between the cantilever and sample surface (R_{gap}).

In addition to these heat paths, there are also heat paths constructed involving the probe with

1. the whole environment, through convection of any air (R_{conv});

2. the base of the probe, through conduction within the cantilever (R_{cant});

Both of these paths can be considered as heat exchanging with heat sinks at room temperature.

In the next section, the probe operated in active mode and passive mode will be discussed individually from the view of these heat transfer paths, aiming to quantify the measurement. It will be illustrated that the measurement is a comprehensive process involving all of these heat transfer mechanisms (which will be treated as uncertain factors during the quantification) and that quantification is essentially an understanding of the effect brought by them.

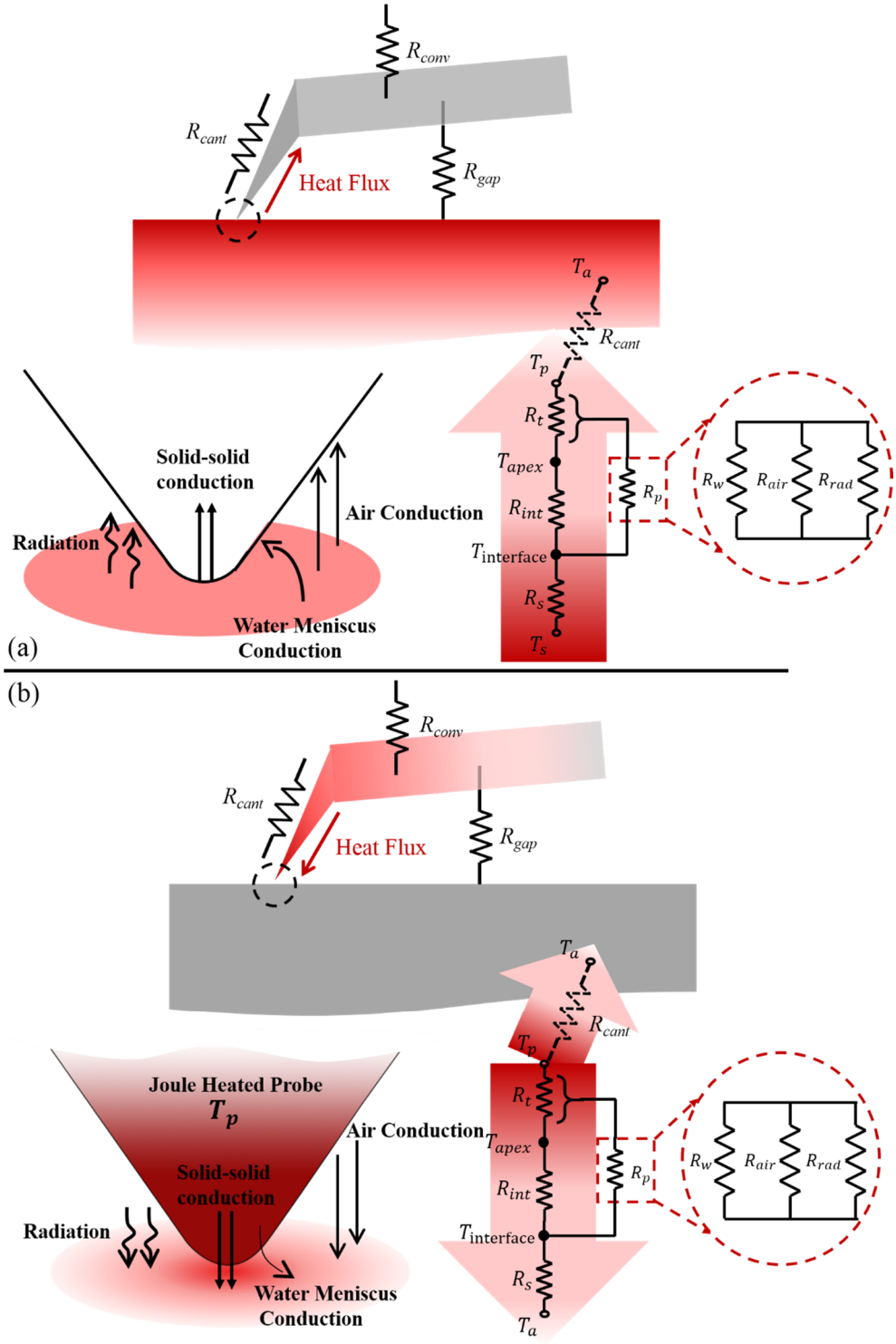

Figure 2.3 Schematic diagram shows the heat transfer interactions between the probe and the sample, together with the thermal resistance network showing the relationship between each interaction for (a) the probe working in passive mode scanning on the active sample, and (b) the probe working in active mode by Joule heating scanning on the passive sample.

2.3.2 Uncertain factors in passive mode measurement

Uncertainties associated with SThM quantitative measurement will be reviewed and discussed here. We can consider the following scenario where a probe, working in passive mode, is used to measure the temperature of an active sample. When contact is made with the heated sample at a temperature T_s, a heat transfer path is created between the probe and the sample. An equation describing this can be written according to the thermal resistance network shown in Figure 2.3 (a) as

$$q = \frac{T_s - T_p}{R_s + R_c} = \frac{T_p - T_a}{R_{cant}} \qquad \text{eq. 2.3}$$

Although the thermal sensor located at the end of the tip has dimensions of less than 10 μm, it is still too large to be regarded as a single-point, localized thermometer. This means that the temperature measured by the probe, T_p, is an average temperature along the whole platinum sensor, with associated thermal resistance, R_t. As proved by Fletcher *et al*. [77], an active sample can be regarded as an isothermal system, meaning that the sample temperature T_s can be assumed the same as the interface temperature at the probe contact area $T_{interface}$. Therefore, thermal spreading resistance R_s can be considered negligible. R_c is the combination of the thermal resistances at the sensor including R_{int}, R_t, and R_p. As the effect of R_p is along the whole thermal sensor, R_c can be written in the form as R_c (R_{int}, R_t, R_p) for simplicity. Therefore, eq. 2.3 can be rewritten as

$$q = \frac{T_s - T_p}{R_c(R_{int}, R_t, R_p)} = \frac{T_p - T_a}{R_{cant}} \qquad \text{eq. 2.4}$$

An expression for the sample temperature can also be derived from eq. 2.4 as

$$T_s = \frac{T_p - T_a}{R_{cant}} R_c\left(R_{int}, R_t, R_p\right) + T_p \qquad \text{eq. 2.5}$$

From this description, we can highlight the factors affecting quantitative determination of the real sample temperature to be the thermal sensor temperature (T_p), the ambient temperature (T_a), thermal resistance of the

cantilever (R_{cant}), the thermal interface resistance (R_{int}), thermal resistance of tip (R_t), and combination resistance of the air, water meniscus and radiative heat transfer (R_p).

2.3.3 Uncertain factors in active mode measurement

Most mechanisms of heat transfer remain the same for a probe working in active mode compared to that in passive mode. However, there are some differences associated with the change of heat flow direction. The heat flow (equals to the heating power, P) passes through two paths: from the tip into the sample through the contact area and from the tip to the probe base along the cantilever. This can be written as

$$P = \frac{T_p - T_a}{R_s + R_c(R_{int}, R_t, R_p)} + \frac{T_p - T_a}{R_{cant}} \qquad \text{eq. 2.6}$$

In this thermal resistance network, the thermal spreading resistance due to heat conduction within the sample, R_s, has to be taken into account. In addition, as the probe is self-heated by Joule heating, the thermal sensor can be considered to have a uniform temperature.

Finally, air conduction between the cantilever and sample will provide another heat path from the probe to the sample. This will cause a disturbance to both the sample temperature and the probe temperature.

Therefore, uncertain factors for a probe working in active mode include all those for passive mode, with the addition of the Joule heating power of the probe and the thermal spreading resistance of the sample.

2.3.4 Determination of uncertain factors

1. Probe temperature (T_p)

Compared with other uncertain factors, the probe temperature is the only value that can be intuitively obtained from its output signal. To date, the probe temperature has been accurately measured using several methods. For

metallic resistance probes, the temperature is usually inferred from the sensor resistance as measured by a Wheatstone bridge [52]. To achieve this, either the relationship between temperature and probe resistance [112] or the probe TCR [113,114] must be determined in advance. Wielgoszewski *et al*. [115,116] designed a modified Wheatstone bridge, which could operate the probe in either passive or active mode, by placing a reference probe in one leg of the bridge. This method allowed the Wheatstone bridge to be used with a 4-terminal probe. However, the requirement of the electrical resistance of the working probes to closely match that of the reference probe, compounded by the randomness of the probe's electrical resistance (as dictated by feature alignment during fabrication), makes this method difficult to achieve with high accuracy. The 3ω method, which measures the 3ω voltage signal caused by a 2ω temperature change, is used by several groups [106,117,118]. The advantages of this method are that the signal is less dependent on disturbance of the ambient temperature and has smaller uncertainty than a DC measurement. For thermocouple probes, the probe temperature can be directly inferred from a thermoelectric voltage. However, as thin film thermocouple junctions typically generate lower thermopower than bulk junctions, a calibration of the probe's thermopower is necessary before a measurement can be made [109]. Apart from this, attention has to be paid on the complexity of methods for knowing and stabilizing the cold junction temperature. For doped silicon probes, electrical resistance is nonlinear with temperature, necessitating a more complicated measurement. Gotsmann's group [119] linked the probe temperature with a heating power, in which several assumptions have been made. In addition, King's group [120] proposed a method measuring the change of the amplitude and phase of AC voltage used for modulating a ramped DC heating power.

The probe used in this thesis can be driven using either DC or AC signals. In a DC measurement, a variable current source, with range from 0 – 2 mA, is connected to the probe and set to achieve either passive or active mode. The voltage across the probe can then be monitored as part of a 4-terminal

resistance measurement. An AC mode was developed at Glasgow to permit the probe to be used on active samples with electrically conductive surfaces. This approach makes use of transformers to electrically isolate the probe from the sample [56,87]. Detailed configurations of these two modes and applications on how to quantify the probe temperature are described in Sections 5.2 and 6.3.

2. Thermal resistance associated with tip-sample contact (R_{int}, R_s, R_t, and R_{cant})

The contact between a probe and sample is usually modelled as a circle formed by a sphere contacting on a planar surface, with the contact radius, b_c, estimated using models for elastic contact [77,121]. When heat flows between two different materials in contact with each other, the reflection of heat carriers will take place at the boundary [122], leading to a thermal interface resistance. By assuming a single-asperity contact between the probe and the sample, this resistance (R_{int}) can be calculated as [123–125]

$$R_{int} = \frac{R_b}{\pi b_c^2} \qquad \text{eq. 2.7}$$

where R_b is the thermal boundary resistance for bulk materials on macroscopically large areas, having units of m^2K/W. Unfortunately, models that predict R_b have limited accuracy above cryogenic temperatures, but experimentally determined values near room temperature typically lie in the range from 1×10^{-9} to 5×10^{-8} m^2K/W [120,126]. Currently, the body of evidence amassed from experiments carried out using the SThM probe, suggest that the tip-sample contact radius equals to the probe's tip radius of curvature [89,121,127,128]. In this thesis, the tip-sample contact radius will also be estimated either by comparing the constriction thermal resistance from calculation with that from model matching (Section 5.3) or by analyzing the thermal ramp at the edge of patterns on the topography-free sample (Section 6.5).

For a probe working in active mode, the thermal spreading resistance R_s is the value used to derive the thermal conductivity of the sample. The most

commonly used method for obtaining thermal conductivity combines SThM scanning results with a heat transfer model, considering both the thermal boundary resistance and the thermal spreading resistance within sample and tip [129,130]. One advancement considers that the tip-sample contact shape is a circle and the thermal spreading resistance for a flat, homogeneous semi-infinite sample is therefore given by [17,104,131]

$$R_s = \frac{1}{4kb_c} \qquad \text{eq. 2.8}$$

where k is the thermal conductivity of the sample. However, for a thin film on a substrate, the effect of the substrate has to be considered and the thermal resistance of the thin film is [132]

$$R_s = \frac{1}{4kb_c} - \frac{1}{2\pi kt}\log\left(\frac{2}{1+\frac{k}{k_{sub}}}\right) \qquad \text{eq. 2.9}$$

where k_{sub} is the thermal conductivity of the substrate and t is the thickness of the thin film. Eq. 2.8, associated with eq. 2.9, is only valid when thermal transport is diffusive. Ballistic heat transport must be taken into account when the sample thermal carriers have a large mean free path (MFP) (e.g. most semiconductors). In this situation, the thermal conductivity of a material is given by [133]

$$k_{db} = \frac{k}{2(\pi K_n)^2}\left[\sqrt{1+(2\pi K_n)^2} - 1\right] \qquad \text{eq. 2.10}$$

where K_n is the Knudsen number representing the ratio of the carrier MFP to the system critical dimension. Therefore, the thermal spreading resistance has to be corrected to [123]

$$R_s = \frac{1}{4kb_c}\left(1 + \frac{8}{3\pi}K_n\right) \qquad \text{eq. 2.11}$$

So far, the model for calculating the thermal spreading resistance into the sample is mostly based on the assumption that one-dimensional (1D) heat transfer is valid. However, in the scenario that a multi-dimensional heat transfer model has to be addressed, it could lead to a misinterpretation of the

measured thermal conductivity if 1D heat transfer is still used. To address this case, a new model based on thermal fin theory will be proposed in Chapter 6 providing a deeper understanding of thermal spreading resistance involved in the SThM measurement.

The thermal resistance of the probe itself, including R_t and R_{cant}, is strongly dependent on the probe geometry, material and shape. Two of the most commonly used probes, the SiN_x probe and doped silicon probe, have been explored in different ways. Figure 2.4 shows a schematic of heat transfer through the probe when in contact with the sample for a heated doped silicon probe and the SiN_x probe (working in active or passive mode). For the doped silicon probe, as the heater is some distance away from the end of the tip and is small and thin, it can be regarded having a uniform temperature without thermal gradient inside the heater itself. Therefore, R_t and R_{cant} can be estimated using the predictions for thermal resistance of silicon nanowires [125,134]. For the SiN_x probe, three methods have been used so far to take R_t and R_{cant} into account when quantifying a measurement. The first method considers probe thermal resistance in 3ω measurements and is based on the thermal conduction equation [106,117]. However, although both R_t and R_{cant} are involved in the determination of sample thermal properties, neither of them can be quantified. The second method employs finite element analysis (FEA) [90,135], and the thermal resistance of the probe can be calculated as ~ 5.06×10^4 K/W. However, this value cannot be considered truly accurate and reliable due to the ambiguous handling of air conduction effect. Recently, Assy *et al*. [121] measured the thermal resistance by experiment in vacuum, obtaining a value of 5.2×10^5 K/W. However, their calculation was based on the assumption that the platinum tip resistor accounted for two-thirds resistance of the whole probe. In reality, due to variations in probe fabrication, the true value of the platinum resistor and the NiCr current limiters cannot be perfectly controlled, which may result in more than 100 % variation in this resistance ratio. In this thesis, experimental measurements employ probes without

current limiters in series with the platinum tip, allowing the Joule heating power of the tip resistor to be calculated more accurately.

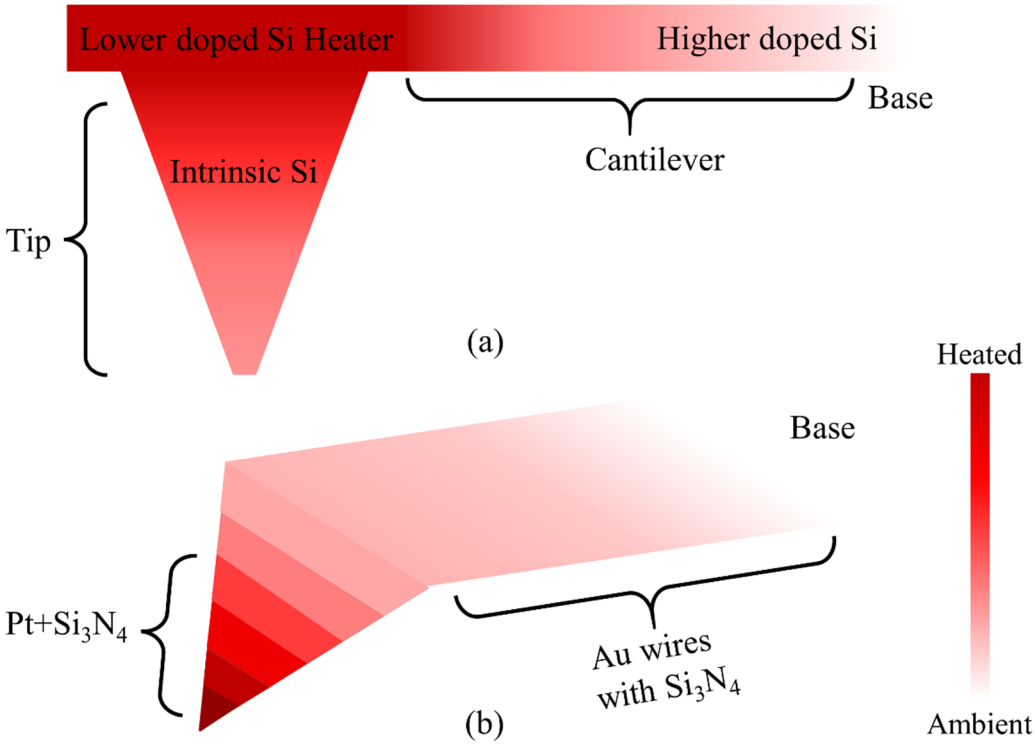

Figure 2.4 Schematic of heat transfer through the whole probe when contacting the probe onto the sample for (a) the heated doped silicon probe working in active mode (as it is seldom used in passive mode), and (b) the SiN_x probe, which has the same profile in both active and passive mode. Both probes are represented by their thermal profiles.

3. Effects of water meniscus, air and radiation (R_w, R_{air}, and R_{rad})

The formation of a liquid meniscus bridging the SThM tip and the sample surface offers an important heat transfer path between the sample and the probe during scanning of SThM probes under ambient conditions [52]. Luo *et al*. [72] first proposed that the water meniscus dominates heat transfer interactions based upon measurements using a thermocouple probe. Shortly after this work, Gomès *et al*. [110] further explored the water meniscus using Wollaston probes on several materials employing the same theory as Luo and concluded that the degree of meniscus importance depended on the thermal conductivity of the sample. However, their estimations were based on an

equation that neglected the thermal resistance provided by the interface between the water meniscus and the tip, which was first realised by Shi *et al*. [109]. They proved that the interface would greatly affect heat transfer through the water meniscus and weaken its contribution. The ambiguousness of the water's effect seem to require quantitative SThM to be carried out under vacuum conditions [128] or heating the probe beyond the evaporation point of water [136] (a challenge for the SiN_x probe). However, comprehensive work carried out by Gomès' group [113,137], who investigated the effect of water meniscus through an experiment illustrating the relationship between capillary forces and probe temperature, finally demonstrated that the thermal conductance attributed to water accounted for just 1 % - 3 % of that of the solid-solid contact, regardless of probe temperature.

Air conduction between the probe and the sample was fully described by Shi *et al*. [109], who observed the difference in probe temperature response when scanning large and small heated areas. They built a model that considered air conduction and thermal interactions associated with tip-sample contact and expressed it using a 1D heat transfer equation as

$$\frac{d}{dx}\left[\frac{dT(x)}{dx}\sum_i [kA(x)_i\right] + h(x)w(x)[T(x) - T_s(x)] = 0 \quad \text{eq. 2.12}$$

where A is the probe cross section area at position x, w is the width of the probe, T and T_s are the probe and sample temperatures at the same position respectively and h is the heat transfer coefficient derived from the thermal conductivity of air as

$$h(x) = \frac{k_{air}}{\delta(x)} \quad \text{eq. 2.13}$$

where δ is the distance between the probe and the sample and k_{air} is the thermal conductivity of air. Several studies have been reported that successfully achieved accurate and quantitative measurement by exploiting this model [138,139]. Most recently, research has become more focused on SThM in vacuum, eliminating the complication of air conduction [89,128].

However, the complexity of a vacuum system and its associated high cost, impedes the wide spread use of this method so far.

Radiation will always offer a heat path between the probe and sample regardless of the surrounding medium [52]. Although it is difficult to distinguish the effect of radiation under ambient conditions, it has been investigated from a theoretical standpoint using the Stefan-Boltzmann equation. This indicates that the thermal resistance to heat flow via far-field radiation is on the order of 10^8 K/W, which is much higher than that from the cantilever into the air (in the order of 10^5 K/W) [124]. Even when the distance of probe and sample is less than 1 μm and near-field radiation must be considered [140], the contribution of the radiation is still negligible regardless of the materials involved [124].

2.4 Artifacts in SThM Measurement

Artifact is defined as "unwanted distortions or added features in measured data arising from lack of idealness of equipment" (see 5.6 in ISO 18115-2:2013 (en)). Specific to the SThM, artifacts are abrupt deviations of the thermal signal captured by the probe due to its weak resistant to disturbance. These deviations may be incorrectly interpreted as temperature or thermal conductivity variations of the sample if they are not appropriately accounted for or eliminated.

Artifacts in SThM are always associated with the disruption of stable heat transfer paths between the probe and the sample. The most dominant of these are changes in the tip-sample solid-solid contact and air conduction, both of which can result in thermal image distortion. These two phenomena are named topographically induced artifacts and air-conduction artifacts respectively.

1. Topographically induced artifacts

Luo *et al*. [72] first observed topographic artifacts when using their nanofabricated thermocouple probe. Topographic peaks and valleys of the sample surface, although at the same temperature as the rest of the heated sample, produced a sudden decrease and increase in the temperature measured by the probe. Their analysis considered this as the result of changes in the tip-sample contact area. Figure 2.5 shows the interaction between a probe and a sample with a rough surface. From eq. 2.7 and eq. 2.8, we know that the thermal interface resistance and thermal spreading resistance are both affected by the contact radius, which is b_{valley} and b_{peak} as shown in Figure 2.5. Therefore, it is clear that topographic artifacts will strongly affect SThM measurements if no knowledge of the true contact size exists.

Gotsmann *et al*. [141] studied the effect of surface roughness on thermal interface conductance at the atomic scale, under vacuum. By constructing a model that described thermal transport across individual contact points, they defined the conductance per atom-atom contact as:

$$G_{atom} = G_Q N\tau \qquad \text{eq. 2.14}$$

where G_Q is the universal thermal conductance of a quantum point contact, N is the number of different phonon modes and τ is the corresponding transmission coefficient. As the number of contact points varied with changes in surface roughness or topography, the thermal signal was seen to vary due to the change in the number of atom-atom contacts. Therefore, topographic artifacts can also be explained by variations in the number of contacting atoms.

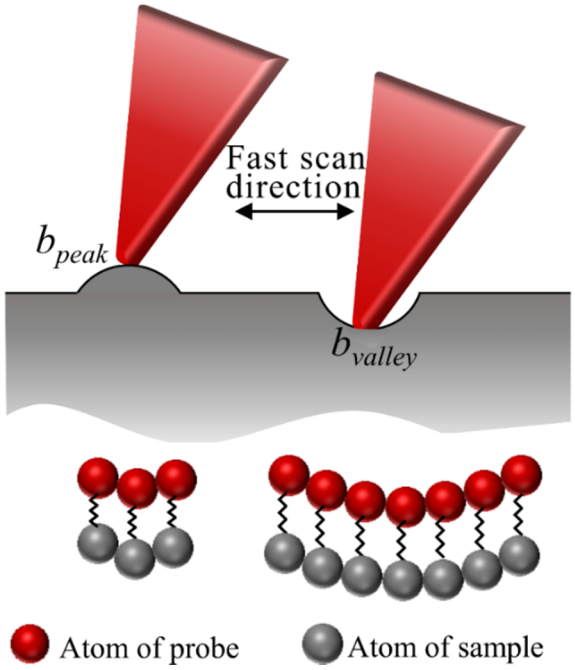

Figure 2.5 Schematic of a SThM probe interacting with the sample by contact with a valley and peak, showing the source of topographical artifacts. The sample is at a uniform temperature, and the probe scans with a constant force. At the bottom showing the atomic scale explanation of the topographic artifacts.

Topographically induced artifacts make it difficult to quantify SThM measurements. For example, Soudi *et al*. [142] reported a "double-line-like" thermal profile when scanning heated nanowires with 40 – 60 nm diameter in both air and vacuum in passive mode. In the presence of these artifacts, the local temperature of the nanowire could only be approximated by averaging the whole region, which was undoubtedly inaccurate. Some experiments on soft materials also reported these artifacts and proposed that the thermal image had to be always considered with the corresponding topographic image when carrying out analysis [143,144].

Efforts have been made to obtain real thermal images without artifacts. Cahill *et al*. [145] proposed that topographic artifacts could be removed from a thermal image only by modelling the artifacts with a deep understanding of the tip-sample heat transfer mechanisms or by a nulling probe. There has also been research into employing an algorithm to post-process the thermal signal [146]. However, this approach is not straightforward for those samples that

exhibit both material and topographic variations. Based on the combination of the image post-process and the determination of tip-sample heat transfer, recently, Menges *et al*. [147] developed a method by quantifying the thermal contact resistance between a DC sensing-voltage-biased probe and a small frequency AC-voltage-biased (10 kHz) sample. A corrected temperature map could then be achieved by involving the position-dependence thermal contact resistance into the original temperature map.

In this thesis, the problem of topographically induced artifacts will be addressed in two ways. First, a fabrication method based on lithographic pattern transfer will be presented for the production of a topography-free sample consisting of two materials with a large difference in thermal conductivity (gold and SiN_x). Thin-film narrow gold wires have been patterned and then scanned in air using the SiN_x probe working in DC active mode. By analyzing these results, the thermal spatial resolution of the probe in the absence of topographically induced artifacts can be clearly observed. Second, new designs for a microfabricated probe, specifically designed for use in nulling SThM will be modelled. This allows performance prediction and selection of the most appropriate designs, which will be put forward for fabrication.

2. Air-conduction artifacts

It can be inferred from eq. 2.12, that the existence of the heat transfer coefficient h will not only be able to assist temperature measurement, but may also result in a variation of the thermal distribution along the probe. This in turn, changes heat flow along the cantilever from the tip, resulting in the difference in tip temperature. The effect of air-conduction artifacts may not appear abruptly in the probe thermal response, but instead act to introduce a gradient to the temperature plot. Dobson *et al*. [88] clearly showed this artifact by scanning a uniform heated membrane, which generated an asymmetric thermal profile from a symmetric structure.

Various methods have been developed to eliminate air-conduction artifacts. Besides the obvious use of SThM in vacuum as mentioned previously, some advanced scanning methods, such as the "double-scan technique" [138] and the "topography-correction technique" [148], have been demonstrated to effectively diminish this artifact.

2.5 Summary

During the 30 years of development experienced by SThM, the probe has shrunk in size from the microscale into the nanoscale, providing the possibility to investigate the thermal properties of modern electronics and materials. Simultaneously, demands on SThM have pushed from simple qualitative measurements of thermal contrast to quantitatively obtaining accurate values. Although a number of efforts have been employed to fulfil this requirement the most pressing unresolved issues remain a lack of deep understanding of the probe itself, as well as a simple model taking into account the thermal interactions involving both the probe and the sample comprehensively.

Research presented in this thesis has employed modelling, nanofabrication and measurement to develop new probes, samples and devices, aimed at investigating the uncertain factors in SThM measurement for quantitative measurement, and progressing SThM by proposing the next generation of probe based on the understanding of the heat transfer mechanisms associated.

3

CHARACTERIZATION AND OPTIMIZATION OF THERMAL PROBE WITH NULLING PROBE DESIGN

With micro-thermal research gaining prominence in recent years, the SiN_x probe, developed in Glasgow, has become one of the most popular thermal probes worldwide. This is primarily due to its availability, simple operating principle and flexible working modes. Given that much current research is focused on detailed mechanisms of thermal transport on the nanoscale, there has been a shift in the demands on thermal probes from basic temperature contrast detection and thermal property mapping, to true quantitative measurement [90,100,106,149,150]. Whichever working mode the probe is used in (active or passive), there is always a link between probe temperature and the electrical signal measured by the instrumentation. Therefore, it is essential to have a solid understanding of the electrical characteristics of a probe. At the most basic level, the function of a resistance-element based SThM probe is dictated by its temperature coefficient of resistance (TCR). Accurately knowing this value will permit conversion of probe electrical resistance into temperature with minimum error. In addition, knowledge of a probe's highest operating temperature, as well as its highest sustainable current, is desirable and typically provides a good indicator of

probe quality and robustness. Another informative parameter, which contributes to the usability of a probe but is often neglected, is the sensitivity of the probe to Joule heating. This value is a function of probe thermal resistance and can be used to distinguish the power at which the probe transitions from insignificant self-heating (passive mode) to heated (active mode). Finally, the stability of the resistive thermal sensor is important, particularly when operating at a high (self-heated) temperature [151]. This can result in significant drifts of resistance when undertaking long experiments, reducing the reliability of scanning results. Although some of these characteristics may be considered trivial to determine, they do often require the destructive testing of a large number of valuable probes. The work presented in this chapter takes advantage of the large number of identical SThM probes available at Glasgow in order to characterize their electrical properties, through several specifically designed experiments.

With the help of the probe characterization described above, a novel, advanced probe, named the 'nulling probe', can be designed. This probe inherits the advantages of the current probe but is more capable of achieving a quantitative measurement. The concept of a nulling probe was first proposed by Chung *et al*. [152], and then implemented in a self-heated thermocouple probe. The name 'nulling probe' comes from the fact that when operating, the heat flux through the tip-sample contact of this probe is zero. The basic principle can be explained by considering the thermal resistance network between the probe and sample, as shown in Figure 3.1.

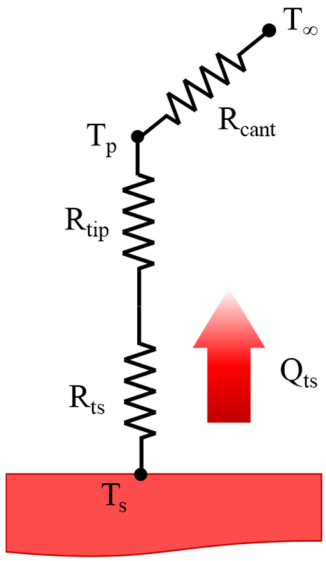

Figure 3.1 Thermal resistance network between the SThM probe in passive mode and the active sample.

When using a traditional thermal probe, a temperature difference will always exist between the probe and sample through the interface. Thus, the real temperature of the sample can only be calculated from the knowledge of R_{ts}, R_{tip} and Q_{ts} as

$$T_s = Q_{ts}(R_{tip} + R_{ts}) + T_p \qquad \text{eq. 3.1}$$

This will change for a "nulling contact" between the probe and the sample. In this situation, T_p is made to have the same temperature as T_s and there is no heat flow between the two points: $Q_{ts} = 0$. Therefore, the nulling probe is able to obtain the real sample temperature directly by measuring its tip temperature, eliminating the need to determine the tip-sample contact thermal resistance. However, nulling probes that have been demonstrated to date are limited in their requirement of double scans, in-contact and non-contact, to obtain all of the data, following which a linear extrapolation is required [152–154]. The nulling probe designed in this work eliminates this limitation and introduces some specific innovations to improve probe performance.

Finally, recognising the importance that the probe can function mechanically in a range of thermal environments, as highlighted by the

emergence of novel materials with extremely high thermal conductivities often associated with high power electrical components, it requires that the probe be able to tolerate high temperatures generated by either its own Joule heating or an active sample [142,155,156]. Under these conditions, the SiN_x probe is typically limited by its thermo-mechanical performance. This problem has previously been addressed by the development of a grooved cantilever design [56]. However, the fabrication process of this feature requires not only a well-controlled groove depth, but also a continuity of metals over the groove edge. These aspects have been optimized in this work, enabling improved device yield.

This chapter will be organized into four sections according to the discussion above, these are: the investigation of probe electrical characteristics in transient and steady state, the design of the new 'nulling probe' based on finite element analysis, the discussion of the nanofabrication process developed for grooved thermal probes, and the fundamental test of the 'nulling probe'.

3.1 Characterization of the SThM Probe

3.1.1 Temperature coefficient of resistance

The TCR of a thermal resistance thermometer is a representation of its relative change of electrical resistance (R) as a function of changing temperature (T). It is usually represented by α, with units of K^{-1} and is not necessarily a constant. When considering SiN_x SThM probes, the thermal sensor is located at the end of the tip and is made from a thin film of platinum. It has a TCR that does not vary significantly with temperature, resulting in a linear relationship between its resistance and temperature

$$R(T) = R(T_0)(1 + \alpha \Delta T) \qquad \text{eq. 3.2}$$

where ΔT is defined as the temperature difference between the working temperature T and reference temperature T_0.

In order to determine TCR, two conditions have to be satisfied: accurate measurement of the resistance, and a stable temperature that is as uniform as possible along the thermal sensor. Previously, probe TCR was approximately measured by placing a probe in a room with controlled, variable temperature. This offered a simple experimental setup that was easy to be build, but suffered from poor temperature control and extremely long settle times. As a result this measurement was considered unreliable and in need of improvement.

In this work, a new platform exploiting an immersion system was built. The experimental setup and measurement system is shown in Figure 3.2. In order to obtain a quickly adjustable uniform temperature along the probe, the SThM probe was immersed in 15 mL of fluorocarbon liquid (flutec pp3, F2 Chemicals Ltd.). Flutec pp3 was chosen since it is a colourless, nontoxic, electrically insulating liquid with an operating temperature range from - 70 °C to 102 °C, which is ample for the TCR measurement. In addition, its low viscosity (1.92 mPa·s, just 0.01% of oils which are commonly used as an insulator), made mechanical damage of the probe a low risk. The only disadvantage was its high evaporation rate but this was avoided by simply employing a sealed plastic cap.

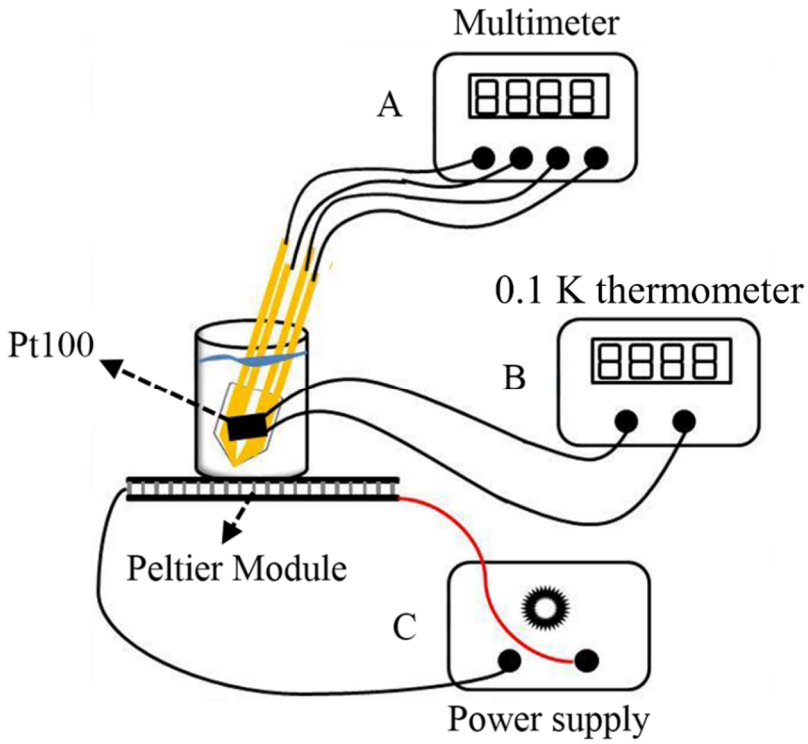

Figure 3.2 Experimental setup showing the measurement of the probe TCR.

In the experiment, a Peltier module with 40 mm × 40 mm active area was used as a controllable heating platform. The maximum cooling capacity was 5.1 W, and the maximum temperature difference between the cold and hot side was 200 K. When used in the experiment, the cold side was fixed to a cooling fin (acting as a heat sink, not shown in the figure) using silver thermal compound to reduce the thermal interfacial contact resistance and help to maintain the cold side at room temperature. A small bottle containing 15 mL flutec pp3 was placed on the hot side also with silver compound at the interface. A power supply (marked as "C" in Figure 3.2) was used to drive the Peltier module and manually control its temperature.

The experiment was carried out by submerging a SThM probe into the flutec and measuring the probe 4-terminal electrical resistance using a multimeter (marked as "A" in Figure 3.2). In order to measure the temperature of flutec, a Pt100 resistance element (a platinum thin film resistor with 100 Ω electrical resistance at 0 °C) was also submerged and fixed as close as possible

to the probe. The temperature of the probe was then assumed to be the same as the temperature of the Pt100 element, which could be read with 0.1 K accuracy using a resistance thermometer (marked as "B" in Figure 3.2).

As the TCR will change slightly with temperature, an averaged TCR over a certain temperature range is usually employed in practical work. On the basis of the fact that the SiN_x SThM probe was designed to work up to a temperature of 80 K above the ambient temperature, TCR was measured in this region [74]. The platinum resistance element of the probe was measured for 14 flutec temperatures as shown in Figure 3.3, giving an average TCR of $0.000961 \pm 0.0000106\ K^{-1}$. The error was calculated as the standard deviation of the 14 values. This value is slightly different from that estimated by Assy *et al*. [121] ($\alpha = 1.37 \times 10^{-3}\ K^{-1}$) and Puyoo *et al*. [118] ($\alpha = 1.2 \times 10^{-3}\ K^{-1}$) using the KNT probe. This is due to the two probe types employing different tip sensor materials, palladium for the KNT probe and platinum for the probes in this work. The same experiment was repeated using a palladium (KNT) SThM probe and results are shown in Figure 3.4. In this case, the average TCR was $0.001171 \pm 0.0000733\ K^{-1}$, which is closer to that described by other groups. It can be also be seen from these results that both the Pd and Pt probes exhibit a very constant TCR as evidenced by the linearity of each plot. This means that both types of probes provide a stable TCR over their operating temperature range.

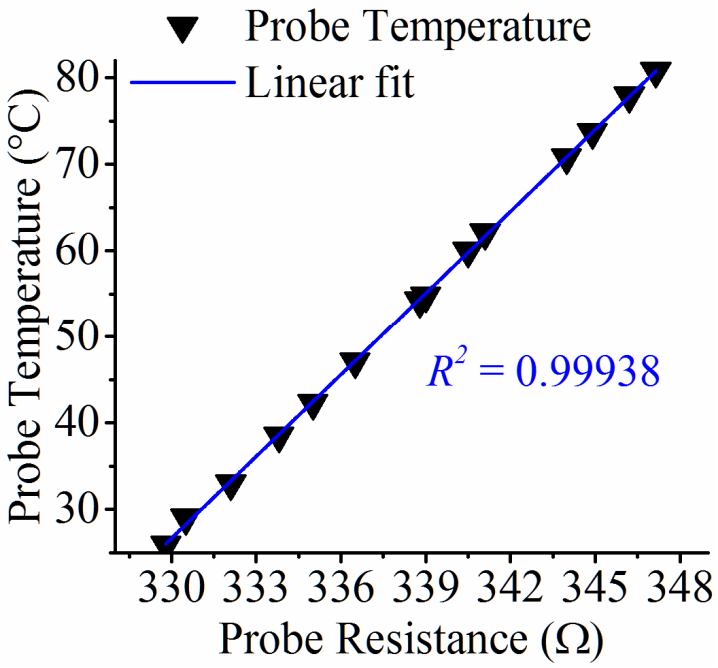

Figure 3.3 Plot of the temperature of SThM probe with platinum resistance element versus its resistance. R^2 is the coefficient of determination indicating the linearity of the fitted line.

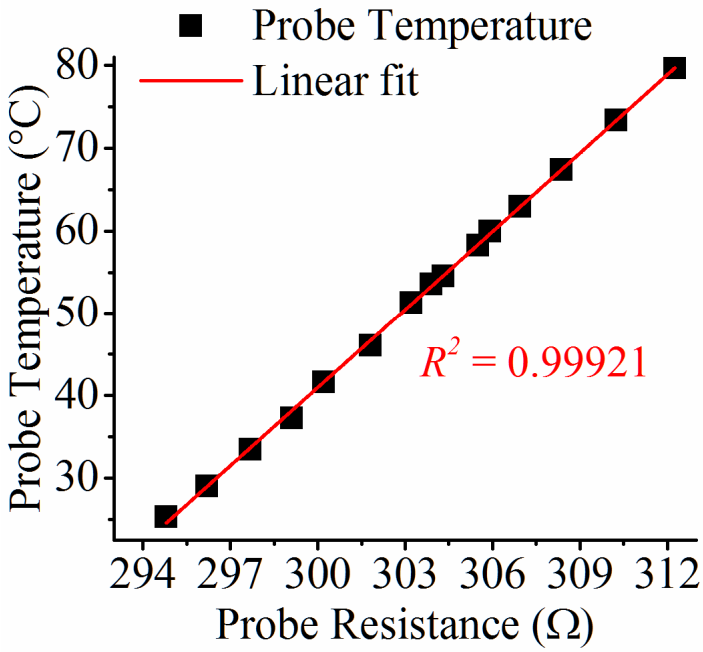

Figure 3.4 Plot of the temperature of SThM probe with palladium resistance element versus its resistance. R^2 is the coefficient of determination indicating the linearity of the fitted line.

With the push to employ SThM on samples with higher temperature and thermal conductivity, it is necessary for the probe to operate under more challenging conditions. For example, group III nitride nanowires operating under high power typically exhibit higher temperature, ~ 120 K above ambient [142]. Studying polycrystalline diamond requires a heater device deposited on the diamond film and working at high temperature [157]. Therefore, the next two sections will explore the extreme limits of operation for the probe.

3.1.2 Failure analysis of the probe

In addition to the two examples already mentioned, there are a range of applications necessitating probes working at high temperature. For example, as the complexity of heat transfer mechanisms between the probe and the sample are recognised, thermal transport at the tip-sample interface has come under scrutiny. In order to study this interface, some experiments have been carried out with probes held at a temperature above the evaporation point of water to avoid the effect of any water meniscus [113]. In addition, when studying high thermal conductivity materials, SThM probes are required to work at higher temperatures to increase their sensitivity [90,127]. Therefore, it is necessary to understand the upper temperature limits at which the SiN_x probe is safe to use and can still produce results reliably and quantitatively.

Eight probes were divided into four groups and were tested using a probe station (Agilent 4156C Precision Semiconductor Parameter Analyzer), equipped with micro-positionable probe needles. Two-terminal measurements were used, since the accurate knowledge of probe resistance was not of great importance. Measurement conditions for each of these four groups are shown in Table 3.1. For all probes, a constantly rising voltage from 0 V was applied with the resultant current being simultaneously measured. Figure 3.5 shows plots of current versus voltage for all eight probes. The failure of each probe can be clearly seen where its current abruptly drops to zero.

Table 3.1 Eight SThM probes in four groups with different test conditions

Group No.	Probe quantity	Condition	Data speed (second/point)	Colour in Figure 3.4
1	Three	In air	0.001	Black
2	One	In air	0.1	Red
3	Two	In air	0.2	Blue
4	Two	In flutec pp3	0.1	Orange

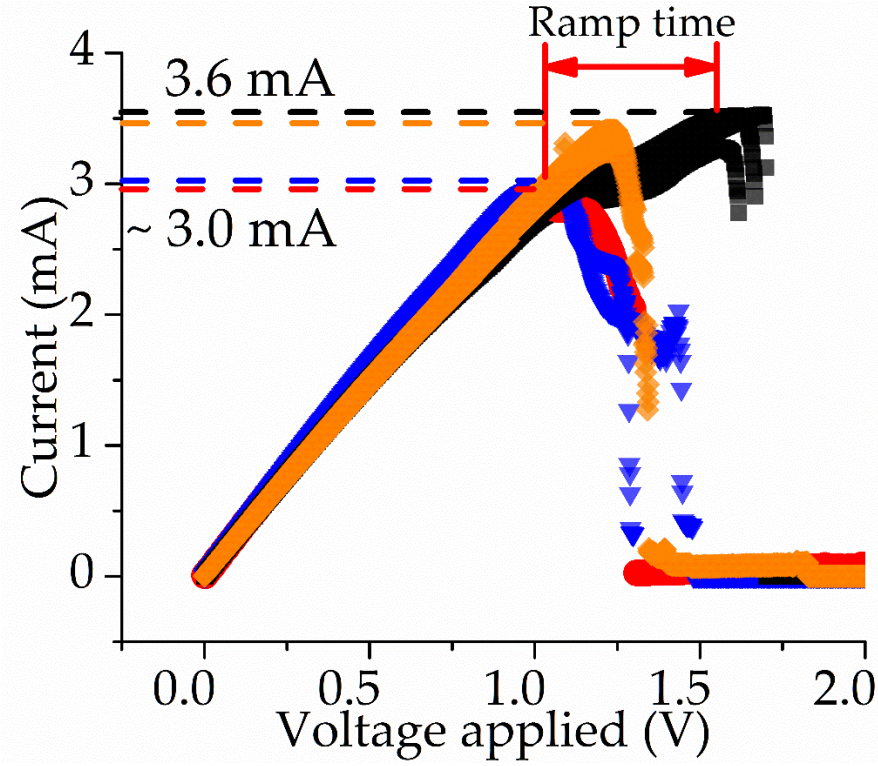

Figure 3.5 Plots of current versus the voltage applied on the probe measured by a probe station in 2-terminal operation mode. The data has been categorised using different colours corresponding to each of the four groups.

In Figure 3.5, the black, red, blue and orange plots represent group No. 1, 2, 3 and 4 respectively. When comparing the six probes tested in air, (Group 1 to 3), it can be seen that probes in Group 1 sustained the largest current. This group were exposed to the fastest voltage ramp, indicating that the device failure did not instantaneously happen at the potential applied here. The highest current that the probe can survive for the two slow groups, Group 2 and 3, is almost the same (~ 3 mA), which however is approximately 0.6 mA lower than that of Group 1. Here, 3 mA is defined as the critical current, beyond which probe failure will occur. The time taken for the probes in Group 1 to ramp from this critical current to the maximum value they failed is ~ 0.25 s. This is comparable to the time interval between two measurement points in the other groups, indicating that probe failure is not instantaneous at the critical current. This explains why probes biased using a slow voltage ramp share a similar critical current, and in the meanwhile reveals that the failure of a probe takes time to happen, a fact that is consistent with the attributed failure mechanisms of electromigration and/or temperature.

If we consider the nature of electromigration in metallic thin films, it is stated that the dissipation of Joule heating sets a limit on the maximum current density for a device [151]. This indicates, in this instance, that it is probably electromigration that dominates the probe electrical failure. This can be supported by a comparison between Group 2 and 4, which shows that submerging the probe into flutec pp3 extends its operating current to approaching that of Group 1, even though both groups have the same power ramp speed. This is due to the liquid environment decreasing the thermal resistance between the probe and its environment. The resultant decrease in self-heating for a given power permits the probes to survive at a higher current. This is in good agreement with the literature claiming that the electromigration is facilitated by increased temperature [151,158]. It also allows us to conclude that the probe failure is not just a function of current but is also dependent on tip temperature.

One of the failed probes was selected from each group and checked using scanning electron microscopy (SEM), with particular attention paid to the tip where the platinum thin film thermometer is located (Figure 3.6). A number of features, resembling voids and hillocks due to the mass flow (depletion and accumulation) and recrystallization of material, typical of electromigration deterioration can be clearly seen on the thin metallic films [151,158,159].

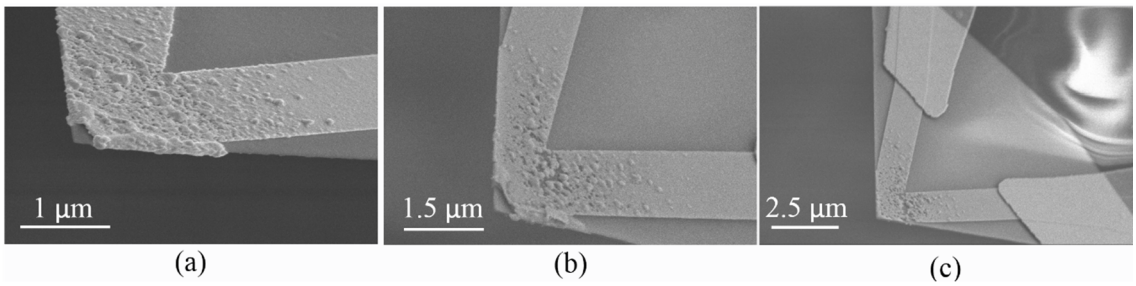

Figure 3.6 SEM image of the failed probes from Group (a) 1, (b) 2 and (c) 4.

It is possible to extract the maximum current density (J_{max}) from this experimental data by considering both the highest current and cross section area of the platinum film. Cross section area A is the product of width (3 μm) and thickness (22 nm) which is 6.6×10^{-14} m^2. By combining this with the highest sustainable current of the probe, I_{max} = 3.0×10^{-3} A, J_{max} can be determined as 4.545×10^{10} A/m^2 by

$$J_{max} = \frac{I_{max}}{A} \qquad \text{eq. 3.3}$$

This falls in the range of the current density for thin-film conductors defined in Ref. [151], which is one to two orders of magnitude larger than that of bulk materials. Previous study has shown that AC operation is able to provide a 10^3 longer lifetime of conductors than DC [160]. This suggests that the probe safe operating range can be extended by employing an AC current supply. In contrast, in-vacuum operation will reduce the safe current density due to the elimination of air, and the resultant increase in probe temperature for a given power.

There is still a question regarding whether the probe can reliably operate over such a wide current range, as its TCR will only be a constant for certain range of temperatures. In order to determine performance under extreme working conditions, a method in which any deviation of TCR can be sensitively detected, was used. It is possible to rewrite eq. 3.2 as

$$\Delta R = \alpha R(T_0)\Delta T \qquad \text{eq. 3.4}$$

where $\Delta R = R(T) - R(T_0)$. $R(T_0)$ is the probe resistance at ambient temperature (regarded as constant) and α is a constant value. Therefore, ΔR shows sensor response linearity as a function of temperature change ΔT. The relationship between the power (P) and temperature (T) is given by

$$Pt = cm\Delta T \qquad \text{eq. 3.5}$$

where c and m are the specific heat and mass of the metallic sensor, and t is time. The relationship between the power and resistance change can therefore be written as

$$P = \frac{cm}{t}\frac{\Delta R}{\alpha R(T_0)} \qquad \text{eq. 3.6}$$

Assuming that c, m, and t do not change, the linearity of temperature against power can represent the stability of TCR. Plots of probe temperature rise versus applied power for all eight probes are shown in Figure 3.7 (a). The conditions remain as described in Table 3.1.

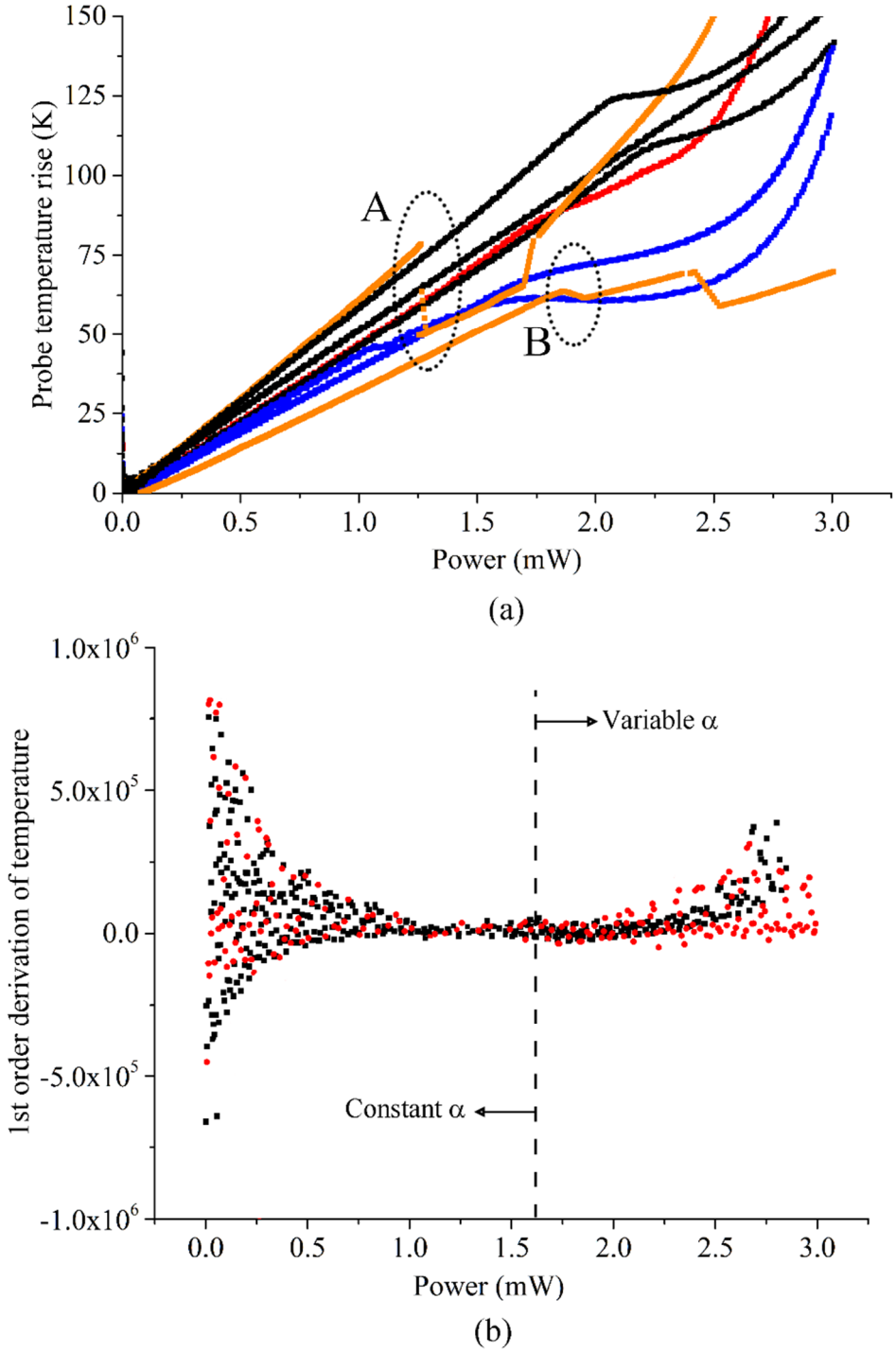

Figure 3.7 (a) Plot of the probe temperature rise versus the power applied to the probe for four groups corresponding to the Figure 3.5, and (b) plot of the 1st order derivation of the temperature rise to the power for the probes in Group 3.

A good linearity of temperature can be observed until the power exceeds ~ 1.5 mW. Two particular points on the plot, where the temperature of the probe in flutec shows a sudden drop should be noticed, and are indicated in circles A and B. It is suspected that this is due to temperature-induced bubble formation and detachment at the tip rather than probe failure, since the plot maintains its linearity after the event. To characterize the maximum power under which the probe has a constant TCR, a 1st order derivation of the temperature rise against the power for probes in Group 3 was calculated and plotted in Figure 3.7 (b). This group was selected since the slowest current ramp is the most informative when comparing the steady-state operation typically employed for practical work. The dashed line at 1.6 mW shows the demarcation point of the power, at left side of which TCR is constant, while at the right side it is changeable. This indicates that the probe can be quantitative with a fixed TCR as long as the DC current density is lower than 3.56×10^{10} A/m^2.

3.1.3 Stability test of probes

Long-term probe stability was investigated by biasing a probe using a current source, which maintained the probe at a current density lower than 3.56×10^{10} A/m^2. The experimental setup for the stability test is shown in Figure 3.8.

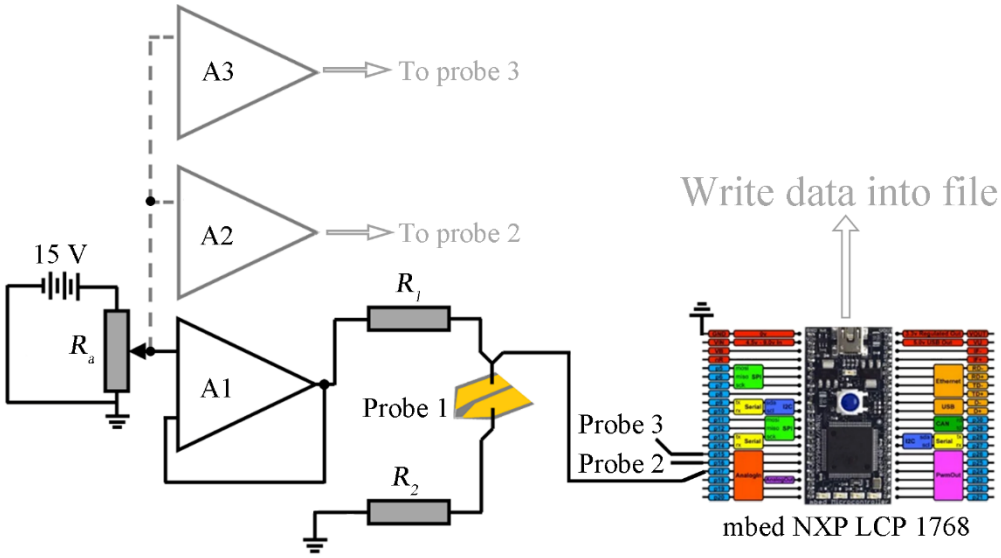

Figure 3.8 Experimental setup for the probe stability test. The mbed NXP LCP 1768 [23] was used to record the voltage across the probe. One probe is shown in the figure with the other two sharing the same setup.

The setup can be divided into two parts: a current source and a data recorder. A stable current, provided by the voltage output of an opamp (A_1) with load resistors (R_1 and R_2) was applied to the probe. To guarantee low noise, batteries were used instead of a bench-top voltage source. The current was adjustable by using a 10 kΩ adjustable resistor (R_a) and the range was set to be 0 to 3 mA. Considering the uniformity of the microfabricated probes, the experiment was carried out on three randomly selected probes. These were tested together, sharing one battery group and were under the same ambient conditions. 1 mA, 1.5 mA and 2 mA were used as biased currents, resulting in current densities of 1.5×10^{10} A/m^2, 2.25×10^{10} A/m^2 and 3.0×10^{10} A/m^2 respectively on the sensors. The probe voltage was recorded every 10 min over 24 hours using the mbed NXP LCP 1768 evaluation board with its 12-bit ADC. Results are shown in Figure 3.9 with the resistance of all three probes on the same scale. The code compiled for controlling the evaluation board is given in Appendix I.

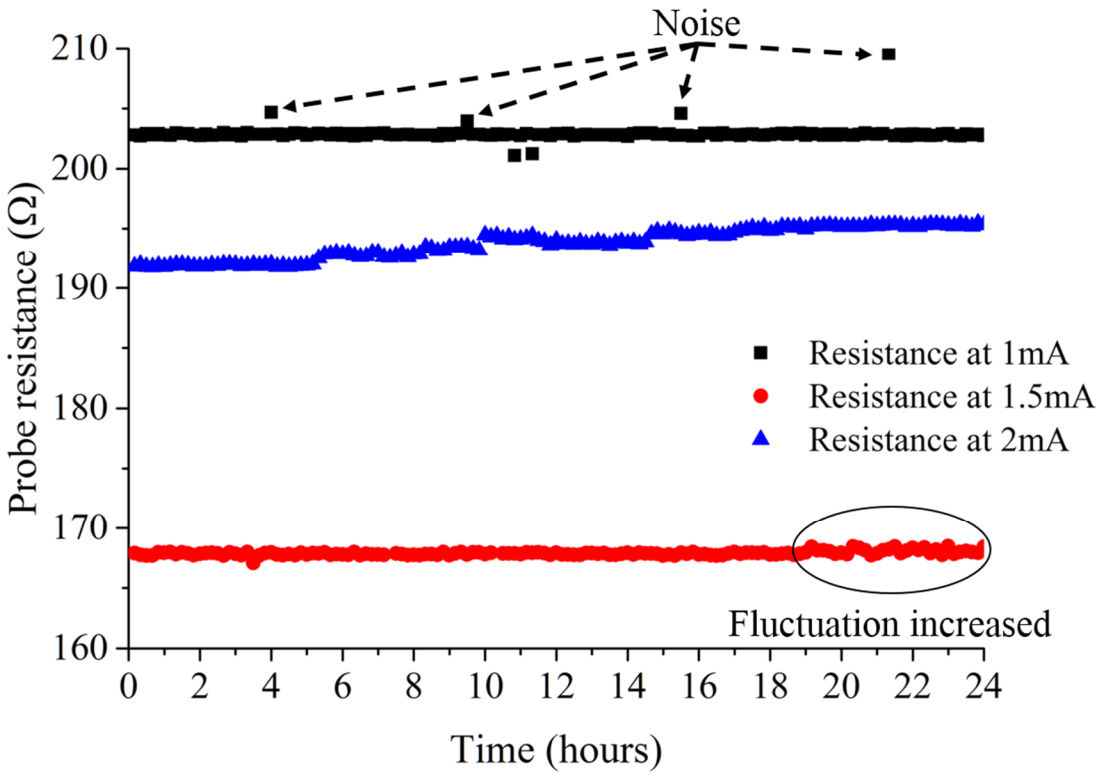

Figure 3.9 Plots of the probe resistance versus time indicating probe stability for probe biased by 1 mA, 1.5 mA and 2 mA.

It can be seen that the probe biased at 2 mA suffered a gradual resistance change after approximately 5 hours' heating. After 24 hours' test, a re-measurement of the probe resistance showed that the probe had been permanently changed, with its resistance increased from 191.6 Ω to 196.5 Ω. It is suspected that this is the result of recrystallization of the platinum thin film [87]. In contrast, probes biased at 1.5 mA and 1 mA did not suffer from a significant change in resistance. The standard deviation of the probe resistance at 1 mA is 0.47 Ω over the course of the experiment. After discarding the noise spikes caused by the electronic circuit, this is 0.23 % variation of the total resistance. On the other hand, the probe biased at 1.5 mA was stable over the course of the first 19 hours (standard deviation 0.61 Ω), after which it became slightly less stable (standard deviation 1.98 Ω). This result indicates that, for long-time use (greater than 4 hours), a current density of less than 3.0×10^{10} A/m^2 is recommended. It has to be stressed that these measurements were

made in air, given that temperature increases the effect of electromigration [151], a lower current density is recommended for vacuum due to the increased thermal resistance (and increased probe self-heating) resulting from that environment.

3.1.4 Self-heating test of the probe

One useful piece of information regarding the probe is identification of the current, below which the probe is negligibly self-heated, and above which, the probe functions as a heater. An experiment that measures the self-heating of the probe can be carried out dynamically. Here, probe resistance change due to self-heating could be clearly distinguished, whilst simultaneously giving the time constant for heating of the probe.

Figure 3.10 shows a schematic of the experimental setup used. In this circuit, when $R_1 = R_2$, the output of opamp 1 equalled the amplitude of the signal from the function generator but with a 180° phase difference. When R_3 had the same resistance as the probe (R_p), the voltage at node A (U_A) would be zero. The output of opamp 2, feeding into an oscilloscope, was used to amplify the changes in voltage. The gain of opamp 2 (Θ) was set as 500.

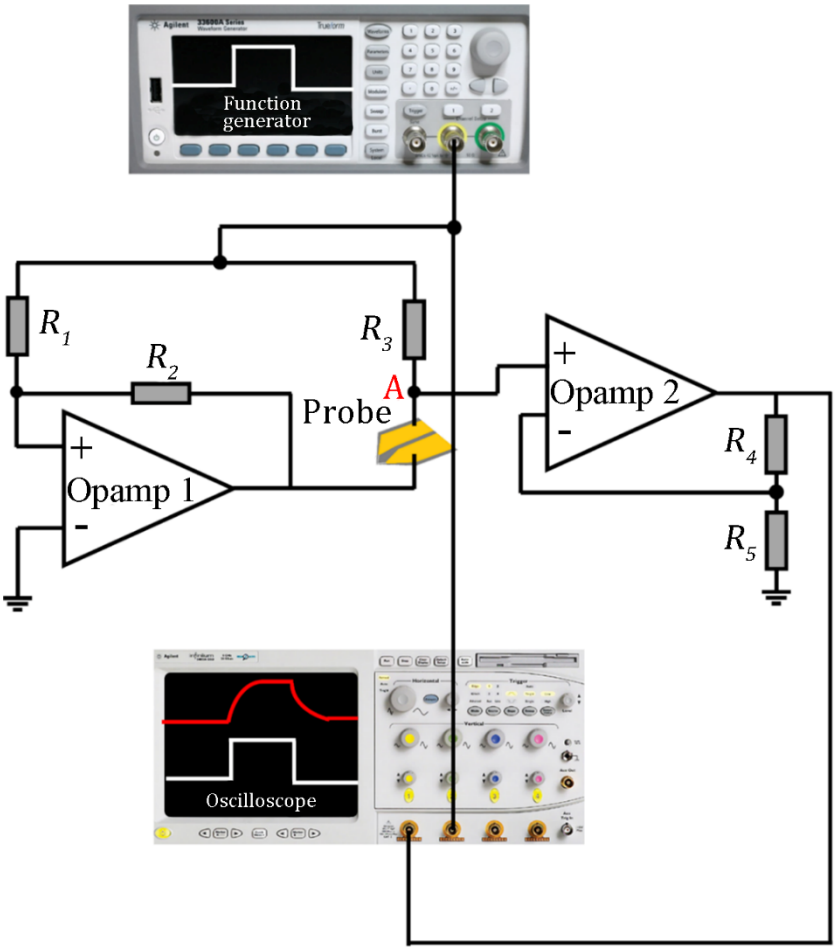

Figure 3.10 Schematic of the circuit used to dynamically measure the self-heating current of the probe.

The current used to bias the probe was controlled using a square wave (with U as peak-peak voltage) produced by a function generator. In this experiment, current was increased from 0.1 mA to 0.5 mA in increments of 0.1 mA. The probe selected was 107 Ω at ambient temperature. The voltage recorded by the oscilloscope (U_o) can be converted into the variation of the probe resistance by

$$\Delta R_p = \frac{2R_p U_0}{\Theta U - U_o} \qquad \text{eq. 3.7}$$

Thus, plots of the variation of probe resistance as a function of time are shown in Figure 3.11. It can be clearly seen that probes passing 0.1 mA current do not show any obvious change in resistance, while currents higher than 0.3 mA do

result in significant self-heating of the metallic sensor. A small change can be observed on the 0.2 mA curve, corresponding to ~ 0.08 K temperature increase above ambient, when converted from electrical resistance using the TCR. This suggests that a probe can be regarded as operating in passive mode when biased with a DC current lower than 0.2 mA. Translating this into the current density, it is recommended that a DC current density of less than 3×10^9 A/m^2 can be employed when using the probe as a passive mode thermometer. When operated by AC signal with peak-peak current ($V_{p\text{-}p}$) equal to the DC current, the Joule heating power will be halved due to the root mean square value (V_{rms}).

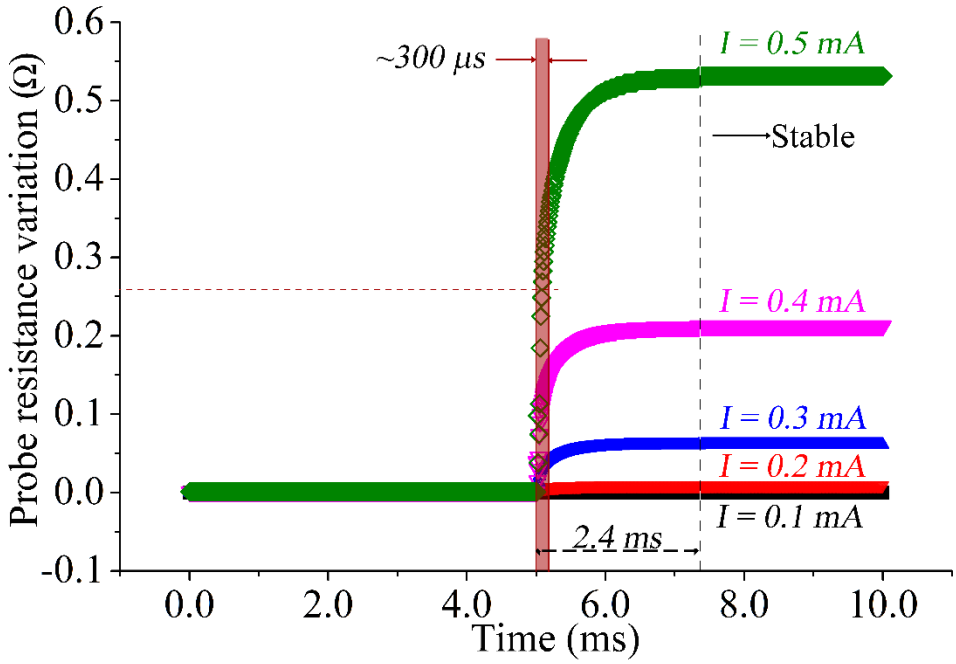

Figure 3.11 Plots of output voltage recorded by the oscilloscope versus time. Probes biased under five different currents are examined and demonstrated individually in different colours.

Knowledge of the Joule heating current has proven helpful when testing the probe using a common multimeter set to measure resistance, a typically procedure often carried out before making a thermal measurement. In order to eliminate Joule heating during this test, a current below 0.2 mA should be used. For example, the general-purpose multimeter used for quick assessment here (Rapid 955 Digital Multimeter) had its resistance measurement range manually set to 4.0 kΩ, as this employed a working current of 62.5 μA [161].

As mentioned above, probe temperature is dictated by Joule heating combined with the thermal resistance of the probe/environment. There are two dominant heat paths, through which the Joule heating power can flow away from the probe: thermal conduction through the probe, along the cantilever and into the silicon base and thermal conduction through the surrounding air. When both of these paths are present, the thermal resistance of probe has been calculated as R_{probe} = 2.273 × 10^5 K/W in Chapter 5, and the contribution of air conduction can be determined from the thermal resistance network shown in Figure 3.12 as R_{air}. I_{th} represents the heat flow through the whole network, which, at steady state, is given by the Joule heating power of 2.69 × 10^{-5} W when heated by 0.5 mA current, and T_a represents the ambient temperature (ground in the circuit). In order to match ΔT_{tip} with experimental observation (5.33 K), R_{air} must be set as 1.56 × 10^6 K/W. Therefore, the contribution of air can be described as heat flux of the probe by Newton's law of cooling as

$$q'' = \frac{q_{air}}{\Delta T A_{probe}} \qquad \text{eq. 3.8}$$

where q_{air} is the heat loss from the air conduction and calculated by $(\Delta T_{tip}/R_{air})$ as 3.41 × 10^{-6} W, and A_{probe} is the surface area of the probe: 1.404 × 10^{-8} m^2. Thus, q'' is determined as 45.57 W/m^2K. This estimation will be used in the FEA model employed to simulate the nulling probe discussed later in this chapter.

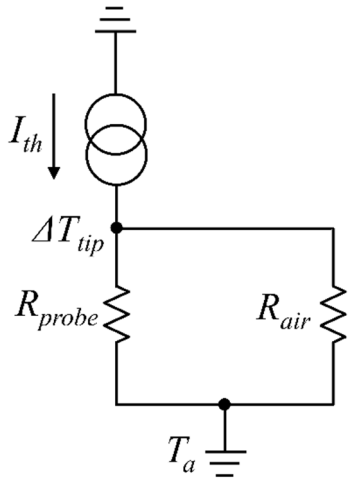

Figure 3.12 Thermal resistance network of Joule heated probe in air.

In addition, thermal diffusivity of the probe (d_{th}), which represents the heat transfer ability of a material, can be obtained from the dynamic measurement by accounting for the expression first proposed by Parker *et al*. [162]

$$d_{th} = \frac{0.139 L_{probe}^2}{t_{50}} \qquad \text{eq. 3.9}$$

where L_{probe} is the probe length and t_{50} is the time the probe takes to reach half of the maximal temperature increase. Given L_{probe} as 150 μm, and t_{50} as 300 μs, thermal diffusivity of probe can be calculated as 1.04×10^{-5} m^2/s. Taken into account the definition expression of thermal diffusivity as [17]

$$d_{th} = \frac{k}{\rho c} \qquad \text{eq. 3.10}$$

the thermal diffusivity of gold wires on the probe can be calculated as 10^{-4} m^2/s, while that of SiN_x as 5×10^{-6} – 10^{-5} m^2/s. This indicates that thermal diffusivity of the probe is not dependent on a single material, but a combination of materials composing the probe. It can also be noted from Figure 3.11 that it takes 2.4 ms for the probe to achieve a truly stable temperature. This value can be linked to the concept of local thermal equilibrium mentioned in Chapter 1, at which stage the temperature of the probe can be defined. In this thesis, when carrying out thermal scans, the scan rate and resolution of the fast scan

direction (the direction that the probe moves fast across the sample surface relative to the slow scan direction) was controlled to be 0.5 Hz and 512 pixels. This gives the probe ~ 4 ms for each pixel and guarantees that the temperature of the thermal sensor can always be defined.

With the help of the probe properties characterized in this section, the design of the 'nulling probe' is provided with baseline. For example, the highest current density decides the highest temperature the nulling probe can work at; the air contribution q'' is helpful in simplifying the FEA model, etc.

3.2 Nulling Probe Design and Simulation

3.2.1 Design strategy

The electrical, thermal and mechanical characterization described above is of great use in interpreting experimental data. However, it also has a secondary use in informing the design of next-generation probes such as the nulling point probe introduced earlier. In order to achieve the nulling point, probe temperature has to be kept as close as possible to the sample temperature. This then permits sample temperature to be obtained directly from the probe. This requires the nulling probe to be able to sense probe-sample temperature difference, alter and then accurately measure its own temperature. The first of these functions was achieved by employing a thin film thermocouple as a localized thermometer at the very end of the tip. This offers the advantage of high-speed response due to its location and small volume [109,163]. By tapping the thermocouple onto the sample, heat flux at the contact point will be broken and built repeatedly. This allows the temperature difference between the probe and the sample to be sensed. As its design maintains a similar shape, dimensions and materials, we can state that the nulling probe will exhibit a similar time constant to the current probe. This information is important since it ultimately decides the limitation of tapping and scanning rate. The accurate measurement of probe temperature makes use of a 4-terminal platinum resistor that can act as a Johnson noise

thermometer. These two features can be seen in the enlarged image in Figure 3.13. It can be found that they have also been placed as close as possible to each other to minimize any temperature difference.

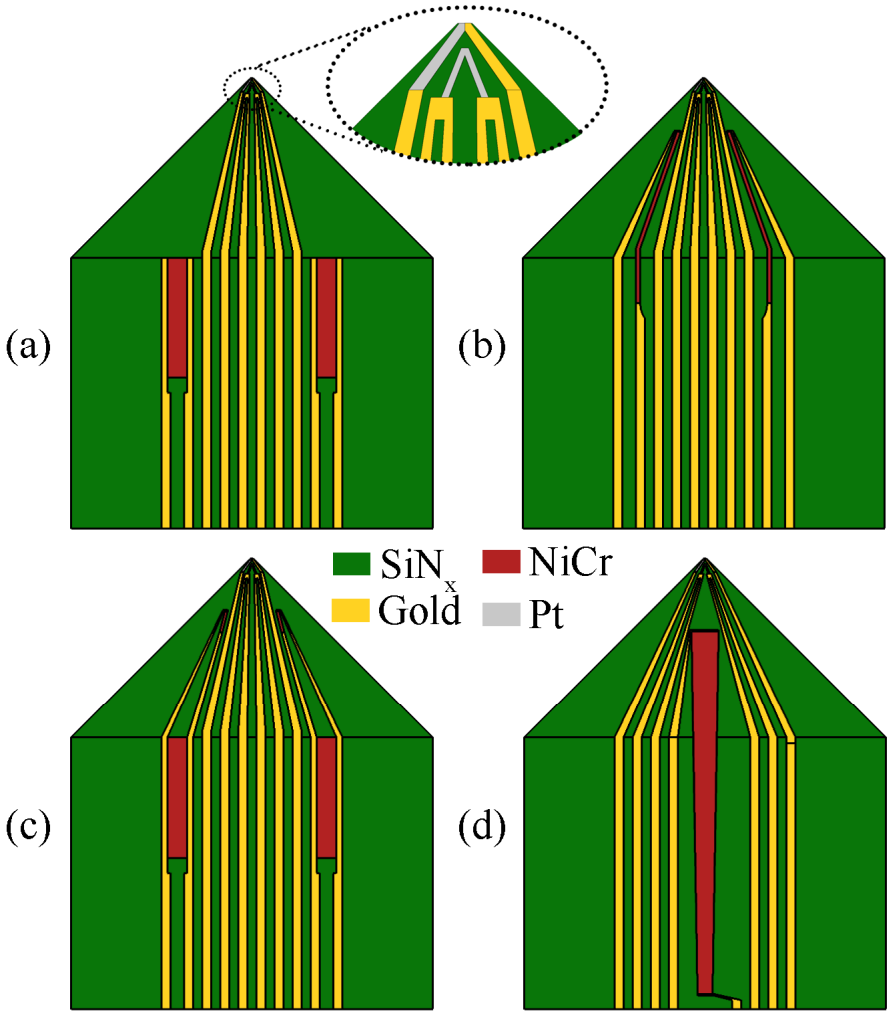

Figure 3.13 (a), (b), (c), and (d) illustrate four designs of nulling probe with the change of position and size of heaters on the cantilever. Thermocouple and Johnson noise thermometer are the same for all designs as shown in the inset.

While the probe thermometers are designed to be small and located close to the tip, ensuring a fast response and good accuracy, the heaters have very different requirements. Their function is to enable a useful self-heating temperature range whilst eliminating the temperature difference between the tip thermometer and the sample. The first of these requirements can be

achieved by employing heaters that are large enough to sustain significant heating power before suffering electrical failure through electromigration. Simultaneously, the thermal gradient on the tip has to be minimized through optimized design of heaters shape and location. Four potential probes with the same tip design, but different heaters are shown in Figure 3.13. Design (a) and (b) employ a similar idea that the nonuniformity of temperature can be minimized at the center of two heaters, inspired from the Helmholtz coil [164]. By varying the position and shape of the heater, it is expected to optimize the thermal gradient at the tip. Design (c) aims to enhance the performance of the multiple-heater layout by employing four heaters, with two large on the cantilever and two small close to the tip. A different design is shown in Figure 3.13 (d) making use of a single trapezoid heater through the centre of cantilever, with the wide side (smaller electrical resistance) close to the tip and narrow side (larger electrical resistance) at the bottom. The aim of this heater is to compensate for heat loss along the probe by increasing the temperature generated gradually from the tip to the bottom. All designs were simulated to evaluate their temperature distribution and current density by FEA using COMSOL MULTIPHYSICS®.

Apart from requirements addressed above, the design also has to fulfil:

1) The cantilever must be grooved to decrease thermal bending.
2) The probe must be relatively easy to fabricate, without great change to the current, mature process.
3) The shape and material should be maintained from the old design in order to share a similar time constant and a general probe holder.

3.2.2 Probe simulation

The simulation model was built in 3D using the actual dimensions and materials employed in KNT probe fabrication. In order to reduce the calculation load, only the tip and cantilever were considered by holding the base of the cantilever at ambient temperature. The “Joule Heat” module was

employed as it combined both electrical heating and heat transfer in a single simulation. An electric potential was applied as one boundary condition of the heater, while the other end was set to ground. In order to include air conduction, the heat flux due to air as determined in the previous section (45.57 W/m^{2}K) was set for the whole probe surface. Simulation results for all four designs with the same temperature at the tip are shown in Figure 3.14. It can be seen that both design (a) and (c) are able to generate uniform temperature over the largest area (almost the whole triangle part), while design (b) and (d) show a large thermal gradient along the whole probe. This can be clearly seen in the temperature distribution plot from the tip to cantilever base for all designs plotted in Figure 3.15.

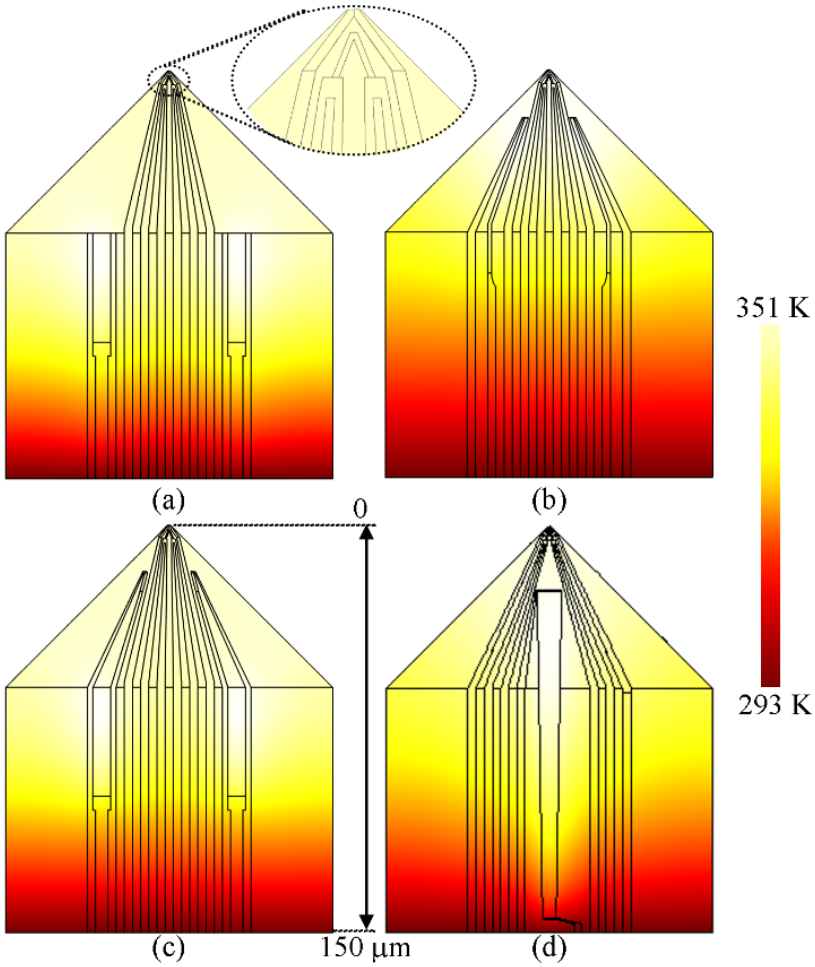

Figure 3.14 Simulation results of four probe designs showing the temperature distribution on the cantilever, with the inset showing the temperature of the tip.

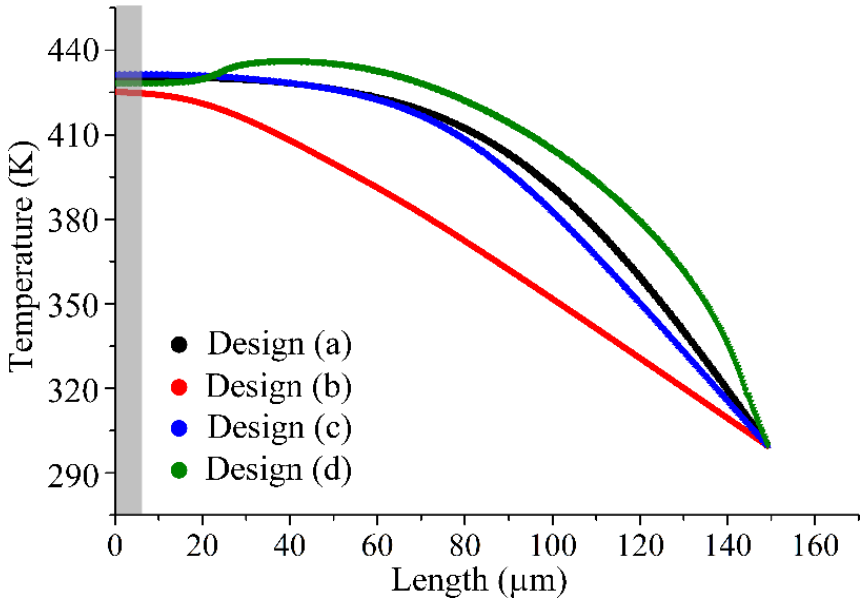

Figure 3.15 Plots of temperature distribution from the tip (0) to the base of the cantilever (150 μm) for all designs.

Although the thermal gradient along the probe cannot be eliminated, it is possible to obtain a minimal temperature difference between the two thermal sensors at the tip. This can be observed from a flat thermal gradient in the shaded area, corresponding to the location of the temperature sensors. The average temperature taken from the junction of the thermocouple (the hot junction) and the whole Johnson noise thermometer indicates that design (b) gives the highest deviation, which accounts for just 0.2 % of the whole probe temperature rise (150 K). This suggests that all four designs are worthy of being fabricated and tested.

Before fabricating the new probe, thermal bending that will severely affect probe performance has to be first discussed. As the nulling probe is designed to operate with a self-heated cantilever, it is more prone to failing due to it. In addition, thermal bending will also induce a perturbation to the heat flow measurement when using the current probe.

3.3 Thermal Bending Compensated SiN_x Probe

3.3.1 Principle and issue

Although a bimorph structure has been exploited in a new form of thermal microscopy based on thermal bending [165], it is considered an unwanted phenomenon for our SiN_x probe. As the SThM probe functions mechanically in the same way as an AFM, the feedback loop maintains a constant force between the tip and sample as the probe scans the sample surface. When the probe is heated, its cantilever will bend away from the sample, which will be misinterpreted by the feedback loop as a rise in topography. As a result, it will lift the probe, resulting in the contact between the probe and sample being broken, and interrupting the scan [56]. Therefore, thermal bending will not only affect the mechanical signal but also heat conductance between the tip and the sample, impeding thermal measurement.

The principle behind eliminating thermal bending is that the concentrated bending moment can be reduced to zero by including a groove in the probe cantilever. A schematic illustrating how the groove works is shown in Figure 3.16. When the probe is heated, differential thermal expansion means that the metallisation on the cantilever will exert a stress (F) against the SiN_x, resulting in a bending moment against the neutral plane (shown as the dash-dot line). The bending moment on a cantilever with a groove can be calculated as [56]

$$M = F\frac{dep-t}{2} \qquad \text{eq. 3.11}$$

where *dep* is the depth of the groove and t is the thickness of the SiN_x cantilever. F will always exist as long as there is a difference in thermal expansion between two materials. Therefore, in order to eliminate the bending moment, *dep* must be set equal to t.

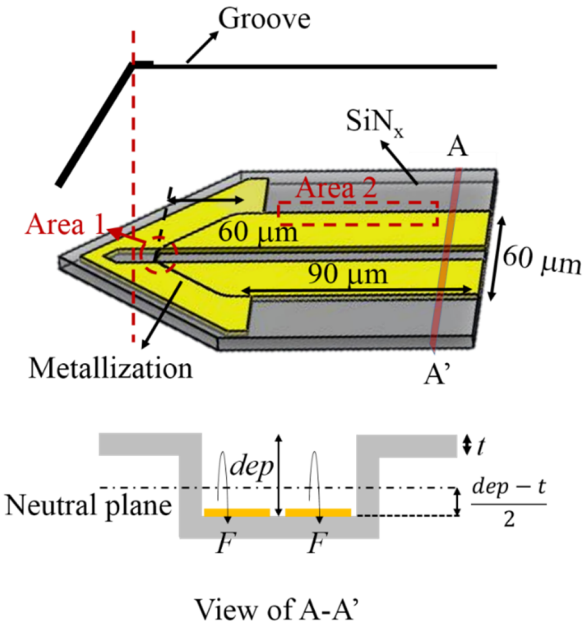

Figure 3.16 Schematic diagram showing the position of the groove on the cantilever, as well as the groove working principle.

In the schematic of probe fabrication shown in Figure 2.2 of Chapter 2, the groove is etched into the silicon wafer in step (V). Original development of the thermal bending compensated probe was carried out by Zhang *et al*. [56] several years ago, however the process was not optimized or commonly adopted. An attempt to repeat the same process in recent work met with failure. After investigating all parameters, one possible reason for this seems to be that properties of the commercial photoresist – AZ4562 have been altered by the manufacturer. In particular, its adhesion and resilience are now different – as clearly shown in Figure 3.17 (a) and (b) respectively. After development, it can be seen that a large gap formed between the AZ4562 and the silicon substrate (the dashed circle in Figure 3.17 (a)), while after plasma etching, the resist shows a rough surface (shown by the arrow in Figure 3.17 (b)). Neither of these features were present with the old resist formulation. Therefore, pattern transfer using the new AZ4562 into the silicon substrate is not possible using the old process. This section describes the re-development of the groove fabrication process. This is a fundamental process step and

essential for the fabrication of the probes used in all experiment in the following chapters and also of the nulling probes.

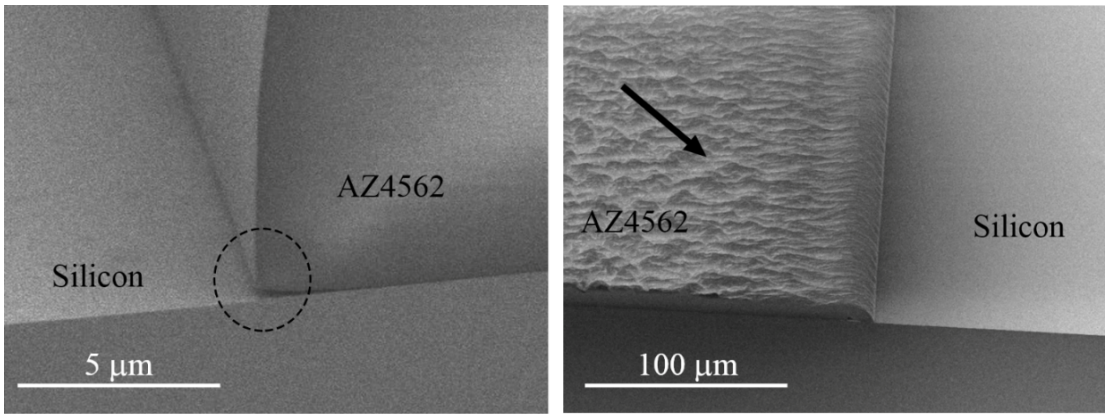

Figure 3.17 SEM image showing the AZ4562 photo resist profile (a) after development, and (b) after dry etching by the original recipe.

The original fabrication process is listed below as

1. Clean substrate: 1:1 MS 20D Nanostrip : RO water 10 min, RO water rinse 5 min;
2. Resist spinning: AZ4562 spinning at 4000 rpm for 30 s, leave for 5 min at room temperature;
3. Softbake: oven bake at 90 °C for 45 min;
4. Second layer resist spinning and softbake: the same as last two steps;
5. Expose: 350 nm UV expose for 100 s by 4 cycles;
6. Development: 1:4 AZ400K : RO water for 8 min;
7. Dry etch by RIE 80+:
    i. 10 sccm O_2 at 10 W and 50 mTorr for 2 min as ash,
    ii. 50 sccm CF_4 at 200W and 55 mTorr for 12.5 min;
8. Resist strip: warm acetone for 1 hour.

The reason for using the thick photoresist AZ4562 is that the groove is etched after the pyramids having been defined on the sample (please refer to the step III and IV in Figure 2.2). As a result, the sample has significant (~ 10 μm) topography that must be fully coated by the resist layer. In order to achieve this and protect the pyramids from damage, a double-layer AZ4562

was employed to generate a ~ 12 μm thick coating. Parameters such as softbake, exposure and development for the double-layer AZ4562 were kept the same as the original recipe, as it was known that this would produce clean patterns without resist residue. Therefore, process development focused on the steps that came after resist development, specifically the hardbake and dry etch parameters.

3.3.2 Process development with large patterns

For the convenience of both optical and electron microscopy inspection, patterns with dimensions of 1000 μm × 5000 μm were used for process development. The hardbake is usually performed immediately after resist development in order to enhance the stability of the resist structure and promote adhesion with the substrate [166]. Specific to AZ4562, reflow will typically happen when the temperature is above 110 °C, at which point a chemical bond between the resist and the substrate will be formed, improving the adhesion. Simultaneously, any remaining solvent will be removed by evaporation, increasing chemical stability against the subsequent plasma etch [167]. Therefore, a 120 °C oven hardbake was carried out for 10 min. Figure 3.18 shows the effect of the hardbake on AZ4562 and the resulting pattern after subsequent plasma etching using the original process. The gap between the substrate and the AZ4562 has vanished, indicating improved adhesion as the result of the hardbake. In addition, a smooth AZ4562 surface after plasma etching demonstrates resistance to the dry-etch plasma (shown in Figure 3.18 (a) and (b) respectively). However, the extremely steep and rough sidewalls transferred into the silicon ((c) and (d)) show that this process is far from compatible with continuous metallisation over the step. Therefore, attention was turned to adjusting the parameters used for plasma etching.

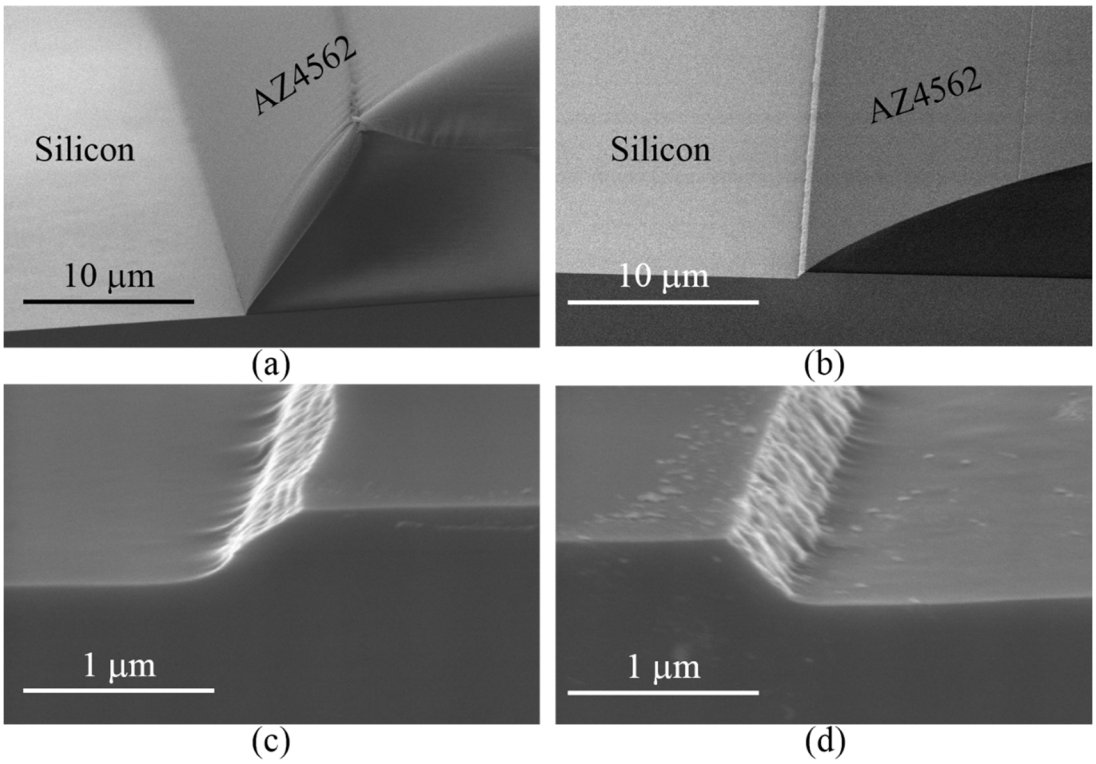

Figure 3.18 SEM image of (a) silicon substrate with the AZ4562 after hardbake, (b) the profile of the silicon substrate and the AZ4562 after dry etching, (c) and (d) the profile of the silicon shallow etching after stripping the AZ4562.

Plasmas used to etch silicon are typically generated from fluorine-based gas. It has been proved that the fluorine in a plasma dominates the reaction with silicon [168], because of which CF_4 was chosen due to its high ratio of fluorine to carbon. However, such fluorocarbon gases can produce unsaturated carbon compounds in the plasma, resulting in polymers forming and depositing on the substrate, which further impede horizontal etching and eventually generate a rough etched surface. Based on Ref. [168], oxygen can help to reduce this polymer formation due to its capability to increase the proportion of available fluorine by reacting with CF_x radicals and also reducing recombination of fluorine atoms with CF_3. By mixing CF_4 with 2 sccm O_2, clear and sloped sidewalls were achieved – Figure 3.19. Although a promising profile, the sidewalls shown in Figure 3.19 are still unsatisfactory, due to their gradually varying slope from bottom to top.

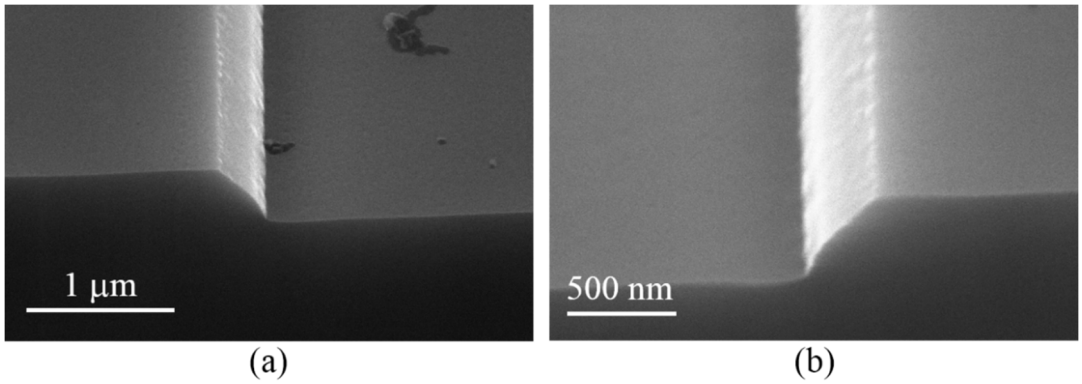

Figure 3.19 SEM images show the profile of sidewalls after mixing the CF_4 with O_2.

In order to fix this, the plasma pressure can be another important parameter to consider. Lee *et al*. [169] proposed the existence of a plasma pressure at which the sputtering effect can be enhanced. This will make the curved sidewall become flattened. Profiles of the sidewall were compared for various pressures, which are shown in Figure 3.20. It can be seen that a satisfactory sidewall with a flat and gentle slope (~ 155°) can be achieved by increasing the pressure to 65 mTorr (a and b). Either increasing the pressure further to 75 mTorr (c) or reducing it to 45 mTorr (d) deteriorates the sidewall profile.

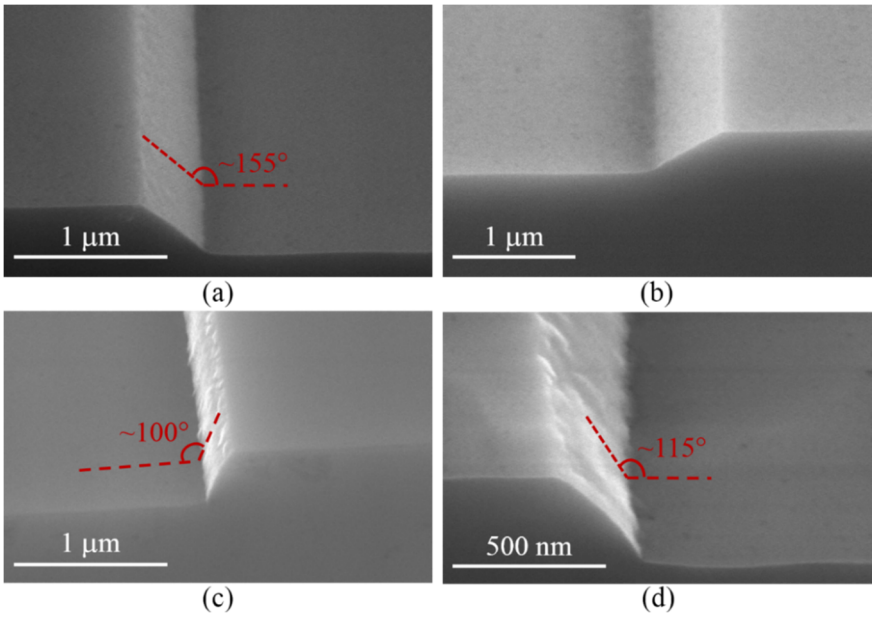

Figure 3.20 SEM images (a) and (b) show the profile of sidewalls achieved by increasing the plasma pressure from 55 mTorr to 65 mTorr, (c) increasing the pressure to 75 mTorr and (d) reducing the pressure to 45 mTorr.

3.3.3 Process development with actual-size patterns

As the newly developed fabrication process worked satisfactorily with large patterns, it was transferred to the real groove pattern, which had smaller dimensions and a more complicated shape. Both the dimensions and shape can be seen in Figure 3.16 (a). Unfortunately, the newly developed recipe produced completely different sidewall profiles on the large and groove patterns. Figure 3.21 (a) and (b) illustrate the etched slope profiles from Area 1 and Area 2 (as marked in Figure 3.16 (a)) with a rough and steep sidewall. 75 nm thick NiCr deposited on the substrate after etching was used to clearly demonstrate the discontinuity caused in metal films by these imperfect sidewalls (Figure 3.21 (c) and (d)). The dark line (shown by arrows) on the sidewall in each figure indicates a discontinuity in the metallisation.

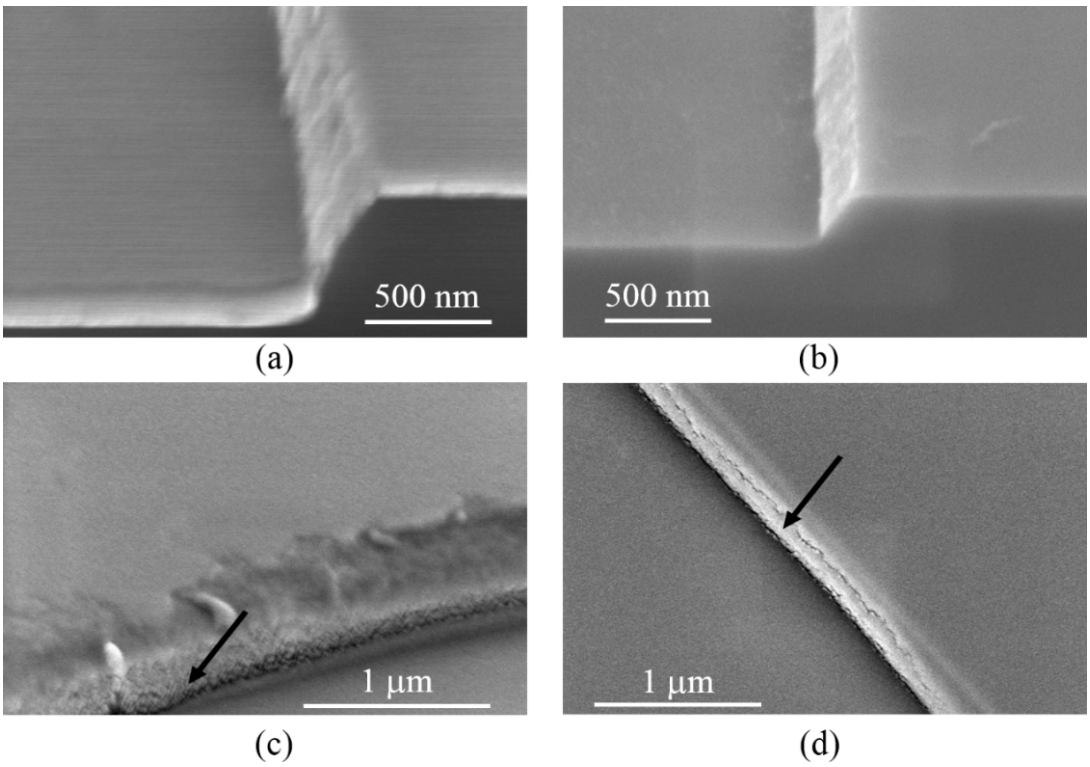

Figure 3.21 SEM image shows the profile of sidewalls by transferring the recipe developed with the large patterns to the actual-size patterns for (a) Area 1, (b) Area 2, with (c) and (d) shows the corresponding area of (a) and (b) respectively after 75 nm thick NiCr deposited.

Checking the photoresist profile using optical microscopy showed that the unsuccessful recipe transfer was caused by rough resist edges before the hardbake and a vertical resist profile after the hardbake (Figure 3.22). In particular, the rough edge was inherited from the resist profile right after development (Figure 3.22 (a)) and could not be remedied after the 120 °C hardbake. Furthermore, it can be seen that Area A was still unfocused under the optical microscope while other parts were in focus (Figure 3.22 (b)). This indicated the existence of significant height variation between Area A and other parts, the possible reason for which was that a gap between the resist and the surface appeared after hardbake. It was decided that enhancing the poor adhesion and a further reflow could offer a solution. Therefore, an increased hardbake temperature of 180 °C was tested. An apparent improvement in Area 1 and Area 2 can be seen in the SEM images (Figure 3.23 (a) and (b)), however, the sidewall slopes were still too steep to allow continuous metallisation. The addition of more O_2 to the plasma gas mixture (from 2 sccm to 4 sccm) helped to decrease the slope allowing an ideal sidewall to be achieved as shown in Figure 3.23 (c) and (d).

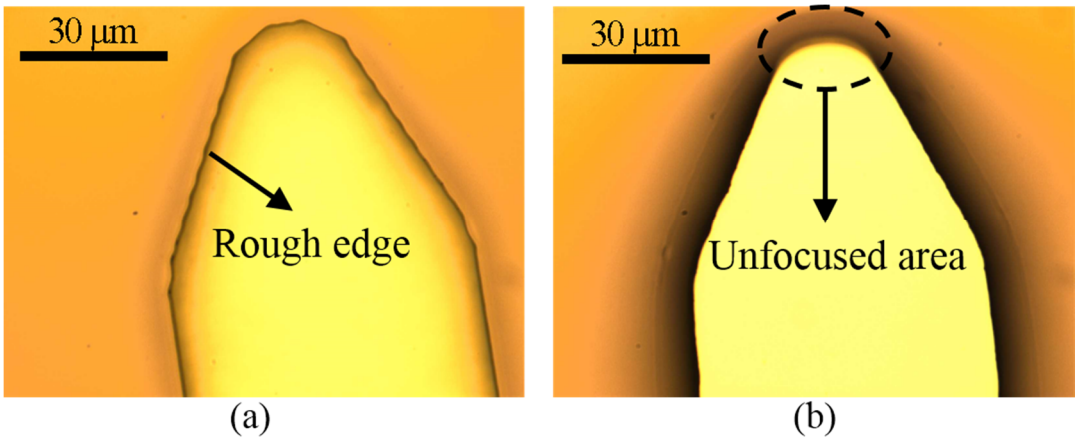

Figure 3.22 Optical microscopy images show the profile of AZ4562 (a) before and (b) after 120 °C oven hardbake.

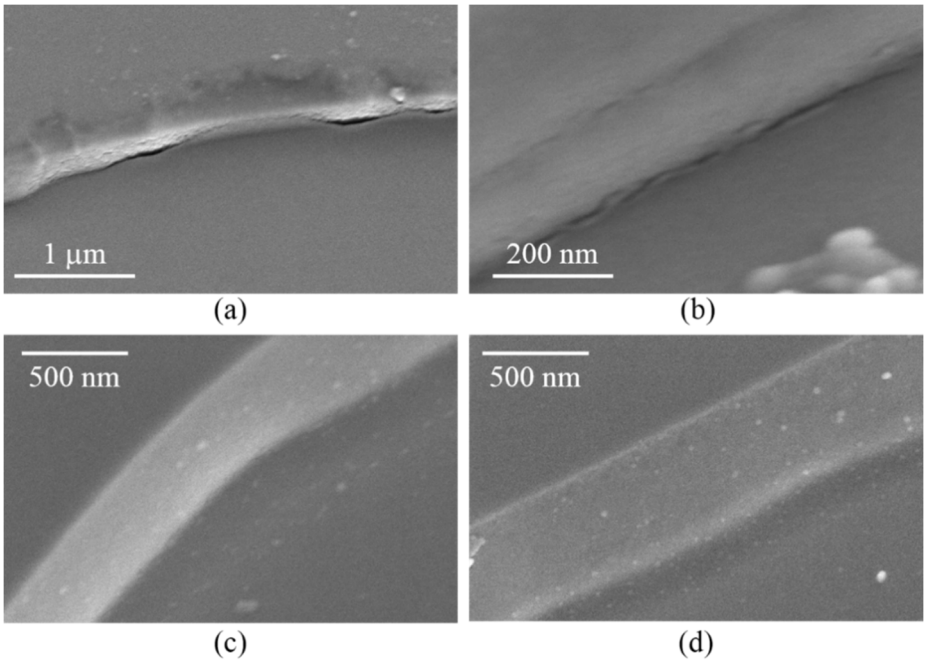

Figure 3.23 SEM images showing the profile of silicon shallow etched sidewalls for (a) Area 1 and (b) Area 2 as the result of raising the hardbake temperature from 120 °C to 180 °C, with (c) and (d) showing the corresponding profile to (a) and (b) respectively after increasing the ratio of O_2 in the plasma. All profiles are checked by depositing a 75 nm thick NiCr onto the sample.

The only issue resulting from the new recipe was the difficulty in resist removal after the 180 °C hardbake, as caused by thermal cross-linking of the AZ4562. This was evident after warm acetone failed to strip the resist residue after 24 hours soaking. The solution was to employ a more aggressive stripper, MS 20D, which was used as in step 1 of the original recipe, but with extended soaking time of 1 hour and one repeat.

As a consequence, the process for silicon shallow etching with a correctly sloped sidewall was changed to:

1. Clean substrate: 1:1 MS 20D Nanostrip : RO water 10 min, RO water rinse 5 min;
2. Resist spinning: AZ4562 spinning at 4000 rpm for 30 s, leave for 5 min at room temperature;
3. Softbake: oven bake at 90 °C for 45 min;

4. Second layer resist spinning and softbake: repeat 2 and 3.
5. Expose: 350 nm UV expose for 100 s by 4 cycles;
6. Development: 1:4 AZ400K : RO water for 8 min;
7. Hardbake: oven bake at 180 °C for 10 min;
8. Dry etch by RIE 80+:
    i. 10 sccm O_2 at 10 W and 50 mTorr for 2 min as ash,
    ii. 50 sccm CF_4 with 4 sccm O_2 at 200W and 65 mTorr for 15 min;
9. Resist strip: 1:1 MS 20D Nanostrip : RO water for 1 hour.
10. Resist further strip: repeat 9.

3.3.4 Test of thermal bending compensated probe

To verify the effectiveness of the shallow etched groove, a comparison was made between a normal SiN_x probe and a thermal bending compensated probe by calibrating them using the Johnson noise calibration device. Details of this device and calibration procedure can be found in Ref. [88]. An alternative method, not used here but described in Ref. [56] is to employ an optical profiling system.

Two probes, one normal and one thermal bending compensated, were selected having resistance as close as possible to each other to ease comparison. The calibration device was used with temperature ranging from ~293 K (room temperature) to ~ 370 K, and both probes were contacting on the calibration target with ~ 20 nN contact force at room temperature. The experiment started at room temperature and the calibration device temperature was steadily increased. The output of the Wheatstone bridge, which is used to monitor the electrical resistance change of the probe, was recorded for each sample temperature and for each probe. The data from the two probes is shown together by different colours and signs in Figure 3.24.

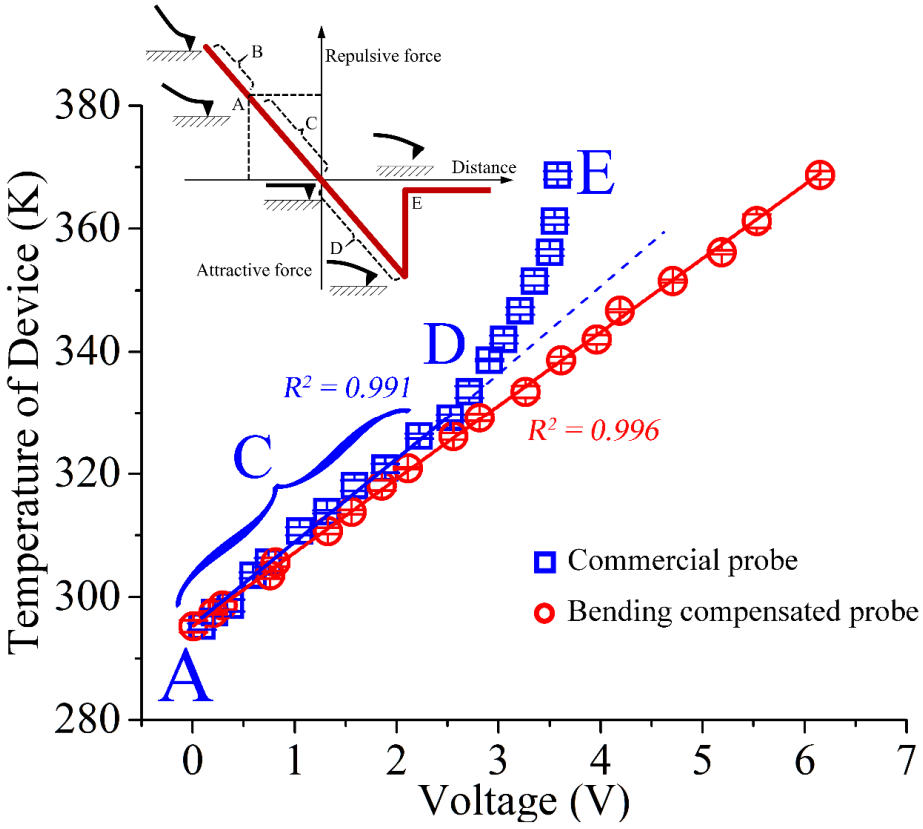

Figure 3.24 Calibration of both the normal probe (blue squares) and the thermal bending compensated probe (red circles), plotted as the temperature of the device against the voltage from Wheatstone bridge.

It can be seen that the response of the thermal bending compensated probe showed good linearity for all device temperatures, while for the normal probe, this was only seen for device temperatures less than 35 K above the ambient. Above this temperature, the probe was not as sensitive to the temperature change. This phenomenon can be explained by considering the force curve shown as an inset to Figure 3.24. At the start of the experiment, the probe was in contact with the calibration device like a normal AFM probe under repulsive force (marked on the response plot as well the force curve). As the temperature of the device increased, the normal probe started to suffer thermal bending, moving its contact force towards region B of the force curve. The feedback loop will interpret this as an excessive force on the cantilever and move the probe away from the device. This pushes the contact into region

C of the force curve and ultimately into region D due to increasing distance between the probe and device. It is possible that this change in tip-sample load will increase the thermal resistance between the probe and the device, decreasing the probe temperature. Finally, the probe will lose contact with the surface, making it insensitive to the device temperature. As the compensated probe is largely immune to thermal bending, it will not suffer from the same problem, as can be seen by its linear plot.

A further complication will occur for probes working in vacuum conditions. Without thermal conduction through air, loss of contact with a heated surface will result in rapid cooling and downward deflection of the probe. This will then cause a re-contact between the probe and the sample and the probe will thermally bended again. This is clearly an unstable situation and as such incompatible with reliable SThM measurements. Therefore, development of the compensated probe is not only helpful for probes working on high temperature device in ambient environments, but also attractive for accurate measurements which are often pursued by employing vacuum conditions.

3.4 Fabrication and Test of Nulling Probe

Employing the developed process of the groove, design (a) and (b) of the nulling probe in Figure 3.13 have been successfully fabricated at Glasgow as part of the QUANTIHEAT EU FP7 project. Figure 3.25 shows SEM images of these probes. The heaters and groove can be clearly observed, as well as the two thermal sensors at the tip in the enlarged image. A simple test was carried out by applying a voltage to the heater and scanning the nulling probe using our currently used SThM probe. A comparison of temperature distribution, showing the same region as simulated in Figure 3.15, and results obtaining from the scan, is shown in Figure 3.26.

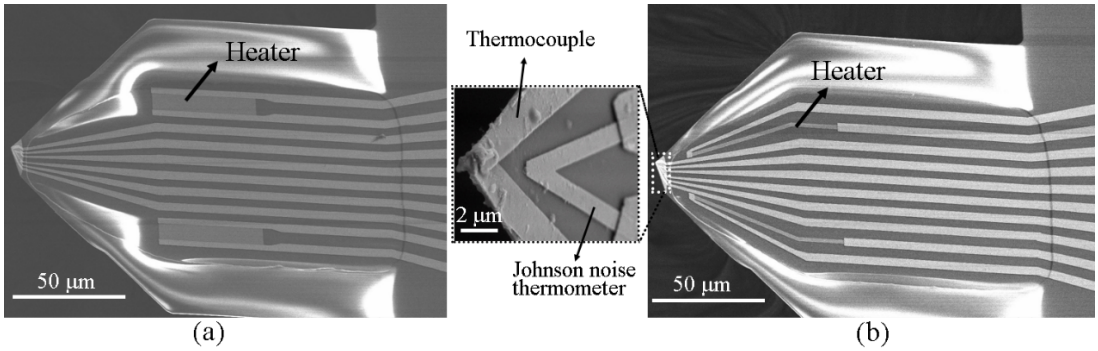

Figure 3.25 SEM image corresponding to (a) design a, and (b) design b of nulling probe demonstrated in Figure 3.13. An enlarged imaged showing the tip is placed between them.

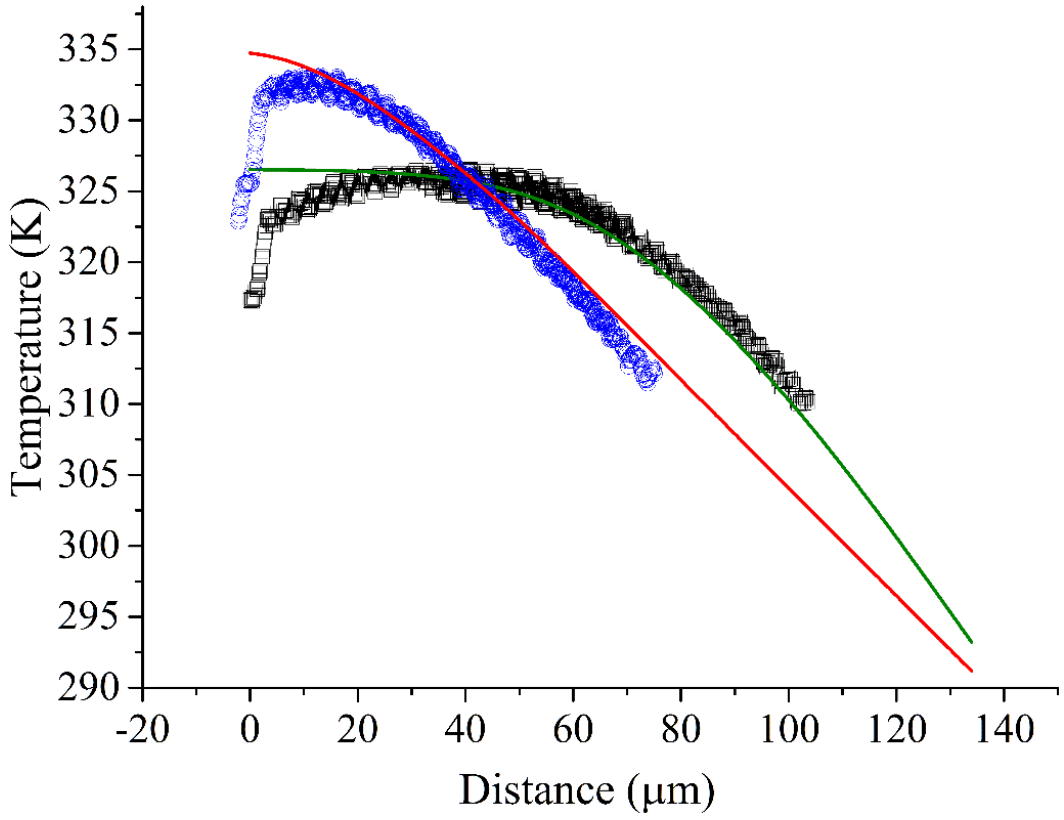

Figure 3.26 Plots of temperature distribution on the trace from the tip to the base of the cantilever. Black squares and blue circles represent the scanning results of design (a) and (b), while the green line and red line shows the data from the corresponding FEA model.

These scanning results show excellent agreement with the simulation, indicating that the FEA model is a good representation of the nulling probe. A mismatch can be observed from 0 to 20 µm however, this can be explained

by the scan being unreliable at the 56° inclined tip. Research on the nulling probe will continue as part of the QUANTIHEAT project and its prospective applications, as well as the issues, will be discussed in Chapter 7.

3.5 Summary

In this chapter, a deep understanding of the probe, obtained from characterization of its electrical properties and optimization of its mechanical performance has been addressed. Several summations can be made:

1) TCR of the probe the can be determined as 0.000961 ± 0.0000106 K^{-1} for the platinum tip and 0.001171 ± 0.0000733 K^{-1} for palladium tip.
2) The TCR can be regarded as constant until the current density exceeds 3.56×10^{10} A/m^2. In addition, this value will be dependent on the temperature of probe, meaning that this value must be revised down when using the probe in vacuum or a high temperature environment.
3) Electromigration is recognized as the main factor that results in probe failure. Methods that reduce electromigration are suggested, such as AC excitation and high thermal conduction medium.
4) The probe is preferably biased below 3.0×10^{10} A/m^2 to ensure long, stable operation.
5) The thermal bending compensated probe is shown to be capable in working at high temperature with a well-controlled contact force.

This thesis is predominantly aimed at understanding and quantifying nanoscale heat transfer in SThM. To this end, the knowledge described in this chapter, together with the thermal bending compensated probe will be used throughout this thesis. Looking to the future, nulling probes have been designed with the assistance of FEA method. Although still in progress, these have already shown their potential by offering a uniform tip temperature distribution, a concept that can be employed in the design of other thermal devices.

4

TOPOGRAPHY-FREE SAMPLE FOR THERMAL SPATIAL RESPONSE MEASUREMENT

As described in Chapter 2, SThM images can exhibit topographically induced artifacts due to the resulting fluctuations in thermal contact between the probe and the sample. This will result in a change of thermal signal, which could be misinterpreted as deviations in the sample's thermal conductivity or temperature. Elimination of these artifacts through post-processing methods requires knowledge of how the thermal response of a probe changes for samples of differing sizes [170]. In contrast to other SThM probes with blunt tips, such as the Wollaston probe [81,137] that exhibit poor lateral resolution (~ 1.5 μm), microfabricated probes have a nanoscale tip radius allowing them to image smaller thermal features [52]. Several studies have been carried out in an attempt to determine the thermal spatial resolution of microfabricated probes. Zhou *et al*. [171] observed a thermal spatial resolution of hundreds of nanometres by scanning a 300 nm to 1500 nm thick palladium acetate thin film with a probe operating 20 – 40 K above room temperature. Sadat *et al*. [76] used a thermocouple tip with ~ 20 nm radius to scan heated features on a metallic surface, successfully achieving sub-100 nm thermal spatial resolution. Shi *et al*. [172] scanned a heated 14 nm diameter multiwall carbon nanotube and observed a resolution of around 50 nm, consistent with the tip-radius of

the SThM probe used. In addition, Hinz *et al*. [128] observed 25 nm thermal spatial resolution under high vacuum conditions in experiments aimed at determining the thermal conductivity of a 3 nm thick HfO_2 film. However, few research works have taken into account the effect of topography on the resolution other than to note its presence. To be specific, the thermal spatial resolution of SThM may be falsely enhanced due to the topographically induced artifacts at the edge of the pattern, which results in features beyond the resolution limit of SThM to be identified as detected.

In this chapter, the nature of contrast in SThM is investigated using a novel fabrication technique to produce multi-material, lithographically defined, topography-free samples. This approach uses a flat sacrificial substrate as the base for fabrication, which is deleted in the final step. This leaves an exposed, flat surface with patterns exhibiting materials contrast defined during the lithography stages. The utility of these samples is then demonstrated using SThM in active mode. To do this the sample is designed to challenge the detection ability of SThM probe. The complete fabrication process is described for this sample, followed by a successful demonstration of topographic/thermal scanning, showing sub-1.5 nm topography with a clear, artifact-free thermal signal from sub-100 nm gold wires. By analyzing the result, thermal spatial resolution is determined for the sample materials and probe used in this study to be in the range of 35 nm to 75 nm.

Although the sample described is focused on SThM studies, many other SPM techniques exhibit artifacts due to sample topographic variation. For example, conductive atomic force microscopy (C-AFM), a tool used to measure the local electronic properties of nanostructures or semiconductor devices, is often based on contact mode AFM and measures the current flowing between the tip and sample, which is greatly affected by changing contact area [173]. Scanning near-field optical microscopy (SNOM) is able to provide sub-wavelength imaging and can, for instance, be employed to study opto-electronics devices [174] as well as being used for near-field lithography

[175]. However, as SNOM works by detecting scattered light, which is highly dependent on the tip-sample distance, meaning that topography can strongly impact the quality of images [176]. Topography free samples, fabricated using the process described in this chapter could easily be produced for these SPM techniques by employing an appropriate change in materials and patterns.

4.1 Sample Design and Fabrication

4.1.1 Pattern-transfer based process

When considering sample planarization, chemical mechanical planarization (CMP), which is widely used in the integrated circuit industry, is an obvious choice [177]. However, this technique has drawbacks such as dishing and erosion, where some regions and materials polish faster than others, limiting the range of different materials that can be used. This is combined with the high complexity and cost of developing a process and the potential for significant surface damage, making CMP unattractive for SPM samples. An alternative approach, employing beam exit argon ion cross-section polishing (BEXP) has been proposed by Kolosov *et al*. [178]. This provides a method to produce a sample surface with topography down to 1 nm, which is suitable for SPM scanning. However, this approach offers limited flexibility in the definition of material patterns, as well as limited control of the feature thickness.

One possible approach for eliminating surface topography of a lithographic pattern is through filling an etched trench using a second material, which is shown in Figure 4.1. This would require two aligned levels of lithography for a single pattern: one for etching and the other for deposition. However, there will be inevitable misalignment between the levels, even if the most accurate alignment methods were employed [179]. This includes the offset error in x and y direction, the scale error changing the size of pattern, and the rotation error. The consequence of any misalignment would be inconsistent thickness resulting from a step or trench between the cavity and

the deposited material, causing an overall increase in peak-to-peak topographic variation. Furthermore, the depth of the etched trench (t_1) and the thickness of the metal (t_2) cannot be guaranteed to be the same, due to finite control of both the etching and deposition process.

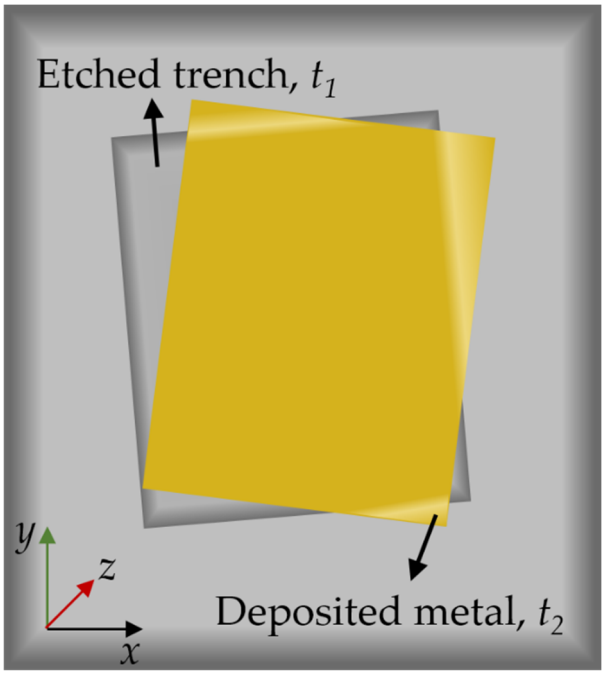

Figure 4.1 Schematic shows the misalignment between two levels of lithography for an etched trench and the metal deposited aiming to fill it. Offset error and rotation error are both illustrated, except for the scale error which changes the size of each alignment layer.

The sample fabricated in this work employed a different approach. The process is based around common, generic resist-based pattern transfer techniques compatible with a wide range of materials: lithographically defined metal patterns were fabricated on a sacrificial substrate before being embedded into an epoxy-supported backing. In the final step, the initial "sacrificial" substrate was deleted. This method takes advantage of the high quality surfaces obtainable using CMP polished wafers, while simultaneously avoiding the chemical and mechanical damage generated by polishing the pattern itself.

The complete fabrication process flow is shown in Figure 4.2. The desired pattern is deposited onto a sacrificial GaAs substrate as shown in step (a). This process employs traditional bilayer PMMA resist patterned using 100 kV electron beam lithography (EBL) [180]. The resist stack consisted of PMMA having a molecular weight of 85 kDa as the bottom layer and another layer of PMMA having a molecular weight of 350 kDa as the top layer. Gold was evaporated as the pattern, followed by "lift-off" in 50 °C acetone for 12 hours. The pattern consisted of wires located in a 1 μm gap between two large gold pads, permitting easy pattern location within the AFM/SThM using optical microscopy. It should be noted that the process is compatible with material of various thickness, which is only dependent with the concentration of the PMMA used (a different thickness will be demonstrated in Chapter 6). It is known that the highest resolution attainable with EBL is dictated by the thickness of the resist; and as a consequence this impacts on the thickness of metal that can be employed for "lift-off". Therefore, to achieve narrow wires, gold thickness is limited to 20 nm. However, lower resolution structures of thickness up to 150 nm have been successfully patterned using this technique.

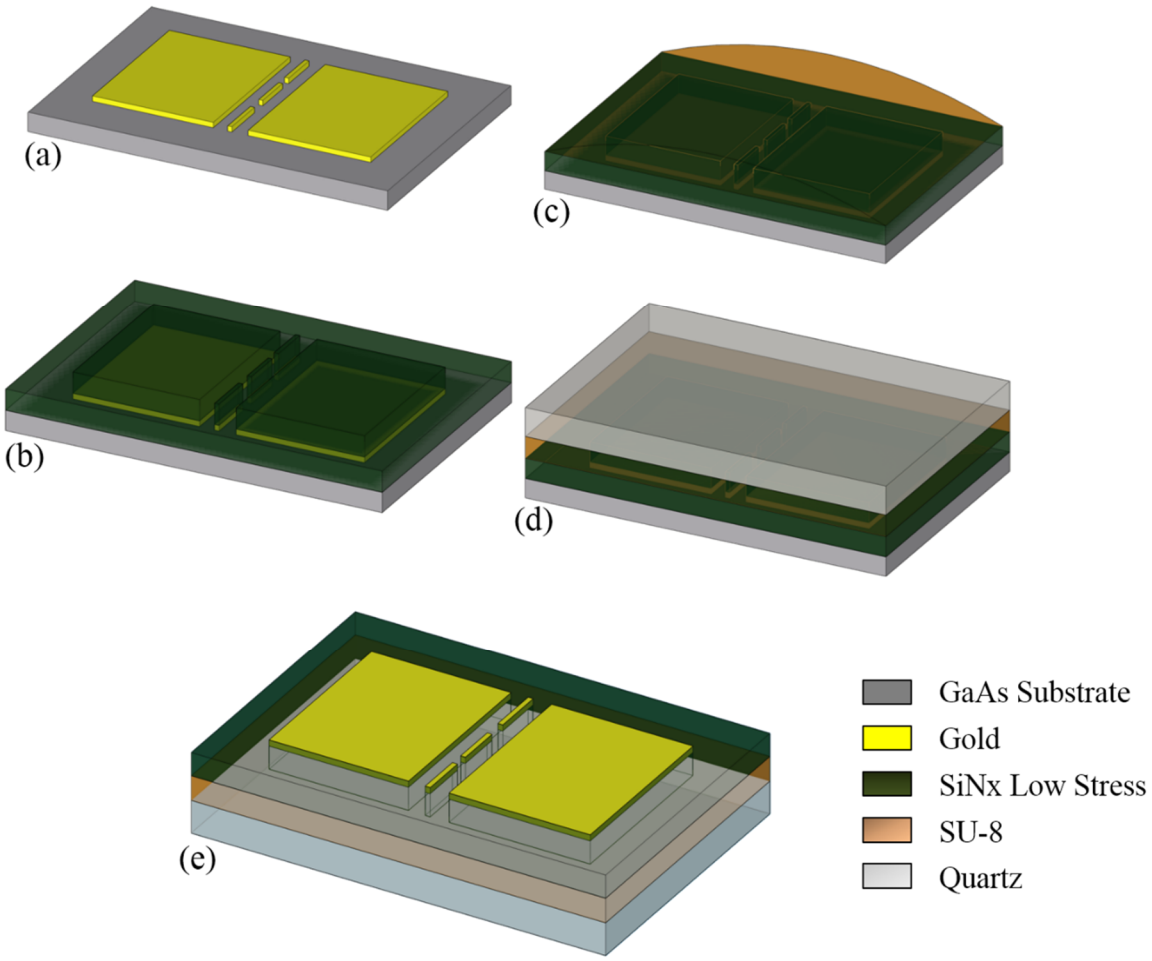

Figure 4.2 Fabrication process flow of the topography-free sample.

The fabrication of the backing substrate is a multi-layer process as shown in the following steps from Figure 4.2:

1. The patterns were generated on the sacrificial GaAs sample using EBL and metal "lift-off" (a). Then 400 nm low stress inductively coupled plasma chemical vapour deposition (ICP CVD) SiN_x was deposited onto the sample [181], which had been dehydrated on a 180 °C hot plate for 5 min to improve the adhesion (b);
2. A 100 µm thick layer of SU-8 3050 was spun onto the processed face of the sample (c);
3. The sample was heated and a piece of quartz was placed onto the hot

SU-8 to provide a rigid mechanical handle for the released sample (d).

4. Once the full material stack was completed, the GaAs substrate was deleted using a 5:1 citric acid/H_2O_2 wet etch at 30 °C, uncovering the gold pattern and SiN_x background. The finished sample is as shown in the step (e) with the replaced substrate facing down.

4.1.2 Design of the pattern

The thermal spatial resolution of SThM probes is commonly claimed to be sub-100 nm, with the heat conduction area considered to be the same as the tip radius of curvature [77,89]. To address these length scales, narrow gold wires with width ranging from 25 nm to 75 nm were designed as patterns, which are shown in Figure 4.3. Patterns were designed in a square arrangement and all had length of 1 μm with variable width. Zooming into a single pattern (Figure 4.3 (b)) shows the detailed design of the scanning object. Although the yield of wires was high, it was not 100 %. Therefore three identical wires were placed together into each l = 1 μm wide gap. This ensured that a wire of the appropriate geometry could always be located when scanning the sample without the need to change the scanning area frequently.

As the separation between wires and gold pads was less than 500 nm, the proximity effect, which is caused by scattering electrons within the resist and the substrate, severely influences the exposure resolution of EBL [182]. Proximity correction, the most commonly used algorithmic method to minimize this effect [183], was not compatible with this sample, since it requires the pattern to be written in one job with a uniform beam size. Therefore, considering the time consumption, the gold wires and pads were written in separate layers with 4 nm and 33 nm beam size respectively. Markers used for aligning the layers are also shown in Figure 4.3 (a). The 1 μm gap between the two pads requires highly accurate alignment between each layer. In order to achieve this, in addition to the four global markers traditionally used, four cell markers located close to the critical pattern were

also employed. The large cross markers were used as a guide to locate the global markers in the EBL tool.

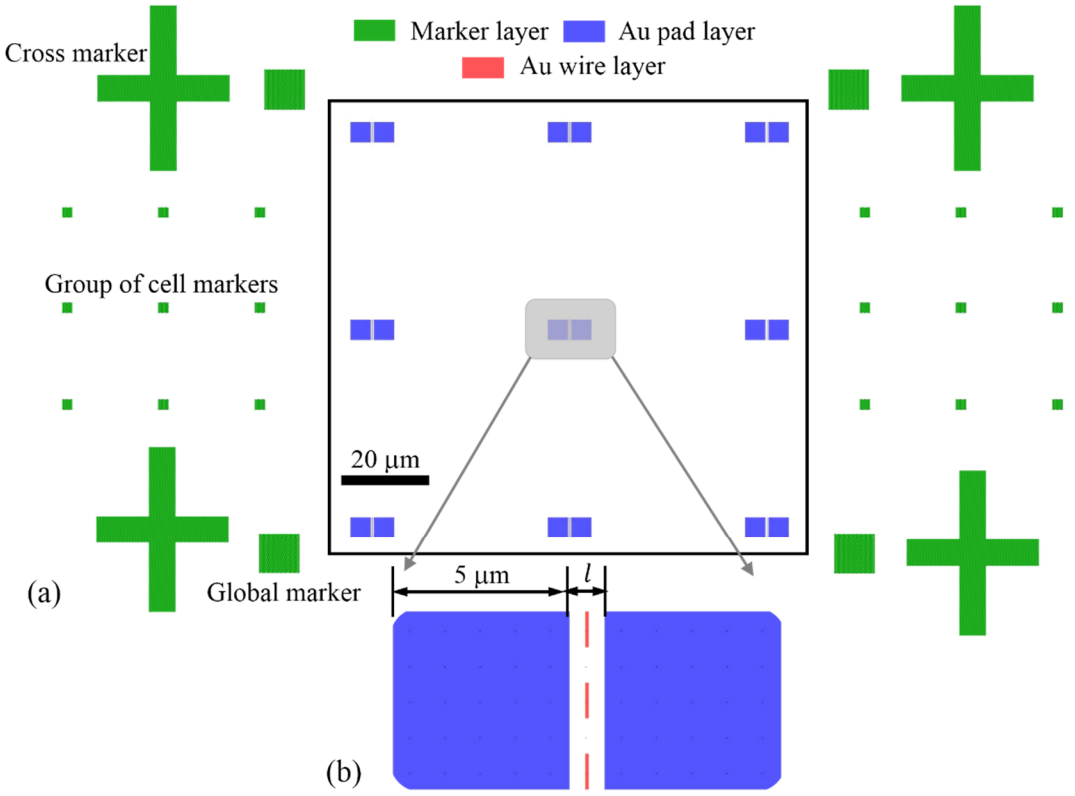

Figure 4.3 (a) Design of the pattern of topography-free sample with the marker strategy for alignment in EBL, and (b) enlarged image showing the single pattern design: three 1 µm long gold wires positioned at the centre of the gap formed by two gold pads.

4.1.3 Development of the process

GaAs was chosen as the substrate due to its availability as a polished wafer, electrical conductivity (useful when using EBL) and relative ease of wet etching [184]. Although silicon would appear to be a more economical choice, the available wet [74] and dry etches [185] would potentially damage the gold/SiN_x pattern resulting in roughening of the surface. Wet etching of GaAs is possible using various solutions such as citric acid, H_2SO_4, HCL and HF with H_2O_2, but it was decided to use 50% citric acid with H_2O_2 to minimize pattern

damage [186]. The GaAs etch rate is strongly dependent on the temperature and the ratio of citric acid and H_2O_2, with 5:1 citric acid: H_2O_2 giving the highest etch rate (~ 250 nm/min) at room temperature. Gold was chosen as an evaporated pattern material due to its ease of fabrication, chemical resistance to etching [186], and high thermal conductivity.

The fabricated backing substrate is a sandwich structure: a conformal layer of SiN_x around the gold structure, a thick layer of SU-8 cured epoxy and a rigid quartz handle. The SiN_x offers three important properties: good adhesion to the gold patterns, large thermal contrast with gold, and resistance to the GaAs wet etch. The stack adopted replaces an initial design for the backing substrate, which was simply to employ a double-layer SU-8 3050. In the initial process, after release etching, few patterns were successfully transferred onto the SU-8 substrate due to the poor adhesion of gold to SU-8. Figure 4.4 shows the sample surface after release etching without using the stack structure. It can be clearly seen (circles marked in dashed lines as I and II) that some patterns became detached from their original positions. Patterns of squares and circles with different sizes were designed to investigate whether shape or size affected the adhesion or if it was simply caused by the adhesion between the epoxy and the gold. Patterns were made of 100 nm thick gold deposited due to the use of thick PMMA layers as no high resolution patterns needed. As a consequence, it was decided that patterns of any shape or size were unlikely to remain adhered, therefore a new material was required.

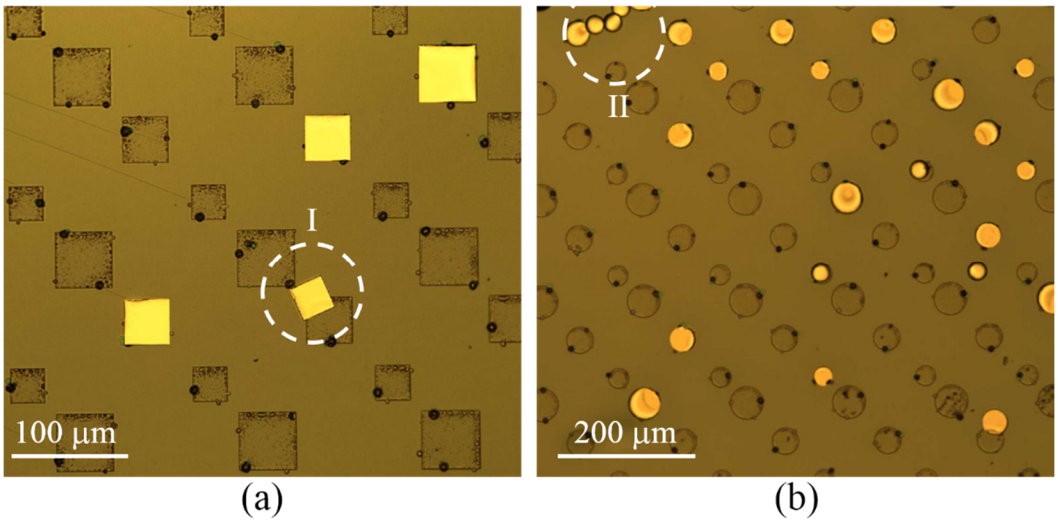

Figure 4.4 The sample surface after release etching without the SiN_x layer to enhance the adhesion. Simple patterns, varying with the shape in square (a) and circle (b) and their size, are designed for testing the process more efficiently.

ICP-CVD SiN_x was chosen due to its ability to be deposited at room temperature, maximizing the possible number of compatible materials for the lithographic pattern and eliminating any topography associated with differential thermal expansion during fabrication. Two layers of SiN_x, compressive low stress (~ 100 MPa) and compressive high stress (~ 3 GPa) were tested [181]. The deposition gas used for both was SiH_4/N_2 with a flow rate of 7/6 sccm under 4 mTorr pressure. Both high stress and low stress SiN_x provided an obvious improvement in pattern adhesion, however, high stress SiN_x induced small wrinkles in the gold pattern. Figure 4.5 shows the optical and topographic AFM images of one such sample after release etching. Wrinkles caused by the high stress SiN_x are clearly visible, particularly in the AFM image (Figure 4.5 (b)). It is reasonable to treat these wrinkles as the result of stress release, since their depth equals to the thickness of the gold. Consequently, further samples were prepared using low stress SiN_x only.

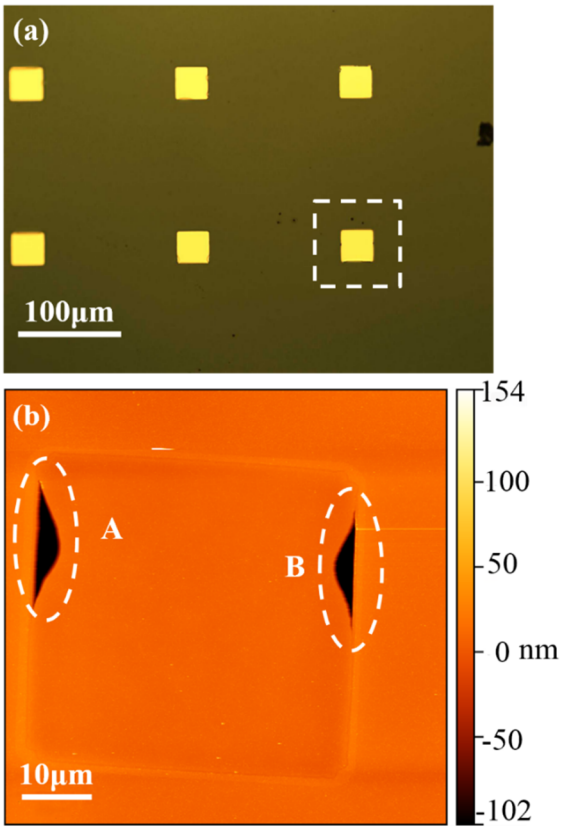

Figure 4.5 (a) Optical microscope image of the topography-free sample with high stress SiN_x adhesion enhancement layer and (b) AFM height image of the same sample, the scan region is indicated by the dashed square in (a). Wrinkles are highlighted in regions A and B.

The SU-8 layer alone did not provide a flat backing material due to its tendency to bow after the GaAs substrate being dissolved. Therefore, a piece of quartz, transparent to UV light, was used to cover the SU-8 at the end of the softbake when the SU-8 was still soft. In the final structure, the SU-8 acts more as an adhesive with low thermal conductivity than a substrate.

Following removal of the GaAs, the freshly exposed surface topography was checked using AFM. During this inspection, a dependence of the residual topography on the thickness of SiN_x was observed. Repeated experiments were used to optimize the SiN_x thickness. Samples with 100 – 800 nm thick low stress SiN_x, deposited under the conditions previously described, were studied. For each sample, the average step height between the gold pattern

and the SiN_x was obtained by averaging the data from eight to ten patterns on each sample, as shown in Figure 4.6. It can be seen that topography reduces with the increasing thickness of SiN_x, until no further improvement is observed at 400 nm and above. This is tentatively ascribed to the increased rigidity of the SiN_x film with increasing thickness. Therefore, a thickness of 400 nm was used during the fabrication of all subsequent samples as this offered a good compromise between minimum topography and short deposition time. The full fabrication process of the topography-free sample can be found in Appendix II.

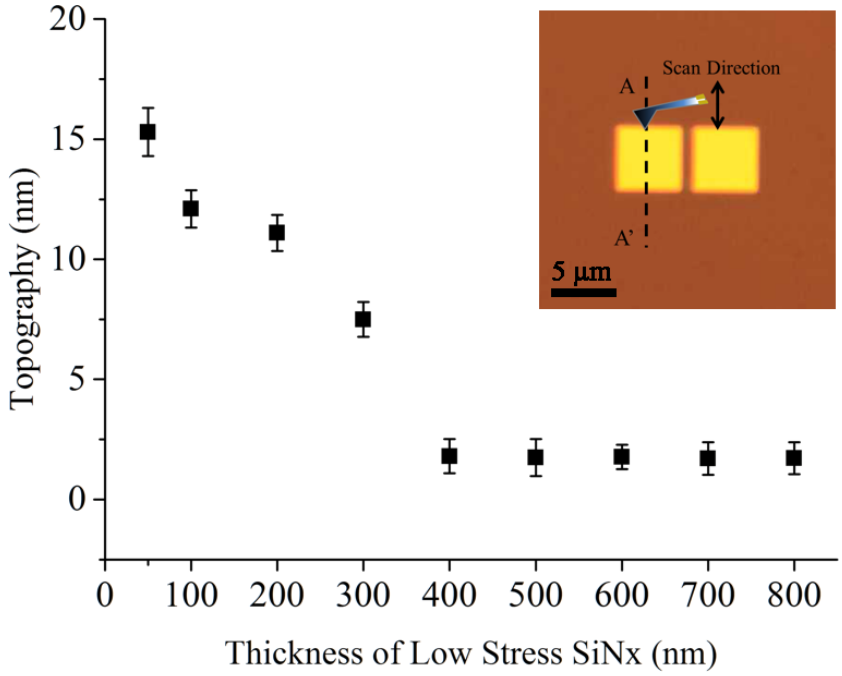

Figure 4.6 Step heights between gold and SiN_x on the sample surface after release etch versus the thickness of SiN_x. The inset image shows the AFM scan used for obtaining the step height.

Figure 4.7 shows SEM and AFM images of the same region on the sample after completion. The images show 60 nm gold narrow wires as an example fabricated at the centre of the gap formed by two gold pads. The high topography dots in Figure 4.7 (d) may have resulted from one of several reasons, for example, the oxidation of the GaAs substrate surface before and during fabrication, contamination of the surface after release etching, or GaAs

residue due to uncompleted release etching. Figure 4.8 shows a photograph of the topography-free sample after release etching. The quartz is slightly larger than the sample and the size is comparable to a 1-inch diameter sample box. The dark patterns on the sample are gold features and EBL markers.

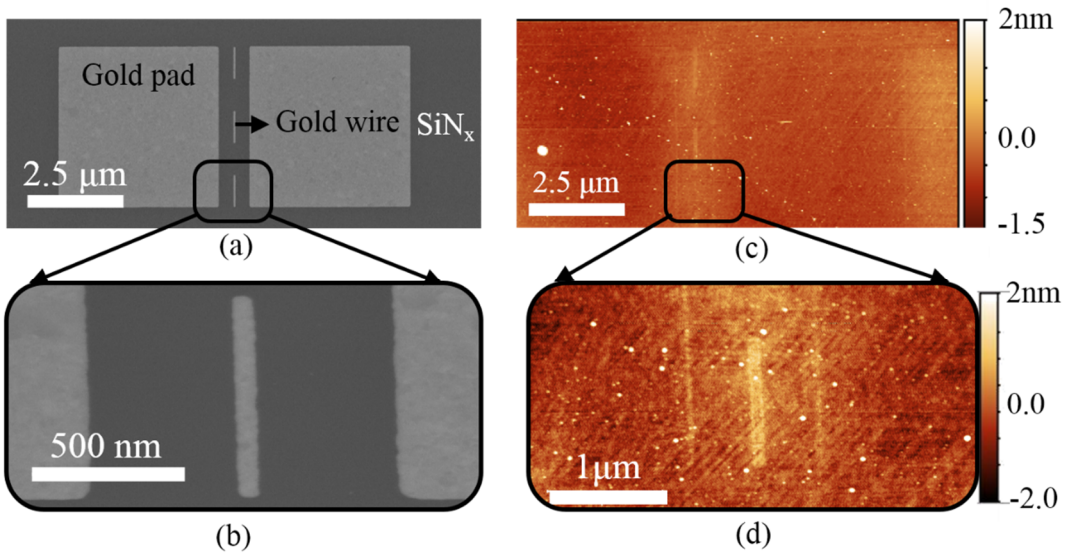

Figure 4.7 (a) SEM image of the pattern after release etching, (b) detail of the narrow wire zoomed in from (a), (c) tapping mode AFM topographic image showing the same area as (a), and (d) detail of the narrow wire zoomed in from (c) showing a residual topographic variation of less than 2 nm.

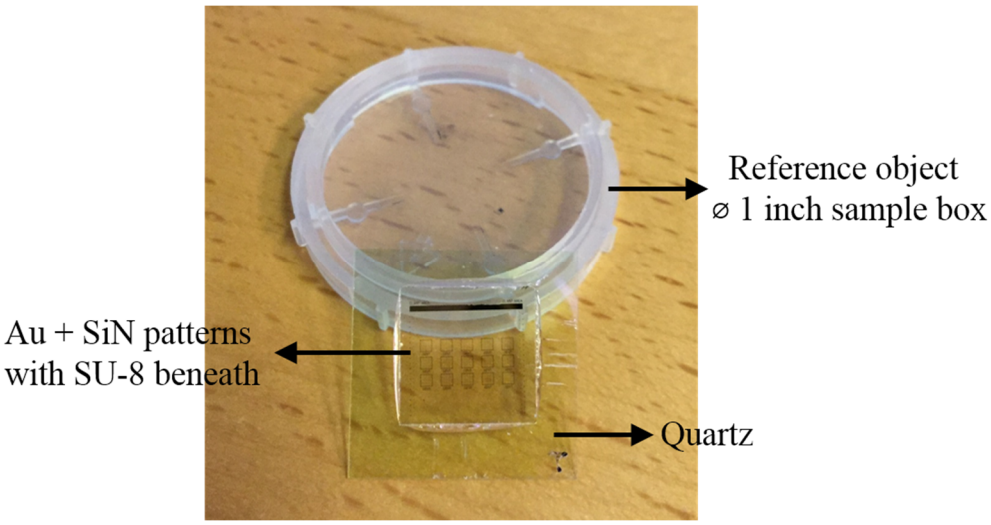

Figure 4.8 Photo of the complete topography-free sample shows that the general view of the sample.

4.2 Experimental Setup

The topography-free sample was scanned using microfabricated, thermally compensated cantilever probes developed in Glasgow. The experimental setup is shown in Figure 4.9. The current source is composed of an adjustable voltage source V with R_1 and R_2, and is able to supply a 0 - 2.0 mA DC current to heat the probe. The probe forms part of a Wheatstone bridge with R_1, R_3 and R_4, enabling its resistance to be continuously monitored. Among them, R_4 is an adjustable resistor in order to balance the bridge output for different probes. The differential voltage from the bridge is amplified by the instrumentation amplifier A_{ins} with the gain being adjusted by R_8. As addressed in Chapter 3, the probe can provide good results working at 3.56×10^{10} A/m^2, thus, 0.8 mA was chosen as the bias current, resulting an out-of-contact probe effective temperature of ~ 55 °C. This provided an appropriate compromise between a high thermal signal-to-noise ratio (SNR) with small residual cantilever thermal bending. The experiment was carried out in the ambient condition using a Veeco Dimension 3000 AFM.

The AFM was operated using contact mode with the SThM probe. The thermal signal obtaining from the probe was transferred to the AFM scanning system through a signal access module, replacing the original friction signal with the thermal signal. This allowed the thermal signal to be recorded by the computer, and combined with the raster scan signal to form a thermal map.

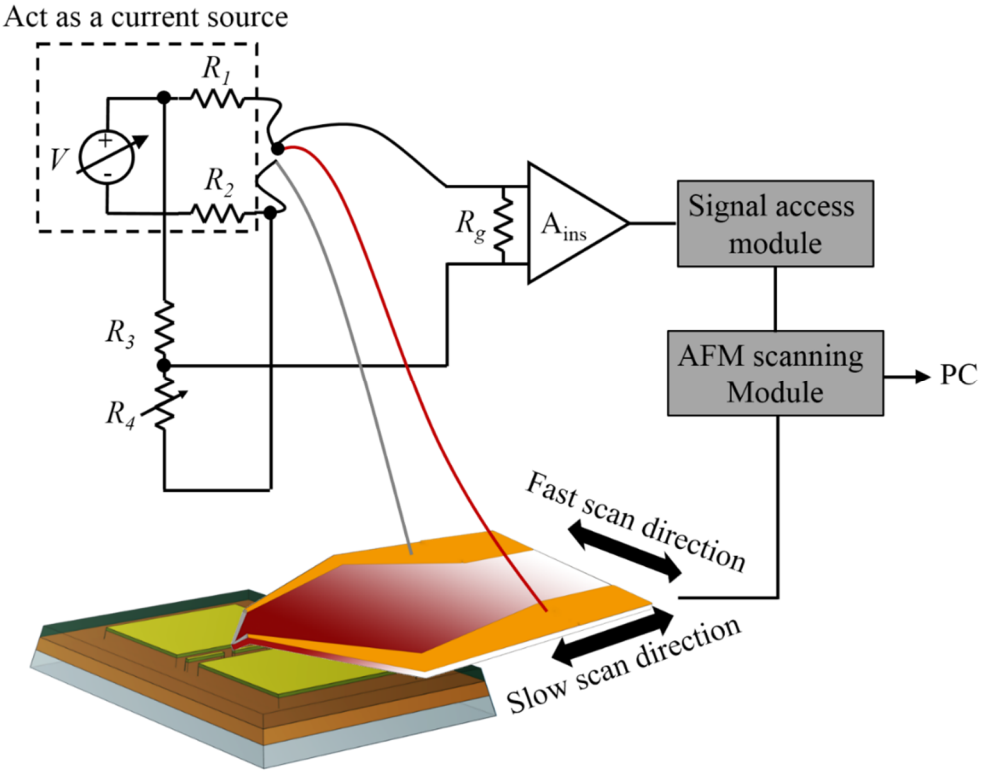

Figure 4.9 Schematic diagrams showing the electrical arrangement used to bias the probe and to detect the probe electrical resistance change.

4.3 Scanning Results and Discussion

4.3.1 Demonstration of 35 nm wide gold wire

First, the 35 nm wide wires were scanned using SEM, AFM and in-air SThM as shown in Figure 4.10. The width of the wire was determined using low vacuum backscatter SEM, efficiently avoiding the well-known errors associated with secondary electron scattering for small linewidth measurement [187]. The topographic AFM image (Figure 4.10 (b)) and thermal image (Figure 4.10 (c)) were obtained simultaneously during the thermal scan, and the 35 nm gold wire could be clearly seen. Data extracted from line traces at the same position on all images are plotted in Figure 4.10 (d) and (e). The step height associated with the 35 nm gold wire is ~ 1.5 nm, and the feature is clearly visible on the thermal image.

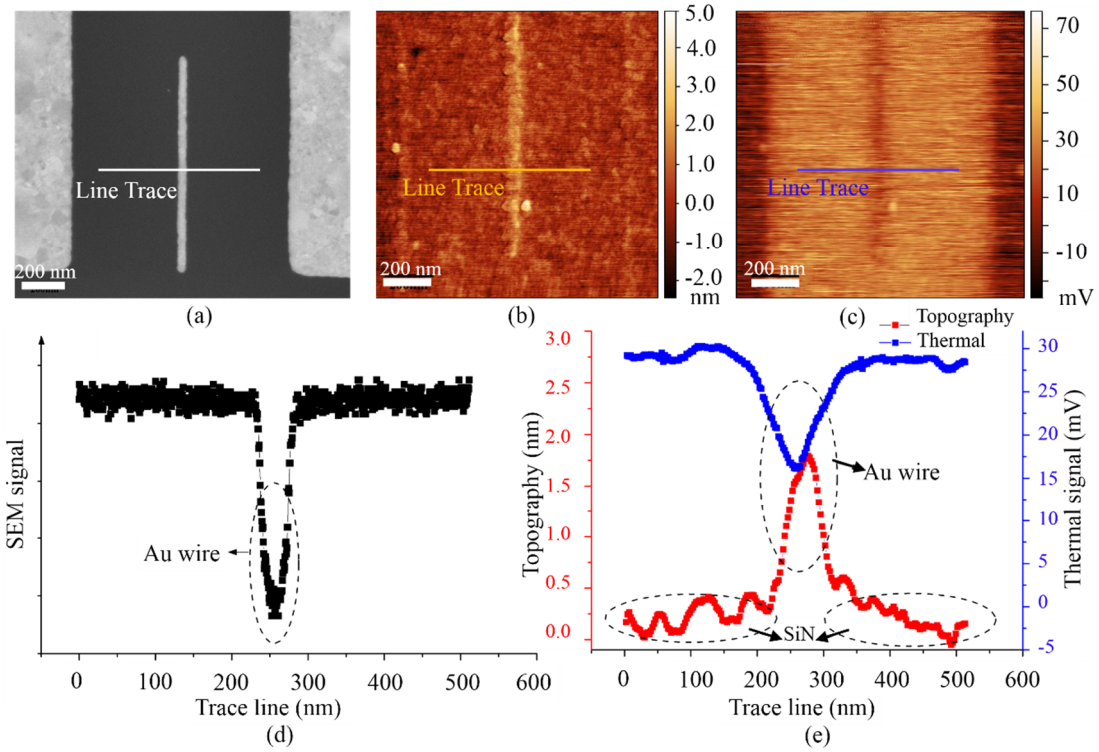

Figure 4.10 (a) Backscatter SEM image shows the 35 nm narrow gold wire, (b) AFM topographic image shows the same wire as (a), (c) thermal image of the same feature scanned by SThM probe, (d) plot of the line trace for SEM image, and (e) topography and thermal signals. Dotted circles in (d) and (e) indicate the signal of the gold wire and SiN_x.

A comparison of the thermal signal intensity from the 35 nm wire with that of the gold pads shows that the magnitude of the thermal signal from the wire is lower than that of the gold pads. Given that the thermal signal of the gold pad as "completely resolved", it suggests that the gold wire is "incompletely resolved", as both the wire and the pad are made of the same material.

4.3.2 Analysis of the incompletely resolved phenomenon

The incomplete resolution can be attributed to the complex heat transfer mechanisms at the tip-sample contact. One powerful approach to aid understanding of the underlying heat transfer mechanisms between the tip and the sample is to use a thermal resistance network, as suggested by Luo *et al*. [72]. Figure 4.11 summarizes the thermal resistance network for interactions in this situation.

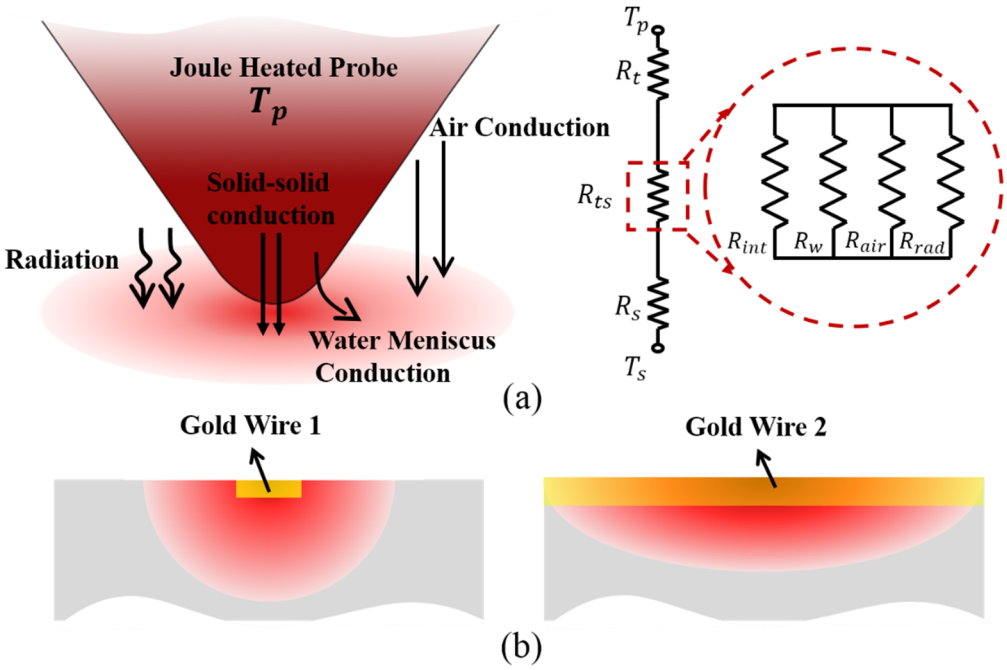

Figure 4.11 (a) Heat transfer interactions between the probe and the sample, together with the thermal resistance network showing the relationship between each interaction, and (b) different thermal diffusion as a result of variation in the width of gold wires. Gold wire 1 and gold wire 2 indicate the narrow and relatively wide wire, respectively. Heat spreading is represented by hemispherical areas surrounding the gold wires.

In the thermal resistance network, R_t and R_s represent the thermal resistance of the tip and the sample, respectively. The thermal resistance of the contact interface, R_{ts}, represents thermal interaction between the tip and the sample, and is a combination of many factors, among which, solid-to-solid contact (R_{int}), water meniscus (R_w) and air conduction (R_{air}) are generally believed to dominate over heat transfer through radiation (R_{rad}) [89,100,108]. Gorbunov *et al*. [188] first proved that heat dissipation to the sample from a

heated tip is a function of the tip-sample contact radius as well as the sample material being scanned. This has been investigated by Gotsmann [141] who indicated that the contact thermal conductance is dependent on the pressure when the contact radius is constant. Hence, the tip-sample force was kept as 20 nN during the experiment. As the geometry and materials comprising the SiN_x tip will not change significantly, the thermal resistance of tip, R_t, is regarded as a constant value.

In order to obtain a fuller understanding of the thermal profile generated by scanning the SiN_x and gold wire, the thermal resistance of each tip-sample interaction can be estimated. As both the sample and probe have features with dimensions comparable to the mean free path of heat carriers (λ), the effect of heat transfer in the ballistic regime must be considered. Thermal spreading resistance including both diffusive and ballistic heat transport can be calculated using [123]

$$R_s = \frac{1}{4kb_c}\left(1 + \frac{8}{3\pi}K_n\right) \qquad \text{eq. 4.1}$$

where K_n is the Knudsen number defined as λ/t. Sultan *et al*. [189] have shown that the mean free path of carriers in SiN_x is smaller than 2 nm at room temperature. Therefore, thermal transport can be regarded, in this instance, as entirely diffusive due to the small Knudsen number. Furthermore, the SiN_x film thickness of 400 nm makes it unnecessary to consider boundary scattering effects. Thus, the thermal spreading resistance of the SiN_x when K_n approaching zero can be given by

$$R_{SiN} = \frac{1}{4k_{SiN}b_c} \qquad \text{eq. 4.2}$$

where k_{SiN} is the thermal conductivity of the SiN_x, which was considered to be 10 W/mK [190]. This gives a value of R_{SiN} in the order of 10^5 K/W. For the gold, the mean free path at room temperature is 10 – 30 nm, dependent on whether the gold is single crystal or polycrystalline [191]. Moreover, the thickness of gold was 20 nm, which is comparable to the mean free path. Thus, substrate

(SiN_x) effects need to be considered when calculating the thermal spreading resistance. Accounting for all of these factors, the thermal spreading resistance can be calculated using [123,132]

$$R_{Au} = \frac{1}{4k_{Au}b_cK_n} - \frac{1}{2\pi k_{Au}t}\log\left(\frac{2}{1+\frac{k_{Au}}{k_{SiN}}}\right) \qquad \text{eq. 4.3}$$

This gives a thermal resistance of the thin film gold as being around 10^4 K/W, which is one order of magnitude smaller than that of SiN_x. In addition to this, other mechanisms also need to be discussed, aimed at determining the dominant factor that causes the temperature variation of the probe.

As mentioned in Chapter 2, the thermal resistance associated with heat transfer through the water meniscus can be neglected compared with the heat conducting through solid-solid contact and air conduction. Furthermore, the thermal interface resistance between the probe and the sample can be described as eq. 2.7. It has been recognized that, under ambient conditions, R_b does not change significantly with sample materials and has a typical value of 1×10^{-9} to 5×10^{-8} m^2K/W. For the hard materials (i.e. those that do not show plastic damage on scanning) used in this work, solid-solid contact radii (~ 50 nm) do not vary greatly. Therefore, it can be expected that the solid-solid contact resistance, R_{int}, will lie in the range of 10^5 – 10^6 K/W.

Heat conduction through the air is another interaction that will affect the probe temperature. As the heat transfer coefficient defined for the air gap between the tip and the sample is independent of the sample material [123,192], the thermal resistance of the air gap will not vary with SiN_x or gold and is considered to be on the order of 10^5 K/W [77].

Comparison between all of these thermal interactions show that the thermal spreading resistance of the sample and the thermal interface resistance between the tip and sample are the most likely candidates for causing the variations observed in the SThM thermal image. It can be summarized that it is the variation of material that changes the probe

temperature. Therefore, the thermal spatial resolution of the SThM can be determined using the topography-free sample, which contains multiple materials. It has been realised that separation of these two factors when using the SThM is always difficult [90]. Therefore, in this chapter, instead of discussing the thermal resistance in detail, we focus on the thermal signal obtained from the topography-free sample. The attempt to quantitatively solve the thermal resistance involved in the thermal interactions will be demonstrated over the following two chapters.

As shown in Figure 4.11 (b), for the gold wire with small width ("Gold wire 1"), heat spreading into the sample will be largely controlled by the SiN_x, resulting in approximately radial thermal diffusion. With an increase in the gold wire's width ("Gold wire 2"), there is more heat spreading within the gold wire, and the diffusion shape becomes more planar, resulting in a lower probe temperature. At the limit of large wire width, the thermal signal measured from the gold wire is expected to tend toward to the same value observed when in contact with the gold pads, which may be considered to constitute an infinite in-plane feature. The scan of the 75 nm wide gold wire, shown in Figure 4.12, is also consistent with this explanation.

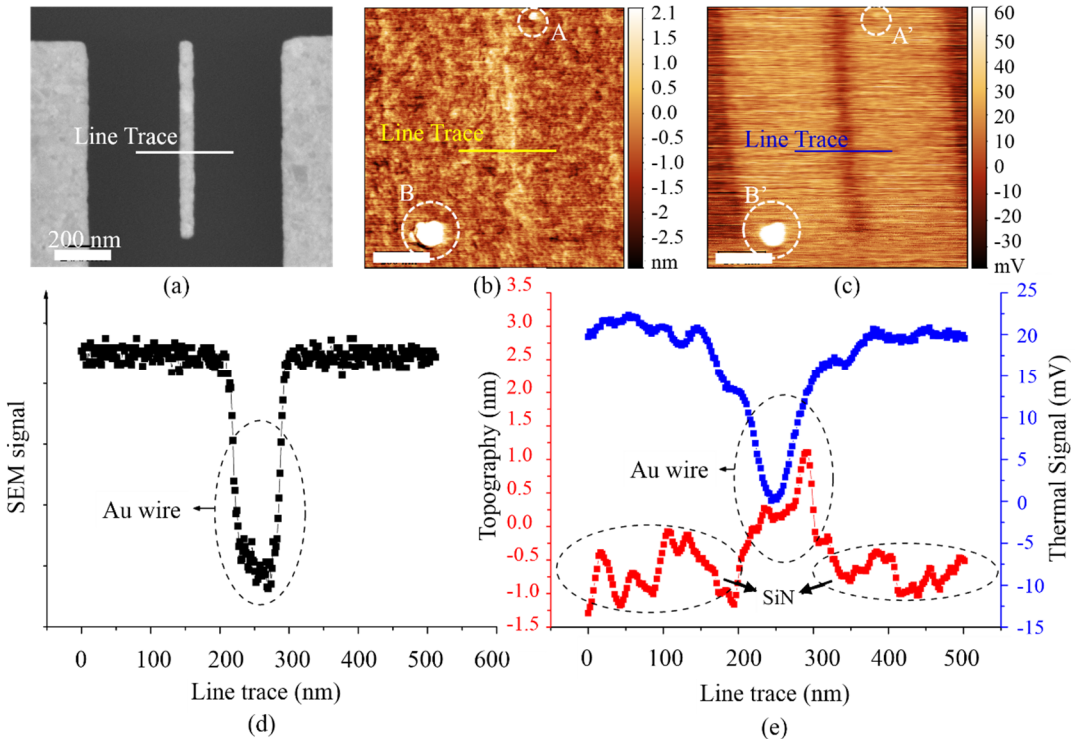

Figure 4.12 (a) SEM image shows the 75 nm narrow gold wire, (b) AFM topographic image, (c) thermal image showing the same feature scanned by SThM probe, and plots of the line traces from (d) SEM image and (e) topography and thermal signals. Dotted circles in (d) and (e) indicate the signal of the gold wire and SiN_x.

The thermal signal of the gold wire shown in Figure 4.12 is obviously larger when compared to that of the 35 nm wire. Specifically, the difference in the thermal signal between the gold wire and the SiN_x are 11.3 mV for the 35 nm wire and 19.8 mV for the 75 nm wire. The large effect of topographic artifacts is also seen in Figure 4.12 (b) and (c) where particles (indicated by the circles A/A' and B/B') are observed to give rise to large thermal contrast.

It should be noted that there is a small amount of topography associated with the gold features. However, this is of the same magnitude as the general roughness of the background SiN_x and gold (~ 1 nm). Therefore, any topographically induced artifacts in the thermal image are expected to be of the same size as the background noise present in the thermal signal. Any effect will certainly be much smaller than that present in an equivalent sample produced without using the method described in this work.

In order to easily visualize the change in thermal signal intensity, wires with width ranging from 35 nm to 75 nm were scanned using the same experimental setup and the thermal signal from different pattern regions analyzed using a simple ratio, defined as

$$Ratio = \frac{V_{wire} - V_{SiN}}{V_{pad} - V_{SiN}} \qquad \text{eq. 4.4}$$

where V_{wire}, V_{pad}, and V_{SiN} represent the thermal signal obtained on the gold wires, gold pads, and SiN_x, respectively. This ratio can be used to easily assess the relative signal magnitude as observed on wires of differing width scaled to that observed on gold pads. As the thermal signal on the wire approaches that of the background SiN_x, the ratio will approach zero, whereas a ratio of one indicates the same signal as that observed on the large gold pads. It can be said that the closer the ratio is to one, the more "resolved" the gold wire is, that is, the signal becomes increasingly characteristic of the material, not the geometry. Figure 4.13 shows the plot of the ratio versus the width of the gold wires from 35 nm to 75 nm.

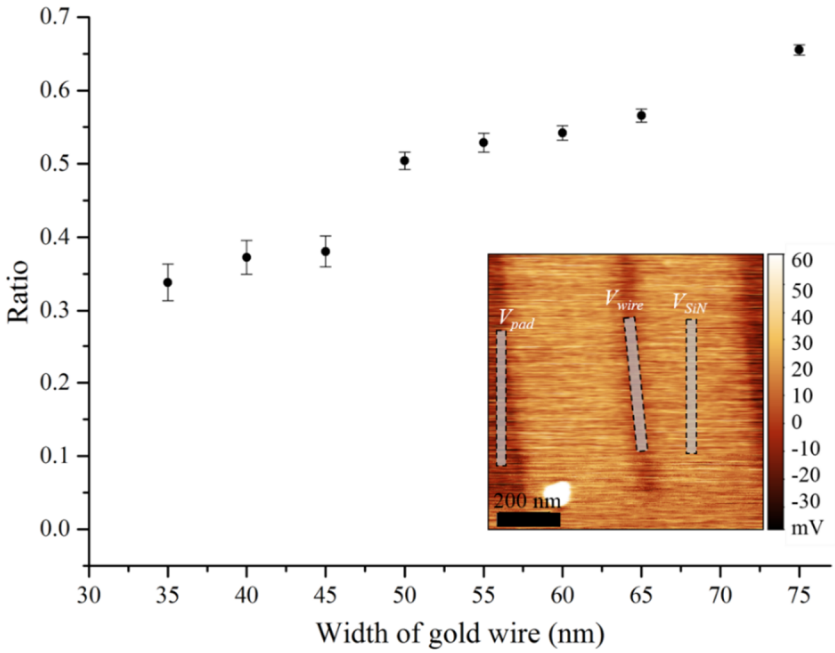

Figure 4.13 Plot of the thermal intensity ratio versus the width of the gold wire. The inset image shows the 5 × 50 pixels rectangular regions used to obtain the averaged signal from wire, gold pad and SiN_x.

Values for V_{wire}, V_{pad} and V_{SiN} were obtained from the SThM images by averaging a rectangular 5 × 50-pixel region on top of each feature as shown in the inset image. The error bars represent ± 1 standard deviation of the averaged values. As expected, the ratio observed on the gold wire slowly increases with an increase in the wires width, simultaneously the standard deviation decreases due to the improved SNR associated with a larger signal. This shows that by employing a microfabricated SThM probe to scan a sample consisting two materials having a large difference in thermal conductivity (SiN_x and gold in this case), the variation of pure thermal materials contrast can be quantified as a function of the size of the object being imaged.

4.3.3 An exception thermal scan – 25 nm wide wire

The thermal scan of the 25 nm wide wire generated a very different result when compared to those from 35 nm to 75 nm wide wires. As seen in the SEM image, fabrication limits resulted in a wire that was discontinuous along its length, but with a width of ~ 25 nm as measured from the Figure 4.14 (d). The topography of the wire was determined as ~ 1 nm and can be seen in Figure 4.14 (b), however, the wire was undetectable in the thermal image (c). Even a plot of the thermal signal along the line trace does not distinguish the 25 nm wire from the background noise. However, high-topography grains, indicated by the dashed circles marked as A, B and C corresponding to the A', B' and C' in Figure 4.14 (b) and (c), are still detected as topographically induced artifacts.

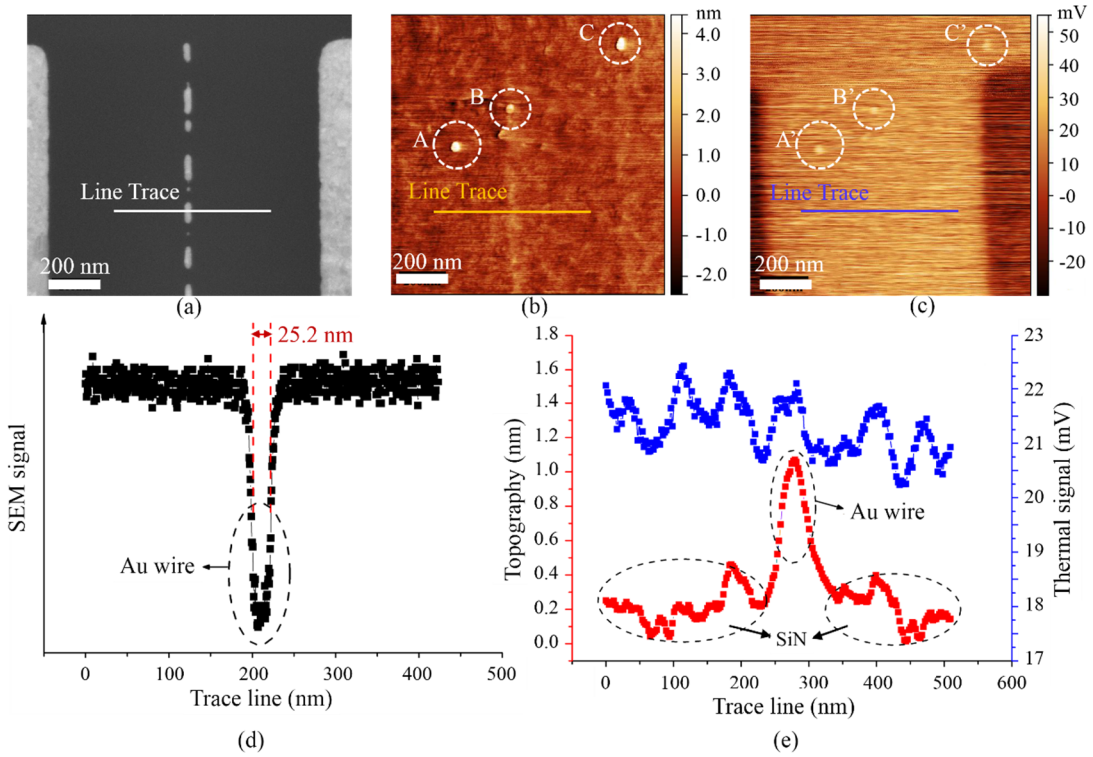

Figure 4.14 (a) SEM image showing the 25 nm narrow gold wire, (b) AFM topographic image, (c) thermal image showing the same feature scanned by SThM probe, and plots of the line traces from (d) SEM image and (e) topography and thermal signals. Dotted circles in (d) and (e) indicating the signal of the gold wire and SiN_x.

One initial interpretation of this thermal image was that 25 nm width is the limitation of SThM spatial resolution for this probe. However, it should be noted that resolution actually measures the ability of a SThM probe to distinguish between two thermal resistances. This is not only affected by the width of the wire, but also by its length. A shorter wire length results in the increase in the thermal resistance exhibited by the gold wire, making the thermal resistance difference between the SiN_x and the gold wire smaller. To test this suspicion, 35 nm wires (already shown to be detectable in Figure 4.10) with shorter length were fabricated and scanned. The resulting SThM thermal image shows that when the length is reduced to 250 nm, the wire cannot be detected (as shown in Figure 4.15). The narrow wire cannot be observed in the topographic image as it is obscured by the residual background roughness of

the sample, which is ~ 2 nm. It is also undetectable in the thermal image for the same reason as described for the 25 nm discontinuous wire above.

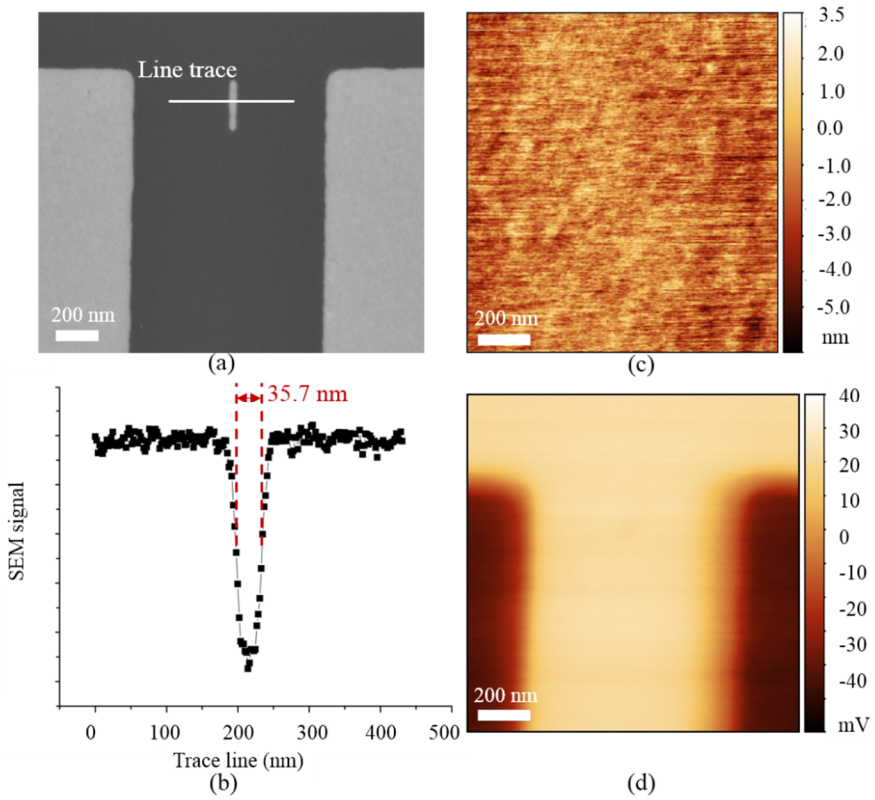

Figure 4.15 (a) SEM image showing the 35 nm narrow gold wire with 250 nm length, (b) plot of line trace from SEM image, (c) AFM topographic image and (d) thermal image showing the same feature scanned using a SThM probe.

If we take into account eq. 4.3, for a given thermal conductivity, the thermal spreading resistance can only be related to material thermal conductivity if the scanned object is assumed as a half-space. If the dimensions of the object are limited, the thermal signal obtained using SThM will change, resulting in possible misinterpretation of the feature's thermal conductivity. Therefore, when defining the thermal spatial resolution of SThM, it is more reasonable to define the minimum detectable difference in thermal resistance rather than just reporting the size of the object measured. Chapter 6 will expand on this by focusing on the understanding of how the feature's dimension and shape affect its thermal resistance.

4.4 Conclusion

In this Chapter, a general procedure to achieve lithographically defined, topography-free samples with significant materials contrast has been demonstrated. The fabrication of the sample uses the commonly available fabrication methods of ebeam lithography, metal evaporation and liftoff, dielectric layer deposition, and wet etching. The utilization of multiple layers provides a stable and robust substrate. The method may be readily extended to allow the production of more complex samples with multiple materials and higher resolution patterns. It is also compatible with photolithographic pattern definition, allowing the low cost production of calibration samples.

The utility of these samples has been illustrated using SThM to generate high-resolution images, free of topographically induced artifacts. Although still a small amount of topography associated with the gold features, which is ~ 1.5 nm in the worst case, artifacts due to it cannot be observed from the thermal image. This can be concluded as a result that the residue of topography has been beyond the sensitivity of the SThM, buried by the circuitry noise. It can also be noticed that even if the gold wire is made of the same material as the pad, the thermal response of SThM probe varies with its dimension. By treating the gold pad as a "resolved" feature, gold wires, showing their weaker thermal response which is dependent on their dimensions, are treated as "incompletely resolved" features. This leads to a phenomenon that is concluded as size effect. The limiting case of the size effect on the thermal signal was observed from SThM images of wires with 25 nm and 35 nm width but less than 300 nm length – gold wires cannot be detected from thermal images. Therefore, thermal spatial resolution of the SThM has to be discussed from two aspects: qualification and quantification. From qualification, as it underlines the ability to "see" the feature, the data in this chapter allowed the in-air thermal spatial resolution of a micromachined SThM probe to pure materials contrast to be unambiguously determined for features in the range of 35 – 70 nm wide and 1 μm long. From quantification,

accurate determination of sample's thermal property is the main purpose. As any deviation of thermal response from the gold pad made by the dimension of gold wires will result in a misinterpretation of thermal conductivity, it is necessary to further consider the thermal spatial resolution with the size effect being involved.

Based on the discussion in this chapter, with the topography-free sample, the variation of thermal response can be attributed as the change of thermal resistance due to the sample. Therefore, a deep understanding of thermal resistance as a function of feature dimension is required to define thermal spatial resolution in a more accurate manner. Besides, sample materials, which will also affect the thermal resistance from the thermal boundary resistance between the probe and the sample, as well as the thermal spreading resistance, is appropriate to be discussed when considering the thermal spatial resolution. This will be investigated in Chapter 6 where a numerical method is employed to evaluate the thermal spreading resistance of thin, narrow wires fabricated as the new topography-free samples, and from which a resolution of in-air SThM will be defined based on the power sensitivity

5

Quantification of Probe-sample Interactions of a SThM Using a Nanofabricated Calibration Sample Having Programmable Size

In Chapter 2, the uncertainties present in SThM quantitative measurement using both passive and active mode were described. Briefly, in passive mode, the translation from a measured electrical signal into temperature, as well as the mismatch between probe and sample temperature as a result of contact thermal resistance raised the requirement for calibration. However, the complication of probe-sample air conduction can result in a deviation between calibration and an actual measurement. In active mode, understanding the thermal interactions between the probe and sample is crucial in quantifying the sample properties. This is often complicated by components of the system having structural dimensions of comparable size to the mean free path of the heat carriers. In particular, the ambiguity of the thermal contact area, thermal interactions at the probe-sample constriction and the thermal performance of the probe itself, make quantification of the measurements difficult. In order to address these problems, to accurately calibrate the probe and to understand the probe-sample air conduction, a

temperature reference device is necessary. If a device can be developed that allows characterization of both the probe and the probe-sample interface, it will offer a great tool for SThM use and development.

In this chapter, a new membrane-based Johnson noise (JN) calibration device has been designed and fabricated following a novel design strategy targeting improved performance and utility. Two working modes of the device are demonstrated through both measurement and FEA modelling, showing an exceptionally uniform temperature distribution across its membrane. With the help of the FEA results, an one-dimensional (1D) heat transfer equation for mathematically describing multiple thermal interactions between the probe and the device, including the solid-solid contact, water meniscus and air conduction, has been constructed based on the SiN_x probe. By matching the calculated tip temperature with experimental results, thermal interface resistance between the tip and the device has been obtained, followed by the determination of the thermal contact radius by comparing two physical models. Finally, a lumped-heat-capacity system is described for modelling the passive SThM probe working in ambient conditions, taking into account the heat exchange between the probe, sample and air.

5.1 JN Device Design and Fabrication

5.1.1 Device design strategy

The new JN device is deigned to achieve a homogeneous temperature distribution by employing a low thermal conductivity membrane and a central-symmetric configuration of heaters. Figure 5.1 (a) shows an overview of the JN device design. The device integrates eight individually addressable heaters, four large and four small, and a metallic 4-terminal thin film resistor, on a 100 nm thick SiN_x membrane.

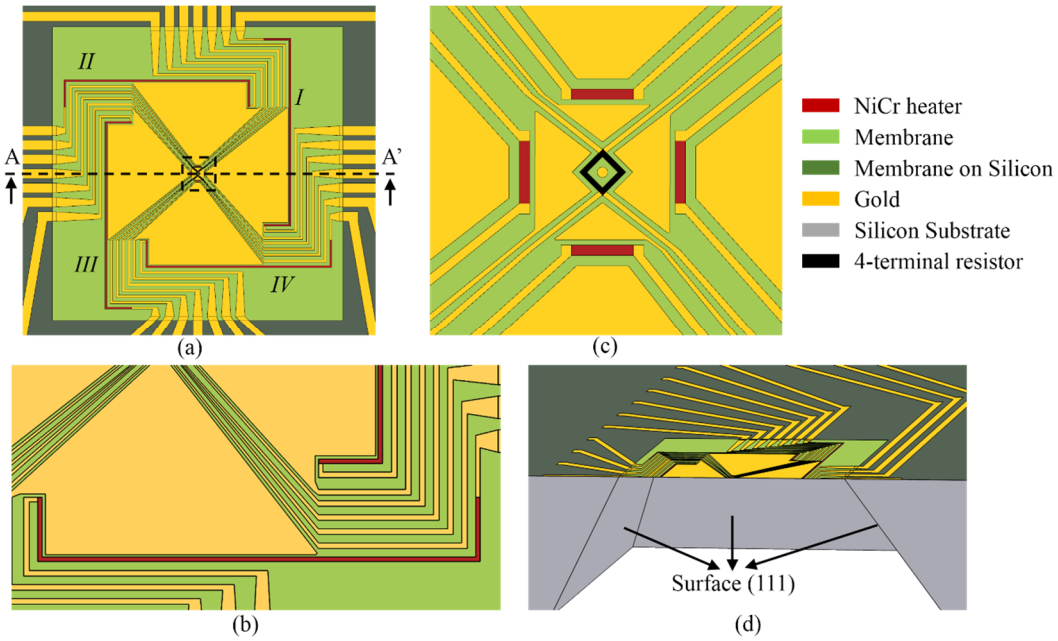

Figure 5.1 (a) General view of the design of the components on the membrane, (b) close up of one of the large heaters IV, (c) close up of the dashed square in (a), and (d) three-dimensional cross-section view taken through line A-A' showing the membrane supported by the silicon substrate. The surface (111) is 54.7° with the horizontal surface (110) and acts as an etch-stop surface.

A thin SiN_x membrane was chosen as the substrate for the active region due to its low thermal conductivity, reducing heat flowing away from the device. The same structure was used by Dobson *et al*. [88] in their device, which although recognized as the most accurate calibration device currently

available [193], still exhibits some thermal nonuniformity due to heat loss through its asymmetric wires into the silicon substrate. To correct this, a symmetric configuration was employed that offers maximum temperature uniformity at the device centre. This is the same concept as that used for the magnetic field at the centre of a Helmholtz coil. It was also necessary to counter heat loss through the gold wires connecting these on-membrane components to external circuit due to their high thermal conductivity. This was achieved by employing a group of U-shape heaters, which are marked as *I* to *IV* in Figure 5.1 (a), to compensate for the heat loss present in the gap between each heater where the device connections exit the membrane. The shape of each of these parts was optimized using FEA models, which will be illustrated in Section 5.2. Details of these features can be seen in Figure 5.1 (b), zoomed in from the bottom right corner of Figure 5.1 (a). The inclusion of four small heaters located at the centre of the membrane, shown in Figure 5.1 (c), offers a simple means of quantifying the effect of air conduction between the cantilever and the sample. This is achieved by using them to vary the heated region between the whole membrane and a small central part, providing a direct measurement of the thermal conduction between sample and tip for different, known distributions of temperature. A 2 μm diameter, electrically isolated gold circle was positioned at the centre of the membrane to identify the optimum contact point for the SThM probe. This circle, the "scanning target", was surrounded by a split 4-terminal resistor (the feature in black). This configuration ensured that the average temperature of the resistor was as close to that of the scanning target as possible. This was further assisted by locating the 4-terminal resistor as close as possible to the scanning target, which was set as 1 μm separation in a compromise between ease of fabrication, yield and device performance.

The size of membrane was also specially designed for conveniently characterizing the grooved SThM probe used throughout this thesis. The membrane was a 560 μm × 560 μm square and the small heaters bounded a region of 32 μm × 32 μm square. With these dimensions, a heated region

equalling the size of the whole SThM probe cantilever (with its length of 150 μm) could be generated using the large heaters, alternatively a region one tenth of the probe length could also be created by employing the small heaters. Importantly, both of these heating regions could be generated in a single experiment whilst the SThM probe maintained contact throughout.

The use of Johnson noise to measure temperature requires a resistor of known resistivity. Therefore, both the heaters and the 4-terminal resistor were made of $Ni_{0.6}Cr_{0.4}$ (abbreviated as NiCr in the following text), offering a low temperature coefficient of resistance – lower than 0.1 % over the temperature range of the experiment [194]. The correlation method, as described by Dobson *et al*. [88], was used to measure the thermal noise of the resistor.

The design also includes large gold regions located between all of the active features, namely, the 4-terminal resistor, large and small heaters. These acted as ground planes for electrical isolation, and also helped spread the heat uniformly across the whole membrane.

5.1.2 Batch fabrication lithography design

The whole device was fabricated using a combination of photolithography and EBL offering an efficient and economical process with high resolution for critical features. The lithography design for a single device is shown in Figure 5.2. All green regions represent lithography layers for the backside of the wafer, specifically membrane and cleave definition. Region I' shows a zoom-in of region I giving details of critical components on the square membrane. All components in the red area of region I' were fabricated using EBL due to the smallest dimension being 600 nm, which is beyond the resolution of basic photolithography, as well as the requirement of accurate overlay. All other parts, including gold wires and gold pads, were fabricated using photolithography. Each gold wire was numbered together with its corresponding gold pad (shown by II' and III' zoomed in from II and III) offering convenience when inspecting and testing the device. The separation

region between the bond pads area and the membrane helped to avoid damage of the membrane during wire bonding and eliminated intrusion of the bond wires into the scan region. Each device was surrounded by an etched cleave line, which allowed easy separation of each device from the batch fabricated wafer.

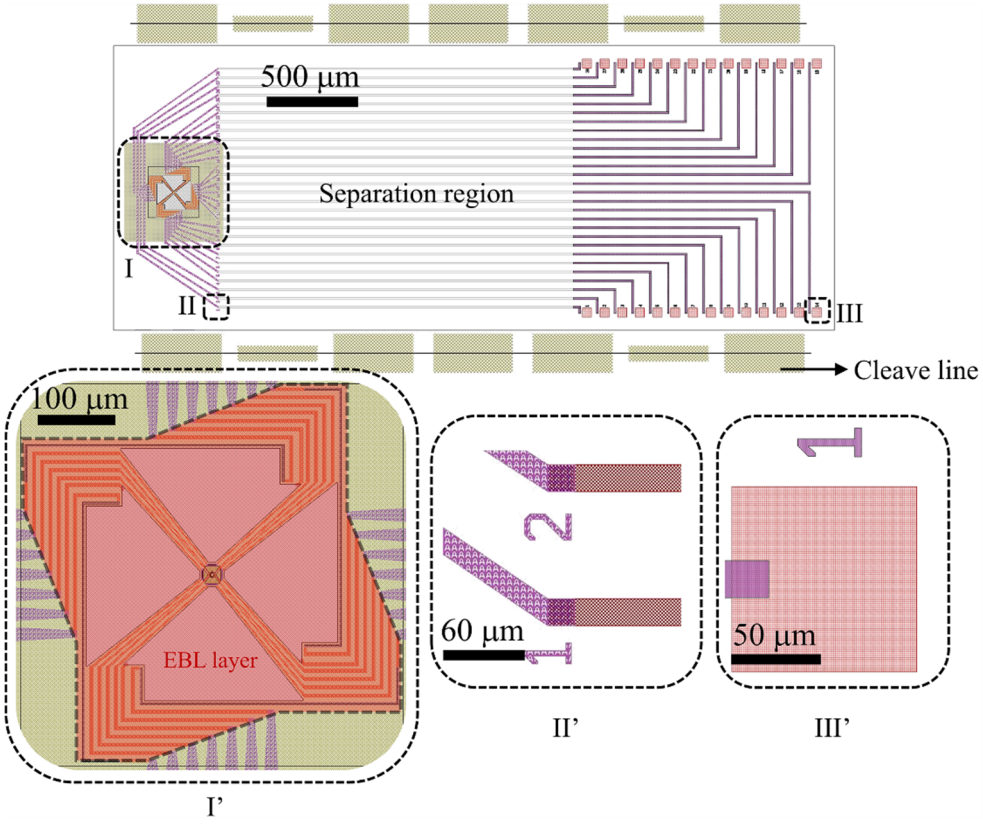

Figure 5.2 Mask design for one single device (top) with three images closed-up showing the detail (bottom).

The layout of the devices on the 3-inch silicon wafer used for batch fabrication is shown in Figure 5.3. The wafer was designed to have four quadrants with 15 devices fabricated simultaneously in each. The separation of each quadrant by a region of un-etched silicon guaranteed that the wafer remained tough enough to survive fabrication.

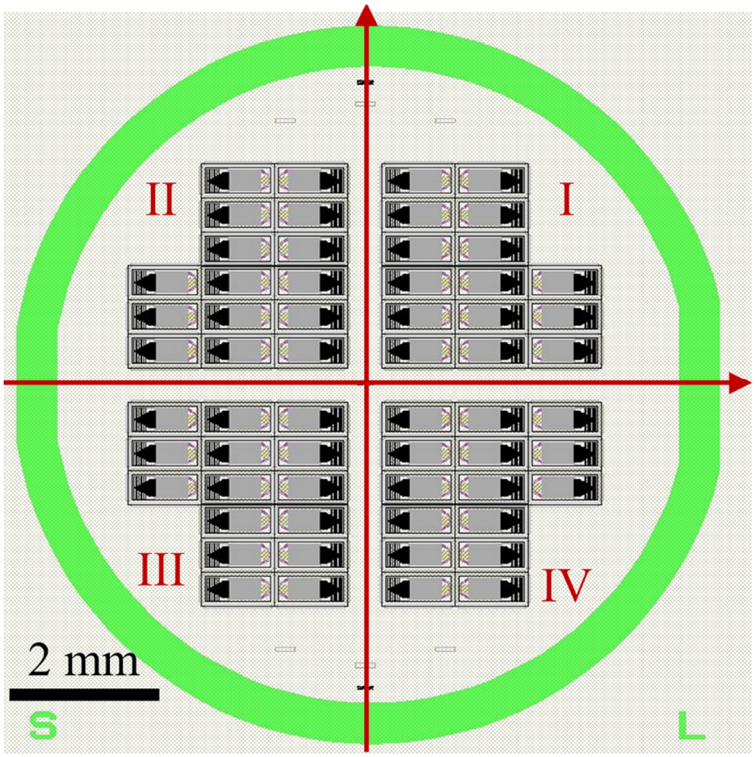

Figure 5.3 Wafer layout design used for a batch of devices. Both EBL and photolithography layer are designed simultaneously in one layout, which can be split during the fabrication. The signs "S" and "L" correspond to the small and large flat of the silicon wafer.

5.1.3 Device fabrication

The complete fabrication process flow is shown in Figure 5.4. The JN devices were batch fabricated on a 3-inch 400 µm thick n-type (100) silicon wafer with a 500 nm thick LPCVD SiN_x film on both sides. First, the backside SiN_x film was removed in photo-lithographically defined regions using reactive ion etching (RIE) with 20 sccm C_2F_6 plasma, 100 V DC bias and 15 mTorr (step i) [91]. These features were used as a wet etch mask to define the membrane. The wet etch employed 7 mol KOH at 115 °C to remove the silicon at a rate of 4.1 µm/min. To ensure a robust front face for subsequent fabrication steps, 50 µm of silicon was left on the front side after etching the backside (step ii). Next, device features were defined on the topside of the wafer in three steps. For all critical features on the membrane, EBL on a double layer PMMA resist followed by liftoff was used [195]. The metal used was a stack of 165 nm thick

polycrystalline gold with 15 nm NiCr under layer deposited through evaporation in "A" of step iii). For the less dimensionally critical gold wires and bond pads located on the silicon substrate, photolithography was used together with liftoff (S1818-LOR 3A) of the same evaporated metal stack shown in "B" of step iv). In the third step a gold etch in KI/I solution was used to expose the underlying NiCr, which would form the heaters and 4-terminal resistor [196]. The etch mask was defined using EBL followed by a gold etch solution of 0.15 mol I_2 in 1 molar KI for 15 seconds (step v). Finally, the remaining 50 µm silicon on the back of the membrane was removed using 25 % TMAH mixed with an additional 25 % by volume isopropanol alcohol (IPA) at 80 °C (step vi). This final silicon wet etch was chosen for its slow etch rate (~ 0.35 µm/min) and high selectivity, ensuring no corrosion of the metallic features and nitride membrane. The completed devices were cleaved from the silicon wafer for individual use. SEM images of the completed JN device are shown in Figure 5.5. The full fabrication process can be found in Appendix III. The complete JN device bonded on a PCB ready for use is illustrated in Figure 5.5 (e). The shape of the PCB was designed to fit the stage of the bonding machine. Two holes were reserved for fixing the PCB firmly to the daughter board using small bolts.

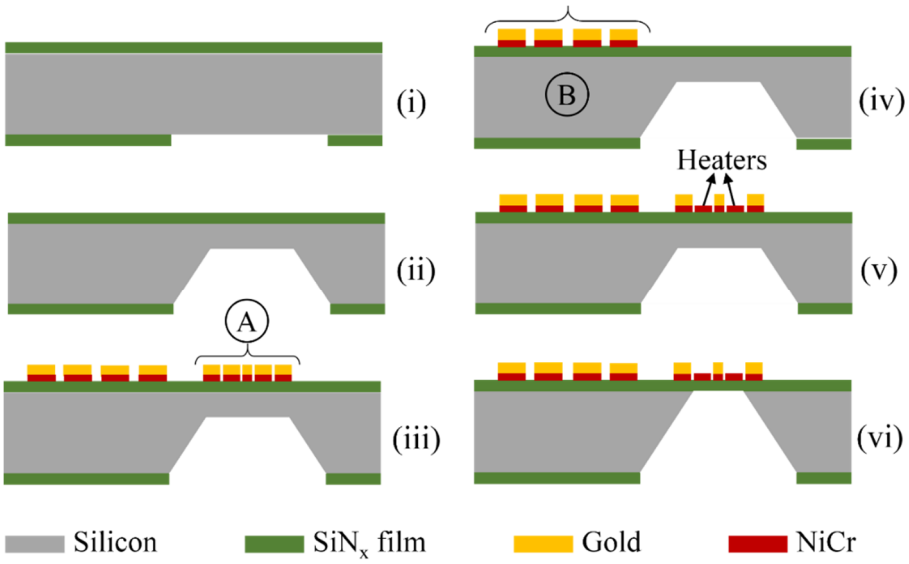

Figure 5.4 Fabrication process of the JN device in the steps (a) to (f).

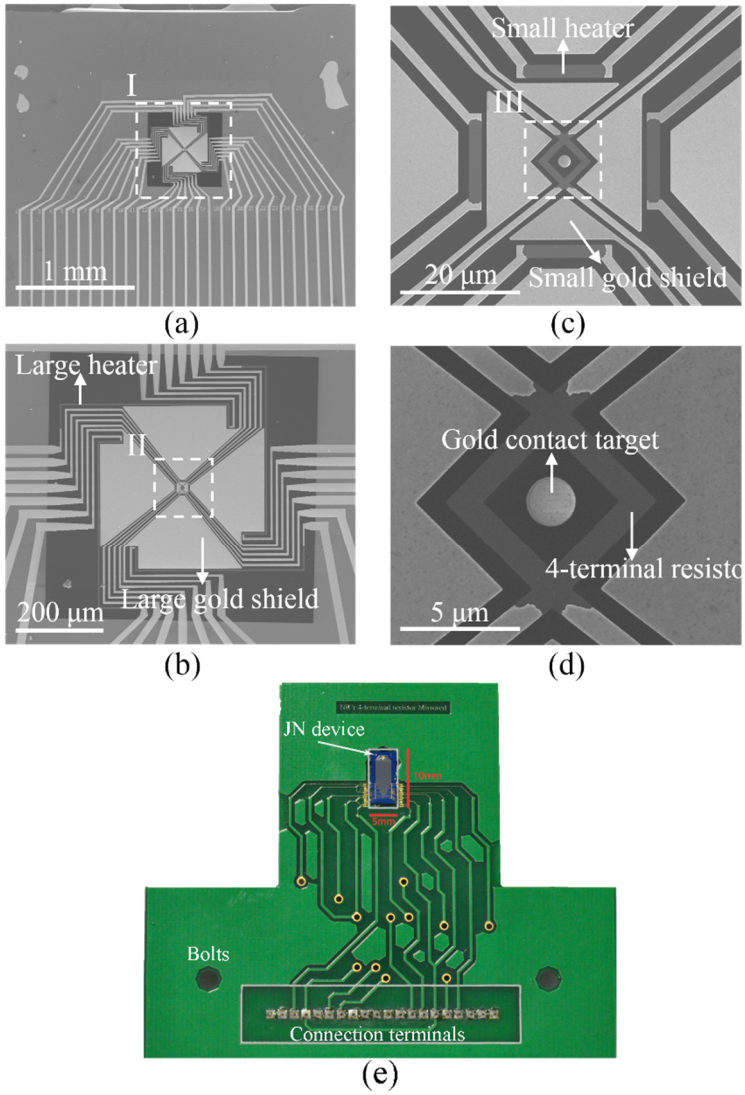

Figure 5.5 SEM image of the JN device: (a) general view of the whole device including the membrane (dark grey area) and gold connecting wires (brightest wires), (b) details of features from the dashed square I in figure (a) showing four large heaters and four large gold shields on the membrane, (c) details of features in the dashed square II in figure (b) showing four small heaters and four small gold shields, and (d) details of features in the dashed square III in figure (c) showing the 2 µm diameter gold contact target with the NiCr 4-terminal split resistor surrounding it. Photo (e) shows the complete JN device bonded onto a specifically designed PCB.

5.2 Experimental Methods

5.2.1 Finite element analysis of the JN device

FEA is commonly used for modelling the temperature distribution of devices on the micrometre scale [90,139]. Considering the complex geometry, the use of multiple materials, heat exchange with surrounding environment, and steady-state operation of the JN device, a 3D model was employed. As most elements in the device are thin films, thermal transport will be affected by their smallest dimension being comparable in length to the mean free path (MFP) of heat carriers. Therefore, the thermal conductivities of materials in the device need to be corrected to take this effect into account.

For metals where values are not readily available in the literature, it is necessary to estimate their thermal conductivity. This can be done from their electrical conductivity (σ) using the Wiedemann-Franz (W-F) Law [197], which states that the ratio of thermal conductivity and electrical conductivity is a function of temperature

$$\frac{k}{\sigma} = cT \qquad \text{eq. 5.1}$$

where $c = 2.45 \times 10^{-8}$ is a constant named Lorenz number. As the resistance of the NiCr small heater can be measured as 792 Ω, and its dimensions are known, the electrical conductivity can be calculated as 5.41×10^5 S/m. Therefore, W-F Law gives a thermal conductivity for the thin-film NiCr at 300 K as 5.1 W/mK. The thermal conductivity of the gold used in wires and shields, as well as that of the LPCVD SiN_x membrane can be taken from the literature for films of the same thickness and composition [198,199]. The silicon wafer (400 μm thick) was considered to be bulk silicon. Table 5.1 shows the thermal conductivity used for each material in this 3D model.

Table 5.1 Thermal conductivity of each element in JN device

Element	Material	Thermal conductivity (W/mK)	Source of data
Substrate	Silicon	130	Bulk intrinsic
Membrane	LPCVD SiN_x	3	Ref. [198]
Wires, shields, and scanning target	Polycrystalline gold	317	Ref. [199]
Heaters and 4-terminal resistor	$Ni_{0.4}Cr_{0.6}$	5.1	W-F Law

In order to analyze the thermal performance of the device, the 3D model was built in COMSOL MULTIPHYSICS®. The steady state model took both Joule heating and heat transfer into account. As the device was used under ambient conditions, the effect of heat exchange with air was considered by incorporating air into the model. All elements on the device were modelled with the same dimensions as those fabricated, however in the interest of computational efficiency, the model only extended 600 μm beyond the membrane, at which point an ambient boundary condition was set. Figure 5.6 (a) shows a general view of the 3D model built for FEA. The effect of air conduction was modelled by covering the whole device with a block with the material properties of air. All inner boundaries were set to have continuity of temperature, and all outer surfaces, including those of the device and the air, were fixed at room temperature (293 K). To simplify the mesh and calculation, the membrane, with all elements on top was set as a "Thin Layer", meaning it was meshed as a 2D structure, but treated in the calculation as a 3D structure. Three thin layers were set in total: the membrane (Figure 5.6 (b)), the gold elements (Figure 5.6 (c)), and the NiCr elements (Figure 5.6 (d)). The initial thermal condition for the model was set to room temperature. As heaters were employed in parallel during the experimental work, electrical boundary

conditions were set the same for each, with an electrical potential on one lead and ground at the other. The simulation results will be described in detail in Section 5.3.

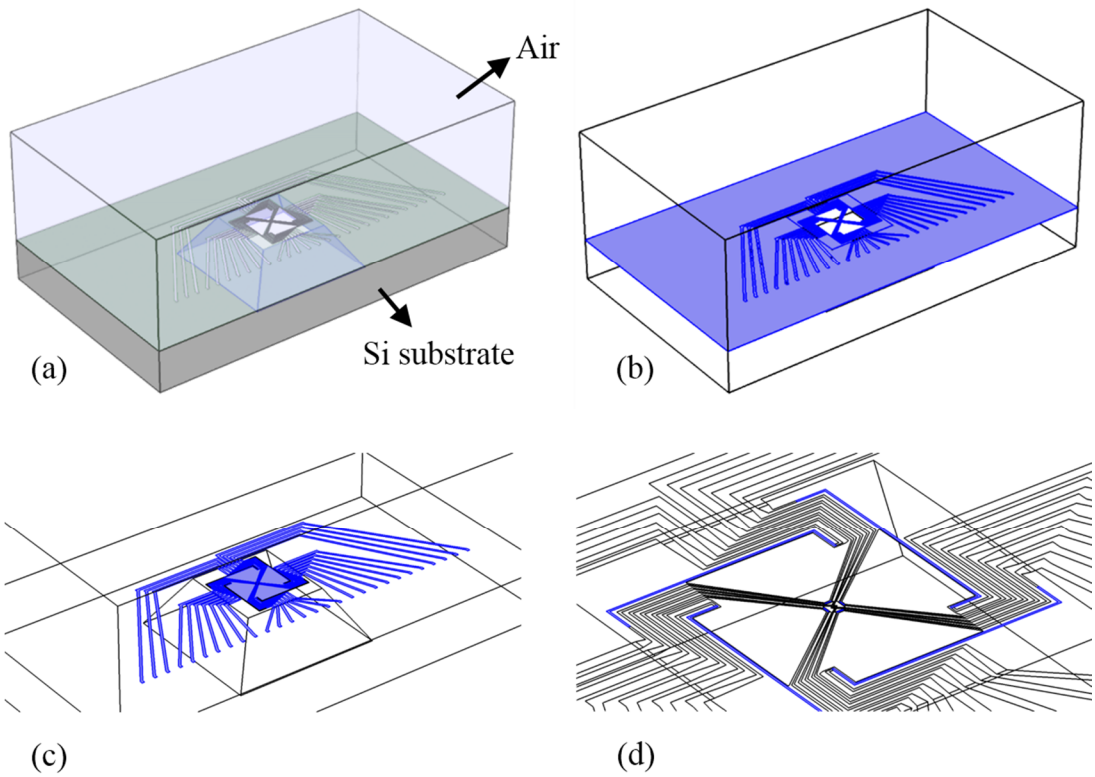

Figure 5.6 3D model built in COMSOL MULTIPHYSICS® for simulating the thermal performance of the JN device. (a) illustrates an overview of the device covered by a block of air, (b) (c) and (d) shows the 'Thin Layer' set on the SiN_x membrane, all gold elements and all NiCr layers respectively.

5.2.2 SThM setup for temperature measurement

The device was scanned using the thermal bending compensated SThM probe operated in passive mode as a nano-thermometer, allowing the measurement of the temperature distribution on the membrane. As the device was heated using a DC voltage, care was taken to avoid an unintended direct electrical path between the device and probe instrumentation. This was achieved by employing the method described by Dobson *et al.* [87], a schematic of which is shown in Figure 5.7. The probe was connected as one of

the legs of a Wheatstone bridge and driven by a 2.5 MHz 140 mV peak-peak sinusoid wave through a transformer. Bodzenta *et al*. [200] observed that thermal sensitivity of a SThM probe varied significantly when the frequency of its driving current exceeded a cut-off value (~ 10 kHz). In contrast, the method employed in this work employed very small RF transformers mounted in close proximity to the probe, minimising the stray capacitance connecting the probe and external circuitry. The measurement itself was of changes in probe resistance, which are substantially at DC. It should also be noted that no significant thermal effects were observed due to heating of the probe at radio frequencies.

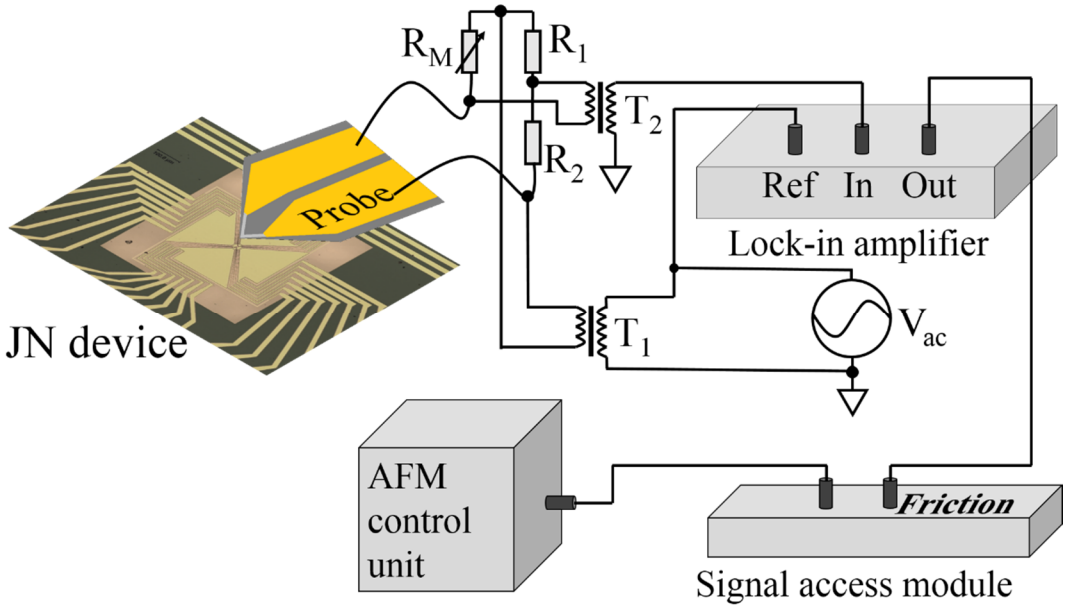

Figure 5.7 Schematic of the experimental setup for passive SThM probe scanning of the *in-situ* JN device. The probe forms a Wheatstone bridge with R_M, R_1, and R_2. T_1 and T_2 are transformers used for exciting and measuring the output of the bridge.

In this configuration, the current passing through the probe was no larger than 230 μA. Previous work by Dobson *et al*. [87] has shown that significant probe self-heating will not occur until the AC current exceeds 1 mA. Therefore, self-heating of the probe could be regarded as negligible during the experiment. When used as a thermometer, the resistance of the platinum tip

changes with temperature, leading to a change in the output of the bridge. This was connected to a lock-in amplifier through another transformer and then compared to a reference signal. The use of phase synchronous detection allows the significant contribution of the pad capacitance of the SThM probes to be eliminated by the choice of a suitable measurement phase, since the thermal signal affects the DC resistance of the probe only, and is therefore in quadrature to the parasitic signal from the reactive impedance of the pads. The DC output voltage from the lock-in amplifier was then fed into the AFM (Veeco Dimension 3000) control unit via a signal access module. This configuration permits the measurement of electrically live samples without requiring dielectric coatings, which increase sample complexity and decrease the accuracy of measured temperature. In order to quantify the output signal, electrical resistance of the probe (R_p) was obtained *in situ* from the adjustable balanced resistor R_M, and the variation of R_p, ΔR_p, instead of its absolute value, was used.

The temperature change on the probe can be found from the output voltage, which can be calculated using the equation

$$U = \left(\frac{V_{ac}}{R_M + R_p} R_p - \frac{V_{ac}}{R_1 + R_2} R_2\right) A \qquad \text{eq. 5.2}$$

where U is the DC voltage output from the lock-in amplifier, V_{ac} is the peak-peak AC voltage supplying the bridge, R_M is value of the matching resistance, bridge resistance R_1 equals to R_2, and A is the gain of the lock-in amplifier. When configuring the probe in the bridge, it is possible to set R_M to be equal to R_p, which gives $U_a = 0$ whilst the probe is out of contact with the sample. When the probe is brought into contact with the sample, the lock-in DC voltage out U_c changes to

$$U_c = \left[\frac{V_{ac}}{R_M + R_p + \Delta R_p}\left(R_p + \Delta R_p\right) - \frac{V_{ac}}{2}\right] A \qquad \text{eq. 5.3}$$

where ΔR_p is the variation of the probe resistance due to the temperature change. Thus, ΔR_p can be derived as

$$\Delta R_p = \frac{2mR_p}{1-m} \quad \text{eq. 5.4}$$

where

$$m = \frac{2U_c}{V_{ac}A} \quad \text{eq. 5.5}$$

We have previously shown that the TCR (α) of the whole probe, consisting the cantilever, gold wires, pads, and the platinum tip is 0.000961 ± 0.0000106 K^{-1}. Thus, the real temperature variation on the probe can be calculated using

$$\Delta T_p = \frac{2m}{(1-m)\alpha} \quad \text{eq. 5.6}$$

In this configuration, the self-heated JN device, with temperature known from the 4-terminal Johnson noise resistor, can be scanned whilst operational by using the AC driven probe. The comparison of the actual device temperature and the SThM probe temperature can then be used to interrogate the heat transfer mechanisms between the probe and the sample.

5.3 Results and Discussion

5.3.1 Experimental verification of the FEA model

The JN device was tested in two modes, with only the large heaters or only the small heaters active. The same measurement system was used as in Dobson *et al.* [88]. The un-biased 4-terminal resistor at the centre of the device was connected to two identical differential amplifiers based on the OPA637 uncompensated DIFET input operational amplifier in a standard instrument amplifier configuration. A correlation measurement of the output of the two amplifiers allows a measure of the thermal noise of the 4-terminal resistor, which is independent of the (uncorrelated) voltage noise contributions of the two amplifiers. The correlation circuit allowing for measurement of Johnson noise and its conversion into the absolute temperature is a simple analogue correlator as used in [88]. Electrical resistance of the small and large heaters was 792 ± 1.1 Ω and 11005 ± 1.3 Ω respectively, as determined from 10 devices.

This variation in resistance will maximally result in a less than 1 % difference in the power from each heater, with negligible effect on the temperature distribution of the membrane. Previous work has shown that the random variation uncertainty in the system is ± 0.73 K [88]. The FEA model was verified by simulating a JN device with defined heater power, the same power was then used in the heaters of a real device, and the simulated temperature averaged from the whole volume of the entire resistor was taken to compare with that from experiment. The heaters were biased using a simple DC voltage source based on a voltage reference and a 10-turn potentiometer, with extensive filtering to prevent capacitive coupling of noise into the system within the bandwidth of the correlator. Figure 5.8 shows plots of both the measured and simulated 4-terminal resistor temperature for only large (a) and small (b) heaters. The FEA results show agreement with the experimental results, demonstrating that the model is valid. The maximum power supplied by the DC voltage source for the large heater is ~ 13 mW and for the small heater is ~ 3.2 mW, which will generate a maximum 80 K and 95 K temperature above the ambient respectively. Therefore, it can be concluded that when using the JN device in practical work at maximum power, the temperature difference between the scanning target and the 4-terminal resistor is less than 0.3 mK and 0.6 mK for large heater mode and small heater mode respectively. Figure 5.8 (c) and (d) show the temperature distribution at the centre of the membrane heated by large and small heaters. The uniformity of the temperature at the central region on the membrane is shown to be better for the large heaters than the small heaters, a phenomenon attributed to the larger distance between the large heaters and the centre than that of small heaters.

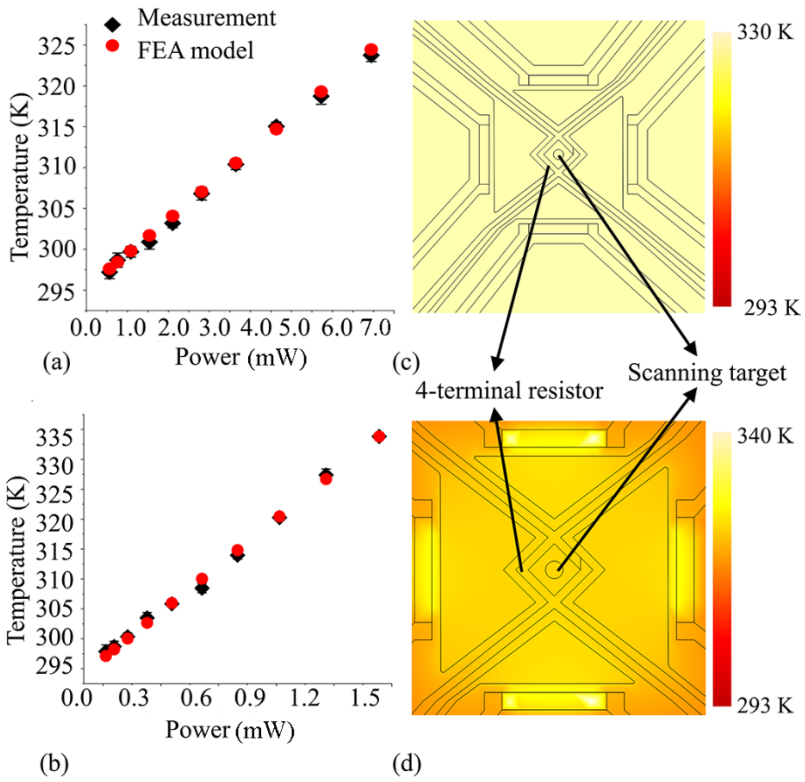

Figure 5.8 Plot of the average temperature on the 4-terminal resistor versus the power on heaters obtained from the experiment (black diamonds) and FEA model (red circles) for JN device working in (a) large heaters and (b) small heaters mode; (c) and (d) shows the temperature distribution at the centre of the membrane for each case.

5.3.2 Probe calibration

The primary purpose of the JN device is to offer a sample with a well-known temperature and thermal distribution for use in calibrating SThM probes. The instrumentation used to achieve this was set up as described previously in Section 5.2.2. The SThM probe was brought into contact with the JN device and positioned on the scanning target. The temperature of the JN device and output from the probe were then recorded for various heater powers. 10 measurements were recorded for each power on the heaters, and the average JN device temperature plotted versus the average probe output. Figure 5.9 shows the probe calibration plots obtained using both the small and the large heaters. A least squares method was used to fit the data to a straight

line (*T-U* line), relating the probe signal to the sample temperature. For small heater mode, $T_1 = (26.365 \pm 0.2201)U_1 + 292.79$ K and for large heater mode, $T_2 = (17.083 \pm 0.1025)U_2 + 293.26$ K.

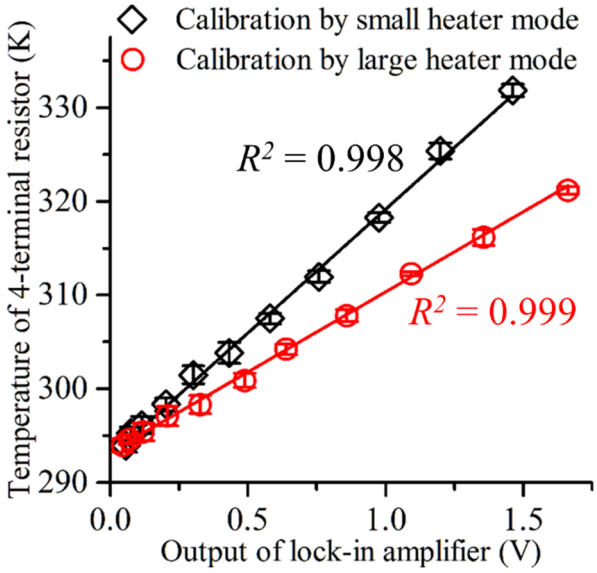

Figure 5.9 The temperature of the 4-terminal resistor on the JN device versus the DC output of the lock-in amplifier for the small heater and large heater. Parameters of the linear fit are shown with the R^2 value. The error bars are one standard deviation as obtained from the random variation in the data points.

It can be clearly seen in Figure 5.9 that a change in the size of the heated region, whilst maintaining the same temperature at the contact point, can result in a large variation in the output from the probe when calibrating in air. This difference can be significant, in this instance being more than 40 times larger than the error in the JN device. This difference can be attributed to the effect of air conduction between the cantilever and the sample as observed by other groups [100,109,172]. One solution to this problem is to employ a vacuum system to eliminate the air conduction effect. However, the complicated setup and high cost associated with a vacuum system preclude its use in many situations. In these situations, it is essential that a clear understanding of probe-sample interactions be employed during the analysis of experimental results in order to avoid misinterpretation.

5.3.3 1D heat transfer model for probe-sample interactions

It is well recognized that there are multiple thermal paths between a SThM probe and sample, and that solid-solid direct contact, water meniscus and air conduction dominate, while thermal radiation is typically negligible [52,100,137]. For a probe working in passive mode, net heat flow is governed by thermal conduction within the probe, thermal conduction through the surface contact point (through the solid-solid and water meniscus), and the air conduction between the probe and the sample. These combined heat paths can be analyzed using eq. 2.12, and can be described by a model that considers the geometry of the probe and active sample as mounted within the microscope, which is shown in Figure 5.10. To achieve this we can rewrite eq. 2.12 as

$$\frac{d}{dx}\left[\frac{dT(x)}{dx}\sum_i [kA(x)]_i\right] + h(x)w(x)[T_s(x) - T(x)] = 0 \qquad \text{eq. 5.7}$$

with all terms being defined in Section 2.3.4 of this thesis.

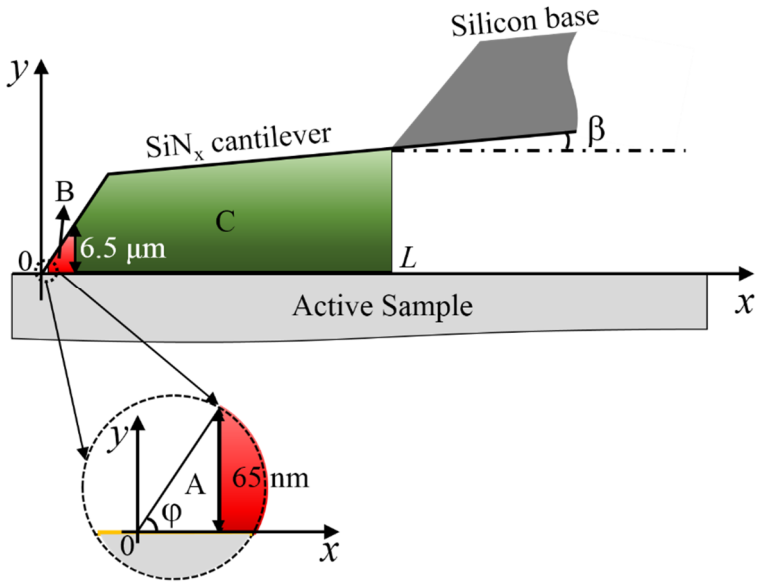

Figure 5.10 Schematic diagram shows the geometry of the passive probe scanning on the active sample. Three regions of heat exchange between the probe and sample through air conduction are determined by the separation and are shown as A, B, and C marked in different colours.

In this work, the probe was mounted with the cantilever at a 13° angle to the sample surface (β), while the tip was at a 69° angle (φ) to the sample. At the contact point (x = 0), heat transfers from the sample surface to the probe through the tip-surface contact with thermal conductance, G_{ts}. The base of the cantilever (x = L) is treated as a heat sink as the silicon base has three orders larger of thickness and one order larger thermal conductivity than the cantilever, and its temperature is assumed to be room temperature T_∞. The same assumption can be found in other work [90,106,121]. Air between the sample surface and the cantilever also provides a medium for heat transfer, and the heat transfer coefficient h will vary with cantilever-sample separation.

The probe dimensions and structure are the same as those used in previous work by Assy *et al*. [113,121] and Puyoo *et al*. [106,118]. These probes have relatively complex geometry and consist of multiple materials; therefore, the probe was split into sub-regions as denoted by subscript i in eq. 5.7. This allowed the combination of multiple materials and variation of the cross section area along the probe length (x), to be considered. The first term in eq. 5.7 represents thermal conduction within the probe, and the second term is heat exchange with the sample through the air. There is no temperature change with time as we only consider the problem in steady state. Two boundary conditions at x = 0 and x = L are

$$G_{ts}[T_s(0) - T(0)] = \sum_i [kA(L)]_i \frac{dT(L)}{dx} \qquad \text{eq. 5.8}$$

$$T(L) = T_\infty \qquad \text{eq. 5.9}$$

with all terms defined previously.

Solving the equation requires knowledge of various thermal properties within the system. The gold on the probe had the same thickness as that on the JN device, therefore the thermal conductivity was taken to be the same as that in Table 5.1 (317 W/mK). For the 500 nm thick SiN_x cantilever, thermal conductivity was taken from the literature as 10 W/mK [190]. For the platinum tip resistor, the thermal conductivity was calculated using W-F law as 22 ± 1.1

W/mK. Conduction through the air is dictated by the distance between the probe and the sample, and was therefore divided into three regimes [109] as dictated by the ratio of the distance (δ) to the MFP of air (λ = 65 nm). In the ballistic regime (shown as region A in Figure 5.10), where $\frac{\delta}{\lambda} < 1$, the original thermal conductivity of air (k_{air}) can be corrected using [123]

$$k_{air-b} = \frac{cv\delta(x)}{3(1+2g)} \qquad \text{eq. 5.10}$$

where c and v are the heat capacity and velocity of air molecules, $\delta(x)$ is the distance between the probe and the device, g is given by

$$g = \frac{2(2-\epsilon)\gamma}{\epsilon(\gamma+1)Pr} \qquad \text{eq. 5.11}$$

where ϵ is the thermal accommodation coefficient, γ is the ratio of air heat capacity and Pr is the Prandtl number. In the slip regime (shown as region B in Figure 5.10), where $1 \leq \frac{\delta}{\lambda} < 100$, the corrected thermal conductivity of air is

$$k_{air-s} = \frac{k_{air}\delta(x)}{\delta(x)+2g\lambda} \qquad \text{eq. 5.12}$$

and finally, for $\frac{\delta}{\lambda} > 100$ (shown as region C in Figure 5.10), the uncorrected value for air thermal conductivity can be used. These corrected values were then converted into heat transfer coefficients (h) by using the appropriate distance, $\delta(x)$, as dictated by the geometry.

Given the complexity of the geometry and the non-uniform temperature distribution, a solution was obtained using a finite difference method. By substituting derivative terms for finite differences, eq. 5.7, 5.8 and 5.9 were transferred from ordinary differential equations (ODEs) into a set of simultaneous algebraic equations [201], which were then implemented in MATLAB. This enabled the temperature distribution as calculated using COMSOL to be related to the signal output of the SThM probe. In order to fully account for the cantilever-sample heat exchange through the air, it was necessary to provide the code with the discrete actual temperature

distribution (as modelled in COMSOL) for the device in the region below the cantilever. The only unknown parameter was the tip-sample thermal conductance, G_{ts}. This was determined by varying the value until an appropriate fit between experimental results and MATLAB modelled data was obtained.

Figure 5.11 shows the FEA results describing the temperature distribution on the membrane when heated by small (a) and large (b) heaters. Heating powers were selected to obtain the same temperature on the 4-terminal resistor in each case: 360 μW - small heaters and 2000 μW - large heaters. For each simulation the temperature distribution profile was extracted along a 65 μm line A-A' as shown in (c). This was the same as the scan length and location used to obtain the experimental data. It can be seen that, in accordance with design intentions, the temperature distribution on the membrane is uniform for the large heaters, whereas, the small heaters produce a much smaller isothermal region. The actual temperature of the probe acquired by experiment is much smaller than the sample temperature in both modes (blue squares in Figure 5.11 (d) and (e)). It also exhibits an asymmetric distribution most clearly observed for the small heaters. This artifact is considered to be the result of varying heat flow through the air between the sample and probe as the result of scanning over a non-uniform sample temperature. This is confirmed by the excellent fit obtained by correcting the FEA data (Figure 5.11 (c)) using the MATLAB code as shown by the red diamonds in Figure 5.11 (d) and (e). This fit was obtained using a tip-sample thermal conductance $G_{ts} = 1.2\times10^{-6}$ W/K ($R_{ts} = 8.33 \times 10^{5}$ K/W). The main error of the finite difference method is due to the assumption of room temperature at the end of the cantilever connected to the silicon base. This can be seen in Figure 5.11 (e) where the experimental results shows a slight gradient that we attribute to the variation in the physical temperature of the silicon probe base as the probe is slowly scanned over the large heated region.

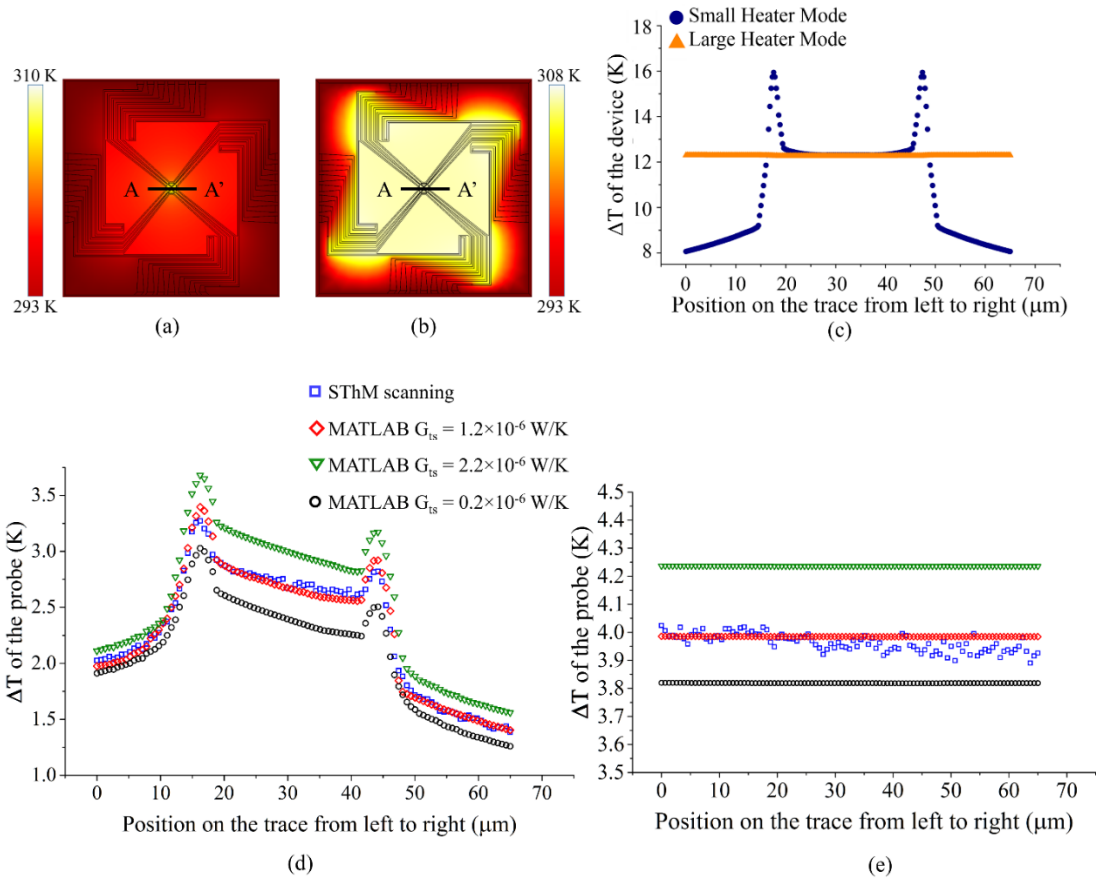

Figure 5.11 (a) and (b) illustrate the JN device temperature distribution from the FEA model. A 65 μm long trace A-A' across the centre of the membrane shows the section used for the data plotted in (c) showing the temperature difference from the ambient. (d) and (e) demonstrate a comparison, for the same region, between experimental data and modelled data corrected in using the heat transfer equation by different G_{ts}.

5.3.4 Analysis of thermal interactions and determination of contact radius

Heat exchange between the probe and sample is a combined interaction consisting of heat transfer through the nanometer-sized constriction at the contact point, heat conduction along the cantilever and heat exchange with the sample through the air. Thermal conduction through the cantilever and the air have been considered as shown in eq. 5.7, however the contribution of the constriction, G_{ts}, which is the reciprocal of R_{ts}, is worth more detailed consideration. A thermal resistance network can be used to analyze the tip-sample interactions at the constriction. It is well understood that the thermal resistance of the constriction ($R_{constriction}$) consists of a number of contributions. These are the thermal resistance of the solid-solid contact (R_{int}), the constriction resistance for the tip side (R_{tip}) and sample side (R_s), the water meniscus and the air in the gap surrounding the constriction. It has been experimentally demonstrated by Assy *et al*. [113,137] that for the probes used in this work thermal conductance of the water meniscus is 1 % – 3 % of total contact conductance, suggesting that this effect can be neglected. The size of the mechanical contact between the probe and the sample has previously been determined using the DMT (Derjaguin, Muller, and Toporov) model [202]. For a contact force of 20 nN, as used in this work, the contact radius is 3 ± 0.5 nm [121]. With this information, it is possible to model the tip as a hemisphere connected to the triangular probe end. The tip-sample contact can then be regarded as a circle, as shown in Figure 5.12 (a), and a resistance model generated as shown in Figure 5.12 (b).

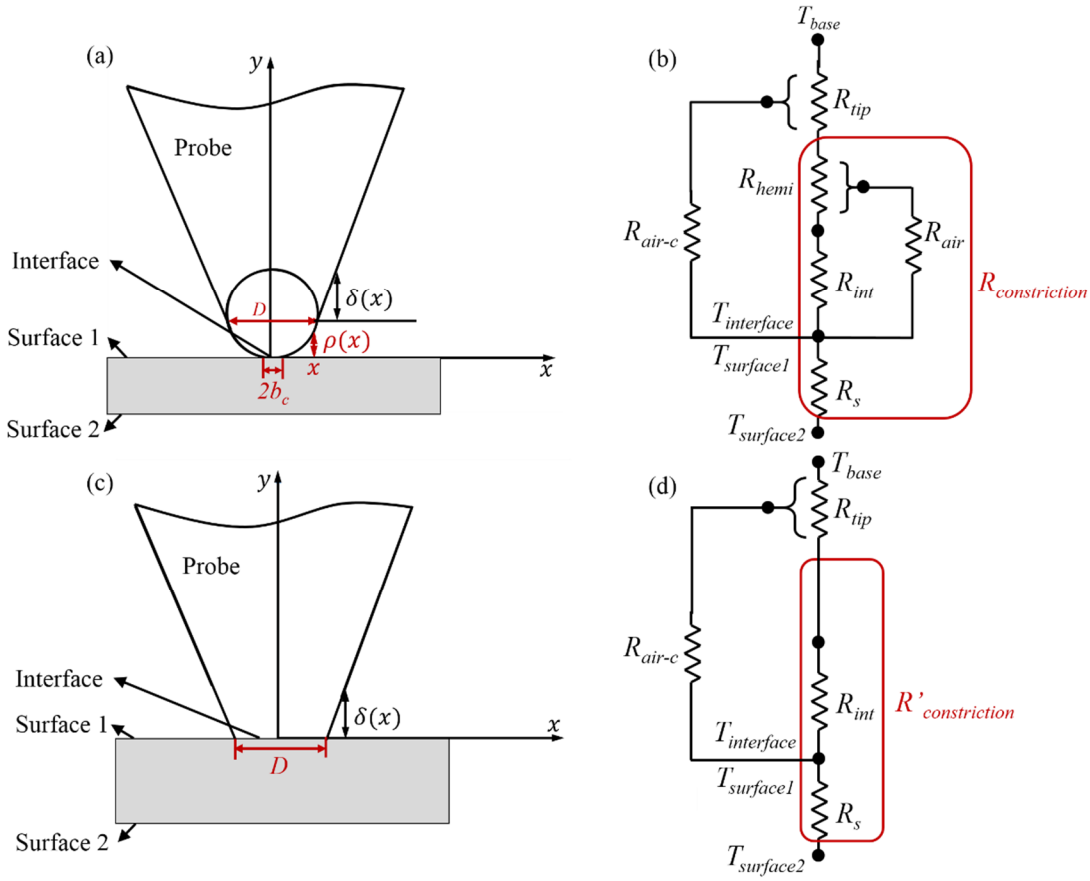

Figure 5.12 (a) Constriction model between the tip and surface based on the DMT model determined contact radius, (b) associated thermal resistance network, (c) constriction model between the tip and surface with the apex radius equal to the contact radius and (d) associated thermal resistance network.

In eq. 5.7, air conduction between the probe and sample ($R_{air\text{-}c}$ in the network) is considered by assuming the probe contact with the sample as a plane without a gap. However, when considering a contact as described by the DMT model, as shown in Figure 5.12 (a), the air surrounding the tip hemisphere must be inserted into the network, which is represented as R_{air}, as well as the thermal resistance associated with heat conducting from the contact point to the apex of the tip (the diameter is D), which is a hemisphere (R_{hemi}). When considering a heated sample, the probe contact can be considered as an isothermal system, as demonstrated by the work of Fletcher *et al.* [77] using a thermoelectric probe. Therefore, we can assume that the temperature

of surface 1 ($T_{surface1}$), surface 2 ($T_{surface2}$) and the interface ($T_{interface}$) are all equal. Therefore, R_s does not need to be considered as contributing to R_{ts}. The constriction resistance ($R_{constriction}$), which is used as R_{ts}, can be then calculated as R_{int} in series with the parallel combination of R_{hemi} and R_{air}, which can be written as

$$R_{constriction} = R_{int} + \sum_j (R_{air}^j || R_{hemi}^j) \qquad \text{eq. 5.13}$$

where j represents the number of the element in parallel, which is infinite.

The thermal resistance of the hemispherical part can be calculated assuming that the temperature is a function of the radius only. Then R_{hemi} can be written as

$$R_{hemi} = \frac{\int_{y_1}^{y_2} \frac{1}{\pi(Dy - y^2 + b_c^2)} dy}{k_{pt}} \qquad \text{eq. 5.14}$$

where k_{pt} is the thermal conductivity of the platinum, 22 W/mK as calculated in Section 5.3.3 and y_1 and y_2 are 0 to 50 nm respectively, giving R_{hemi} as 1.04×10^6 K/W. As the maximum distance between any point on the hemisphere and the sample surface is smaller than the MFP of air at room temperature (λ = 65 nm), thermal transport is in the ballistic regime and the elementary heat flow through the gap is given by

$$dQ_{air} = p(x) k_{air-b} \frac{\Delta T(x)}{\rho(x)} dx \qquad \text{eq. 5.15}$$

where p is the perimeter of the tip at x, and ρ is the distance between the tip and the sample surface. The heat flow across the whole gap can be written as

$$Q_{air} = 2\pi k_{air-b} \int_{b_c}^{\frac{D}{2}} x \cdot \frac{\Delta T(x)}{\rho(x)} dx \qquad \text{eq. 5.16}$$

and this gives the R_{air} as 1.09×10^9 K/W.

Finally, the solid-solid contact thermal resistance at the contact point with radius determined by the DMT model can be calculated as

$$R_{int} = \frac{R_b}{\pi b_c^2} \qquad \text{eq. 5.17}$$

As described in Chapter 2, R_b lies in the range of 1×10^{-9} to 5×10^{-8} m^2K/W. Thus, R_{int} is considered to fall into the range of 2×10^7 to 10^9 K/W with b_c equal to 3 nm.

Using all of these parameters in eq. 5.13, $R_{constriction}$ can be determined to be larger than 2×10^7 K/W, which is at least two orders of magnitude larger than the R_{ts} required to obtain a good fit to the experimental data as shown in Figure 5.11 (d) and (e). However, as reported in recent work by Assy [121], Puyoo [118], Gotsmann [141], and Pettes [89], it may be more appropriate to consider the contact radius to be the same as the probe's tip radius of curvature. This is due to the tip becoming flattened when contacting the sample with normal SPM imaging loads [141,203]. In this instance, the thermal resistance model can be modified as shown in Figure 5.12 (c) and (d). The tip can be regarded as a cone with a round, planar contact to the surface of diameter equal to the probe's tip radius of curvature (~ 50 nm). In this case, no air conduction has to be considered and $R'_{constriction}$ equals to R_{int}. R_b in this model can be calculated as 6.5×10^{-9} m^2K/W by using $R_{int} = R_{ts} = 8.33 \times 10^5$ K/W and b_c = 50 nm, which is in good agreement with the thermal resistance of a metal-metal interface (10^{-9} m^2K/W) [77,204]. It should be noted that SThM probes always have a rough tip apex and tend to establish a multi-asperity contact. In this work, this complicated contact scheme was simplified to a single contact for two reasons: On the larger scale, there were no obvious multi-contact artifacts visible in the topographic image. On the smaller scale, it has been shown by Gotsmann's work that even a rough tip should be treated as flattened due to the pressure exerted by imaging and that heat transport will increase as a function of true contact area [141]. This is an effective approach as demonstrated in other research works employing SThM probes [89,113,121].

5.3.5 Characterization of the SThM probe using JN device

Unlike the single-material, doped-silicon probe for which the thermal resistance can be directly calculated from its dimensions and thermal conductivity [124,125], the SThM probe used in this work is difficult to characterize due to its complex, multiple-material structure. Current methods for modelling this probe are either difficult to apply due to the heavy calculation load [149] or inaccurate [205], with direct measurement of the probe thermal resistance only achievable in vacuum [121]. However, by utilizing the uniform thermal distribution and accurately known temperature of the JN device, the thermal behaviour of the probe can be determined in air. This permits the construction of a multiple lumped system model that describes the thermal behaviour of the probe. This lumped model may provide a simple way to evaluate the characterization of the probe and assist in modifying its design.

The multiple materials, complex geometry and various probe-sample thermal conduction regimes require a model consisting of five parts, which are shown in Figure 5.13 (a) to (e). One advantage of our probe is that when mounted in an AFM, the ballistic and slip regimes only have impact on the platinum sensor, reducing the number of parts to model. Parts A and B consist of SiN_x with platinum in the ballistic and slip regimes respectively. Part C is SiN_x with gold on the 69° angled tip region. Part D and E are SiN_x and gold, each with differing geometries on the 13° inclined cantilever. Each part of this lumped model requires its individual thermal resistance to be determined. Fin theory, as previously used for this probe type, is invalid here due to its requirements for an invariable shape and known thermal conductivity. However, the temperature uniformity can still be assumed as the Biot number, is much smaller than one [17]. In order to calculate the thermal resistance of the cantilever heat flow through each part in both the SiN_x and the platinum for parts A and B or SiN_x and gold for parts C, D and E must be accounted for. To achieve this a coordinate system was built, of which the x-axis is in the

plane of the sample and will not change direction with the probe orientation. This is shown in Figure 5.13 (f). The elementary heat flux can be written as

$$q(x) = -A(x)k_i \frac{dT}{dx} \qquad \text{eq. 5.18}$$

where thermal conductivity k_{SiN} is for SiN_x, k_{Au} is for gold and k_{pt} is for the platinum thermometer.

The summation of the heat flux Q can be derived by integration of the elementary heat flux from x_1 to x_2 as

$$Q \int_{x_1}^{x_2} \frac{dx}{A(x)} = -\int_{T_1}^{T_2} k_i \, dT = k_i \cdot \Delta T \qquad \text{eq. 5.19a}$$

which gives

$$Q = \frac{k_i \Delta T}{\int_{x_1}^{x_2} \frac{dx}{A(x)}} \qquad \text{eq. 5.19b}$$

Thus the thermal resistance of the probe is

$$R_i = \frac{\Delta T}{Q} = \frac{\int_{x_1}^{x_2} \frac{dx}{A(x)}}{k_i} \qquad \text{eq. 5.20}$$

The variation of the cross section area is dependent of the geometry of each material.

Eq. 5.15 can be used to calculate the thermal resistance of the air between the probe and sample by modifying $p(x)$ with the width of the probe. The thermal convective resistance R_{conv} between the probe and the air above, assumed as room temperature, is given by [17]

$$R_{conv} = \frac{1}{h_{air} S} \qquad \text{eq. 5.21}$$

where h_{air} is the heat transfer coefficient of the natural convection which is generally lower than 10 W/m^{2}K, and S is the surface area of each part of the probe.

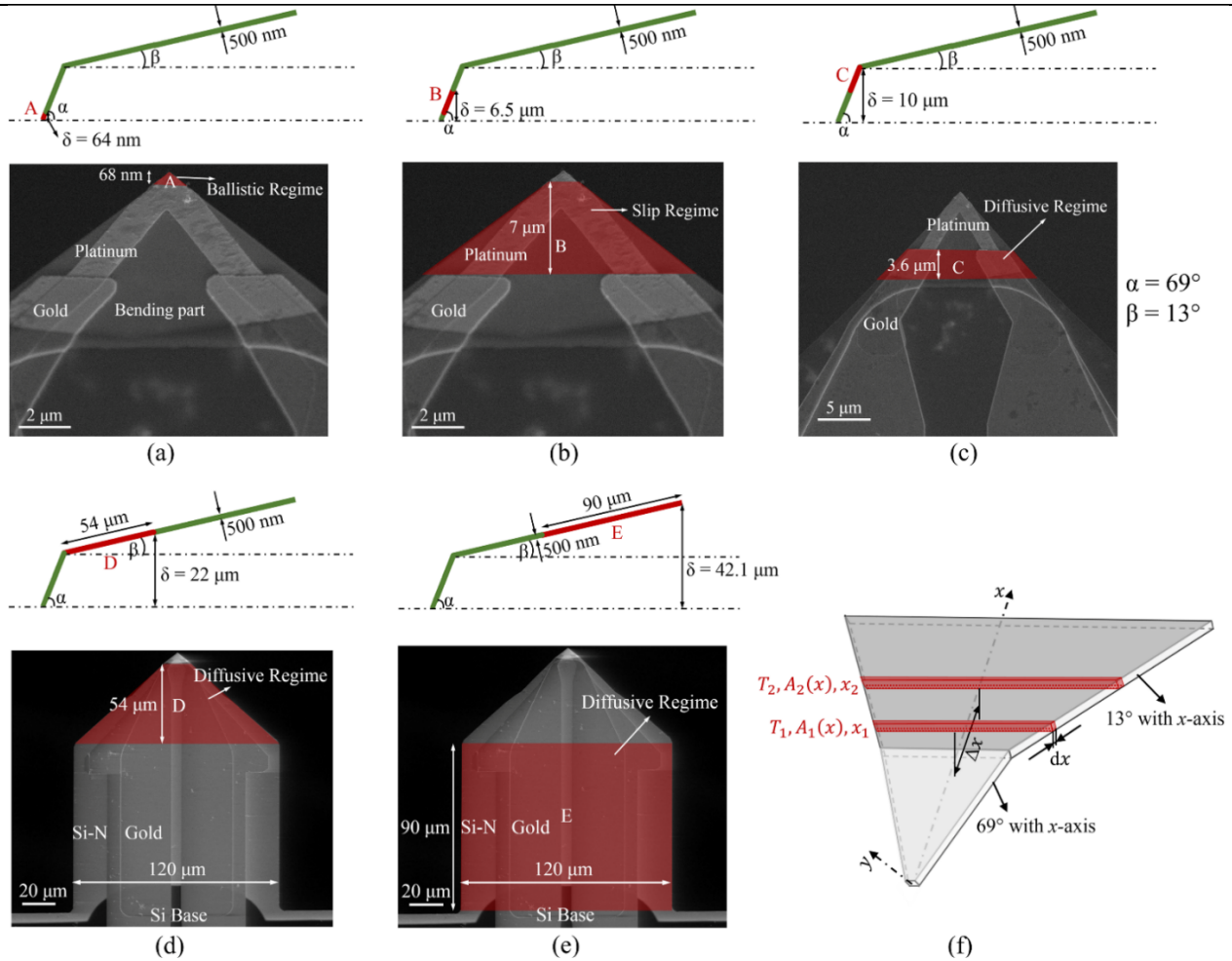

Figure 5.13 (a) – (e) shows the five parts A-E of the probe, each having different dimensions, materials and air conduction regimes. The probe with 69° and 13° oriented components as used in the coordinates of the calculation, and (f) model used for calculating the heat flow thermal resistance through the probe.

To generate the lumped model of the probe, each part of the probe is represented by three components: probe-sample thermal resistance due to air conduction (R_i^{air}), resistance to heat flow along the cantilever ($R_i^{material}$) and resistance due to air convection (R_i^{conv}). Figure 5.14 shows the resistance network of the probe in contact with the gold scanning target when the JN noise device is heated up by large heaters, ensuring that the temperature beneath the whole probe is uniform and accurately known. Heat capacities can be neglected from the network as the model only considers steady-state interactions. For convenience of modelling, temperature is represented by electric potential: with ground being room temperature T_∞, positive voltages represent a temperature above ambient, as represented by U_{th}. The five individual probe parts have been highlighted in Figure 5.14 as A to E. Values of all components used, associated with equations involved, are shown in Table 5.2.

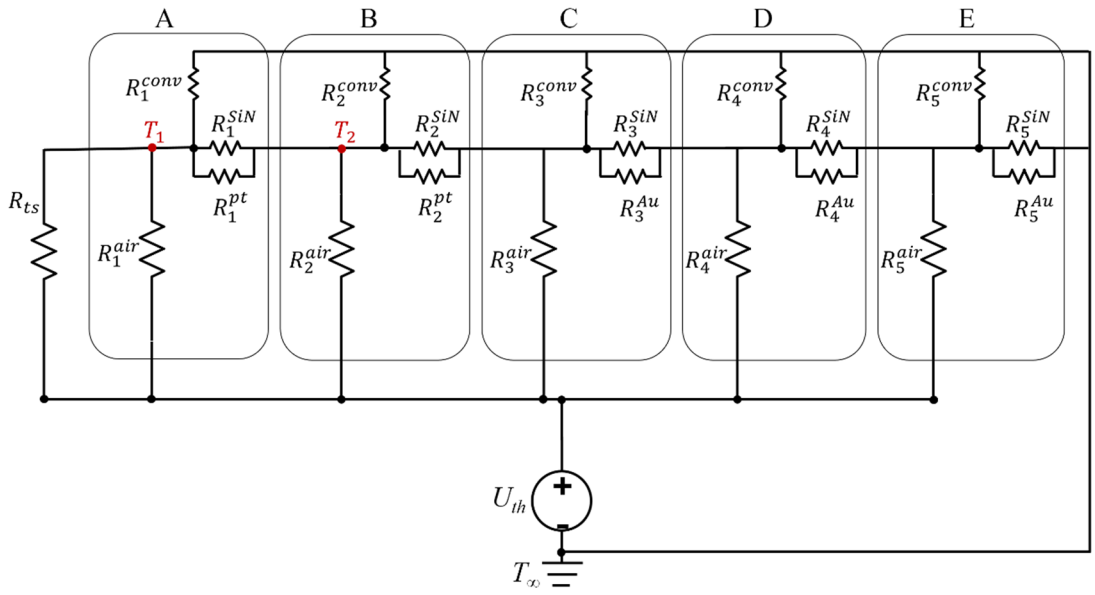

Figure 5.14 Thermal resistance network for the lumped model of the probe contacting a heated surface. The voltage source represents the temperature of JN device, in this instance providing a uniform temperature beneath the probe cantilever.

Table 5.2 Values of each thermal resistor used in the lump-heat-capacity system

Thermal resistance	Expression	Value (K/W)	Equation involved
Air conduction with sample part			
A	R_1^{air}	6.383×10^9	eq. 5.15
B	R_2^{air}	6.99×10^6	eq. 5.15
C	R_3^{air}	1.192×10^7	eq. 5.15
D	R_4^{air}	1.404×10^5	eq. 5.15
E	R_5^{air}	9.819×10^4	eq. 5.15
Heat flow for SiN_x in part			
A	R_1^{SiN}	3.046×10^4	eq. 5.20
B	R_2^{SiN}	1.468×10^5	eq. 5.20
C	R_3^{SiN}	1.492×10^4	eq. 5.20
D	R_4^{SiN}	1.732×10^5	eq. 5.20
E	R_5^{SiN}	1.462×10^5	eq. 5.20
Heat flow for Pt/Au in part			
A	R_1^{Pt}	3.14×10^5	eq. 5.20
B	R_2^{Pt}	3.15×10^6	eq. 5.20
C	R_3^{Au}	3.22×10^4	eq. 5.20
D	R_4^{Au}	3.31×10^4	eq. 5.20
E	R_5^{Au}	2.37×10^4	eq. 5.20
Air convection for part			
A	R_1^{conv}	8.94×10^{12}	eq. 5.21
B	R_2^{conv}	3.91×10^9	eq. 5.21
C	R_3^{conv}	1.92×10^9	eq. 5.21
D	R_4^{conv}	2.61×10^7	eq. 5.21
E	R_5^{conv}	9.26×10^6	eq. 5.21

Probe measurement of temperature T is an interpretation of an electrical signal resulting from the temperature at the platinum tip resistor. Therefore, both parts of the platinum resistor have to be combined when interpreting the results of the model. In the model, there is a small portion of the resistor in the ballistic air conduction regime (T_1 in Figure 5.14). The length of region A at the direction of electrical current is 1/600 of whole length of platinum resistor. Therefore, region A is responsible for less than 1/1000 of the total resistance

after considering the correction factor of corner effect for the resistor, which is 0.56 for a straight corner and will be smaller for an acute angle [206]. This indicates that T_1 can be neglected when calculating the average temperature of the platinum sensor. Therefore, T_2 alone is used as the probe temperature. Figure 5.15 shows a plot comparing the probe temperature experimentally obtained by measuring the scanning target of JN device and its temperature calculated using the lumped system model. In the plot, U_{th} is the actual temperature of JN device and ΔT_p is the probe temperature relative to ambient. The experimental SThM temperature was obtained from the output of the lock-in amplifier as described in section 5.2.2 and the modelled probe temperature taken as T_2 from lumped system. The error bars were calculated as one standard deviation of the averaged value for 10 measurements. Uncertainties in the calibration come from various sources, including the uncertainty of JN device temperature measurement, R_{ts} fitting and the TCR of the probe, among these the former two dominate. Uncertainty of JN device has been regarded as a constant (± 0.73 K) as determined in previous work [88]. The data fitting will generate a maximum 9 % variation on the R_{ts}, which will provides a 13 % variation in calculated device temperature as interpreted from the measured probe temperature.

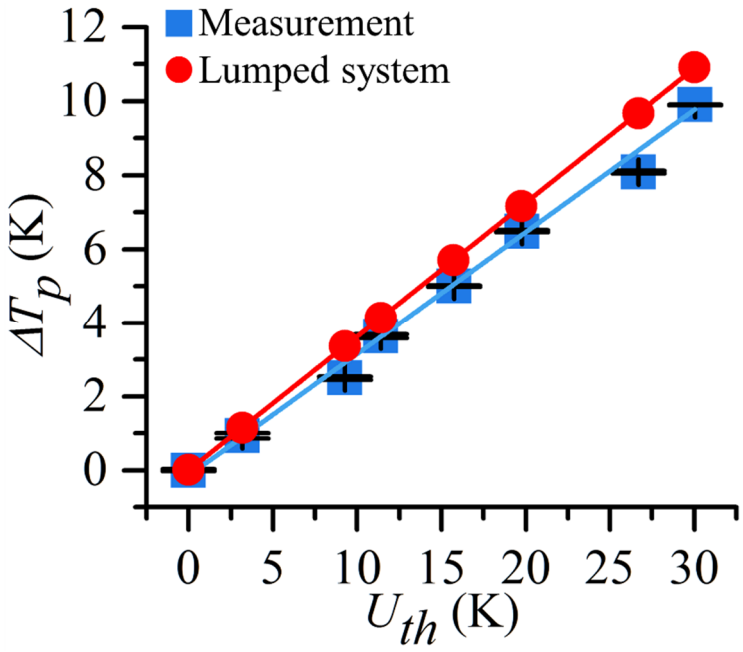

Figure 5.15 Probe temperature obtained from the thermal scan experiment (blue squares) and from the lumped system model (red circles).

In order to quantify the measurement of samples with heating regions smaller than 16 μm (which is related to minimum size attainable in small heater mode), for example heated nanowires, additional information has to be included in the lumped system model. The tip-sample thermal resistance, which will differ with materials in contact, must be reconsidered and determined [106,121,131]. In addition, the lumped system would have to be modified to account for the dimensions of the actual heated region, which dictates the effect of thermal resistance due to air conduction to and from the probe. This can be achieved by manipulating the thermal resistance of air conduction in the lumped system. One extreme condition is that the heated region has negligible area, in which case, there will be no air conduction effect on the probe. Figure 5.16 shows the comparison of probe temperature between the 16 μm heated region and the extreme condition. It can be concluded that for a sample with heated region smaller than 16 μm, there will be less than 10 % variation from the probe calibrated by small heater mode.

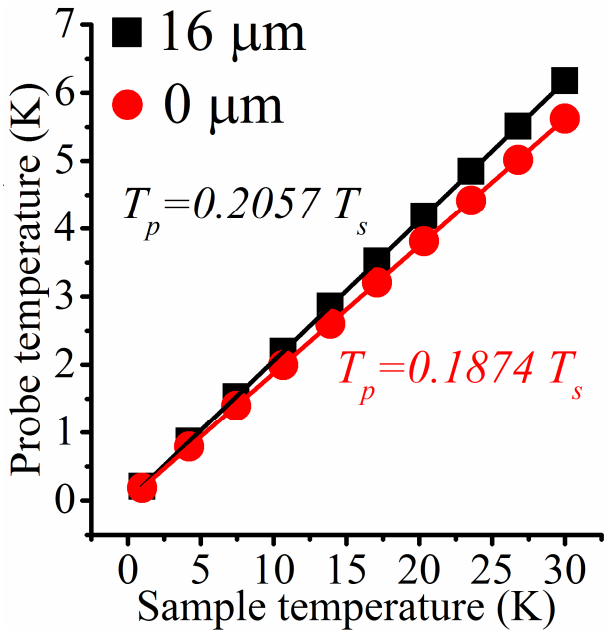

Figure 5.16 Probe temperature versus the sample temperature with a heated region of 16 µm (black squares) and 0 as an extreme condition (red circles). Both the probe temperature and the sample temperature represent the temperature higher than that of the ambient.

Thermal resistance of the whole cantilever can also be extracted from the model as being 2.26 × 10^5 K/W. This value is of the same order as that determined by Assy *et al.* as 5.2 × 10^5 K/W, who measured it for a self-heated probe under vacuum [121]. This is approximately twice the size of the value determined in this chapter, although the probe geometry and materials used are the same in both cases. This difference can be explained as being due to the effect of the two NiCr thin film resistors in series with the platinum tip. In Assy's work, the power on the platinum tip was considered to be 2/3 of the power applied to the probe based on the assumption that the resistance of the platinum tip is 2/3 of the resistance of the whole probe. However, this ratio can vary considerably between probe batches. In addition, the NiCr resistors would also experience Joule heating, decreasing the thermal gradient along the cantilever, which will manifest as a larger cantilever thermal resistance. The NiCr resistors are not present in the probes used for this work, eliminating these limitations here.

The thermal resistance network can be easily converted for use in modelling active probes by substituting the voltage (temperature) source with a current (heating power) source. The relationship between an active probe and sample thermal properties can thus be built to deeply understand heat transfer when measuring complex samples.

5.4 Conclusion

We have designed and fabricated a novel Johnson-noise-based calibration device for the calibration and study of SThM probes. The device provides a known temperature sample with a highly uniform distribution across a suspended membrane, enabling the whole system to be regarded as an isothermal system. A 1D heat transfer equation was built for a SThM probe interacting with the device, which, combined with a FEA model, has been used to characterize the thermal interactions between the probe and sample. This model strongly suggests a larger contact radius than predicted by the frequently used DMT model. Instead, it indicates a contact with the same radius as the apex of the probe. This is the first time this characteristic has been determined in a simple experiment carried out under ambient conditions. Finally, this information was used in the construction of a lumped model considering both the shape and the complex materials of the probe. This model yields a probe thermal resistance in close agreement with that determined by other researchers.

6

ANALYSIS OF HEAT TRANSFER IN THIN FILMS WITH FINITE DIMENSIONS

In Chapter 4, a novel fabrication process, employing pattern transfer to create topography-free samples was described. These samples permitted SThM images to be generated without topographic artifacts. Analysis of the data obtained from these samples demonstrated that the (active probe) thermal signal varied as a function of feature width. This was easily described using the ratio of measured signal and the signal from large features, which could be considered to have infinite extent. As concluded in Chapter 4, this phenomenon could be explained by the varying contact area between the probe and the gold wire/SiN_x background. Recognising that the differing thermal conductivity of materials dominates the variations seen in SThM thermal images, another question arises – if the probe is fully in contact with the gold wire, do its other characteristics e.g. length or width have any impact on the signal measured?

In this chapter, the design and fabrication of topography-free samples with more advanced patterns, aimed at investigating feature dimensional effect on thermal resistance, are described. Similar to that in Chapter 4, the SThM probe was operated in active mode using DC voltage. In addition, knowledge of the measurement instrument described in Chapter 3 will be

employed in an attempt to quantify the scanning results. The complex geometry of the tip-sample interaction necessitates a relatively advanced model to assist interpretation of the results. However, to avoid the challenges associated with solving 2D heat transfer equations, a new model, in which a gold wire can be regarded as a fin, will be described. The thermal resistance of a gold wire can then be extracted from the new model as a function of its dimensions. Using this information, the temperature of the probe can be calculated by employing an extension of the lumped-system model for active probes built in Chapter 5. A comparison between probe temperature predicted by the model and that obtained experimentally shows the validity of this approach, as well as the effectiveness of this method in determining SThM behaviour. Finally, the new heat transfer model is extended to consider the effect of sample feature shape and then used to analyze experimental data, obtaining the probe-sample effective contact size.

6.1 Motivations

As discussed in previous chapters, SThM can be used in active mode for measuring the thermal conductivity of materials. This can be seen by rewriting eq. 2.6 as

$$T_p = \frac{PR_{cant}(R_s+R_c(R_{int},R_t,R_p))}{R_{cant}+R_s+R_c(R_{int},R_t,R_p)} + T_\infty \qquad \text{eq. 6.1}$$

It can be stated that, at steady state, the Joule heating power of the probe (P) is equal to the heat loss from the thermal sensor (which is also acting as the heater) to the surrounding environment, including the sample, the air and the cantilever base. Thermal resistance of the tip (R_t), the cantilever (R_{cant}) and the environment in the vicinity of the contact area (R_p) are independent of the sample if the probe and scan conditions remain unchanged. R_{int} is the interfacial thermal resistance resulting from the solid-solid contact, which will vary according to the materials in contact. As contact diameter for our SThM tip on hard materials was determined in Chapter 5 to be the same diameter as

the curvature of probe's tip, R_{int} will remain constant for patterns of the same material. With power and ambient temperature (T_∞) considered to be constant, probe temperature, T_p, will only vary with the thermal spreading resistance R_s of the sample. Therefore, quantification of sample thermal conductivity may be determined from R_s.

Whether the probe is driven using an AC or DC signal, the process of determining R_s is similar: build a thermal resistance network based on heat transfer mechanisms between the probe and sample, define the value of each thermal element through calculation or experiment and finally extract thermal conductivity from R_s. However, this final step is not trivial and warrants further consideration. Recent work on SThM measurement of graphene demonstrates how thermal conductivity can be extracted from R_s. In this work, Menges *et al*. [127] used a self-heated doped silicon probe to successfully determine the thermal conductivity of graphene (k_{grap}) on different substrates. This was achieved by treating the tip-sample thermal interaction as a nanoscopic constriction in contact with a semi-infinite surface. In this case, thermal spreading resistance within the graphene film (R_{grap}) could be expressed using a 1D equation in spherical coordinates

$$R_{grap} = \frac{1}{4b_c k_{grap}}\left(1 - \frac{2b_c}{\pi t_{grap}} log\left[\frac{2}{1+\frac{k_{grap}}{k_{sub}}}\right]\right) \qquad \text{eq. 6.2}$$

where b_c, t_{grap}, and k_{sub} represent the contact radius between the probe and the graphene film, thickness of the graphene and thermal conductivity of the substrate. The lateral dimensions of the graphene sheet are not considered in eq. 6.2, as only film thickness needs to be considered in such semi-infinite, thin structures. The same strategy has also been adopted to characterize hafnium oxide (HfO_2) and SiO_2 thin films [128]. Beyond simple thin films, Puyoo *et al*. [106] utilized the SThM 3ω method to carry out accurate measurement of individual silicon nanowires. With the determination of nanowire thermal resistance, R_{NW}, thermal conductivity (k_{NW}) was extracted from

$$R_{NW} = \frac{L_{NW}}{k_{NW} A_{NW}} \quad \text{eq. 6.3}$$

where L_{NW} and A_{NW} represent the length and cross-section area respectively. Characterization of carbon nanotubes shares similarities with nanowires. Shi *et al*. [101] investigated carbon nanotubes by employing a heat diffusive equation

$$k_{cnt} A_{cnt} \frac{\partial^2 T_{cnt}}{\partial x^2} + \frac{Q_{cnt}}{L_{cnt}} - g_{cnt}(T_{cnt} - T_\infty) = \rho_{cnt} C_{cnt} A_{cnt} \frac{\partial T_{cnt}}{\partial t} \quad \text{eq. 6.4}$$

where T_{cnt}, A_{cnt}, L_{cnt}, Q_{cnt}, ρ_{cnt}, and C_{cnt} are local temperature, cross-section area, length, electrical heating rate, density and specific heat of the carbon nanotube and g_{cnt} is the nanotube-substrate thermal conductance per unit length. In both cases, dimensions of the objects being interrogated played an important role in the measured thermal spreading resistance due to the similarity between their dimensions and the tip-sample contact size. Recently, research on suspended graphene disks revealed that it was necessary to consider both their dimensions and the contact size of the heat source [207,208] when the sample was in an intermediate regime, i.e. where the sample was larger than the probe contact size but too small to be considered as infinite. Hwang *et al*. [207] derived the thermal spreading resistance of graphene disks in spherical coordinates, incorporating both the thermal diffusion model of a nanoscopic contact and the shape of the disks. In their work, the disks were analyzed as two serial components, one from the contact point to the edge of the suspended region and the other from that edge to the substrate. These were written as

$$R_{s-sus} = \frac{\ln\left(\frac{D}{2}\right) - \ln(b_c)}{2\pi t_{grap} k_{grap}} \quad \text{eq. 6.5}$$

$$R_{s-sup} = \frac{1}{2\pi\left(\frac{D}{2}\right)\sqrt{g_{grap} t_{grap} k_{sub}}} \frac{K_0(Z_{D/2})}{K_1(Z_{D/2})} \quad \text{eq. 6.6}$$

where D is the diameter of the disk, g_{grap} is the total interface thermal conductance per unit area between graphene and substrate as well as the

sounding air, and $Z_{D/2} = \left(\frac{g}{k_{sub} t_{grap}}\right)^{\frac{1}{2}} (D/2)$. An alternative approach would be to employ 1D heat transfer equations in the same form as used for semi-infinite and 1D structures as these permit the inclusion of feature dimensions, contact size, and substrate. However, validation of the 1D thermal diffusion model reaches its limits when there is an inconsistency between the thermal diffusion profile of the nanoscopic contact and the finite shape of the features.

So far, little attention has been paid to thermal conductivity measurement of thin film features with slightly more complex geometries, for example rectangles. Rectangular thin films have shown their applications in several areas including VLSI interconnects [209], graphene nanoribbons [210,211] and research into nanoscale heat transfer due to ease of fabrication for this geometry [199]. Thermal spreading resistance of rectangles has been discussed and summarized by Yovanovich [212,213], however, cases in their discussion either consider rectangular heat sources on a half-space or the shape of heat source being the same as the substrate. One reason for the complexity is the ambiguity of heat transfer mechanisms between the probe and the sample, including the resolution of dominant heat paths and probe-sample contact size. Recent work, including that presented in this thesis, has progressively determined these parameters, making this a good time to analyze size-dependent thermal resistance as measured by SThM. One complicating factor stems from the complexity of modelling and solving heat transfer problems beyond 1D. Given the lack of an appropriate coordinate system, the 1D heat transfer equation can no longer be considered valid in scenarios with dimensions larger than the contact diameter but too small to be considered infinite. This chapter presents a relatively simple approach to overcoming this problem. Fins are typically used to define an object exchanging heat by both thermal conduction and convection. It is possible to extend this description for use in modelling the thermal interactions between a SThM probe and a thin, structured film. This is achieved by combining a radial and a rectangular fin, allowing “nanoscopic to finite-dimensional”

thermal conduction to be modelled in 1D, making the thermal analysis relatively simple. Finally, experimental results, based around a variation of the topography-free sample described in Chapter 4 will be presented demonstrating the validity of the model.

6.2 Sample Design and Fabrication

6.2.1 Pattern design

A general rule to be followed when designing patterns on a sample being used to evaluate characterization techniques is to minimise the number of uncertainties that need to be determined during the measurement. As discussed above, for a correctly designed and controlled SThM sample and experiment, the only value that will vary is the probe-sample contact resistance R_{int}, which is dependent on the thermal boundary resistance R_b and contact size b_c, and has been mentioned previously in Chapter 2 as

$$R_{int} = \frac{R_b}{\pi b_c^2} \qquad \text{eq. 6.7}$$

It can be assumed that R_b will vary with changes in the material in contact with the tip, and, given that no soft materials are used, b_c will be a constant equal to the probe's tip radius of curvature [214]. This permits us to formulate a list of pattern design rules:

1. The sample surface must consist of materials with widely differing thermal conductivities in order to provide clear thermal contrast;
2. The pattern must be large enough to ensure complete contact between the tip and pattern can be achieved, meaning the smallest dimension of the pattern has to be larger than the tip-sample contact diameter;
3. A sample with variously sized patterns is preferred to permit acquisition of the maximum amount of data in a single experiment.

Following these rules, the patterns shown in Figure 6.1 were designed with three layers on one sample. The green patterns shown in Figure 6.1 (a) was

used as frames for classifying the gold wires according to their width, and had no special requirement on their thickness. The blue and red pattern were used for scanning and designed as the same thickness.

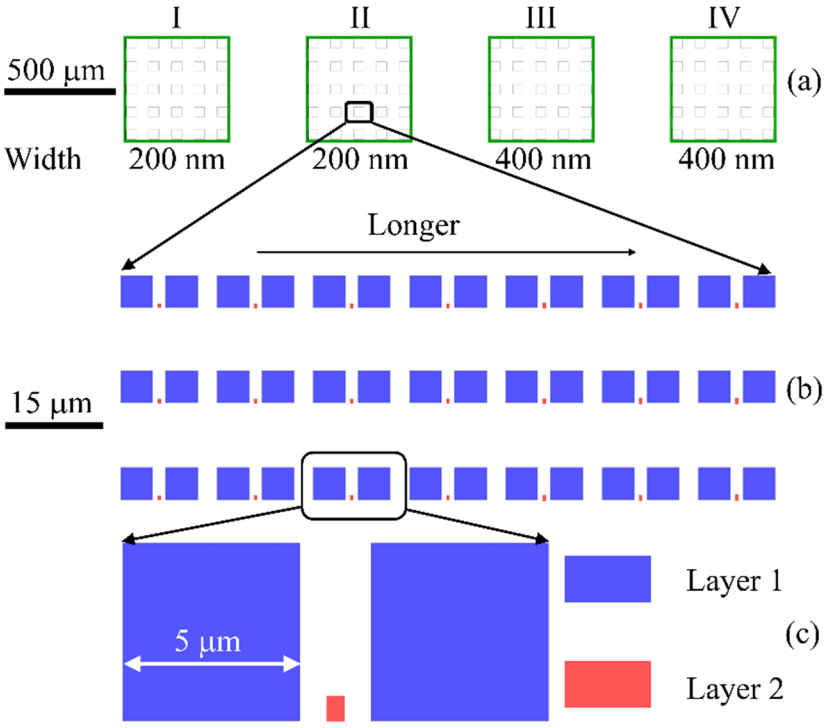

Figure 6.1 Patterns designed to investigate the size dependence of thermal conductivity measurements. (a) shows four blocks, in which contains gold wires in the same width but different length, (b) shows an enlarged view of one block, demonstrating the pattern arrangement with constant feature width but variable length (increasing left to right), and (c) shows an enlarged image demonstrating the detail of a single pattern.

Following the procedure described for the topography-free samples in Chapter 4, patterns for scanning were fabricated in two steps. Step one was for Layer 1, which had large, easily located features called 'pads' with a 1 µm gap between each pair. Inside this gap layer 2 was located (as the second step), containing the real scanning target. All patterns were still made from gold, which showed high thermal contrast with the background SiN_x as described in Chapter 4. Gold wires were designed with two widths: 200 nm and 400 nm, permitting complete contact between the tip and pattern (diameter of the

probe contact area is ~ 100 nm as discussed previously). These were located in blocks (I) and (III) respectively, with duplicates (II) and (IV) used as backup (shown in Figure 6.1 (a)) in case of low yield. The length of these gold wires was varied from 400 nm to 2500 nm in 100 nm increments until 1000 nm length, after which the increment was 500 nm until 2500 nm length.

6.2.2 Sample fabrication

The fabrication process followed that described in Chapter 4 with some minor changes. The gold film thickness was increased from 20 nm to 50 nm. This was done due to reports in the literature that 50 nm thick gold films on SiN_x deposited under similar conditions to this work, showed good agreement between thermal conductivity measured by frequency-domain thermoreflectance (FDTR) and the the Wiedemann-Franz law [215]. The same work also observed that 22 nm thick gold films exhibited a 40 % discrepancy between these two methods, adding uncertainty to any value used in this work.

This variation in gold thickness necessitated a change in the electron beam resist used from 2.5 % 2010 PMMA (38 nm thick at 5000 rpm) with 2.5 % 2041 PMMA (38 nm thick at 5000 rpm) to 4 % 2010 PMMA (110 nm thick at 5000 rpm) with 2.5 % 2041 PMMA for a successful liftoff. As the electron dose was maintained at 650 $\mu C/cm^2$, the concentration of developer was increased from 1: 3 to 1: 2.5 MIBK: IPA to ensure clear development.

In addition to the metallisation, SiN_x deposition was also optimized. The original 400 nm low stress SiN_x deposited by ICP-CVD did not function well when fabricating the new sample. Specifically, after the release etch, the entire SiN_x film exhibited wrinkles (as shown by white arrows in Figure 6.2 (a)), a problem that was not solved by increasing the thickness. As shown in Figure 6.2 (b), even with a SiN_x film thickness of 800 nm the problem remained. It was initially suspected these wrinkles were caused by poor adhesion between the GaAs and the SiN_x surface due to oxidation of the GaAs substrate. However,

this was proved false when a chemical 'de-ox' clean using HCl and HF [216] failed to remedy the problem. Next, attention was turned to the quality of the SiN_x. As detailed by Zhou *et al*. [181], ICP-CVD is able to deposit high-quality SiN_x films, however they do contain a proportion of H and O leading to a compositional description of $SiN_xO_yH_z$. A low content of H and O is necessary for high SiN_x corrosion resistance in an acid environment. Several factors can impact on the H and O content of the deposited film, including the pressure, RF power, and chamber contamination [217]. In an attempt to improve the SiN_x quality, the ICP-CVD was replaced in the process by an advanced ICP380 deposition tool newly available in the laboratory. The recipe employed SiH_4 /N_2 9.5 sccm /7.3 sccm with 250 Watt ICP power at 30 °C and was able to reach a 10.7 nm/min deposition rate. Figure 6.3 shows the surface of a completed sample prepared using this new tool and it can be clearly seen that the wrinkles have been eliminated. Therefore, this new fabrication procedure was followed for all subsequent samples.

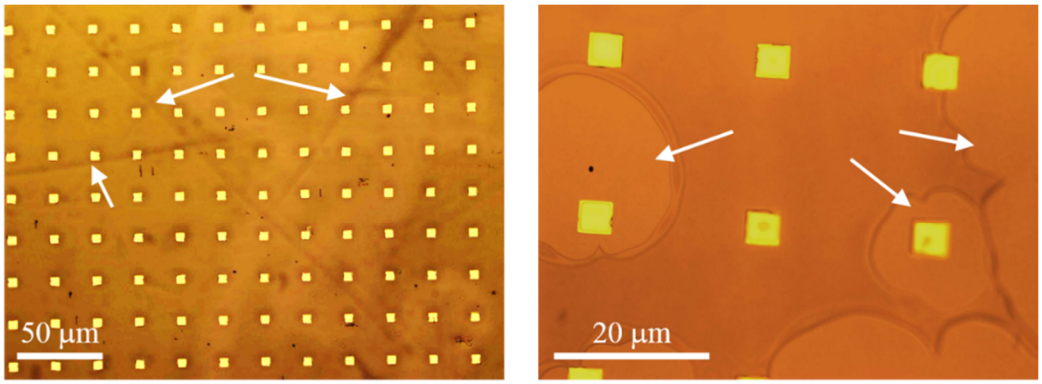

Figure 6.2 Optical image of the sample surface after release for (a) 400 nm and (b) 800 nm thick low stress ICP-CVD SiN_x. A simple pattern was employed to permit rapid process optimization.

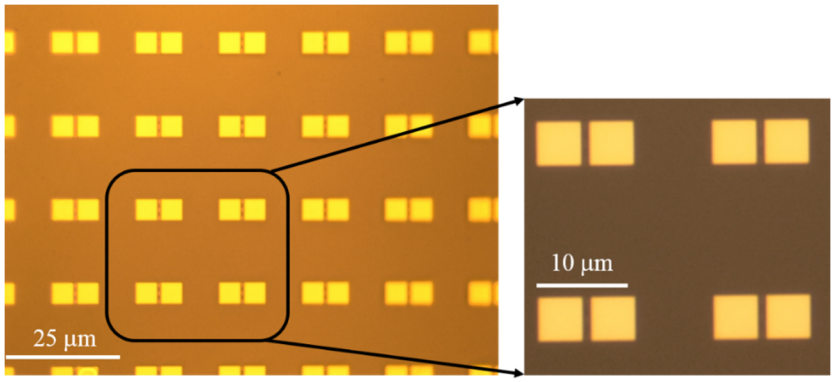

Figure 6.3 Sample surface after release with 500 nm thick low stress ICP380 SiN_x film observed by optical microscopy.

6.3 Experimental Methods

Topography-free samples were investigated in Chapter 4 using a probe operated in DC active mode. Although a value defined as "*Ratio*" allowed the gold wires to be described somewhat quantitatively, this was too basic an analysis to deeply understand the heat transfer mechanisms at play in thin films with finite extent. In order to achieve this the true probe temperature must be accurately known as interpreted from its electrical response.

The probe was operated with constant power as part of a Wheatstone bridge. Figure 6.4 shows the schematic layout of the circuit. The whole circuit was battery driven in order to eliminate AC noise from any power supply. The combination of a current regulator diode, J511, with a voltage reference, LM4040AIZ5.0, generated a stable 5.0 V voltage. A voltage ranging from 0 – 5.0 V (U_b) was generated by opamp A1 associated with a 10 kΩ adjustable resistor and this used as one power supply to the Wheatstone bridge. Meanwhile, an inverted voltage of U_b was generated by A2 ($-U_b$) and used as the other power supply. Leg 1 and Leg 2 marked in red compose the bridge: the probe was connected in a 4-terminal configuration, with R_1 and R_2 forming one leg, and R_4, R_5, together with R_m forming the other. R_{ref} provided a negative voltage to leg 2 equal to that of leg 1. Any voltage difference across the bridge was amplified by an instrumentation amplifier (A4) with gain set by R_g. R_1 and

R_2 were selected to be 2200 Ω, 10 times larger than the resistance of the probe, in order to maintain constant power. Assuming a typical probe resistance of 220 Ω, and a maximum voltage supply of 10V, it can be calculated that a 25 K variation in probe temperature will only cause a 1 % power disturbance. In practical work, the voltage employed is 5 V and any temperature variation caused by changes in sample thermal resistance is much smaller than 25 K, meaning that variation in power supply on the probe will be smaller than 0.25 %.

Ultimately, the output voltage from this circuit was recorded as a thermal signal. Therefore, in order to obtain the temperature of probe, the thermal signal had to be converted from sensor resistance. There are a number of obstacles to achieving this. First, the experiment requires a probe working in active mode, meaning that its resistance has already been changed as the result of Joule heating. However, probe 'base' resistance is typically only measured *ex situ* by an ohmmeter applying an undefined current. In addition, further measurement uncertainties are associated with R_4, R_5, R_g and R_m. Therefore, it is necessary to find a method to link the thermal signal with probe resistance.

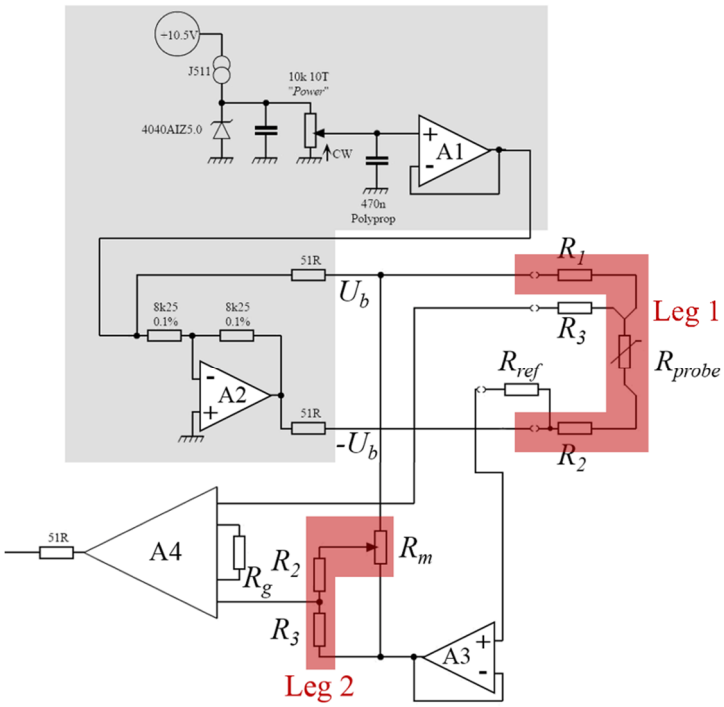

Figure 6.4 The schematic diagram of the circuit used for driving the probe working in either the passive or the active mode.

The strategy employed can be named the "resistor replacement method", which requires a range of precise resistors with values close to that of the probe. This method does not require components with exact values expect for R_1 and R_2. The procedure is listed below:

1. A probe was selected and its resistance roughly measured using an ohmmeter, it was then connected to the circuit and mounted on the AFM;
2. As described in Chapter 3, probe self-heating is detectable only when the current density exceeds 3×10^9 A/m^2. Therefore, a current lower than 0.1mA (equating or less than 1.5×10^9 A/m^2 current density at the tip resistor) was passed through the probe. The circuit output was then balanced to 0 V by adjusting R_m;
3. The probe was replaced with a precise resistor with 0.1 % tolerance. If the output was still 0 V, this resistor could be considered to have the same resistance as the probe at ambient temperature (R_0). If the

output was not 0 V, a different value of resistor was selected and step 3 repeated;

4. Steps 2 and 3 were repeated, and this time increasing the current to determine the resistance of the Joule heated probe (R_p);
5. The current through the heated probe was measured using an Ammeter (I);
6. To remove any ambiguity in the gain and resistance of Leg 2, the product of supply voltage and gain was used. When replacing the probe with a precise resistor (R_p), the output voltage can be written as:

$$UA\left(\frac{R_p}{R_1+R_2+R_p}-\frac{R_5}{R_4+R_5+R_m}\right)=V_1 \qquad \text{eq. 6.8}$$

where U is the voltage applied to the bridge, A is the gain, and V_1 is the output of the circuit when the probe is Joule heated. By replacing R_p with a different precise resistor with a slightly different value, R_p'. the output voltage changes to:

$$UA\left(\frac{R_p'}{R_1+R_2+R_p'}-\frac{R_5}{R_4+R_5+R_m}\right)=V_2 \qquad \text{eq. 6.9}$$

The product voltage and gain (UA) can be defined by substituting $\frac{R_5}{R_4+R_5+R_m}$ in eq. 6.8 by that deduced from eq. 6.9, eliminating any inaccuracy associated with Leg 2.

Based on procedures above, the probe had a resistance at ambient temperature (R_o) of 156.1 Ω, and under Joule heating using 0.8 mA R_p was 159.1 Ω. Probe TCR has been previously determined as 0.000961 ± 0.0000106 K^{-1}, therefore the temperature of the probe heated by 0.8 mA is 19.81 K above ambient. Joule heating power is $P = I^2R = (0.8 \times 10^{-3})^2 \times 159.1 = 1.02 \times 10^{-4}$ W, and UA is 1821.

6.4 Model for Nanoscopic to Finite-dimensional Contact Heat Transfer

Calculation of thermal spreading resistance at the probe-sample contact is always regarded as a point contacting a half-space (defined as infinity in *x* and *y* and finitude in *z*). When the film is 10 times larger in thickness than the contact radius (b_c), thermal transport within the half space is modelled as hemispherical conduction in spherical coordinates and thermal spreading resistance can be written as [218]

$$R_s = \frac{1}{4kb_c} \qquad \text{eq. 6.10}$$

However, in our situation, the thickness of the gold pad (t) is far from the scenario where eq. 6.10 can be used. Instead, thermal spreading resistance has to be corrected by considering the effect of the substrate [132]

$$R_s = \frac{1}{4kb_c} - \frac{1}{2\pi kt}\log_{10}\left(\frac{2}{1+\frac{k}{k_{sub}}}\right) \qquad \text{eq. 6.11}$$

where k_{sub} is the thermal conductivity of the substrate.

When extending the problem to a finite-dimensional plane, where not only the thickness, but also width and length are too small to be regarded as infinite, the thermal diffusive model for a half-space is no longer valid. Hence, a more complex heat transfer model has to be employed. Figure 6.5 (a) is a schematic showing heat transfer in a gold wire contacted by a Joule heated SThM probe at its centre. This is representative of the gold wires fabricated on the topography-free samples (Chapter 4), with one surface exposed to air and the other five in contact with SiN_x.

If we consider the contact between the SThM probe and the thin film gold wire (the black dot in Figure 6.5 (a)), thermal transport close to the tip can be expressed in spherical coordinates, the same as the half-space model. However, the heat path quickly changes at the interface between the gold wire

and SiN_x substrate in *y* direction, and spherical coordinates are no longer valid. In addition, unlike the superficially similar graphene disk described in the literature [207] which only exchanges heat with substrate at its boundary, there is a constant heat path between the gold wire and the SiN_x substrate through the gold-SiN_x interface, complicating the problem. In summary, the wire presents a system where heat is conducted through a body but is simultaneously lost along its length by thermal conduction into its surroundings. This is similar to the widely described and used conduction-convection for a fin (e.g. see [17]). In this fin model, heat is conducted through the material while being simultaneously dissipated into its surroundings by convection.

One prerequisite for treating an object as a fin is that it should have uniform temperature through its cross section. For our finite-dimensional, nanoscale gold wire in contact with a probe, the contact size is comparable to the thickness of wire. Therefore, it can be assumed that there is no thermal gradient within the cross section across *O-O'* (Figure 6.5 (b)). In addition, heat loss from the interfaces with air and SiN_x, will be far less than conduction within the gold wire, resulting in a Biot number much less than 0.1 (< 0.01 for our gold wires). This allows us to consider the gold wire as two joined fins: a radial fin from the contact point to the boundary of the *y* direction (marked as I in Figure 6.5 (a)) and a straight fin from the boundary of the radial fin to the boundary of the *x* direction (marked as II in Figure 6.5 (a)). Convection in an actual fin is considered using an "*h*" value with units of "W/m^2K", which represents the thermal conductance per unit area resulting from air convection. Therefore, in order to employ a fin model to describe probe-wire thermal interactions, heat conduction through both the interface into the SiN_x substrate as well as the air has to be quantified with "*h*" values. Then the two fins will be analyzed individually and combined together.

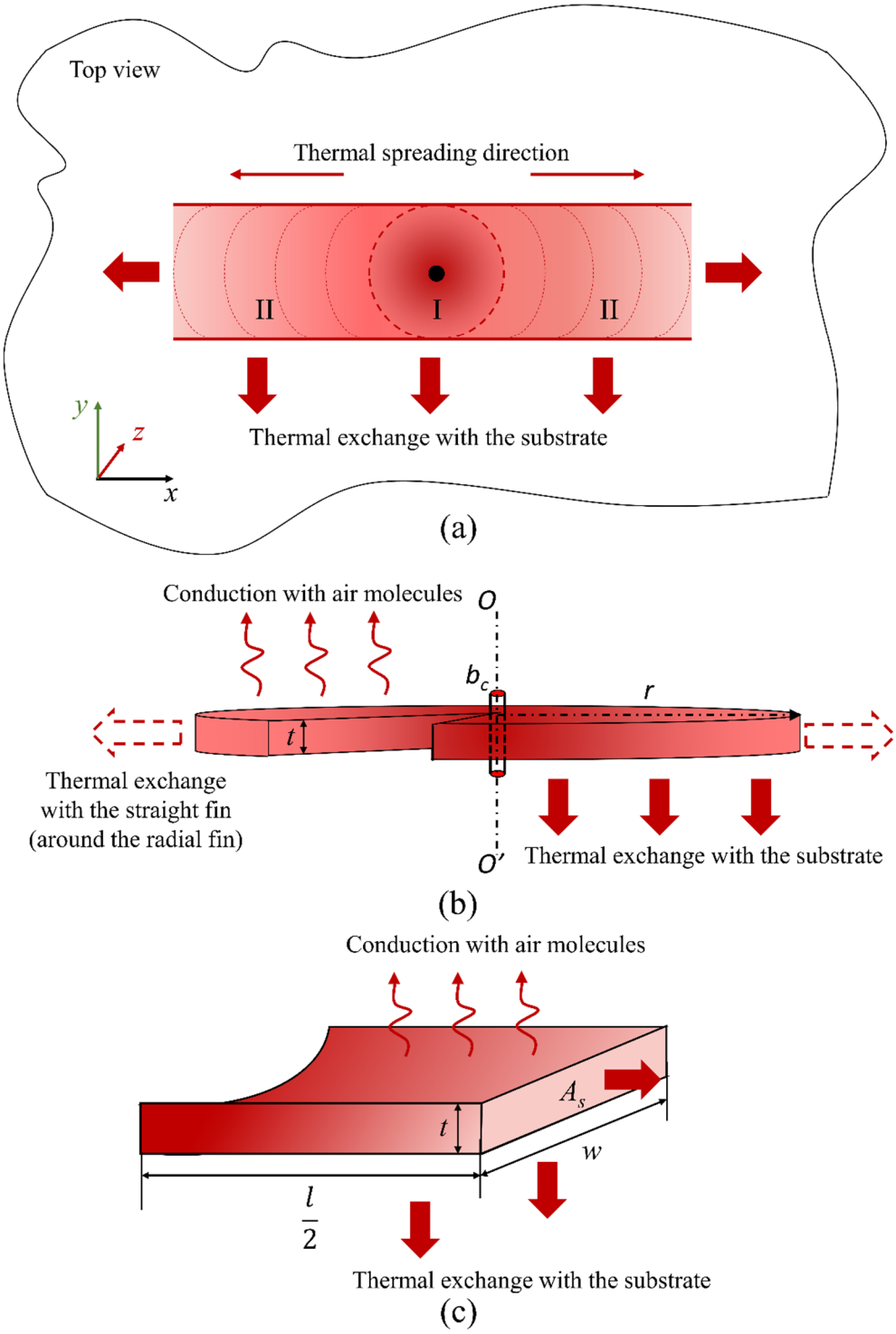

Figure 6.5 Heat transfer in finite-dimension gold film. (a) top view of the film on a substrate that is regarded as bulk, (b) heat transfer mechanisms in spherical coordinates of a radial fin, the diameter of which equals to the width of gold wire, and (c) heat transfer mechanisms in a plane wall connected to the radial fin.

Figure 6.5 (b) illustrates heat transfer of a radial fin in spherical coordinates. In this scenario, heat spreads radially from the contact point between the probe and the gold wire and the heat transfer equation can be expressed mathematically as

$$-kA\frac{dT}{dr}\Big|_r = -kA\frac{dT}{dr}\Big|_{r+dr} + h_a A_t(T - T_\infty) + h_s A_b(T - T_\infty) \qquad \text{eq. 6.12}$$

where k is the thermal conductivity of the gold wire, $A = 2\pi rt$ is the cross-section area at position r, $A_t = A_b = 2\pi r \times dr$ is the elemental area of the top and bottom surface respectively, h_a is the thermal conductance per unit area between the gold wire and the surrounding gas molecules which is taken as 1×10^5 W/m^{2}K from the work of Chen *et al*. [208], and h_s is the equivalent thermal conductance per unit area between the gold wire and the substrate considering both the heat conduction through the interface and thermal diffusion within the substrate. The equation can be rewritten by substituting all areas by their expressions

$$\frac{r\frac{dT}{dr}\Big|_{r+dr} - r\frac{dT}{dr}\Big|_r}{dr} - \frac{h_a r}{kt}(T - T_\infty) - \frac{h_s r}{kt}(T - T_\infty) = 0 \qquad \text{eq. 6.13}$$

At the limit where dr is infinitely close to zero, the equation becomes

$$r^2\frac{d^2T}{dr^2} + r\frac{dT}{dr} - \frac{hr^2}{kt}(T - T_\infty) = 0 \qquad \text{eq. 6.14}$$

where $h = h_a + h_s$. To simplify the calculation, the dimensionless expression$\theta = \frac{T - T_\infty}{T_w - T_\infty}$, where T_∞ and T_w represents the temperature of contact area and the ambient respectively, is used to substitute T, giving

$$r^2\frac{d^2\theta}{dr^2} + r\frac{d\theta}{dr} - \frac{hr^2}{kt}\theta = 0 \qquad \text{eq. 6.15}$$

Eq. 6.15 can be then solved by being written into a modified Bessel function as

$$\frac{d^2\theta}{dr^2} + \frac{1}{r}\frac{d\theta}{dr} - \frac{h}{kt}\theta = 0 \qquad \text{eq. 6.16}$$

the general solution of which can be written as

$$\theta = C_1 I_0(mr) + C_2 K_0(mr) \qquad \text{eq. 6.17}$$

where $m = \sqrt{\frac{h}{kt}}$ (defined as "m value"), I_0 and K_0 are zero order modified Bessel functions of the first and second kind respectively, and C_1 and C_2 are integration constants.

Then boundary conditions have to be considered before solving the general solution numerically. At the contact point where $r = R_0$, $T = T_w$, eq. 6.17 is written as

$$1 = C_1 I_0(mR_0) + C_2 K_0(mR_0) \qquad \text{eq. 6.18}$$

At the edge of the radial fin, where $r = R_1$, heat flows into the straight fin and we have

$$h_c A\theta = -kA\frac{d\theta}{dr} \qquad \text{eq. 6.19}$$

where h_c is the equivalent thermal conductance per unit area at the edge of the radial fin, which will be defined later from the thermal resistance of straight fin. Substituting the θ in eq. 6.19 with eq. 6.17 gives

$$h_c A[C_1 I_0(mR_1) + C_2 K_0(mR_1)] = -kA[C_1 m I_1(mR_1) - C_2 m K_1(mR_1)] \qquad \text{eq. 6.20}$$

where I_1 and K_1 are first order modified Bessel functions of first and second kind respectively.

MATLAB was used to solve the Bessel function by simply providing the order and expression to the defined formula "*I = besseli (nu, z)*" and "*K = besselk (nu, z)*". By combining eq. 6.18 and eq. 6.20, C_1 and C_2 can be solved and written as

$$C_1 = \frac{-[K_0(mR_1)h_c - K_1(mR_1)km]}{[I_0(mR_1)K_0(mR_0)h_c - I_0(mR_0)K_0(mR_1)h_c + I_0(mR_0)K_1(mR_1)km + I_1(mR_1)K_0(mR_0)km]}$$

$$C_2 = \frac{[I_0(mR_1)h_c + I_1(mR_1)km]}{[I_0(mR_1)K_0(mR_0)h_c - I_0(mR_0)K_0(mR_1)h_c + I_0(mR_0)K_1(mR_1)km + I_1(mR_1)K_0(mR_0)km]}$$

Finally, thermal resistance of the radial fin can be determined as

$$R_{radial} = \frac{\theta_w}{q_f} \qquad \text{eq. 6.21}$$

where θ_w is the temperature gradient at the contact point, which equals 1 and q_f is the heat transfer rate within the radial fin that can be calculated as

$$q_f = -kA\frac{d\theta}{dr}\Big|_{r=R_0} \qquad \text{eq. 6.22}$$

If follows that

$$q_f = 2\pi k R_0 tm[C_2K_1(mR_0) - C_1I_1(mR_0)] \qquad \text{eq. 6.23}$$

As discussed above, equivalent thermal conductance per unit area at the edge of radial fin (h_c) has to be determined by taking into account the thermal resistance of straight fin ($R_{straight}$), which is written as [219]

$$R_{straight} = \frac{1}{\eta_f\left[R_1\frac{l}{2}h_a + (R_1+2t)\frac{l}{2}h_s\right]} \qquad \text{eq. 6.24}$$

where η_f is the fin efficiency as defined by $\eta_f = \tanh(m_sL)/m_sL$, where $L = l/2 + t/2$ is the corrected length of the fin due to the existence of heat exchange with the SiN_x at the end of the straight fin, and $m_s = \sqrt{[h_s(\pi R_1 + 2t) + h_a\pi R_1]/k\pi R_1 t}$. Thus, equivalent thermal conductance per unit area due to the straight fin is

$$h_c = \frac{1}{R_{straight}\frac{A}{2}} \qquad \text{eq. 6. 25}$$

All MATLAB code for solving these equations can be found in Appendix IV at the end of the thesis.

6.5 Experimental Results and Discussion

6.5.1 Determination of equivalent temperature coefficient of the substrate "h_s"

As mentioned above, in order to describe the gold wire as a fin, the contribution of the thermal interfacial resistance combined with the thermal spreading resistance in the SiN_x substrate has to be converted into thermal conductance per unit area, "h_s". A difficulty in determining value stems from the uncertainty of the thermal interfacial resistance between the gold and the SiN_x, as well as the complicated model for calculating the thermal spreading resistance induced by a rectangular heat source on a half-space. Laraoui *et al*. [220] recently proposed a method to achieve this, which is however fully based on the use of a silicon probe and data fitting. Here an alternative, simple approach is used, in which the combined thermal resistance will be considered together by combining eq. 6.11 and a radial fin model built to describe a 5 μm × 5 μm gold pad.

Compared to finite-dimensional features, large gold pads can be regarded as a half-space in the x and y direction. Therefore, the thermal resistance of a gold pad accounting for substrate effects can be deduced from eq. 6.11 as 3.42×10^4 K/W by using k_{Au} = 250 W/mK, k_{SiN} = 10 W/mK, b_c = 50 nm and t = 50 nm.

The same gold pad is modelled by treating it as a radial fin with infinite radius, with the temperature at the end of the fin being ambient. Assumptions described above can then be written as two boundary conditions, which are

At the contact point where $r = R_0$,

$$1 = C_1 I_0(mR_0) + C_2 K_0(mR_0) \qquad \text{eq. 6.26}$$

At the end of the fin where $r \to \infty$

$$0 = C_1 I_0(mr) + C_2 K_0(mr) \qquad \text{eq. 6.27}$$

By solving C_1 and C_2 from the combination of eq. 6.26 and eq. 6.27, thermal resistance of the gold pad can be extracted from eq. 6.21 (Appendix IV.*i*). When thermal resistance equals 3.42×10^4 K/W, h_s is determined as 3.071×10^7 W/m^{2}K. Reassuringly this agrees with the thermal boundary conductance between gold and dielectric materials as obtained by other researchers [215,221–223].

6.5.2 Determination of size effect by both modelling and measurement

I. Thermal interfacial resistance due to probe-sample contact

In order to link thermal resistance calculated from the fin models above to the temperature measured by a SThM probe, thermal interactions between the probe and the sample have to be taken into account. Based on the lumped system network built in Chapter 5, a probe working in active mode interacting with a passive sample can also be modelled in a similar method, where electrical heating power applied on the probe can be described as a current source ($I_{th} = P = 1.02 \times 10^{-4}$ A). For a probe contacting on the SiN_x, a thermal resistance network can be built as shown in Figure 6.6.

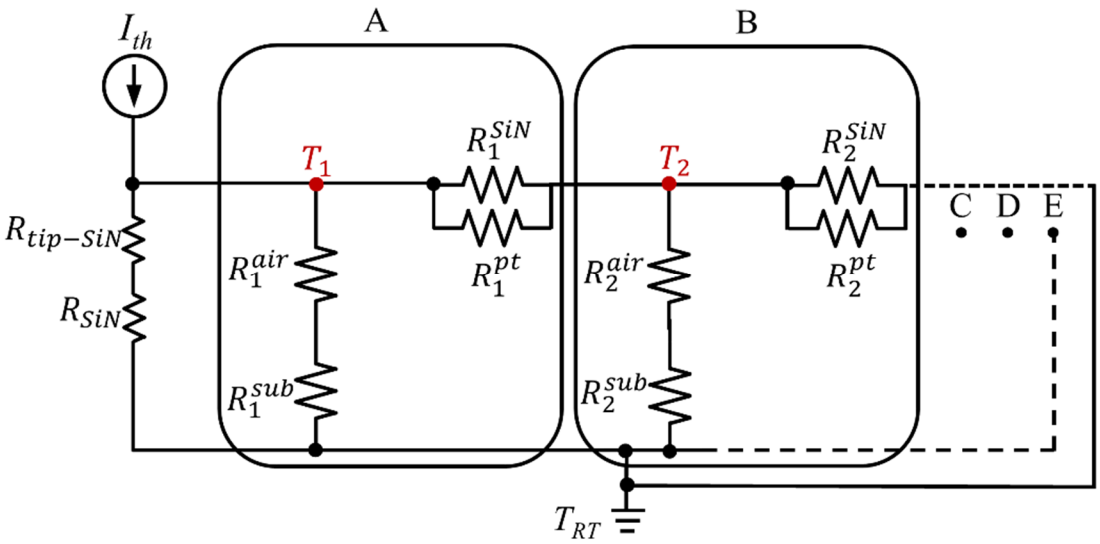

Figure 6.6 Thermal resistance network of a probe in contact with SiN_x. $R_{tip-SiN}$ is the thermal interfacial resistance between the tip and SiN_x, R_{SiN} is thermal spreading resistance of SiN_x substrate, R_i^{SiN} and R_i^{pt} are thermal resistance due to thermal conduction within the probe and R_i^{air} with R_i^{sub} represents the air conduction effect on the sample.

In addition to replacing the voltage source of the network from Chapter 5 with a current source, thermal resistance of the sample has to be included as a resistor in series with thermal interfacial resistance $R_{tip-SiN}$. As the probe-SiN_x contact can be regarded as a nanoscopic to half-space contact, thermal spreading resistance R_{SiN} can therefore be calculated using eq. 6.10 as 5×10^5 K/W. In addition, heat flowing through the air from the probe to the sample will also result in a thermal spreading resistance within the sample, marked as R_i^{sub}, which can be treated as a circular heat source on a half-space [77]. They can also be calculated using eq. 6.10 by setting the radius to the same dimension as each part of probe and leads to a value at least three orders of magnitude lower than R_i^{air}. The ground still represents ambient temperature and the potential for each node is therefore the temperature above ambient (ΔT). As with the passive probe, T_2 will be used as the average temperature of the platinum sensor. By inputting all of the parameters described above and in Chapter 5, ΔT was obtained using NI Multisim (circuit analysis software based on simulation program with integrated circuit emphasis (SPICE)). R_{int-}

$_{SiN}$ was varied until a match was achieved between the simulated results with those obtained through experimentation – for a tip temperature $\Delta T_{tip\text{-}SiN}$ = 17.06 ± 0.012 K, $R_{int\text{-}SiN}$ was determined to be 1.25 × 10^6 K/W.

A similar thermal resistance network was then modelled to describe the probe in contact with a gold pad. This was achieved by replacing R_{SiN} with the $R_{Au\text{-}pad}$ (3.42 × 10^4 K/W), again the simulation was matched to experimental results for $\Delta T_{tip\text{-}Au}$ = 15.82 ± 0.021 K. This revealed a thermal interfacial resistance $R_{int\text{-}Au}$ equal to 0.985 × 10^6 K/W.

By employing eq. 6.7, the thermal boundary resistance between the platinum SThM tip and SiN_x sample was calculated as 9.8175 × 10^{-9} m^2K/W, while that between the platinum tip and the gold wire/pad was 7.736 × 10^{-9} m^2K/W. Both of these values are comparable to values determined in the literature, which put them in the range of 10^{-9} m^2K/W to 10^{-8} m^2K/W [100,121,124]. It should be also noticed that thermal boundary resistance of the metal-dielectric (Pt tip on SiN_x) is larger than that of the metal-metal (Pt tip on gold), which is in agreement with published results focused on the tip-substrate contact [46,77,204,224–226].

II. Comparison between the tip temperature from model and measurement

When a SThM probe is brought into contact with a gold wire, the thermal interfacial resistance $R_{int\text{-}Au}$ will be identical to that for the same probe in contact with a gold pad, given that there is no difference in materials. The thermal resistance of the gold wire can be described by a series of resistors $R_{wire} + R_{Au-SiN} + R_{SiN}$, with R_{wire} representing the thermal spreading resistance within the gold wire, $R_{Au\text{-}SiN}$ the thermal interfacial resistance between the gold wire and SiN_x substrate, and R_{SiN} is the thermal spreading resistance within the SiN_x substrate. These individual resistances cannot easily be distinguished from the single measured value of the gold wire. The thermal resistance network is shown in Figure 6.7. Here, thermal resistance of the wire

is considered as a combination of all three thermal resistors and written as R_{Au}, which is the thermal resistance of the combined fin as described above. With assistance of MATLAB, R_{Au} for 200 nm and 400 nm wide gold wires with length changing from 400 nm to 2500 nm was acquired. Code used for this calculation can be found in Appendix IV.*ii*. These values were then used in the network shown in Figure 6.7, from which the ΔT corresponding to different dimensions of gold wires were acquired.

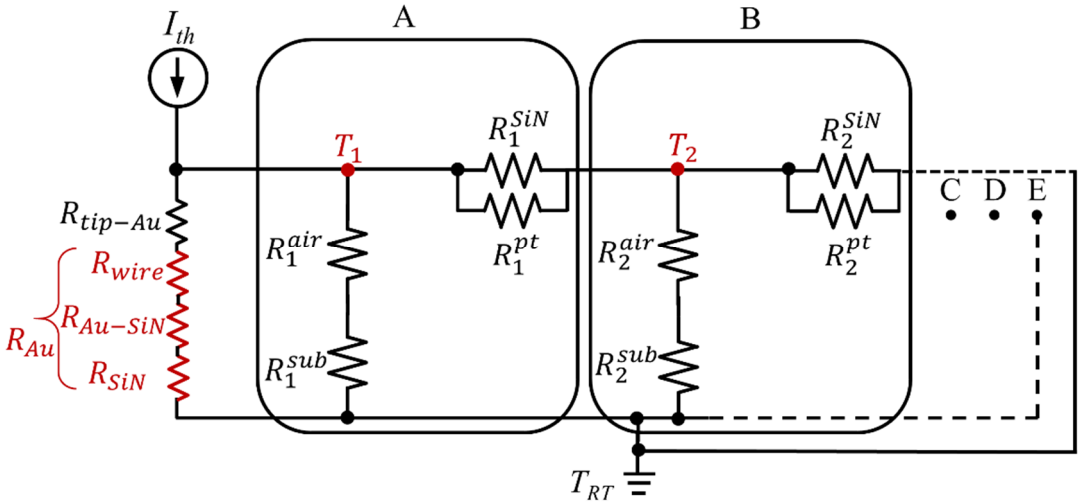

Figure 6.7 Thermal resistance network for probe contacting on the gold wire. A and B inherit from the model shown in Figure 5.14 with the addition of R_i^{sub}. C, D and E share the same structures as A and B, and have been simplified its expression here.

Experimentally, the gold wires were imaged using SThM with the scan size set to be 2.5 µm × 2.5 µm, with a resolution of 512 × 512 pixels. The scan speed was chosen to be 0.5 Hz (4 ms per point), which ensured tip temperature was at steady state for each pixel (see Section 3.1.4 for the determination of probe response speed). Figure 6.8 shows a thermal image of a wire with 400 nm width and 700 nm length as an example showing how the thermal signals used for analysis were picked from the thermal map. The thermal signal is represented by voltage, which is directly acquired from the output of the measurement circuit.

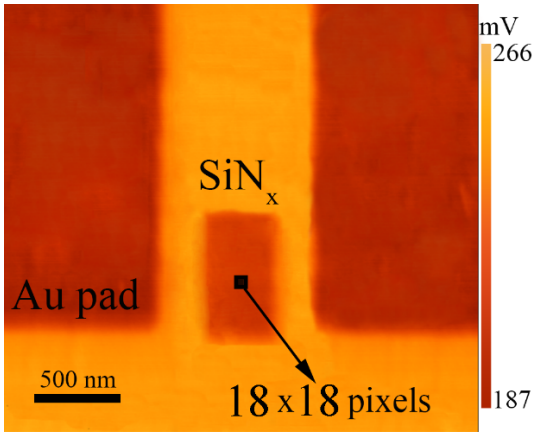

Figure 6.8 Thermal image of a gold wire on topography-free sample with 400 nm width and 700 nm length. The thermal signal is shown as the output of the measurement instrumentation and represented as electrical voltage.

In order to analyze the probe temperature, a square with 18 × 18 pixels was selected at the centre of the gold wire (see the black square on the gold wire), and the tip temperature taken as the average of these 324 values. For a 2.5 μm square image consisting of 512 pixels per line, this square has a similar size to the probe-sample contact area as described previously.

This process was repeated for all of the wire geometries with both the modelled and measured tip temperature shown in Figure 6.9, classified by width. The error bar represents ± 1 standard deviation of the averaged experimental values. It can be seen that the trend of both curves matches well, suggesting that thin films with finite dimension can be modelled as a radial fin connected with a straight fin when measured by nanoscopic contact. The calculated thermal resistance of the wires as a function of length is also plotted as an inset for each width. There is a temperature variation between the measured and modelled values and it is believed that this may result from probe-sample air conduction, together with the local environment within the microscope causing some sample heating. This will result in a slight mismatch between the effective experimental ambient temperature and that used in the model. The magnitude of the offset (0.1 K and 0.2 K) is certainly within the

margin of error expected between room temperature and that of the sample surface.

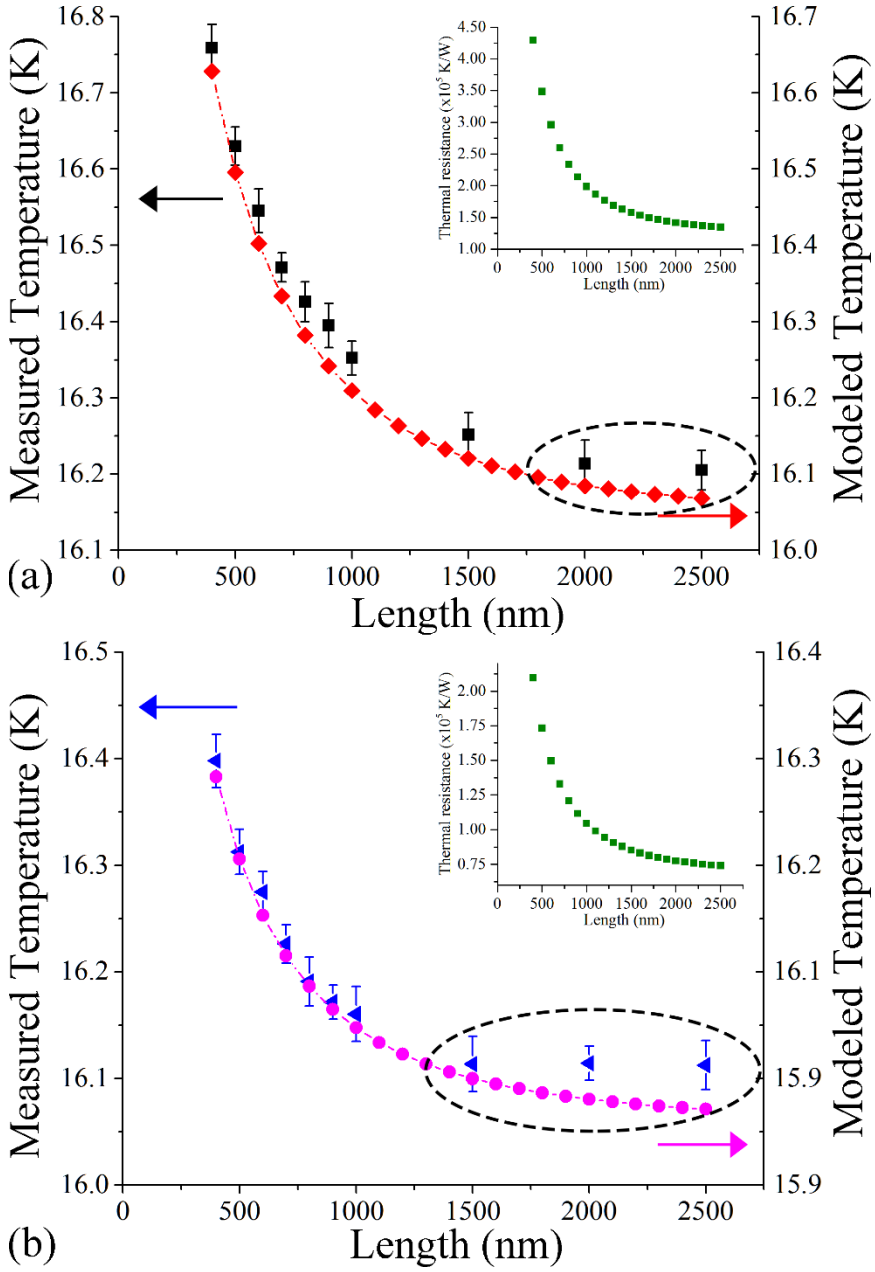

Figure 6.9 Plots of tip temperature from both measurement (black squares in (a) and blue triangles in (b)) and thermal resistance network (red diamonds in (a) and purple circles in (b)) versus the length of gold wire in (a) 200 nm wide and (b) 400 nm wide. All temperature represents the temperature relative to the ambient temperature. The insets in (a) and (b) shows the thermal resistance calculated from the model for 200 nm and 400 nm respectively.

Except for those points shown in the dashed circles in both Figure 6.9 (a) and (b), the probe shows a sensitivity to thermal resistance affected by the dimension. Comparison between the tip temperature and the calculated thermal resistance reveals that only variation in thermal resistance that exceeds 9×10^3 K/W will result in a measurable deviation. However, if this is considered together with the signal to noise of the electrical signal, this sensitivity will decrease. The noise comes from various sources, with sensor circuitry, variations in ambient conditions and residual sample topography all contributing [116]. The root-mean-square value of noise in this experiment is 0.038 K. This value however cannot be directly used to define the sensitivity of the probe, since the sensitivity is dependent on the thermal interfacial resistance between the probe and sample, which means that it changes with the material of sample. According to the argument proposed by Menges *et al*. [147], variation in heat flux (ΔQ) is more suitable for expressing the detection sensitivity. Here, by referring to the thermal resistance network in Figure 6.7, ΔQ can be determined as ~ 200 nW and a temperature change of 0.038 K at the tip. This value is three orders larger than that obtained by Menges *et al*. in their work (~ 100 pW), which may be attributed to their advanced "AC+DC" measurement strategy as well as the use of a high-vacuum system with electromagnetic shielding in a temperature stable lab. To demonstrate the dimensional effect more intuitively, eq. 6.11 can be used to calculate the thermal conductivity from thermal resistance of wires with all dimensions. This tells us that for the wire 200 nm wide and 400 nm long (the largest thermal resistance), the thermal conductivity is 11.8 W/mK. This is much smaller than that of the real bulk value, and is close to that of SiN_x.

Moreover, following the trend of the thermal resistance as a function of length, we can say that it will never equal that of the gold pad. This means that not only the length, but also width has a significantly effect on the heat transfer mechanisms within the gold wire. Therefore, interpretation of measured thermal resistance into thermal conductivity must take dimensions of sample into account.

6.5.3 Investigation of shape dependence of thermal spreading resistance

I. Motivation and new pattern design

As discussed above, the thermal resistance of a thin film with finite dimensions is intimately related to the equivalent thermal conductance at the boundary of the radial fin, h_c. By considering the theoretical analysis of straight fins above, it can be observed that not only length and width, but also heat transfer at the boundaries will affect h_c. For gold wires with uniform geometry, the boundary condition at the end of the straight fin is thermal conduction with the surrounding SiN_x as described by h_c. However, if the straight fin is instead connected at its end to an ambient temperature heat sink, the calculation of h_c detailed above must be reconsidered.

A pattern named "Dogbone" was designed to vary the boundary condition present at the end of the straight fin. Figure 6.10 (a) shows the design where length of wires (l) were set to 1 μm and width (w) varied from 200 nm to 500 nm. The 5 μm × 5 μm gold pads are shown in a different colour (blue) to the gold wires (red) for clarity of illustration only. During fabrication, both the wires and pads were written using EBL in the same layer resulting in a continuous feature. Below the "Dogbone" patterns, as shown in Figure 6.10 (b), a similar set of individual wires were produced, sharing the same dimensions and material as the "Dogbone" wires. However, these wires included a small gap between the wire and pads with the intention of demonstrating the shape effect more clearly. Both the "Dogbone" and "fake Dogbone" patterns were successfully fabricated as topography-free samples and their SEM images have been demonstrated in Figure 6.10 (c). The fabrication process and thickness of patterns remained unchanged from those discussed in previous section.

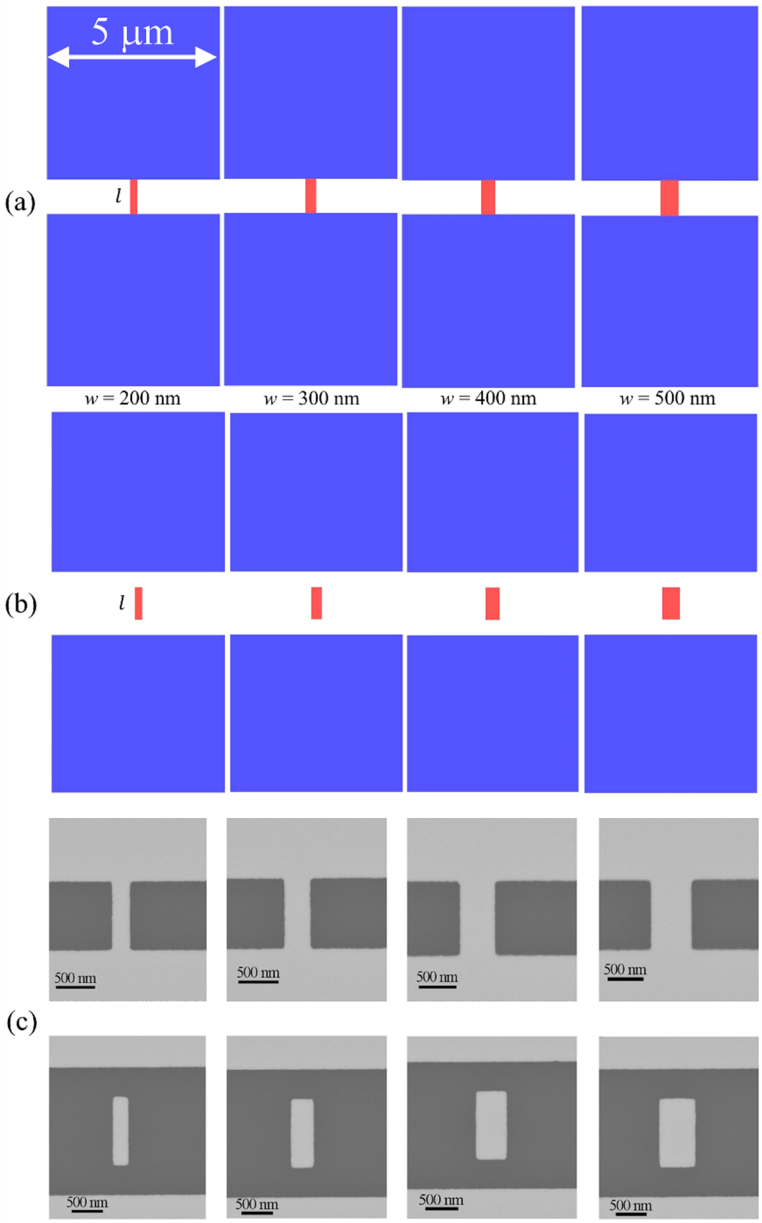

Figure 6.10 Design of (a) "Dogbone" patterns with (b) individual wires named as "fake Dogbone" in the same schematic. (c) SEM images showing the two types of patterns fabricated as topography-free samples.

II. Comparison between the modelled and measured temperature

The thermal resistance of this new feature was calculated in a similar way to the wires in the previous section with the difference that the 5 µm × 5 µm gold pad at each end was assumed to be a perfect heat sink at ambient temperature. Therefore, the boundary conditions could be written as:

$$\epsilon_1 = T_1 - T_\infty \qquad \text{eq. 6.28}$$

$$\epsilon_2 = 0 \qquad \text{eq. 6.29}$$

where ϵ_1 and ϵ_2 is the excess temperature defined as $(T - T_\infty)$ at the edge of the radial fin and the straight fin respectively. This allows the heat transfer rate within the straight fin to be defined as [219]:

$$q_s = m_s k A \epsilon_1 \frac{\left(\cosh m\frac{l}{2} - \frac{\epsilon_2}{\epsilon_1}\right)}{\sinh m\frac{l}{2}} \qquad \text{eq. 6.30}$$

Thermal resistance of the straight fin in this condition is therefore:

$$R'_{straight} = \frac{\epsilon_1}{q_s} \qquad \text{eq. 6.31}$$

Thus the thermal conductance per unit area at the edge of radial fin is:

$$h'_c = \frac{1}{R'_{straight} A} \qquad \text{eq. 6.32}$$

Similar to the individual gold wires, thermal resistance of these features was determined and used as the thermal resistance in the probe heat transfer network, allowing the tip temperature to be calculated.

The experiment was carried out using the same SThM setup and settings as described previously. In addition to obtaining thermal scans of the "Dogbone" patterns, the "fake Dogbone" patterns were also imaged in order to demonstrate the shape effect more clearly and a comparison is shown in Figure 6.11. The temperature is represented by the voltage (mV) output from the instrument. It can be immediately seen that wires of "Dogbone" patterns exhibit a similar probe temperature to the gold pads. In addition, although the wires become wider, there is no strong width-dependence phenomenon present in their signal. In contrast, the isolated wires demonstrate a higher temperature than gold pads, indicating a larger thermal resistance.

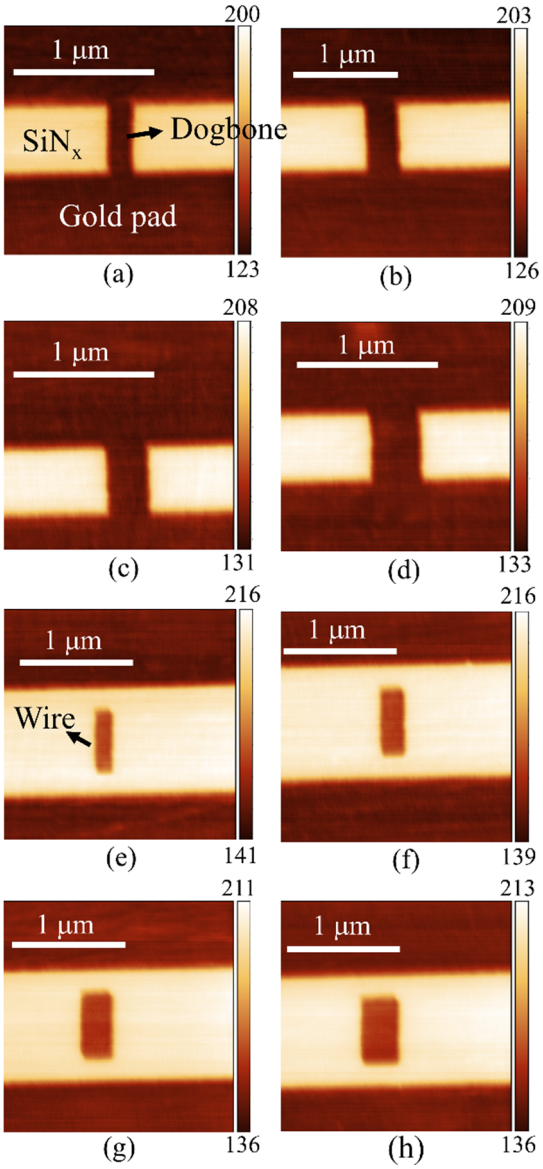

Figure 6.11 Thermal images of "Dogbone" patterns with widths (a) 200 nm, (b) 300 nm, (c) 400 nm and (d) 500 nm, in comparison to isolated wires with the same widths (e), (f), (g) and (h).

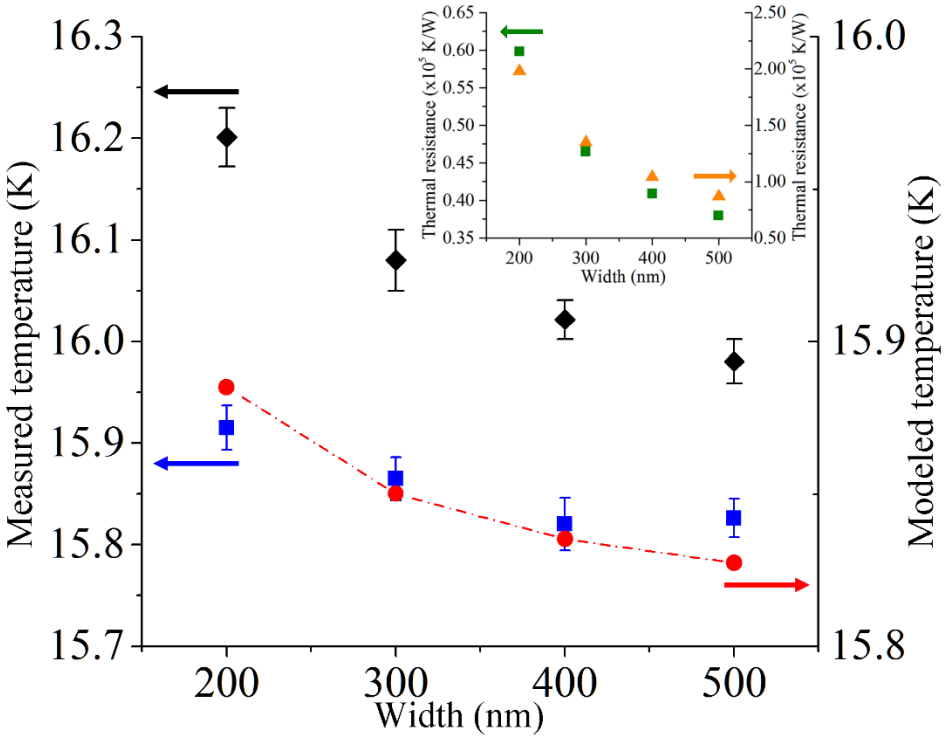

Figure 6.12 Plots of the SThM tip temperature when measuring the "Dogbone" pattern. Blue squares and red circles indicate the measured and modelled tip temperature of the "Dogbone", for comparison, the measured tip temperature for isolated wires is shown by black diamonds. All temperature represents the relative temperature to the ambient temperature. The inset figure gives the plot of thermal resistance of the "Dogbone" pattern (green squares) with that of individual wires (orange triangles).

The results from the experimentally measured SThM tip temperature when in contact with "Dogbone" wires, together with the associated modelled values are shown in Figure 6.12 as blue squares and red circles respectively. From the simulation result, the trend of temperature can still be observed to follow the feature thermal resistance with changes in width (green squares in inset). However, the variation is small and can hardly be observed experimentally, especially when the measurement standard deviation is taken into account. In contrast, the probe temperature from isolated wires (black diamonds) demonstrates much stronger dependence on thermal resistance (orange triangles in inset) resulting in higher tip temperatures. This is in good

agreement with the images (Figure 6.11) where "Dogbone" patterns exhibit similar signal between gold pads and wires, while isolated wires show a clear difference between the two. The impact of changing the end the boundary conditions can be clearly seen. In addition, the same model described above can effectively model both scenarios with only the simple replacement of boundary conditions.

If we consider the analysis above, it can be said that the effect of boundary shape is able to modify the impact of feature dimensions on thermal resistance. It can be therefore predicted that dimension effects can also be enhanced, if the shape results in less interaction at the interface of the feature. For example, a fin with cross-section that decreases along its length is more likely to be thermally isolated at its boundary.

Perhaps the most important conclusion that can be drawn from this work, is the impact of nano-scale feature shape on quantitative thermal analysis using SThM. Based on the observations above, it can be stated that a detailed knowledge of a feature's dimensions and shape is essential if its thermal conductivity is to be reliably extracted from a measurement of its thermal resistance. This is reasonable for nano-fabricated samples such as those employed in this work. However, the question remains as to whether this can be truly achieved for other, less constrained samples such as composite materials. For the same probe and experimental setup in this work, we can state that an object can be treated as a half-space if its thermal resistance deviates from bulk insufficiently to cause a change in heat flux larger than ~ 200 nW. More specifically, if considering the gold employed in this work, rectangular samples with thermal resistance within 1.41×10^4 K/W of that exhibited by the gold pad (3.42×10^4 K/W) can be treated as a half-space. Figure 6.13 is a contour plot showing thermal resistance against the width and length of a gold wire. The plot is mirrored along the $x = y$ line, therefore only half has been shown for clarity. The areas shaded red represent gold wires that can be treated as a half space corresponding to a thermal resistance smaller than 4.83

× 10^4 K/W. It shows us that all gold wires with width larger than 1100 nm can be analysed as a half-space, while with any wire with width smaller than 750 nm must have dimensional effects taken into account. It should be noted that this plot is only valid for the materials and shapes considered in this chapter.

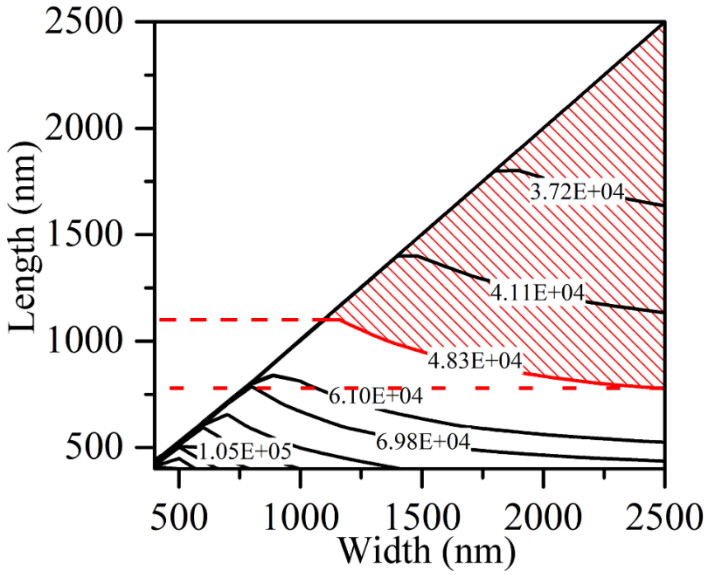

Figure 6.13 Contour showing the thermal resistance with the unit K/W against the width and length of gold wires with both the length and width varying.

6.5.4 Determination of effective contact radius

The advantage of the topography-free sample is that the thermal signals at the edge of the pattern can be obtained without topographically induced artifacts. This can be used to create another simple measurement of SThM probe-sample effective contact radius. A schematic of this measurement is shown in Figure 6.14. When a SThM probe moves from the SiN_x onto the gold, the transition of the thermal response is not an abrupt change but a ramp, which can be observed in Figure 4.10 (e) and Figure 4.12 (e). It is suspected that this phenomenon is the result of several factors. It has been proposed in Chapter 4 that, for hard materials, it is reasonable to treat the contact size as independent of material. Combining this assumption with the work presented in this chapter, we can state that three factors dictating this ramp will be i) the transition of a circular contact across an abrupt thermal feature; ii) the

difference in probe-sample thermal interfacial resistance during this transition; iii) the nonuniformity of thermal resistance of gold wire along the length from its edge to the centre.

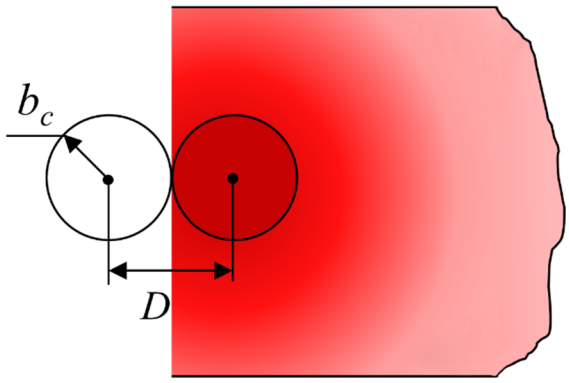

Figure 6.14 Principle of the effective contact radius measurement.

Employing the analysis described in the previous section, the thermal interfacial resistance between the probe and SiN_x has been determined as 1.25 × 10^6 K/W, and that between the probe and gold as 0.985 × 10^6 K/W. This leads to an interesting observation: this difference alone would be enough to generate strong thermal contrast during a SThM scan, even if both materials had the same thermal conductivity.

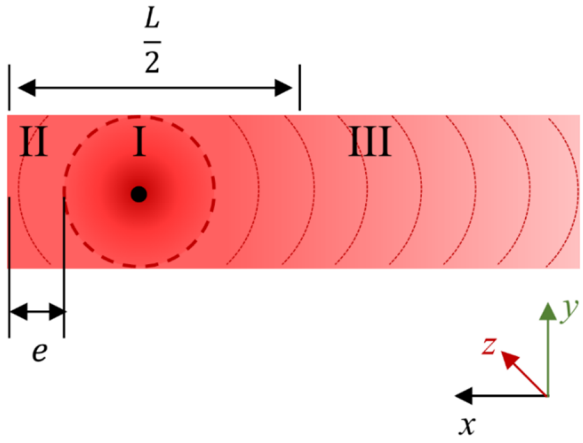

Figure 6.15 Schematic of probe in contact with a gold wire at the position away from the centre.

We can now consider the effect of probe contact position on the gold wire. As already described, we can model the thermal resistance of the gold wire by treating it as a combination of a radial fin with the heat source at the centre and two straight fins of equal length. Following this, we can state that the thermal resistance will vary with position on the wire due to the differing ratio of the length for the two fins. As shown in Figure 6.15, when a probe is in contact near the edge of a wire, we can divide the model into three sections. Section I is still a radial fin as described previously, with diameter equal to the width of the wire. Sections II and Section III are two straight fins separated by the contact point. This configuration necessitates only slight changes to the thermal model, specifically a revised value of "h_c" at the edge of the radial fin. This can obtained from eq. 6.25 by substituting $R_{straight}$ with the thermal resistance of the two straight fins in parallel, and using the cross-section area of the whole radial fin instead of half of it. The MATLAB code modified for this calculation can be found in Appendix IV.*iii*, with the modifications highlighted in red.

The modelled thermal resistance difference between the probe contacting at the edge and at the centre of the gold wire is recorded as ΔR_{th}. Figure 6.16 shows the ΔR_{th} varying with the length of wires in 200 nm and 400 nm wide. It has been clearly shown that the maximum variation happens when the length is 2500 nm, smaller or larger than which, the variation of thermal resistance along their length will decrease.

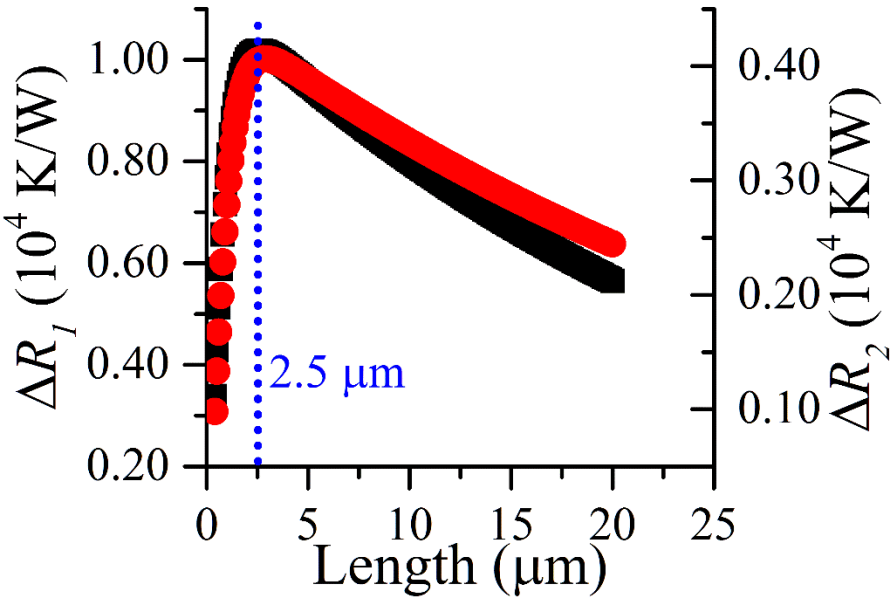

Figure 6.16 Thermal resistance difference between the probe contacting at the edge and the centre of the gold wire. ΔR_1 is for 200 nm wide wire (black squares), and ΔR_2 is for 400 nm (red circles).

It can be seen that, even for 2500 nm long wires, there is only ~ 1×10^4 K/W variation as the probe moves from the centre of the wire to the edge. This is comparable to the ideal maximum sensitivity of the probe, 1.41×10^4 K/W, as defined previously. Therefore, we can conclude that any probe temperature change is dominated by the transition from one contact material to the other.

This simplifies the determination of effective contact size between the probe and the sample through analysis of the thermal image. Figure 6.17 shows the thermal response signals from two line traces at the top (A-A') and the bottom (B-B') edges of the wire in Figure 6.17 (a). These traces are then plotted against the length of trace as shown in Figure 6.17 (b). Both traces correspond to 18 pixel (x) by 70 pixel (y) rectangles allowing the signal at each y location to be averaged from 18 points. This results in an actual scan length of 118 nm, approximately corresponding to the accepted probe-sample contact diameter of the probes used as discussed in Chapter 5. A simple description for the thermal spatial resolution of SThM in air can be obtained from the full width of half maximum (FWHM) of the trace using a Boltzmann sigmoidal fit:

$f(y) = y_2 + (y_1 - y_2)/(1 + e^{(x-x_0)/\Delta x})$ [30,227]. This gives an estimation of resolution of $2 \times \Delta x = 45$ nm, which compares well with the value obtained in using the same probe in other work and agrees with the observation that the radius of the probe limits the thermal spatial resolution [53,90,118].

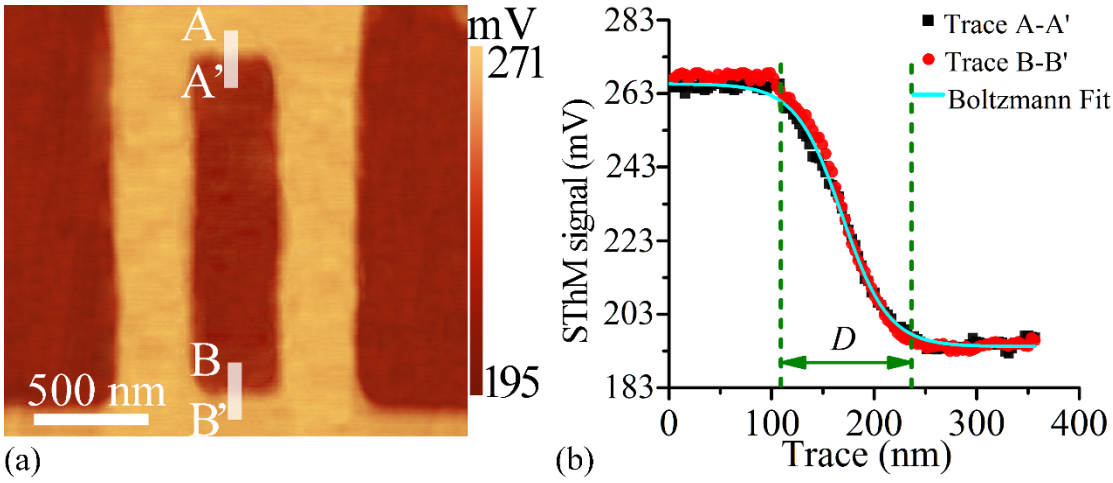

Figure 6.17 (a) Thermal image of gold wire with two traces (A-A′ and B-B′) at top and bottom edges, and (b) plots of the thermal response for these two traces against scan length.

6.6 Conclusion

Although SThM has a proven ability to measure thermal conductivity, feature size and shape, may result in the misinterpretation of thermal signals and is seldom considered as reducing accuracy of a measurement. Work in this chapter highlights these effects by measuring topography-free samples consisting of gold wires with various dimensions. In addition to demonstrating the problem, a model based on the combination of two fins has be proposed that avoids complicated multi-dimensional heat transfer analysis. It can be seen that knowledge of sample dimensions and shape can benefit interpretation of results, identifying whether to treat the sample as a half-space or a one-dimensional structure. Furthermore, the sensitivity of the probe working in air has been determined to be ~ 200 nW, placing a practical limit on the impact of dimensional effects. Finally, the effective probe-sample contact size has been determined as being comparable to the probe's tip radius

of curvature with the topography-free sample. It should be noted that continued development of the proposed model would benefit from use of in vacuum SThM as this will greatly simplify the thermal resistance network and eliminate temperature deviations caused by air.

7

FINAL REMARKS

7.1 Summary and Conclusions

With ever increasing importance of nanoscale heat transfer, SThM is receiving more attention than ever before. There have been several breakthroughs in the development of SThM since its invention. In addition, various kinds of probes have emerged and become common, from the Wollaston probe at the micro-scale to the nanosized batch fabricated probes. Employing these innovations, temperature measurement and thermal data analysis have also made great progress in the field. This has permitted the application of SThM probes to be extended from temperature measurement to the determination of material thermal properties. However, due to complex heat-transfer mechanisms, as well as ambiguity in the understanding of the heat transfer at point contacts, thermal measurement using SThM could still be considered a relatively immature technology.

In order to satisfy the requirement of analysis at the nanoscale, SThM must be developed into a quantitative measurement technique. Efforts have focused on several aspects to achieve this, including the use of SThM under high vacuum conditions (10^{-6} mbar) to simplify the heat path between the probe and the sample, modelling the probe biased with AC/ DC signals and

introducing a new nulling probe technique. In this work, a well-characterized probe has been combined together with accurate instrumentation, providing a fundamental tool in the push towards quantitative SThM. Given the fact that global thermal equilibrium cannot be established during a scan, tip-sample interactions have to be thoroughly understood and accounted for in order to extract the actual tip-sample temperature difference, the key information in a measurement. The employment of specifically designed samples in this work has permitted heat transfer mechanisms within the probe-sample system to be more clearly understood. Based on the results and data presented in chapters of this thesis, the following summary and key conclusions can be made:

1. The commercial SiN_x SThM probe (named as KNT-SThM-01a in the market) is not ideal for quantitative measurements due to ambiguity in the value of its NiCr thin film resistors, acting as current limiters in series with the tip. In order to eliminate this complexity, all work done in this thesis employed the thermally compensated platinum probe without any on-probe current limiter. Driven by either DC or AC, the real temperature of the probe can be derived from changes of its resistance by employing its TCR which is measured as $0.000961 \pm 0.0000106\ K^{-1}$. In addition, several fundamental but critical probe parameters have been determined, which can be employed to identify the most appropriate experimental conditions as well as informing new SThM probe designs. The maximum current density of the probe was convincingly quantified as $3.56\times10^{10}\ A/m^2$, under which, the TCR showed perfect linearity. The current at which the probe transitioned from insignificant Joule heating (passive mode) to significant self-heating (active mode) was determined as $3\times10^{9}\ A/m^2$. The same experiment also provided an indication of the heat flux due to the air conduction, which was subsequently employed in modelling the newly designed 'nulling probe'. In addition, the time constant of the probe, at which the local thermal equilibrium can be established, was determined as 2.4 ms. This value informs not only the maximum scan rate, but also the nulling probe instrumentation.

2. Utilization of a neutral plane on the cantilever provides the

possibility to operate the probe at a higher temperature than previously possible without severe thermal bending. This was achieved using an optimized fabrication process and has been verified as effective by demonstrating a linear response to a higher temperature sample than can be achieved with a normal probe. With this improvement, the new probe exhibited a stable contact force during the scan of ~ 20 nN, resulting in an invariable contact area. This optimized fabrication method provides a more robust and reliable manufacturing process for new probes.

3. The newly optimized Johnson noise device provides an accurate temperature reference for calibrating the probe. As air conduction between the probe and the sample plays an important role in dictating the temperature of the tip, the new Johnson noise device allows switching between small and large heater modes, enabling a direct measurement of the effect of air conduction between the cantilever and sample. By developing and then employing a 1D heat transfer model involving all dominant thermal interactions between the probe and sample, two critical properties, the thermal resistance of the probe and thermal conductance through the contact interface, have been determined. This information allowed a lumped system model to be built describing the temperature difference between the tip and sample. This provides a simple way to model the SThM probe, offering a convenient method to optimize probe performance by considering changes to probe shape or material.

4. The topography-free sample successfully eliminates topographically induced artifacts, providing an efficient way to study the heat transfer mechanisms between the probe and sample. Patterns with flexible size and shape were demonstrated, verifying the capability of the fabrication process. With the help of this flexible fabrication method, a phenomenon dictated by the dimension and shape dependence of sample thermal spreading resistance was investigated using SThM working in active mode. This phenomenon was then described using a model consisting of a combined radial-straight fin, which greatly simplifies the calculation of the 2D heat transfer within this sample geometry. This was then combined with the

modified lumped-system model developed for the Johnson noise device, permitting this sample dimension and shape effect to be verified by comparison of the model with experimental results. This demonstrates that the thermal spreading resistance of the sample could be greatly misinterpreted unless the exact sample dimensions and shape are known. The combined fin model also allows the effect of SThM contact position to be considered as it scans across a feature with finite dimensions. A novel use of this permits probe-sample contact size to be determined by analyzing scans obtained on the topography-free sample, specifically the transition area between the high and low thermal conductivity materials. When combined, this permitted the conclusion that the probe exhibits nano-watt heat flux resolution with tens of nanometers thermal spatial resolution.

In conclusion, this thesis has aimed to demonstrate the capability of quantitative thermal measurement when employing the micromachined SiN_x probe in both active and passive mode. Acknowledging that a thorough understanding of the probe behaviour is a *prerequisite*, the work is arranged as steps required to achieve quantified measurements. The thorough probe characterization in Chapter 3 provides *the fundamental values* needed to operate the probe and interpret its electrical resistance as temperature. When the probe is operated with a current density lower than its limiting value, the determined TCR can be applied in both passive and active mode. After realising that topographic artifacts influence the thermal signal, greatly complicating characterization of the probe, a solution is proposed in Chapter 4 through the production of a topography-free sample. This was then employed to investigate the contribution of different heat transfer mechanisms in active mode to the measured thermal resistance, and observed that the thermal spreading resistance of different materials will dominate. The new JN device presented in Chapter 5, combined with heat transfer calculations, results in *the second fundamental value* – the tip-sample contact size. This understanding is then employed in the development of *an efficient tool for the analysis of SThM data* – the lumped thermal resistance network model.

The work to achieve truly quantitative thermal measurement using SThM requires both the knowledge and application of *the two values* described above, in combination with a model such as *the tool* developed in Chapter 5. The advantages of this combined approach can be seen in the study of thermal resistance of thin films with finite dimension presented in Chapter 6, which fundamentally relies on quantitative SThM measurements to investigate complicated samples.

7.2 Outlook

Although the SThM has made great progress since its first appearance nearly thirty years ago, there are still some issues and unfulfilled potential associated with this technique.

As discussed in Chapter 2, determination of areas of uncertainty within the SThM system is essential to quantify SThM measurements. Among these, air conduction can be considered as one of the most difficult to accurately account for - it has a ubiquitous impact throughout the SThM/sample system, both in the vicinity of tip-sample contact and along the entire cantilever. However, it is relatively easy to eliminate this complication by employing vacuum conditions. Whilst experimentally more complicated than ambient measurement, this does provide an effective solution, resulting in much simpler heat transfer, which only involves thermal interactions due to the probe and sample. However, knowledge of the SThM probe thermal resistance along with that of the tip-sample interface is still a necessity. The 'nulling probe' has shown its potential in solving this issue in quantitative temperature measurement when employed in a vacuum system. With this approach, probe temperature faithfully reflects that of the sample, making measurement of active samples, for example heated nanowires, carbon nanotubes and semiconductor junctions, more direct and accurate. In addition, the 'nulling probe' can effectively eliminate topographically induced artifacts without having to resort to topography-free samples [214] or extensive data

post-processing [147] due to the fact that heat flux through the (topographically varying) tip-sample interface is zero due to the absence of a temperature gradient.

Despite this huge potential, the 'nulling probe' remains difficult to use due to the extremely complicated measurement instrumentation it requires, which combined with the need for specialist probes, currently impedes its widespread use.

If we consider 'normal' SThM employing more commonly employed approaches as discussed throughout this thesis, we can consider future developments that will make it more advanced and accessible. The clear and detailed characterization of SThM heat transfer mechanisms under ambient conditions will, with the help of appropriate models, improve the accuracy and interpretation of data obtained using even the most basic systems. There is scope to further optimize the SThM probe through changes to its dimensions or shape, further improving its performance and simplifying its heat transfer analysis. Specifically, when considering SThM probe design, one problem with the current probe is its complex shape and non-localized thermal sensor, making it difficult to accurately model. One possibility would be to redesign the probe with the consideration of modelling. For example, a cantilever with regular shape, instead of the current nonuniform one, will reduce the number of lumped components to describe the probe. With improved alignment during fabrication [228] the thermal sensor could be made small enough that it could be assumed to be a localized temperature sensor, further simplify probe models. In order to encourage the extensive application of SThM, accurate models that describe the heat transfer between the probe and sample must be established. A good example of innovation in this area is the expression of sample thermal resistance when the mean free path is larger than the tip-sample contact size, as is currently being developed [100,121]. Furthermore, advanced instruments (such as SThM-SEM, or combined SThM-optical IR) and more advanced data processing (e.g. real-

time data processing), offer the promise of improved understanding by exploring the nature of heat transfer through the nanoscale contact and user friendly advanced data analysis. It is clear that the true aim for SThM is for it to become an easily accessible, accurate tool that is employed as ubiquitously as other, well-established SPM techniques.

BIBLIOGRAPHY

[1] Shi L 2003 Nanoscale thermal and thermoelectric mapping of semiconductor devices and interconnects *AIP Conf. Proc.* **683** 462–8

[2] Cahill D G, Ford W K, Goodson K E, Mahan G D, Majumdar A, Maris H J, Merlin R and Phillpot S R 2003 Nanoscale thermal transport *J. Appl. Phys.* **93** 793–818

[3] Cahill D G, Braun P V., Chen G, Clarke D R, Fan S, Goodson K E, Keblinski P, King W P, Mahan G D, Majumdar A, Maris H J, Phillpot S R, Pop E and Shi L 2014 Nanoscale thermal transport. II. 2003-2012 *Appl. Phys. Rev.* **1** 011305

[4] Pop E 2010 Energy dissipation and transport in nanoscale devices *Nano Res.* **3** 147–69

[5] Cho J, Chu K K, Chao P C, Mcgray C, Asheghi M and Goodson K E 2014 Thermal conduction normal to thin silicon nitride films on diamond and GaN *Fourteenth Intersociety Conference on Thermal and Thermomechanical Phenomena in Electronic Systems (ITherm)* 1186-91

[6] Kuzmik J, Bychikhin S, Pogany D, Pichonat E, Lancry O, Gaquière C, Tsiakatouras G, Deligeorgis G and Georgakilas A 2011 Thermal characterization of MBE-grown GaN/AlGaN/GaN device on single crystalline diamond *J. Appl. Phys.* **109** 086106

[7] Cho J, Bozorg-Grayeli E, Altman D H, Asheghi M and Goodson K E 2012 Low thermal resistances at GaN-SiC interfaces for HEMT technology *IEEE Electron Device Lett.* **33** 378–80

[8] Dekker C 1999 Carbon nanotubes as molecular quantum wires *Phys. Today* **52** 22

[9] Mirza M M, MacLaren D A, Samarelli A, Holmes B M, Zhou H, Thoms S, MacIntyre D and Paul D J 2014 Determining the electronic performance limitations in top-down-fabricated Si nanowires with mean widths down to 4 nm. *Nano Lett.* **14** 6056–60

[10] Hicks L D and Dresselhaus M S 1993 Effect of quantum-well structures on the thermomagnetic figure of merit *Phys. Rev. B* **47** 727–31

[11] Castro Neto A H, Peres N M R, Novoselov K S, Geim A K, Guinea F and Neto A 2009 The electronic properties of graphene *Rev. Mod. Phys.* **81** 109–62

[12] Cai W, Moore A L, Zhu Y, Li X, Chen S, Shi L and Ruoff R S 2010 Thermal transport in suspended and supported monolayer graphene grown by chemical vapor deposition *Nano Lett.* **10** 1645–51

[13] Boukai A I, Bunimovich Y, Tahir-Kheli J, Yu J-K, Goddard W A and

Heath J R 2008 Silicon nanowires as efficient thermoelectric materials. *Nature* **451** 168–71

[14] Callen H B 1985 *Thermodynamics and an Introduction to Thermostatistics* (New York: John Wiley & Sons)

[15] Klapetek P 2013 Thermal measurement *Quantitative Data Processing in Scanning Probe Microscopy SPM Application for Nanometrology* ed P Klapetek (Oxford: William Andrew, Elsevier) pp 247–64

[16] Cahill D G, Goodson K and Majumdar A 2002 Thermometry and thermal transport in micro/nanoscale solid-State devices and structures *J. Heat Transfer* **124** 223

[17] Holman J P 2010 *Heat Transfer* (New York: McGraw-Hill)

[18] Greffet J J 2007 Laws of macroscopic heat transfer and their limits *Microscale and Nanoscale Heat Transfer* vol 107, ed S Volz (Berlin/Herdelberg: Springer) pp 1–13

[19] Wolfe J P 1998 Ballistic heat pulses and phonon imaging – A first look *Imaging Phonons* (Cambridge: Cambridge University Press) pp 21–59

[20] Majumdar A 1993 Microscale heat conduction in dielectric thin films *J. Heat Transfer* **115** 7

[21] McConnell A D, Uma S and Goodson K E 2001 Thermal conductivity of doped polysilicon layers *J. Microelectromechanical Syst.* **10** 360–9

[22] Chen G 2001 Ballistic-diffusive heat-conduction equations *Phys. Rev. Lett.* **86** 2297–300

[23] Anderson C V D R and Tamma K K 2006 Novel heat conduction model for bridging different space and time scales *Phys. Rev. Lett.* **96** 1–4

[24] Hoogeboom-Pot K M, Hernandez-Charpak J N, Gu X, Frazer T D, Anderson E H, Chao W, Falcone R W, Yang R, Murnane M M, Kapteyn H C and Nardi D 2015 A new regime of nanoscale thermal transport: Collective diffusion increases dissipation efficiency *Proc. Natl. Acad. Sci.* **112** 4846–51

[25] Volz S and Carminati R 2007 Microscale and nanoscale heat transfer *Topics in Applied Physics* vol 107 (Berlin/Herdelberg: Springer)

[26] Chapuis P-O 2016 Introduction to heat transfer at the nanoscale *Thermometry at the Nanoscale: Techniques and Selected Applications Edited* ed L D Carlos and F Palacio (London: The Royal Society of Chemistry) pp 39–78

[27] Chu D C, Wong W K, Goodson K E and Pease R F W 2003 Transient temperature measurements of resist heating using nanothermocouples *J. Vac. Sci. Technol. B* **21** 2985–9

[28] Costescu R M, Bullen A J, Matamis G, O'Hara K E and Cahill D G 2002 Thermal conductivity and sound velocities of hydrogen-silsesquioxane low-k dielectrics *Phys. Rev. B* **65** 094205

[29] Koh Y K, Cao Y, Cahill D G and Jena D 2009 Heat-transport mechanisms in superlattices *Adv. Funct. Mater.* **19** 610–5

[30] Tovee P D and Kolosov O V 2013 Mapping nanoscale thermal transfer in-liquid environment-immersion scanning thermal microscopy. *Nanotechnology* **24** 465706

[31] Duvigneau J, Schönherr H and Vancso G J 2010 Nanoscale thermal AFM of polymers: Transient heat flow effects *ACS Nano* **4** 6932–40

[32] Aigouy L, Tessier G, Mortier M and Charlot B 2005 Scanning thermal imaging of microelectronic circuits with a fluorescent nanoprobe *Appl. Phys. Lett.* **87** 1–3

[33] Tessier G, Bardoux M, Boué C, Filloy C and Fournier D 2007 Back side thermal imaging of integrated circuits at high spatial resolution *Appl. Phys. Lett.* **90** 171112

[34] Christofferson J, Maize K, Ezzahri Y, Shabani J, Wang X and Shakouri A 2007 Microscale and nanoscale thermal characterization techniques *Thermal Issues in Emerging Technologies, THETA 1* (Cairo, Egypt) pp 3–9

[35] Kuball M, Rajasingam S, Sarua a., Uren M J, Martin T, Hughes B T, Hilton K P and Balmer R S 2003 Measurement of temperature distribution in multifinger AlGaN/GaN heterostructure field-effect transistors using micro-Raman spectroscopy *Appl. Phys. Lett.* **82** 124–6

[36] Brites C D S, Lima P P, Silva N J O, Millán A, Amaral V S, Palacio F and Carlos L D 2012 Thermometry at the nanoscale. *Nanoscale* **4** 4799–829

[37] Lüerßen D, Hudgings J A, Mayer P M and Ram R J 2005 Nanoscale thermoreflectance with 10mK temperature resolution using stochastic resonance *Annual IEEE Semiconductor Thermal Measurement and Management Symposium* pp 253–8

[38] Christofferson J and Shakouri A 2005 Thermoreflectance based thermal microscope *Rev. Sci. Instrum.* **76** 024903

[39] David R and Hunter I W 2005 A liquid-in-glass thermometer read by an interferometer *Sensors Actuators A Phys.* **121** 31–4

[40] Fujii T, Taguchi Y, Saiki T and Nagasaka Y 2012 Near-field fluorescence thermometry using highly efficient triple-tapered near-field optical fiber probe *Rev. Sci. Instrum.* **83** 124901

[41] Zhang Y, Docherty K E and Weaver J M R 2010 Batch fabrication of cantilever array aperture probes for scanning near-field optical microscopy *Microelectron. Eng.* **87** 1229–32

[42] Shi L, Kwon O, Miner A C and Majumdar A 2001 Design and batch fabrication of probes for sub-100 nm scanning thermal microscopy *J. Microelectromechanical Syst.* **10** 370–8

[43] White D R, Galleano R, Actis A, Brixy H, Groot M De, Dubbeldam J, Reesink A L, Edler F, Sakurai H, Shepard R L and Gallop J C 2003 The

status of Johnson noise thermometry *Metrologia* **33** 325–35

[44] Cahill D G 1990 Thermal conductivity measurement from 30 to 750 K: The 3 omega method *Rev. Sci. Instrum.* **61** 802–8

[45] Frank R, Drach V and Fricke J 1993 Determination of thermal conductivity and specific heat by a combined 3ω/decay technique *Rev. Sci. Instrum.* **64** 760

[46] Yamane T, Nagai N, Katayama S and Todoki M 2002 Measurement of thermal conductivity of silicon dioxide thin films using a 3 omega method *J. Appl. Phys.* **91** 9772–6

[47] Tong T and Majumdar A 2006 Reexamining the 3-omega technique for thin film thermal characterization *Rev. Sci. Instrum.* **77** 104902

[48] Bourgeois O, Fournier T and Chaussy J 2007 Measurement of the thermal conductance of silicon nanowires at low temperature *J. Appl. Phys.* **101** 016104

[49] Choi T Y, Poulikakos D, Tharian J and Sennhauser U 2005 Measurement of thermal conductivity of individual multiwalled carbon nanotubes by the 3-ω method *Appl. Phys. Lett.* **87** 1–3

[50] Choi S R, Kim J and Kim D 2007 3 Omega Method To Measure thermal properties of electrically conducting small-volume liquid. *Rev. Sci. Instrum.* **78** 084902

[51] Brintlinger T, Qi Y, Baloch K H, Goldhaber-Gordon D and Cumings J 2008 Electron thermal microscopy. *Nano Lett.* **8** 582–5

[52] Majumdar A 1999 Scanning thermal microscopy *Annu. Rev. Mater. Sci.* **29** 505–85

[53] Pumarol M E, Rosamond M C, Tovee P, Petty M C, Zeze D A, Falko V and Kolosov O V 2012 Direct nanoscale imaging of ballistic and diffusive thermal transport in graphene nanostructures *Nano Lett.* **12** 2906–11

[54] Park K W, Nair H P, Crook A M, Bank S R and Yu E T 2013 Quantitative scanning thermal microscopy of ErAs/GaAs superlattice structures grown by molecular beam epitaxy *Appl. Phys. Lett.* **102** 061912

[55] Volz S 2007 *Microscale and nanoscale heat transfer* ed C E Ascheron (Berlin Heidelberg: Springer-Verlag)

[56] Zhang Y, Dobson P S and Weaver J M R 2012 High temperature imaging using a thermally compensated cantilever resistive probe for scanning thermal microscopy *J. Vac. Sci. Technol. B* **30** 010601

[57] Cretin B, Gomes S, Trannoy N and Vairac P 2006 Scanning thermal microscopy *Microscale and Nanoscale Heat Transfer* Topics in Applied Physics ed S Volz (Berlin/Herdelberg: Springer Berlin Heidelberg) pp 181–238

[58] Binnig G, Rohrer H, Gerber C and Weibel E 1982 Surface studies by

scanning tunneling microscopy *Phys. Rev. Lett.* **49** 57–61

[59] Binnig G, Rohrer H, Gerber C and Weibel E 1982 Tunneling through a controllable vacuum gap *Appl. Phys. Lett.* **40** 178

[60] Binnig G and Quate C F 1986 Atomic force microscope *Phys. Rev. Lett.* **56** 930–3

[61] Williams C C and Wickramasinghe H K 1986 Scanning thermal profiler *Appl. Phys. Lett.* **49** 1587–9

[62] Weaver J M R, Walpita L M and Wickramasinghe H K 1989 Optical absorption microscopy and spectroscopy with nanometre resolution *Nature* **342** 783–5

[63] Williams C C and Wickramasinghe H K 1990 Microscopy of chemical-potential variations on an atomic scale *Nature* **344** 317–9

[64] Nonnenmacher M and Wickramasinghe H K 1992 Scanning probe microscopy of thermal conductivity and subsurface properties *Appl. Phys. Lett.* **61** 168–70

[65] Majumdar A, Carrejo J P and Lai J 1993 Thermal imaging using the atomic force microscope *Appl. Phys. Lett.* **62** 2501–3

[66] Gurrum S P, King W P, Joshi Y K and Ramakrishna K 2008 Size effect on the thermal conductivity of thin metallic films investigated by scanning joule expansion microscopy *J. Heat Transfer* **130** 082403

[67] Dazzi A, Prazeres R, Glotin F and Ortega J M 2005 Local infrared microspectroscopy with subwavelength spatial resolution with an atomic force microscope tip used as a photothermal sensor *Opt. Lett.* **30** 2388

[68] Samson B, Aigouy L, Lo̎w P, Bergaud C, Kim B J and Mortier M 2008 AC thermal imaging of nanoheaters using a scanning fluorescent probe *Appl. Phys. Lett.* **92** 023101

[69] Kaushal P, Chand S and Osvald J 2012 Current–voltage characteristics of Schottky diode simulated using semiconductor device equations *Int. J. Electron.* **7217** 1–13

[70] Heisig S, Danzebrink H U, Leyk A, Mertin W, Münster S and Oesterschulze E 1998 Monolithic gallium arsenide cantilever for scanning near-field microscopy *Ultramicroscopy* **71** 99–105

[71] Leinhos T, Stopka M and Oesterschulze E 1998 Micromachined fabrication of Si cantilevers with Schottky diodes integrated in the tip *Appl. Phys. A Mater. Sci. Process.* **66** 65–9

[72] Luo K, Shi Z, Varesi J and Majumdar A 1997 Sensor nanofabrication, performance, and conduction mechanisms in scanning thermal microscopy *J. Vac. Sci. Technol. B* **15** 349

[73] Mills G, Zhou H, Midha A, Donaldson L and Weaver J M R 1998 Scanning thermal microscopy using batch fabricated thermocouple

probes *Appl. Phys. Lett.* **72** 2900–2

[74] Zhou H, Midha A, Mills G, Thoms S, Murad S K and Weaver J M R 1998 Generic scanned-probe microscope sensors by combined micromachining and electron-beam lithography *J. Vac. Sci. Technol. B* **16** 54

[75] Kim K, Jeong W, Lee W and Reddy P 2012 Ultra-high vacuum scanning thermal microscopy for nanometer resolution quantitative thermometry *ACS Nano* **6** 4248–57

[76] Sadat S, Tan A, Chua Y J and Reddy P 2010 Nanoscale thermometry using point contact thermocouples *Nano Lett.* **10** 2613–7

[77] Fletcher P C, Lee B and King W P 2011 Thermoelectric voltage at a nanometer-scale heated tip point contact *Nanotechnology* **23** 035401

[78] Pylkki R J, Moyer P J and West P E 1994 Scanning near-field optical microscopy and scanning thermal microscopy *Jpn. J. Appl. Phys.* **33** 3785–90

[79] Lopez L D P, Grauby S, Dilhaire S, Salhi M A, Claeys W, Lefèvre S and Volz S 2004 Characterization of the thermal behavior of PN thermoelectric couples by scanning thermal microscope *Microelectronics J.* **35** 797–803

[80] Hammiche A, Reading M, Pollock H M, Song M and Hourston D J 1996 Localized thermal analysis using a miniaturized resistive probe *Rev. Sci. Instrum.* **67** 4268–74

[81] Hammiche A, Pollock H M, Song M and Hourston D J 1996 Sub-surface imaging by scanning thermal microscopy *Meas. Sci. Technol.* **7** 142–50

[82] Gomés S, Chapuis P O, Nepveu F, Trannoy N, Volz S, Charlot B, Tessier G, Dilhaire S, Cretin B and Vairac P 2007 Temperature study of sub-micrometric ICs by scanning thermal microscopy *IEEE Trans. Components Packag. Technol.* **30** 424–31

[83] Buzin A I, Kamasa P, Pyda M and Wunderlich B 2002 Application of a Wollaston wire probe for quantitative thermal analysis *Thermochim. Acta* **381** 9–18

[84] Mills G, Weaver J M R, Harris G, Chen W, Carrejo J, Johnson L and Rogers B 1999 Detection of subsurface voids using scanning thermal microscopy *Ultramicroscopy* **80** 7–11

[85] Price D M, Reading M, Hammiche A and Pollock H M 1999 Micro-thermal analysis: Scanning thermal microscopy and localised thermal analysis *Int. J. Pharm.* **192** 85–96

[86] Zhou H, Mills G, Chong B K, Midha A, Donaldson L and Weaver J M R 1999 Recent progress in the functionalization of atomic force microscope probes using electron-beam nanolithography *J. Vac. Sci. Technol. A* **17** 2233–9

[87] Dobson P S, Weaver J M R and Mills G 2007 New methods for calibrated Scanning Thermal Microscopy (SThM) *Proc. IEEE Sensors* 708–11

[88] Dobson P S, Mills G and Weaver J M R 2005 Microfabricated temperature standard based on Johnson noise measurement for the calibration of micro- and nano-thermometers *Rev. Sci. Instrum.* **76** 054901

[89] Pettes M and Shi L 2013 A reexamination of phonon transport through a nanoscale point contact in vacuum *J. Heat Transfer* **136** 032401

[90] Tovee P, Pumarol M, Zeze D, Kjoller K and Kolosov O 2012 Nanoscale spatial resolution probes for scanning thermal microscopy of solid state materials *J. Appl. Phys.* **112** 114317

[91] Zhang Y, Dobson P S and Weaver J M R 2011 Batch fabricated dual cantilever resistive probe for scanning thermal microscopy *Microelectron. Eng.* **88** 2435–8

[92] Chui B W, Stowe T D, Kenny T W, Mamin H J, Terris B D and Rugar D 1996 Low-stiffness silicon cantilevers for thermal writing and piezoresistive readback with the atomic force microscope *Appl. Phys. Lett.* **69** 67–70

[93] King W P, Bhatia B, Felts J R, Kim H J and Kwon B 2013 Heated Atomic Force Microscope Cantilevers and Their Applications *Annu. Rev. Heat Transf.* **XVI** 287–326

[94] Despont M, Brugger J, Drechsler U, Dürig U, Häberle W, Lutwyche M, Rothuizen H, Stutz R, Widmer R, Binnig G, Rohrer H and Vettiger P 2000 VLSI-NEMS chip for parallel AFM data storage *Sensors Actuators, A Phys.* **80** 100–7

[95] Corbin E A and King W P 2010 Electrical noise characteristics of a doped silicon microcantilever heater-thermometer *Proc. IEEE Sensors* **263107** 2373–6

[96] Goericke F, Lee J and King W P 2008 Microcantilever hotplates with temperature-compensated piezoresistive strain sensors *Sensors Actuators A* **143** 181–90

[97] Lantz M A, Binnig G K, Despont M and Drechsler U 2005 A micromechanical thermal displacement sensor with nanometre resolution *Nanotechnology* **16** 1089–94

[98] Lee J, Beechem T, Wright T, Nelson B, Graham S and King W 2006 Electrical, thermal, and mechanical characterization of silicon microcantilever heaters *J. Microelectromechanical Syst.* **15** 1644–55

[99] Bae J H, Ono T and Esashi M 2003 Scanning probe with an integrated diamond heater element for nanolithography *Appl. Phys. Lett.* **82** 814–6

[100] Gomès S, Assy A and Chapuis P 2015 Scanning thermal microscopy: A review *Phys. status solidi* **212** 477–94

[101] Shi L, Zhou J, Kim P, Bachtold A, Majumdar A and McEuen P L 2009 Thermal probing of energy dissipation in current-carrying carbon nanotubes *J. Appl. Phys.* **105** 10–5

[102] Thiery L, Toullier S, Teyssieux D and Briand D 2008 Thermal contact calibration between a thermocouple probe and a microhotplate *J. Heat Transfer* **130** 091601

[103] Lefèvre S, Volz S, Saulnier J B, Fuentes C and Trannoy N 2003 Thermal conductivity calibration for hot wire based dc scanning thermal microscopy *Rev. Sci. Instrum.* **74** 2418–23

[104] David L, Gomès S and Raynaud M 2007 Modelling for the thermal characterization of solid materials by dc scanning thermal microscopy *J. Phys. D. Appl. Phys.* **40** 4337–46

[105] Lefèvre S, Saulnier J B, Fuentes C and Volz S 2004 Probe calibration of the scanning thermal microscope in the AC mode *Superlattices Microstruct.* **35** 283–8

[106] Puyoo E, Grauby S, Rampnoux J M, Rouvìre E and Dilhaire S 2011 Scanning thermal microscopy of individual silicon nanowires *J. Appl. Phys.* **109** 024302

[107] Kim K, Chung J, Hwang G, Kwon O and Lee J S 2011 Quantitative measurement with scanning thermal microscope by preventing the distortion due to the heat transfer through the air *ACS Nano* **5** 8700–9

[108] Shi L and Majumdar A 2004 Micro-nano scale thermal imaging using scanning probe microscopy *Applied Scanning Probe Methods* ed B Bhusha, H Fuchs and S Hosaka (Springer Berlin Heidelberg) pp 327-62

[109] Shi L and Majumdar A 2002 Thermal transport mechanisms at nanoscale point contacts *J. Heat Transfer* **124** 329

[110] Gomès S, Trannoy N and Grossel P 1999 DC thermal microscopy: study of the thermal exchange between a probe and a sample *Meas. Sci. Technol.* **10** 805–11

[111] David L, Gomès S, Galland P, Vassort B and Raynaud M 2005 Characterization of thin films using scanning thermal microscopy in 17th European Conference on Thermophysical Properties (ECTP) Bratislava

[112] Rangelow I W, Gotszalk T, Abedinov N, Grabiec P and Edinger K 2001 Thermal nano-probe *Microelectron. Eng.* **57-58** 737–48

[113] Assy A and Gomès S 2015 Temperature-dependent capillary forces at nano-contacts for estimating the heat conduction through a water meniscus *Nanotechnology* **26** 355401

[114] Hirotani J, Amano J, Ikuta T, Nishiyama T and Takahashi K 2013 Carbon nanotube thermal probe for quantitative temperature sensing *Sensors Actuators, A Phys.* **199** 1–8

[115] Wielgoszewski G, Sulecki P, Janus P, Grabiec P, Zschech E and Gotszalk

T 2011 A high-resolution measurement system for novel scanning thermal microscopy resistive nanoprobes *Meas. Sci. Technol.* **22** 094023

[116] Wielgoszewski G, Sulecki P, Gotszalk T, Janus P, Szmigiel D, Grabiec P and Zschech E 2010 Microfabricated resistive high-sensitivity nanoprobe for scanning thermal microscopy *J. Vac. Sci. Technol. B* **28** C6N7

[117] Lefvre S and Volz S 2005 3ω - scanning thermal microscope *Rev. Sci. Instrum.* **76**

[118] Puyoo E, Grauby S, Rampnoux J M, Rouvìre E and Dilhaire S 2010 Thermal exchange radius measurement: Application to nanowire thermal imaging *Rev. Sci. Instrum.* **81** 2–6

[119] Menges F, Riel H, Stemmer A and Gotsmann B 2012 Quantitative thermometry of nanoscale hot spots *Nano Lett.* **12** 596–601

[120] Nelson B A and King W P 2007 Measuring material softening with nanoscale spatial resolution using heated silicon probes *Rev. Sci. Instrum.* **78**

[121] Assy A and Gomès S 2015 Heat transfer at nanoscale contacts investigated with scanning thermal microscopy *Appl. Phys. Lett.* **107** 043105

[122] Swartz E T and Pohl R O 1989 Thermal boundary resistance *Rev. Mod. Phys.* **61** 605–68

[123] Prasher R 2005 Predicting the thermal resistance of nanosized constrictions *Nano Lett.* **5** 2155–9

[124] Gotsmann B, Lantz M A, Knoll A and Dürig U 2009 Nanoscale thermal and mechnical interactions studied using heatable probes *Nanotechnology* vol 6, ed H Fuchs (Weinheim: Wiley-VCH) pp 121–69

[125] Nelson B A 2007 *Nanoscale Thermal Processing Using a Heated Atomic Force Microscope Tip* – Thesis (Georgia Institute of Technology)

[126] Stoner R J and Maris H J 1993 Kapitza conductance and heat-flow between solids at temperatures from 50 to 300K *Phys. Rev. B* **48** 16373–87

[127] Menges F, Riel H, Stemmer A, Dimitrakopoulos C and Gotsmann B 2013 Thermal transport into graphene through nanoscopic contacts *Phys. Rev. Lett.* **111** 205901

[128] Hinz M, Marti O, Gotsmann B, Lantz M A and Dürig U 2008 High resolution vacuum scanning thermal microscopy of HfO_2 and SiO_2 *Appl. Phys. Lett.* **92** 043122

[129] Goodson K E, Flik M I, Su L T and Antoniadis D A. 1993 Annealing-temperature dependence of the thermal conductivity of LPCVD silicon-dioxide layers *IEEE Electron Device Lett.* **14** 490–2

[130] Callard S, Tallarida G, Borghesi A. and Zanotti L 1999 Thermal

conductivity of SiO_2 films by scanning thermal microscopy *J. Non. Cryst. Solids* **245** 203–9

[131] Lefèvre S, Volz S and Chapuis P O 2006 Nanoscale heat transfer at contact between a hot tip and a substrate *Int. J. Heat Mass Transf.* **49** 251–8

[132] Yovanovich M M, Culham J R and Teertstra P 1998 Analytical modeling of spreading resistance in flux tubes , half spaces , and compound disks *IEEE Trans. Components, Packag. Manuf. Technol. Part A* **21** 168–76

[133] Alvarez F X and Jou D 2007 Memory and nonlocal effects in heat transport: From diffusive to ballistic regimes *Appl. Phys. Lett.* **90** 0–3

[134] Volz S G and Chen G 1999 Molecular dynamics simulation of thermal conductivity of silicon nanowires *Appl. Phys. Lett.* **75** 2056–8

[135] Juszczyk J, Wojtol M and Bodzenta J 2013 DC experiments in quantitative scanning thermal microscopy *Int. J. Thermophys.* **34** 620–8

[136] Gomès S, David L, Lysenko V, Descamps A, Nychyporuk T and Raynaud M 2007 Application of scanning thermal microscopy for thermal conductivity measurements on meso-porous silicon thin films *J. Phys. D. Appl. Phys.* **40** 6677–83

[137] Assy A, Lefèvre S, Chapuis P O and Gomès S 2014 Analysis of heat transfer in the water meniscus at the tip-sample contact in scanning thermal microscopy *J. Phys. D. Appl. Phys.* **47** 442001

[138] Kim K, Chung J, Won J, Kwon O, Lee J S, Park S H and Choi Y K 2008 Quantitative scanning thermal microscopy using double scan technique *Appl. Phys. Lett.* **93** 203115

[139] Kim K J and King W P 2009 Thermal conduction between a heated microcantilever and a surrounding air environment *Appl. Therm. Eng.* **29** 1631–41

[140] Volokitin A I and Persson B N J 2004 Resonant photon tunneling enhancement of the van der Waals friction. *Phys. Rev. Lett.* **69** 045417

[141] Gotsmann B and Lantz M A 2012 Quantized thermal transport across contacts of rough surfaces *Nat. Mater.* **12** 59–65

[142] Soudi A, Dawson R D and Gu Y 2011 Quantitative heat dissipation characteristics in current-carrying gan nanowires probed by combining scanning thermal microscopy and spatially resolved raman spectroscopy *ACS Nano* **5** 255–62

[143] Royall P G, Craig D Q M, Price D M, Reading M and Lever T J 1999 An investigation into the use of micro-thermal analysis for the solid state characterization of an HPMC tablet formulation *Int. J. Pharm.* **192** 97–103

[144] Six K, Murphy J, Weuts I, Craig D Q M, Verreck G, Peeters J, Brewster M and Van Den Mooter G 2003 Identification of phase separation in solid dispersions of itraconazole and eudragit® E100 using

microthermal analysis *Pharm. Res.* **20** 135–8

[145] Cahill D G, Goodson K and Majumdar A 2002 Thermometry and thermal transport in micro/nanoscale solid-state devices and structures *J. Heat Transfer* **124** 223

[146] Harding L, Wood J, Reading M and Craig D Q M 2007 Two- and three-dimensional imaging of multicomponent systems using scanning thermal microscopy and localized thermomechanical analysis *Anal. Chem.* **79** 129–39

[147] Menges F, Mensch P, Schmid H, Riel H, Stemmer A and Gotsmann B 2016 Temperature mapping of operating nanoscale devices by scanning probe thermometry *Nat. Commun.* **7** 10874

[148] Somnath S and King W P 2014 An investigation of heat transfer between a microcantilever and a substrate for improved thermal topography imaging *Nanotechnology* **25** 365501

[149] Bodzenta J, Chirtoc M and Juszczyk J 2014 Reduced thermal quadrupole heat transport modeling in harmonic and transient regime scanning thermal microscopy using nanofabricated thermal probes *J. Appl. Phys.* **116** 054501

[150] Aubry R, Jacquet J C, Weaver J, Durand O, Dobson P, Mills G, di Forte-Poisson M A, Cassette S and Delage S L 2007 SThM temperature mapping and nonlinear thermal resistance evolution with bias on AlGaN/GaN HEMT devices *IEEE Trans. Electron Devices* **54** 385–90

[151] Ho P S and Kwok T 1989 Electromigration in metals *Rep. Prog. Phys.* **52** 301

[152] Chung J, Kim K, Hwang G, Kwon O, Jung S, Lee J W J, Lee J W J and Kim G T 2010 Quantitative temperature measurement of an electrically heated carbon nanotube using the null-point method *Rev. Sci. Instrum.* **81** 114901

[153] Chung J, Kim K, Hwang G, Kwon O, Choi Y K and Lee J S 2012 Quantitative temperature profiling through null-point scanning thermal microscopy *Int. J. Therm. Sci.* **62** 109–13

[154] Hwang G, Chung J and Kwon O 2014 Enabling low-noise null-point scanning thermal microscopy by the optimization of scanning thermal microscope probe through a rigorous theory of quantitative measurement *Rev. Sci. Instrum.* **85** 114901

[155] Asnin V M, Pollak F H, Ramer J, Schurman M and Ferguson I 1999 High spatial resolution thermal conductivity of lateral epitaxial overgrown GaN/sapphire (0001) using a scanning thermal microscope *Appl. Phys. Lett.* **75** 1240

[156] Sano M, Yudasaka M, Kikuchi R and Yoshimura S 1997 Anomalous resolutions in scanning thermal microscopy of graphite *Langmuir* **13**

4493–7

[157] Zhang Y, Dobson P S, Weaver J M R, Rossi S, Alomari M, Kohn E, Bychikhin S and Pogany D 2015 Accurate measurement of thermal conductivity of nanocrystalline diamond film using scanning thermal microscopy *Unpublished*

[158] Mogro-Campero A 1982 Simple estimate of electromigration failure in metallic thin films *J. Appl. Phys.* **53** 1224

[159] Aronstein J and Hare T K 2005 AC and DC electromigration failure of aluminum contact junctions *IEEE Trans. Components Packag. Technol.* **28** 701–9

[160] Liew B K, Cheung N W and Hu C 1989 Electromigration interconnect lifetime under AC and pulse DC stress *Reliability Physics Symposium, 1989. 27th Annual Proceedings* 215-9

[161] Anon 2003 Rapid 955 Digital multimeter operator instuction manual

[162] Parker W J, Jenkins R J, Butler C P and Abbott G L 1961 Flash method of determining thermal diffusivity, heat capacity, and thermal conductivity *J. Appl. Phys.* **32** 1679

[163] Heichal Y, Chandra S and Bordatchev E 2005 A fast-response thin film thermocouple to measure rapid surface temperature changes *Exp. Therm. Fluid Sci.* **30** 153–9

[164] Ramsden E 2006 *Hall-Effect Sensors - Throry and Application* ed Edward (Amsterdam: Elsevier) pp 195

[165] McConney M E, Kulkarni D D, Jiang H, Bunning T J and Tsukruk V V 2012 A new twist on scanning thermal microscopy *Nano Lett.* **12** 1218–23

[166] Gatzen H H, Saile V and Leuthold J 2015 Lithography *Micro and Nano Fabrication Tools and Processes* ed H H Gatzen, V Saile and J Leuthold (Berlin Heidelberg: Springer-Verlag) pp 313–96

[167] Microchemicals Ltd. 2013 Application Notes - Hardbake of photoresist structures

[168] Mogab C J, Adams A C and Flamm D L 1978 Plasma etching of Si and SiO_2—The effect of oxygen additions to CF_4 plasmas *J. Appl. Phys.* **49** 3796

[169] Lee H, Chung K and Yu J 2009 Selective etching of thick Si_3N_4, SiO_2 and Si by using CF_4/O_2 and C_2F_6 gases with or without O_2 or Ar addition *J. Korean Phys. Soc.* **54** 1816–23

[170] Klapetek P, Ohlídal I and Buršík J 2006 Applications of scanning thermal microscopy in the analysis of the geometry of patterned structures *Surf. Interface Anal.* **38** 383–7

[171] Zhou L, Xu G Q, NG H T and Li S F Y 1997 Scanning thermal microscope tip-induced chemical reaction on solid organometallic

compound thin films *J. Vac. Sci. Technol. B* **15** 1871

[172] Shi L, Plyasunov S, Bachtold A, McEuen P L and Majumdar A 2000 Scanning thermal microscopy of carbon nanotubes using batch-fabricated probes *Appl. Phys. Lett.* **77** 4295

[173] Klapetek P 2013 Local current measurements *Quantitative Data Processing in Scanning Probe Microscopy: SPM Application for Nanometrology* (Burlington: Elsevier) pp 221–45

[174] Hsu J W P 2001 Near-field scanning optical microscopy studies of electronic and photonic materials and devices *Mater. Sci. Eng.* **33** 1–50

[175] Dryakhlushin V F, Klimov A Y, Rogov V V. and Vostokov N V. 2005 Near-field optical lithography method for fabrication of the nanodimensional objects *Appl. Surf. Sci.* **248** 200–3

[176] Fenwick O, Latini G and Cacialli F 2004 Modelling topographical artifacts in scanning near-field optical microscopy *Synth. Met.* **147** 171–3

[177] Banerjee G and Rhoades R L 2008 Chemical mechanical planarization historical review and future direction *ECS Trans.* **13** 1–19

[178] Kolosov O V, Grishin I and Jones R 2011 Material sensitive scanning probe microscopy of subsurface semiconductor nanostructures via beam exit Ar ion polishing. *Nanotechnology* **22** 185702

[179] Docherty K E, Thoms S, Dobson P and Weaver J M R 2008 Improvements to the alignment process in a commercial vector scan electron beam lithography tool *Microelectron. Eng.* **85** 761–3

[180] Brophy J J, Epstein M and Webb S L 1965 Correlator-amplifier for very low level signals *Rev. Sci. Instrum.* **36** 1803–6

[181] Zhou H, Elgaid K, Wilkinson C and Thayne I 2006 Low-hydrogen-content silicon nitride deposited at room temperature by inductively coupled plasma deposition *Jpn. J. Appl. Phys.* **45** 8388–92

[182] Wind S J, Gerber P D and Rothuizen H 1998 Accuracy and efficiency in electron beam proximity effect correction *J. Vac. Sci. Technol. B* **16** 3262

[183] Docherty K E 2010 *Improvements to the alignment process in electron-beam lithography* – Thesis (University of Glasgow)

[184] Lebedev M V., Mankel E, Mayer T and Jaegermann W 2008 Wet etching of GaAs (100) in acidic and basic solutions: A synchrotron−photoemission spectroscopy study *J. Phys. Chem. C* **112** 18510–5

[185] Kastenmeier B E E, Matsuo P J, Beulens J J and Oehrlein G S 1996 Chemical dry etching of silicon nitride and silicon dioxide using $CF_4/O_2/N_2$ gas mixtures *J. Vac.* **14** 2802–13

[186] Williams K R, Gupta K and Wasilik M 2003 Etch rates for micromachining processing - Part II *J. Microelectromechanical Syst.* **12**

761–78

[187] Thoms S and Macintyre D S 2010 Linewidth metrology for sub-10-nm lithography *J. Vac. Sci. Technol. B* **28** C6H6

[188] Gorbunov V V., Fuchigami N, Hazel J L and Tsukruk V V 1999 Probing surface microthermal properties by scanning thermal microscopy *Langmuir* **15** 8340–3

[189] Sultan R, Avery A D, Underwood J M, Mason S J, Bassett D and Zink B L 2013 Heat transport by long mean free path vibrations in amorphous silicon nitride near room temperature *Phys. Rev. B* **87** 214305

[190] Zhang X and Grigoropoulos C P 1995 Thermal conductivity and diffusivity of free-standing silicon nitride thin films *Rev. Sci. Instrum.* **66** 1115–20

[191] Canchal-Arias D and Dawson P 2005 Measurement and interpretation of the mid-infrared properties of single crystal and polycrystalline gold *Surf. Sci.* **577** 95–111

[192] Bahadur V, Xu J, Liu Y and Fisher T S 2005 Thermal resistance of nanowire-plane interfaces *J. Heat Transfer* **127** 664

[193] Wielgoszewski G and Gotszalk T 2015 Scanning thermal microscopy (SThM): How to map temperature and thermal properties at the nanoscale *Advances in Imaging and Electron Physics* vol 190, ed P W Hawkes (London: Elsevier Inc.) pp 177–221

[194] Rölke J 1981 Nichrome thin film technology and its application *Electrocompon. Sci. Technol.* **9** 51–7

[195] Cumming D R S, Thoms S, Weaver J M R and Beaumont S P 1996 3 nm NiCr wires made using electron beam lithography and PMMA resist *Microelectron. Eng.* **30** 423–5

[196] Elgaid K, Edgar D L, Ferguson S M, Beaumont S P and Thayne I G 2001 Fabrication of on-wafer MMIC compatible integrated NiCr loads *Microelectron. Eng.* **57-58** 801–6

[197] Jones W and March N H 1985 *Theoretical Solid State Physics: Non-Equilibrium and Disorder* (Mineola, NY: Dover Publications)

[198] Cardenas C, Fabris D, Tokairin S, Madriz F and Yang C Y 2012 Thermoreflectance measurement of temperature and thermal resistance of thin film gold *J. Heat Transfer* **134** 111401

[199] Ftouni H, Blanc C, Tainoff D, Fefferman A D, Defoort M, Lulla K J, Richard J, Collin E and Bourgeois O 2015 Thermal conductivity of silicon nitride membranes is not sensitive to stress *Phys. Rev. B* **92** 125439

[200] Bodzenta J, Juszczyk J and Chirtoc M 2013 Quantitative scanning thermal microscopy based on determination of thermal probe dynamic resistance. *Rev. Sci. Instrum.* **84** 093702

[201] Chapra S C 2012 Applied numerical methods with matlab for engineers

and scientists *Applied Numerical Methods with MATLAB for Engineers and Scientists* ed M Lange (New York: McGraw-Hill) pp 628–40

[202] Derjaguin B V, Muller V M and Toporov Y P 1975 Effect of contact deformations on the adhesion of particles *J. Colloid Interface Sci.* **53** 314–26

[203] Liu J, Notbohm J K, Carpick R W and Turner K T 2010 Method for characterizing nanoscale wear of atomic force microscope tips *ACS Nano* **4** 3763–72

[204] Gundrum B C, Cahill D G and Averback R S 2005 Thermal conductance of metal-metal interfaces *Phys. Rev. B* **72** 245426

[205] Puyoo E, Grauby S, Rampnoux J, Claeys W, Rouviere E and Dilhaire S 2010 Simultaneous topographic and thermal imaging of silicon nanowires using a new SThM probe *Therm. Investig. ICs Syst. (THERMINIC), 2010 16th Int. Work.* 1–6

[206] Baker R J 2008 *CMOS Circuit Design, Layout, and Simulation* ed S K Tewksbury and J E Brewer (Honoken, New Jersey: John Wiley & Sons Ltd.)

[207] Hwang G and Kwon O 2016 Measuring the size dependence of thermal conductivity of suspended graphene disks using null-point scanning thermal microscopy *Nanoscale* **8** 5280–90

[208] Chen S, Moore A L, Cai W, Suk J W, An J, Mishra C, Amos C, Magnuson C W, Kang J, Shi L and Ruoff R S 2011 Raman measurements of thermal transport in suspended monolayer graphene of variable sizes in vacuum and gaseous environments *ACS Nano* **5** 321–8

[209] Chiang T Y, Banerjee K and Saraswat K C 2002 Analytical thermal model for multilevel VLSI interconnects incorporating via effect *IEEE Electron Device Lett.* **23** 31–3

[210] Chen Z, Lin Y-M, Rooks M J and Avouris P 2007 Graphene nano-ribbon electronics *Phys. E Low-dimensional Syst. Nanostructures* **40** 228–32

[211] Yang N, Zhang G and Li B 2009 Thermal rectification in asymmetric graphene ribbons *Appl. Phys. Lett.* **95** 033107

[212] Yovanovich M M 1998 Conduction and thermal contact resistance (Conductance) *Handbook of Heat Transfer* ed W M Rohsenow, J P Hartnett and Y I Cho (New York: McGraw-Hill) pp 111–83

[213] Yovanovich M M, Muzychka Y S and Culham J R 1999 Spreading resistance of isoflux rectangles and strips on compound flux channels *J. Thermophys. Heat Transf.* **13** 495–500

[214] Ge Y, Zhang Y, Weaver J M R, Zhou H and Dobson P S 2015 Topography-free sample for thermal spatial response measurement of scanning thermal microscopy *J. Vac. Sci. Technol. B* **33** 06FA03

[215] Schmidt A J, Cheaito R and Chiesa M 2010 Characterization of thin

metal films via frequency-domain thermoreflectance *J. Appl. Phys.* **107** 024908

[216] Parfenova M A, Protasov D Y, Malin T V, Nastoviak A E, Devyatova S F and Zhuravlev K S 2014 Study of gallium nitride surface treatment prior to PE CVD SiN_x:H passivation *2014 15th International Conference of Young Specialists on Micro/Nanotechnologies and Electron Devices (EDM)* (IEEE) pp 36–8

[217] Hattangady S V, Fountain G G, Rudder R A and Markunas R J 1989 Low hydrogen content silicon nitride deposited at low temperature by novel remote plasma technique *J. Vac. Sci. Technol. A* **7** 570

[218] Jansen A G M, van Gelder A P and Wyder P 1980 Point-contact spectroscopy in metals *J. Phys. C Solid State Phys.* **13** 6073–118

[219] Incropera R P, Dewitt D P, Bergman T L and Lavine A S 2006 *Fundamentals of Heat and Mass Transfer* (Chichester, United Kingdom: John Wiley & Sons Ltd)

[220] Laraoui A, Aycock-Rizzo H, Gao Y, Lu X, Riedo E and Meriles C A 2015 Imaging thermal conductivity with nanoscale resolution using a scanning spin probe *Nat. Commun.* **6** 8954

[221] Smith A N, Hostetler J L and Norris P M 2000 Thermal boundary resistance measurements using a transient thermoreflectance technique *Microscale Thermophys. Eng.* **4** 51–60

[222] Stevens R J, Smith A N and Norris P M 2005 Measurement of thermal boundary conductance of a series of metal-dielectric interfaces by the transient thermoreflectance technique *J. Heat Transfer* **127** 315

[223] Yang J, Ziade E and Schmidt A J 2016 Uncertainty analysis of thermoreflectance measurements *Rev. Sci. Instrum.* **87** 014901

[224] Lee S M and Cahill D G 1997 Heat transport in thin dielectric films *J. Appl. Phys.* **81** 2590

[225] Chien H, Yao D, Huang M and Chang T 2008 Thermal conductivity measurement and interface thermal resistance estimation using SiO_2 thin film *Rev. Sci. Instrum.* **79** 054902

[226] Jeong T, Zhu J, Chung S and Gibbons M R 2012 Thermal boundary resistance for gold and CoFe alloy on silicon nitride films *J. Appl. Phys.* **111** 083510

[227] Kiracofe D and Raman A 2012 Nonlinear dynamics of the atomic force microscope at the liquid-solid interface *Phys. Rev. B* **86** 205405

[228] Thoms S, Zhang Y and Weaver J M R 2014 Improved alignment algorithm for electron beam lithography *J. Vac. Sci. Technol. B* **32** 06F509

APPENDIX I

CODE FOR CONTROLLING THE MBED NXP LCP 1768 DEVELOPMENT BOARD

Keynotes:

- The data was recorded every 10 minutes for 24 hours;
- Three AnalogIn pins were used together for three probes in test: p15, p16 and p17 for probe biased at 1 mA, 1.5 mA and 2 mA respectively;

Code:

```
//********SThM Probe Stability Test for 1mA 1.5mA and 2 mA ********//
//********* Yunfei Ge ********//
//********* 05/Dec/2013 *******//

#include "mbed.h"
LocalFileSystem local("local");   // Create the local filesystem under the name "local"
Timer t;                          // Timer for receiving data per hour

AnalogIn voltage1(p15);           // p15 receives data from probe one: 1 mA
AnalogIn voltage2(p16);           // p16 receives data from probe two: 1.5 mA
AnalogIn voltage3(p17);           // p17 receives data from probe three: 2 mA

int main()
{
int a=60*60*24;                   // The total number that the mbed counts: 1day = 60s*60min*24h
    int i=0;                      // +600 when every loop finished


    float v1=0.0;
    float v2=0.0;
    float v3=0.0;          // Define the floating number v1, v2 and v3 for storing the data

  FILE *fp1 = fopen("/local/out1.txt", "w");  // Open "out1.txt" on the local file system
for writing
```

```
    FILE *fp2 = fopen("/local/out2.txt", "w");  // Open "out2.txt" on the local file system
   for writing
    FILE *fp3 = fopen("/local/out3.txt", "w");  // Open "out3.txt" on the local file system
   for writing

     while(a-i>0) {
                          // Pick up data every 10 mins (the value in the function wait means only the
   wait(60*10);           seconds)

   v1 = voltage1;       // Read the value of p15 by a float variable

   v2 = voltage2;       // Read the value of p16 by a float variable

   v3 = voltage3;          // Read the value of p17 by a float variable

   fprintf(fp1,"%f, \n",v1);// Write the value of the p19 into the file that is stored in the flash of mbed
   fprintf(fp2,"%f, \n",v2);// Write the value of the p20 into the file that is stored in the flash of mbed
   fprintf(fp3,"%f, \n",v3);// Write the value of the p17 into the file that is stored in the flash of mbed

   i=i+60*10;             //Record the data every 10 min
  }

fclose(fp1);              // When using .txt file to save data, it is possible to save multiple datas into
fclose(fp2);              one file
fclose(fp3);
}
```

APPENDIX II

FABRICATION PROCESS OF TOPOGRAPHY-FREE SAMPLE

1. **Markers**

   Substrate clean – for both the GaAs and covering quartz, acetone 5 min with ultrasonic + IPA 5 min with ultrasonic.

   Resist spinning – 12 % 2010 PMMA spin 5000 rpm for 60 s, 160 °C hot plate baking for 7 min. 2.5 % 2041 PMMA spin 5000 rpm for 60 s, 160 °C hot plate baking for 7 min.

   Ebeam exposure – VB6 ebeam lithography. Dose 600 μC/cm^2, beam current 64 nA, VRU 25 nm.

   Development – IPA: MIBK 1:1 at 23 °C for 60 s, IPA rinse for 30 s.

   Metallisation – barrel ash 80 W for 30 s (by PlasmaFab), Ti/Au 50 nm / 150 nm evaporation, liftoff in 50 °C warm acetone for 30 min, IPA rinse and blow dry without RO water.

2. **Gold pads**

   Resist spinning – 4 % 2010 PMMA spin 5000 rpm for 60 s, 160 °C hot plate baking for 7 min. 2.5 % 2041 PMMA spin 5000 rpm for 60 s, 160 °C hot plate baking for 7 min.

   Ebeam exposure – VB6 ebeam lithography. Dose 600 μC/cm^2, beam current 64 nA, VRU 25 nm.

   Development – IPA: MIBK 2:1 at 23 °C for 60 s, IPA rinse for 30 s

   Metallisation – barrel ash 80 W for 30 s (by PlasmaFab), Au 20 nm evaporation without Ti as sticky layer, liftoff in 50 °C warm acetone for 4 hours, IPA rinse and blow dry without RO water.

3. **Gold narrow wires**

   Resist spinning – 2.5 % 2010 PMMA (for 25 nm to 75 nm wires)/ 4 % 2010 PMMA (for > 200 nm wires) spin 5000 rpm for

60 s, 180 °C hot plate baking for 10 min. 2.5 % 2041 PMMA spin 5000 rpm for 60 s, 180 °C hot plate baking for 10 min.

Ebeam exposure – VB6 ebeam lithography. Dose 650 μC/cm^2, beam current 1 nA, VRU 2 nm.

Development – IPA: MIBK 3:1 at 23 °C for 30 s (for 25 nm to 75 nm wires), IPA: MIBK 2.5:1 at 23 °C for 30 s (for > 200 nm wires), IPA rinse for 30 s.

Metallisation – barrel ash 80 W for 30 s (by PlasmaFab), Au 20 nm evaporation without Ti as sticky layer, liftoff in 50 °C warm acetone for 4 hours, IPA rinse and blow dry without RO water.

4. Replaced substrate

SiN_x deposition – ICP CVD SiH_4/N_2 = 7/6 sccm, ICP/Platen = 100/0 W, 4 mTorr at 25 °C for 25 min giving 400 nm thick low stress SiN_x.

Epoxy formation – SU-8 3050 spinning: 500 rpm with 100 rpm/s ramp for 5s, 2000 rpm for 30 s, then stop with 10000 rpm/s.

65 °C hot plate baking for 10 min, 95 °C hot plate baking for 2 hours.

Repeat SU-8 3050 spinning by the same settings.

65 °C hot plate baking for 10 min, 95 °C hot plate baking for 4 hours.

Quartz covering – Cover the sample with a piece of quartz on the hot plate, waiting for the quartz to be flat, MA6 flood exposure to crosslink the SU-8 3050, hardbake at 65 °C hot plate for 2 min, then 95 °C hot plate for 2 min. Repeat another twice.

5. Sacrificed substrate removal

Wet etching – citric acid: H_2O_2 5:1 with 30 °C water bath shaking 80 times/min for ~ 30 hours.

APPENDIX III

FABRICATION PROCESS OF JOHNSON NOISE CALIBRATION DEVICE

Initial wafer: 3-inch 400-μm thick silicon wafer with LPCVD 100 nm SiN_x deposited in Chalmers.

1. **Membrane, cleave pattern and etched markers defining**

   Wafer topside protection – S1818 spin 4000 rpm for 30 s, bake in 90 °C oven for 30 min.

   Backside resist spin – Primer 80/20 spin 4000 rpm for 5s, without delaying, S1818 spin 4000 rpm for 30 s, bake in 90 °C oven for 30 min.

   Exposure and development– MA6 set as hard contact for 5 s, MicroDeveloper: RO water 1: 1 for 75 s, RO water rinse for 30 s, postbake in 120 °C oven for 20 min.

   SiN_x stripping – BP80 RIE 20 sccm C_2F_6 at 100 W with 15 mTorr pressure for 5 min, acetone and IPA clean for 5 min without ultrasonic to clean the resist, barrel ash 200 W for 5 min.

   Silicon wet etch – 7 mol KOH at 115 °C gives ~ 4.1 μm/min etching rate for 80 min.

2. **Gold wires and bondpads defined by photolithography**

   Resist spin – dehydration on 200 °C hotplate for 5 min, spin LOR 3A 3000 rpm for 60 s, bake on 190 °C hot plate for 5 min, cool down to room temperature, spin S1818 4000 rpm for 30 s, bake on 118 °C hot plate for 75 s.

   Exposure and development – MA6 backside alignment to the wet etch

marker, set as hard contact for 5 s, MicroDeveloper: RO 1: 1 for 75 s, RO water rinse for 30s, barrel ash 40 W for 30 s, hardbake on 129 °C hot plate for 5 min, undercut by CD 26 for 90 s, RO water rinse for 30 s, barrel ash 40 W for 30 s.

Metallisation – NiCr 5 nm with Au 165 nm by Plassys II/IV, liftoff in warm SVC14 for 6 hours.

3. **Gold patterns defined by EBL on the membrane**

Resist spin – 8 % 2010 PMMA spin 2500 rpm for 30 s, bake in 180 °C oven for 15 min, 4 % 2041 PMMA spin 2500 rpm for 30 s, bake in 180 °C oven for 90 min.

Ebeam exposure – VB6 ebeam lithography. Dose 650 μC/cm^2, beam current 128 nA, VRU 50 nm for gold shields and beam current 2 nA, VRU 8 nm for other features.

Development – 2.5: 1 IPA: MIBK at 23 °C for 60 s, barrel ash 80 W for 30 s.

Metallisation – NiCr 15 nm with Au 165 nm by Plassys II/IV, liftoff in warm acetone for 2 hours with 15 s ultrasonic.

4. **Heaters and 4-terminal resistor defining**

Resist spin – 8 % 2010 PMMA spin 5000 rpm for 60 s, bake in 120 °C oven for 90 min.

Ebeam exposure – VB6 ebeam lithography. Dose 1000 μC/cm^2, beam current 1 nA, VRU 2 nm.

Development – 1: 1 IPA: MIBK at 23 °C for 30 s, barrel ash 80 W for 30 s.

Gold etch – solution of 0.15 mol I_2 in 1 molar KI for 15 s, RO water rinse for 5 min.

5. **Membrane and cleave pattern final defining**

Silicon gentle wet etch – 25 % 1.4 L TMAH with 350 mL IPA at 80 °C gives ~ 300 nm/min etch rate for 165 min

Final cleanness – Methanol rinse for several times due to the small surface tension it has.

APPENDIX IV

MATLAB CODE OF COMBINED FIN MODEL

i. Code for determining the "h_s" value

```
%%%%%%%% Calculate the equivalent heat transfer coefficient
"hs" %%%%%%%%%

%%% define parameters used in the equation %%%
t = 50e-9;      % thickness of gold
k = 250;        % thermal conductivity of gold
syms w;         % define the width as a variable
L = 5e-6;       % length of the gold pad
R0 = 50e-9;     % contact radius between the probe and sample
R1 = w./2;      % radius of the radial fin

ha = 100000;        % heat transfer coefficient for air
syms hs;        % define the hs as a variable

m = sqrt((ha+hs)./(t*k)); % m value for Radial Fin

%%% Solve the Bessel function of zero order and 1st order %%%

% 1. solve the Bessel function for using in boundary condition 1 %

z0 = m.*R0;

I00 = besseli(0,z0);
K00 = besselk(0,z0);

% 2. solve the Bessel function for using in boundary condition 2 %

z1 = m.*(R1);

I01 = besseli(0,z1);
K01 = besselk(0,z1);

% 2. solve the Bessel function for using in qf %

I10 = besseli(0,z0);
K10 = besselk(0,z0);

% Solve the C1 and C2 %

[C1,C2]=solve('C1*I00+C2*K00=1','C1*I01+C2*K01=0','C1,C2');

C1value = eval(C1);
C2value = eval(C2);

%%% define the heat flux in the radial fin as qf %%%
```

```
qf = 2*pi*k*R0*t*m.*(C2value.*K10-C1value.*I10);  % heat flux in the
fin
qflim = limit(qf,w,inf); % finding the answer when w -> infinite

Rradi = 1./qflim    % calculate the thermal resistance of the radial
fin
```

ii. Code for determining the R_{Au} of 200 nm and 400 nm wide wires

```
%%%%%%%% Calculate the thermal resistance of gold wires %%%%%%%%%
% parameters for gold wires: START%
t = 50e-9;      % thickness of gold
k = 250;        % thermal conductivity of gold
w = 200e-9;     % for the 200 nm wide wires
% w = 200e-9;   % for the 400 nm wide wires
L = (400e-9:100e-9:2.5e-6);       % length of the gold wire
Lc = L + t/2;   % corrected length of the gold wire for convection
tip
R0 = 50e-9;     % contact radius between the probe and sample
R1 = w/2;       % radius of the radial fin
% parameters for gold wires: END%
% parameters for radial and straight fins: START %
ha = 100000;         % heat transfer coefficient for air
hs = 3.146e7;   % hs determined
m = sqrt((ha+hs)./(t*k)); % m value for radial fin: m = square root
(h/tk)
ms = sqrt(((ha*pi*R1)+(hs*(pi*R1+s*t)))./(k*pi*R1*t)) % m value for
rectangular fin
% parameters for radial and straight fins: START %

Arec1 = (w*L)./2; % area of half of the rectangular fin
Arec2 = ((w+2*t)*L)./2; area of half of the rectangular fin

msL = (ms.*Lc)./2;        % mL value for rectangular fin
theta = tanh(msL)./msL;  % efficiency of the rectangular fin
Rrec = 1./(theta.*(Arec1.*ha + Arec2.*hs)); % thermal resistance of
rectangular fin
hc = 1./ (Rrec.*(pi*R1.*t));  % hc is the heat transfer coefficient
of the sidewall of
                                    % half of radial fin
%%% Solve the Bessel function of zero order and 1st order: START %%%

% 1. solve the Bessel functio for using in boundary condition 1 %

z0 = m.*R0;
I00 = besseli(0,z0);
K00 = besselk(0,z0);

I10 = besseli(1,z0);
K10 = besselk(1,z0);

% 2. solve the Bessel functio for using in boundary condition 2 %
```

```
z1 = m.*(R1);

I01 = besseli(0,z1);
I11 = besseli(1,z1);
K01 = besselk (0,z1);
K11 = besselk(1,z1);

% Solve the C1 and C2 %

A = 2*(w/2).*pi*t;   % area of the edge of the radial fin
[C1,C2]=solve('C1*I00+C2*K00=1','hc*A*(C1*I01+C2*K01)+
k*A*(C1*m*I11-   C2*m*K11)=0','C1,C2'); % Solve the two boundary
conditions

C1value = eval(C1);
C2value = eval(C2);
%%% Solve the Bessel function of zero order and 1st order: END %%%
%%% calculate the thermal resistance of the radial fin: START %%%

qf = 2*pi*k*R0*t*m*(C2value.*K10 - C1value.*I10);  % heat flux in
the fin

thetaradi = qf./(hs*pi*(R1^2-R0^2) + ha*pi*(R1^2-R0^2) +
hc*2*pi*R1*t); % efficiency of

 % the radial fin

Aradi = pi*(R1^2-R0^2);   % surface area of the radial fin of the
upper side or lower side

Rradi = 1./(thetaradi.*(hs*pi*(R1^2-R0^2) + ha*pi*(R1^2-R0^2) +
hc*2*pi*R1*t));

Rradi2 = 1./qf;             % thermal resistance of the gold wire
%%% calculate the thermal resistance of the radial fin: END %%%
```

iii. Code for determining the R_{Au} with different contact positions

```
%%%%%%%% Calculate the thermal resistance of gold wires %%%%%%%%%

% parameters for gold wires: START %
   KEEP SAME AS BEFORE
% parameters for gold wires: END %
% parameters for radial and straight fins: START %
   KEEP SAME AS BEFORE
% parameters for radial and straight fins: END %

N = (2:1:100); % divider

ArecA = (w*L)./N; % area of the rectangular fin with air
ArecS = ((w+2*t)*L)./N; area of the rectangular fin with SiN

ArecA2 = (N-1).*(w*L)./N; % area of the other part rectangular fin
with air
```

```
ArecS2 = (N-1).*((w+2*t)*L)./N; area of the other part rectangular
fin with SiN


msL1 = (ms.*Lc)./N;          % mL value for rectangular fin 1
msL2 = (N-1).*(ms.*Lc)./N;  % mL value for rectangular fin 2

theta1 = tanh(msL1)./msL1;  % efficiency of the rectangular fin 1
theta2 = tanh(msL2)./msL2;  % efficiency of the rectangular fin 2

Rrec1 = 1./(theta1.*(ArecA.*ha + ArecS.*hs)); % thermal resistance
of rectangular fin 1
Rrec2 = 1./(theta2.*(ArecA2.*ha + ArecS2.*hs)); % thermal resistance
of rectangular fin 1
Rrec = (Rrec1.*Rrec2)./(Rrec1+Rrec2); % thermal resistance of
rectangular in parallel

hc = 1./ (Rrec.*(2*pi*R1.*t));  % hc is the heat transfer
coefficient of the sidewall of
                                    % half of radial fin

%%% Solve the Bessel function of zero order and 1st order: START %%%
   KEEP THE SAME AS BEFORE
%%% Solve the Bessel function of zero order and 1st order: END %%%

%%% calculate the thermal resistance of the radial fin: START %%%
   KEEP THE SAME AS BEFORE
%%% calculate the thermal resistance of the radial fin: END %%%
```